

Redox dual-flow battery for combined electricity storage and hydrogen production

Présentée le 28 janvier 2022

Faculté des sciences de base
Laboratoire d'électrochimie physique et analytique
Programme doctoral en chimie et génie chimique

pour l'obtention du grade de Docteur ès Sciences

par

Danick REYNARD

Acceptée sur proposition du jury

Prof. K. Sivula, président du jury
Prof. H. Girault, directeur de thèse
Dr K. Toghill, rapporteuse
Dr D. Crettenand, rapporteur
Dr L. Gubler, rapporteur

To my dear grandfather...

À mon cher grand-père...

*« Sans la curiosité de l'esprit, que serions-nous?
Telle est la beauté et la noblesse de la science: un
désir sans fin de repousser les frontières du savoir,
de traquer les secrets de la matière et de la vie sans
idée préconçue des conséquences éventuelles. »*

Marie Curie

*« Pour examiner la vérité, il est besoin, une fois
dans sa vie, de mettre toutes choses en doute autant
qu'il se peut. »*

René Descartes

*« The more I learn, the more I realize how much I
don't know. »*

Albert Einstein

*« You can't connect the dots looking forward, you
can only connect the dots looking backwards. So you
have to trust that the dots will somehow connect in
your future. You have to trust in something - your
gut, destiny, life, karma, whatever. This approach
has never let me down, and it has made all the
difference in my life. »*

Steve Jobs

Acknowledgements

The accomplishment of a thesis is a long and difficult path full of pitfalls. This journey would not have been possible without the contribution and the support of many people.

First and foremost, I would like to express my sincere gratitude to my thesis advisor, Professor Hubert Girault for giving me the opportunity to achieve a PhD in LEPA. I sincerely thank him for the trust and the support. During those years, I appreciated his scientific spirit full of optimism, creativity and determination. I was inspired by his motivation to always relieve new challenges and broaden his knowledge in various field of science.

It was my honor to have Professor Kevin Sivula, Doctor Kathryn Toghil, Doctor David Crettenand and Doctor Lorenz Gubler as members of the Jury. I would like to acknowledge them for taking the time to read and review my thesis and for the fruitful discussion and the relevant suggestions they gave me during the oral exam.

This thesis would not have been possible without the help of many scientific collaborators in LEPA. First of all, I would like to thank the members of the Martigny team, where I started my PhD journey. I am especially grateful to Dr. Alberto Battistel and Dr. Christopher Dennison who introduced me to the beautiful world of electrochemistry and Dr. Heron Vrabel who was the great pioneer of the demonstrator and helped me a lot with his outstanding scientific and technical skills. I would like also to thank Dr. Véronique Amstutz and Dr. Yorick Ligen for their continuous help and support. In the laboratory of Sion, I am especially grateful to Dr. Pekka Peljo and Dr. Bhawna Nagar for their help and a special thank for Dr. Sunny Maye and Dr. Mikaël Frossard for their scientific support and their friendship. Finally, since LEPA is a very big family, I would like to thank all the people I met during these four years of PhD. It was a chance to work and discuss with all of you and I will remind for long many of our adventures we had.

I would like to express my deep gratitude to the secretaries of LEPA for their administrative and mental support: Patricia Byron, Sandrine Jaussi, Annick Evéquoz and Chantal Donaghey (it sounds like you are part of LEPA to me). Thank you for your constant help and your kindness.

This work would not have been completed without all the collaborators of EPFL Valais who make our life easier. I would like to sincerely thank Laurent Seydoux and Annabelle Coquoz from the chemical store for their availability and their warm welcome in all instances (with the renown slogan of the shop: "Revenez quand vous voulez"). I also want to thank Cédric Passerini et Jean Perruchoud from the IT Support, Patrick Favre from the electronic workshop and Stéphane Voeffray and Robin Délèze from the mechanical workshop for their continuous help and technical support. Furthermore, I would like to thank Dr. Emad Oveisi, Dr. Natalia Gasilova and Dr. Mounir Mensi for their precious help regarding the analytical equipment (SEM, MS and XPS). Finally, I am also thankful to all the technical team of EPFL.

Besides my research activities, it was a great pleasure for me spending time for the teaching duties. I strongly believe that I learn a lot from my students. I would like to thank all of them

and I address a special thanks to Guillaume Bolik-Coulon and Vimanshu Chanda that I had the opportunity to supervise for their Master thesis.

L'accomplissement d'une thèse va bien au-delà des compétences professionnelles et intellectuelles. En fin de compte, le diplôme n'a que peu d'importance lorsque l'on met en lumière l'enrichissement sur le plan personnel acquis lors de cette aventure. Une expérience qui peut se comparer à un marathon semé d'embûches testant l'endurance de notre esprit et de notre mental face au stress, à la frustration, à l'échec, à la remise en question, à la solitude et à l'abnégation. Toutes ces étapes font partie intégrante de l'expérience et contribue fortement à la réussite de l'épreuve. Cependant, ce marathon n'aurait pas été possible sans l'énorme soutien de mes proches.

Tout d'abord, j'aimerais remercier tous mes amis qui m'ont tant apporté ces dernières années. Que ce soit en Valais, à Lausanne (ou plus précisément à l'Arcadie) ou ailleurs, j'ai eu la chance de m'entourer de personnes extraordinaires avec qui j'ai partagé des moments inoubliables (dans la joie ou dans la tristesse). Merci pour tous ces bons souvenirs et pour tout votre soutien: Carole, Jo, Quennoz, Dimi, Denis, Cha, Laura, Marie, Chloé, Elo, Benoit, Alex, Swen, Lenny, Ricky, Vince, Romaine, Sandrine, Julien, J-F, Guillaume, Jean, Etienne, Aurélien, Aline, Gontran, Robin, et encore bien d'autres...

La fin de cette thèse restera marquée par ma rencontre avec 'mi querida' Vanessa Moren. Je la remercie infiniment de m'avoir accompagné jusqu'au bout de ce périple avec tant de bienveillance et de tendresse. Merci pour son encouragement quotidien, son optimisme et sa capacité à me redonner le sourire en toutes circonstances. Merci également à la famille Moren-Abbet pour leur chaleureux accueil et les bons moments partagés.

Finalement, comment ne pas finir ces remerciements en adressant ma sincère gratitude à ma famille qui m'a soutenu de manière inconditionnelle depuis le début de mes études. J'aimerais remercier mon frère Dan, sa chérie Priscilla et mon neveu Evan (Tu n'es pas obligé de faire autant d'années d'études que 'ponpon', mais je te souhaite de rester curieux toute ta vie et de ne jamais perdre l'envie d'apprendre). Je remercie tendrement mes grands-parents Hermanda et Clément pour leur générosité et leur amour. Pour clôturer ces remerciements, j'aimerais exprimer ma profonde gratitude envers ma très chère maman Daniella, sans qui rien de cela n'aurait été possible. Beaucoup d'années se sont écoulées depuis ma première année d'école, mais une chose est sûre, elle n'a jamais douté de moi et m'a toujours encouragé dans mes choix. Un merci infini pour son éducation, son soutien, sa confiance et son amour inconditionnel. Cette thèse est pour elle.

Abstract

The energy transition towards a carbon-neutral and sustainable economy is one of the greatest challenges of the 21st century to combat global warming and pollution. The decarbonization process is affecting every sector of the economy (electricity, transportation, industrial...). For power generation, renewable energy resources are realistic alternatives to replace fossil resources such as gas and coal. However, the intermittent nature of wind and solar power limits their penetration into the conventional grid and increases the need for energy storage (battery, hydrogen storage...) for smoothing out fluctuations between electric supply and demand.

In this context, the concept of the redox dual-flow battery was introduced to propose a hybrid storage solution that can store electrical energy both electrochemically and in the form of hydrogen fuel. The system differs from a traditional redox flow battery by including a secondary energy platform, in which the electrolytes can be discharged chemically in external catalytic reactors through redox-mediated water electrolysis to produce clean hydrogen. The dual storage feature improves the flexibility and enhances significantly the capacity of the system by storing energy beyond the capacity of the electrolytes in the form of hydrogen. Additionally, the redox-mediated water electrolysis offers several advantages over conventional electrolysis in terms of safety, durability and purity.

In this thesis, the proof-of-concept of a dual-flow circuit using a vanadium-manganese redox flow battery for combined electricity storage and hydrogen production is demonstrated. The redox flow battery employs vanadium sulfate (V^{3+}/V^{2+}) and manganese sulfate (Mn^{3+}/Mn^{2+}) dissolved in concentrated sulfuric aqueous solution as negative and positive electrolyte, respectively. The galvanic cell achieves energy efficiency of 68% at a current density of 50 $mA \cdot cm^{-2}$ (cell voltage = 1.92 V) and a relative battery energy density 45% higher than the conventional all-vanadium RFB in the same conditions. Once charged, the electrolytes can be spontaneously discharged through redox-mediated oxygen evolution reaction (OER) and hydrogen evolution reaction (HER) in RuO_2 and Mo_2C catalytic reactors, resulting in an energy consumption for hydrogen production of ca. 50 kWh/kg H_2 . The system provides a competitive alternative for large-scale energy storage in renewable energy and transport applications.

Keywords: Redox flow battery, hydrogen, energy storage, water electrolysis, redox mediator

Résumé

La transition énergétique vers une économie durable et neutre en carbone est l'un des plus grands challenges du 21^{ème} siècle dans la lutte contre le réchauffement climatique et la pollution. Le procédé de décarbonisation affecte tous les secteurs de l'économie (électricité, transport, industrie...). Concernant la production électrique, les énergies renouvelables sont considérées comme des alternatives réalistes aux énergies fossiles telles que le charbon et le gaz. Cependant, la nature intermittente de ces énergies limite l'implémentation de ces centrales au sein du réseau électrique et augmente les besoins en termes de stockage d'énergie (batteries, hydrogène...) pour atténuer les fluctuations entre l'approvisionnement et la demande en électricité.

Dans ce contexte, le concept de la batterie redox à double flux a été introduit afin de proposer une solution de stockage hybride pour le stockage énergétique sous forme électrochimique et sous forme de carburant hydrogène. Le système est différent d'une batterie à flux traditionnelle car il est constitué d'une plateforme de stockage supplémentaire permettant la décharge chimique des électrolytes dans des réacteurs catalytiques externes où se produit l'électrolyse médiée de l'eau. Le stockage sous forme hybride améliore la flexibilité et augmente de manière significative la capacité du système en stockant l'énergie au-delà de la capacité des électrolytes sous forme d'hydrogène. De plus, l'électrolyse de l'eau médiée par les espèces redox offre plusieurs avantages en termes de sécurité, de durabilité et de pureté par rapport à l'électrolyse conventionnelle.

Dans cette thèse, une batterie vanadium-manganèse redox à double flux est développée et démontrée comme une solution efficace pour le stockage d'énergie et la production d'hydrogène. Le système utilise un électrolyte négatif composé d'une solution aqueuse de sulfate de vanadium (V^{3+}/V^{2+}) et un électrolyte positif composé d'une solution aqueuse de sulfate de manganèse (Mn^{3+}/Mn^{2+}), tout deux acidifiés à l'acide sulfurique. La cellule galvanique a démontré une efficacité énergétique de 68% à une densité de courant de $50 \text{ mA}\cdot\text{cm}^{-2}$ (tension de cellule = 1.92 V) et une capacité énergétique 45% au-dessus de celle mesurée pour une batterie redox à flux au vanadium conventionnelle. L'électrolyte positif et l'électrolyte négatif sont spontanément déchargés dans les réacteurs catalytiques composés de RuO_2 et de Mo_2C *via* les réactions médiées d'évolution de l'oxygène et d'hydrogène. La consommation énergétique pour la production d'hydrogène est estimée à environ 50 kWh/kg H_2 . Le système propose une alternative performante pour le stockage d'énergie à grande échelle en vue du déploiement des énergies renouvelables et des infrastructures pour la mobilité électrique.

Mots-clefs: Batterie redox à flux, hydrogène, stockage d'énergie, électrolyse de l'eau, médiateur redox

List of abbreviations

AAS	Atomic absorption spectroscopy
AC	Alternative current
AOS	Average oxidation state
ASV	Anodic stripping analysis
BEV	Battery electric vehicle
BMS	Battery management system
CAES	Compressed air energy storage
CC	Carbon cloth
CE	Coulombic efficiency
CES	Cryogenic energy storage
CF	Carbon felt
CNT	Carbon nanotube
CPE	Constant phase element
CPE-R	Constant phase element-resistance
CV	Cyclic voltammetry
CVD	Chemical-vapor deposition
DC	Direct current
DMF	Dimethylformamide
DTZ	Dithizone
ECSA	Electrochemically active surface area
EDLS	Electric double layer supercapacitor
EDX	Energy-dispersive X-ray spectroscopy
EE	Energy efficiency
EIS	Electrochemical impedance spectroscopy
EOGN	Mildly edge-oxidized graphene nanosheet
EPFL	Ecole polytechnique fédérale de Lausanne
ETD	Everhard-Thronley secondary electron detectors
FCEV	Fuel cell electric vehicle
FES	Flywheel energy storage
GC	Glassy carbon

GC	Gas chromatography
GDL	Gas diffusion layer
HER	Hydrogen evolution reaction
HHV	Higher heating value
ICP-MS	Inductively coupled plasma mass spectrometry
ICP-OES	Inductively coupled plasma-optical emission spectroscopy
IEA	International Energy Agency
ISO	International Organization for Standardization
LDPE	Low-density polyethylene
LEPA	Laboratoire d'électrochimie physique et analytique
LHV	Lower heating value
Li-ion	Lithium ion
LSV	Linear sweep voltammetry
MOF	Metal organic framework
NaS	Sodium-sulfur
NiCd	Nickel-cadmium
NMP	N-Methyl Pyrrolidone
NP	Nanoparticle
NT	Nanotube
OCP	Open circuit potential
OCV	Open circuit voltage
OER	Oxygen evolution reaction
PCM	Phase change material
PEEK	Polyetheretherketone
PEM	Polymer exchange membrane
PET	Polyethylene terephthalate
PFS	Photonic flash synthesis
<i>p</i> H	Potential of hydrogen
PHS	Pump hydro storage
ppm	Parts-per-million
PTFE	Polytetrafluoroethylene
PV	Photovoltaic
PVDF	Polyvinylidene fluoride

RDE	Rotating disk electrode
RDS	Rate determining step
RFB	Redox flow battery
RDFB	Redox dual-flow battery or dual-circuit redox flow battery
RHE	Reversible hydrogen electrode
RRD	Rotating ring-disk device
SEM	Scanning electron microscopy
SHE	Standard hydrogen electrode
SMES	Superconducting magnetic energy storage
SMR	Steam methane reforming
SNG	Synthetic natural gas
SOC	State-of-charge
SOEC	Solid oxide electrolysis cell
TEMPO	(2,2,6,6-Tétraméthylpipéridin-1-yl)oxy
TES	Thermal energy storage
TMC	Transition metal carbide
TPR	Temperature-programmed reduction
UPS	Uninterruptible power supply
UV-vis	Ultraviolet-visible
VE	Voltage efficiency
VPSA	Vacuum assisted pressure swing adsorption
VRFB	All-vanadium redox flow battery
XPS	X-ray photoelectron spectrometry
XRD	X-ray diffraction

List of symbols

A	Absorbance	-
A	Geometric area	m^2
C_A, c_A or $[A]$	Concentration of A	M or $\text{mol}\cdot\text{L}^{-1}$
C_{dl}	Double layer capacitance	F
C_s	Specific capacitance	$\text{F}\cdot\text{m}^{-2}$
D	Diffusion coefficient	$\text{m}^2\cdot\text{s}^{-1}$
E	Potential	V
E°	Standard redox potential	V
E	Energy	J
F	Faraday constant	$96\,485\text{ C}\cdot\text{mol}^{-1}$
$\Delta_r G$	Gibbs free of reaction	J
$\Delta_r H$	Enthalpy of reaction	$\text{J}\cdot\text{mol}^{-1}$
$\Delta_r H^\circ$	Enthalpy standard of reaction	$\text{J}\cdot\text{mol}^{-1}$
I or i	Current	A
I or j	Current density	$\text{A}\cdot\text{m}^{-2}$
k	Kinetic rate constant	-
l	Optical path length	m
m	Mass	kg
M	Molar mass	$\text{g}\cdot\text{mol}^{-1}$
n	Number of electrons	-
n_A	Amount of compound A	mol
p	Pressure	Pa
Q	Charge	C
q	Heat	J
R	Ideal gas constant	$8.314\text{ J}\cdot\text{mol}^{-1}\cdot\text{K}^{-1}$
R	Resistance	Ω
T	Temperature	K
t	Time	s
U	Internal energy	J
V	Voltage	V
V	Volume	m^3

\dot{V}	Volumetric flow	$\text{mol}\cdot\text{L}^{-1}$
w	Work	J
Z	Impedance	Ω

α	Charge transfer coefficient	-
α and γ	Order of reaction	-
ε	Molar extinction coefficient	$\text{L}\cdot\text{mol}^{-1}\cdot\text{m}^{-1}$
η	Overpotential	V
η	Efficiency	%
θ	Fractional surface coverage	-
λ	Wavelength	m
μ	Dynamic viscosity	$\text{Pa}\cdot\text{s}$
ν	Scan rate	$\text{V}\cdot\text{s}^{-1}$
ν	Kinematic viscosity	$\text{m}^2\cdot\text{s}^{-1}$
ν_{rxn}	Rate of reaction	$\text{mol}\cdot\text{L}^{-1}\cdot\text{s}^{-1}$
ρ	Volumetric mass density	$\text{kg}\cdot\text{m}^{-3}$
ω	Angular rotation rate	$\text{rad}\cdot\text{s}^{-1}$

Table of contents

CHAPTER I Introduction	1
1.1 Why do we need to store energy at large-scale?	1
1.2 How do we store electrical energy at large-scale?	3
1.2.1 A thermodynamic approach	3
1.2.2 A technological approach	5
1.1.1.1 Mechanical energy storage	6
1.1.1.2 Electrical and magnetic energy storage.....	7
1.1.1.3 Thermal energy storage.....	7
1.1.1.4 Electrochemical and chemical energy storage	8
1.3 Stationary battery for large-scale energy storage	11
1.3.1 Conventional secondary batteries	11
1.3.2 Redox flow battery.....	13
1.4 Hydrogen economy.....	17
1.5 Electromobilitis demonstrator.....	20
1.5.1 General layout.....	20
1.5.2 Redox flow battery operation.....	22
1.5.3 Hydrogen infrastructure and operation	24
1.6 Redox dual-flow battery	24
1.6.1 Concept	24
1.6.2 Advantages.....	27
1.6.3 State-of-the-art	28
1.7 Challenges and objectives of the thesis.....	29
References	32
 CHAPTER II Failure analysis and purification strategy of copper-contaminated vanadium electrolytes	 39
2.1 Introduction	40
2.2 Experimental Section	44
2.2.1 Chemicals.....	44
2.2.2 Instrumentation	44
2.2.3 Determination of Cu ²⁺	45
2.2.4 Anodic stripping voltammetry	45
2.2.5 Single-cell measurements	45
2.2.6 Scale-up.....	46
2.3 Results and Discussion	46
2.3.1 Effect of copper on VRFB operation	46
2.3.2 Copper determination.....	48
2.3.3 Purification strategy	50
2.3.4 Scale-up and demonstration	54
2.4 Conclusion.....	56
References	57
Appendix II	59

CHAPTER III Stabilization of manganese electrolyte ($\text{Mn}^{3+}/\text{Mn}^{2+}$) 61

3.1	Introduction	62
3.2	Experimental section.....	64
3.2.1	Materials and methods	64
3.2.2	Electrochemical characterization	64
3.2.3	Spectroelectrochemistry	64
3.2.4	Study of manganese oxide formation	65
3.2.5	Iodometry for Mn^{3+} titration	66
3.3	Results and discussion.....	67
3.3.1	Electrochemical study of electrolytes	67
3.3.2	Surface analysis of electrografted oxide layers	71
3.3.3	Study of Mn^{3+} disproportionation in solution by spectroelectrochemistry.....	76
3.4	Conclusion.....	78
	References	80
	Appendix III.....	82

CHAPTER IV Kinetic model of redox-mediated hydrogen production ... 89

4.1	Introduction	90
4.2	Experimental method.....	91
4.2.1	Chemicals.....	91
4.2.2	Electrolyte synthesis	92
4.2.3	Instrumentation	92
4.2.4	Mo_2C film preparation	93
4.2.5	Kinetic study in transient conditions.....	93
4.2.6	Kinetic study in steady-state conditions	94
4.3	Theoretical basis	95
4.4	Results and discussion.....	98
4.4.1	Kinetic experiments in transient conditions.....	98
4.4.2	Kinetic experiments in steady-state conditions.....	100
4.4.2.1	Description of the RRD method	100
4.4.2.2	Electrochemical characterization of Mo_2C film.....	102
4.4.2.3	Kinetic study	107
4.4.3	Conversion study	110
4.4.4	Model prediction for the production of hydrogen in a semi-batch reactor	112
4.5	Conclusion.....	113
	References	115
	Appendix IV.....	119

CHAPTER V Photonic flash synthesis of Mo_2C electrocatalyst for the hydrogen evolution reaction 123

5.1	Introduction	124
5.2	Experimental method.....	126
5.2.1	Chemicals.....	126
5.2.2	Instrumentation	126
5.2.3	Precursor ink formulation	126
5.2.4	Photonic flash synthesis route.....	127

5.2.5	Electrochemical characterization	127
5.3	Results and discussion.....	128
5.4	Conclusion.....	138
	References	139
	Appendix V	144

CHAPTER VI Vanadium-manganese redox dual-flow battery for electricity storage and hydrogen production..... 147

6.1	Introduction	147
6.2	Experimental section.....	150
6.2.1	Electrolytes preparation	150
6.2.2	Catalysts preparation.....	150
6.2.2.1	Molybdenum carbide	150
6.2.2.2	Ruthenium oxide.....	150
6.2.3	Instrumentation	151
6.2.4	Physical and electrochemical characterization	151
6.2.4.1	Mediators	151
6.2.4.2	Electrocatalysts	151
6.2.5	Dual-circuit RFB set-up	152
6.2.6	Single-cell and catalytic water splitting experiments	154
6.3	Results and discussion.....	155
6.3.1	Mediators and electrocatalysts.....	155
6.3.2	Vanadium-Manganese redox flow battery for energy storage.....	160
6.3.3	Redox-mediated water splitting	164
6.4	Conclusion.....	169
	References	170
	Appendix VI.....	173

CHAPTER VII Conclusion and perspectives..... 181

CURRICULUM VITAE 185

CHAPTER I

Introduction

1.1 Why do we need to store energy at large-scale?

Electrical energy has changed the face of our society and our standard of living. In 2018, worldwide human activity required 24'739 TWh of electricity (IEA).¹ In comparison, the Grande Dixence Dam in Switzerland generates approximately 2 TWh annually, and 11'848 of them would have been needed to meet the global electricity consumption this year.² The International Energy Agency (IEA) reported that the rapid growth of developing countries, the expansion of population and the urbanization process will increase the demand in electrical energy by 30% in 2040.¹

To-date, the worldwide electrical production is essentially generated from fossil resources such as coal, crude oil or gas (64% in 2018).¹ Although practical in terms of storage and transportation, those resources come from a heritage of several millions of years and their burning emits an excessive amount of CO₂, causing the global warming.³ Adding to the pollution and public health concerns, the modern society is currently facing one of the major challenge of the 21th century: **the energy transition**.⁴ In 2017, the Swiss electorate accepted the "Energiesstrategie 2050" with the promotion of renewable energy (*e.g.* solar and wind) and a progressive withdrawal from nuclear energy production.⁵

The rapid growth of photovoltaic system (PV) and wind turbine development set them as realistic candidates to replace fossil energy resources.^{6,7} However, the renewable energy resources depends on meteorological conditions that generates periodical fluctuations (daily, weekly and yearly) of the electrical production. This intermittence complicates the integration of large shares of renewables power into the conventional grid in terms of stability and reliability.⁸ In fact, the one-way transportation of electricity involves to use it precisely at the time of the generation, requiring a near-instantaneous balance between supply and demand. Until now, variability of load demand has been offset using operating reserves, which consist of either increasing the power output of internal generators (spinning reserves) or using

external power units (non-spinning reserves). During off-peak times, the power generated by these turbines is not exploited.^{8–10}

To avoid the implementation of oversized generators, a sustainable alternative is to implement large-scale stationary energy storage systems within the electrical grid (*e.g.* peak shaving, load leveling...). As shown on Figure 1.1, the energy storage solution accumulates electrical energy from power systems during periods of low demand, low cost or high supply in order to deliver it back during periods of high demand, high cost or low supply.¹¹ This affords to inject or absorb temporarily large amount of energy and plays the role of a power buffer between the unpredictable power output of intermittent renewable generators and the fluctuating electrical demand. Owing to the lack of mature, reliable and cost-effective technology, only few stationary energy storage systems have been implemented in practical applications. Additionally, the charging management of the in-coming expansion of battery electric vehicle (BEV) and fuel-cell electric vehicle (FCEV) infrastructure addresses even more the need for energy storage system implementation.^{12,13}

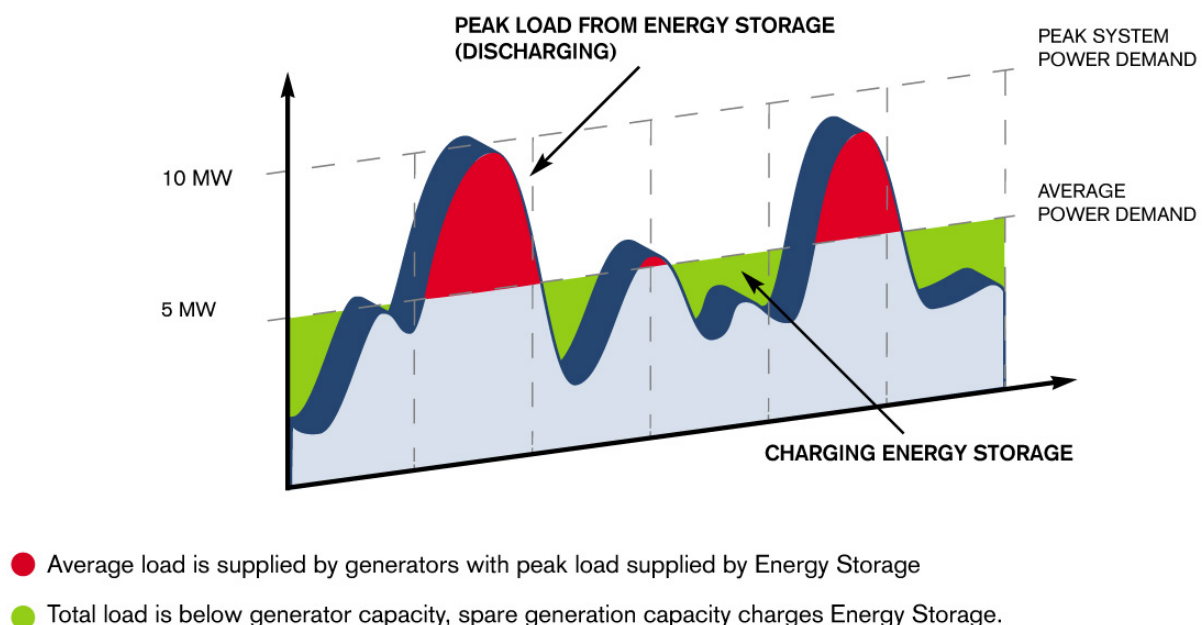


Figure 1.1 Illustration of the concept of load levelling using energy storage solution to reduce large fluctuations of the loads.¹⁴

1.2 How do we store electrical energy at large-scale?

1.2.1 A thermodynamic approach

The first law of thermodynamics¹⁵, also known as the law of conservation of energy, states that the total internal energy (U) of an isolated system remains always constant. In other words, the energy can neither be created nor destroyed and the total amount of energy remains invariant in the nature. In general, energy can only be transferred from one closed system to another and the resulting change in the internal energy of the system is expressed as the sum of heat (Q) and work (W) variations.¹⁶

$$\Delta U = Q + W \quad (\text{Eq. 1.1})$$

The notion of heat and work are often misunderstood by associating those concepts to a form of energy. In fact, heat and work are the modes of energy transfer from a system to another and can be distinguished only at the surroundings.¹⁶

Work is an energy transfer caused by the motion of the system against an opposing force.¹⁶ As an example, we transfer energy as work to a weight when we raise it in the field of gravity. In this case, there is a net and uniform motion of all the atoms towards the rising point. The transferred work is a gain of energy and enhances the capacity of the system to do work.^{16,17} Heat is a transfer of energy caused by a temperature difference between a system and its surroundings. From a molecular point of view, the temperature is a parameter that reveals the distribution of molecules over the available energy states in a system. The higher the temperature is, the higher the average energy states of the molecules is, and so the higher the random agitation of the molecules is (speed, vibration and rotation).^{16,17} Given this, heat corresponds to the energy transfer that makes use of the random motion of atoms. Thus, when a hotter mass is brought in contact with a colder mass, energy as heat is transferred without net motion until reaching thermal equilibrium.^{16,17}

Once an amount of energy is injected as work or/and heat in a closed system, the energy can be stored under various forms: thermal energy, kinetic energy, potential energy, chemical energy, electrical energy, radiative energy and nuclear energy. However, the system has no memory of the mode of transfer, but only of the quantity of energy it possesses (*1st law of*

thermodynamics).¹⁴ Therefore, a human of 100 kg can increase his total energy of 1 million of Joule by either elevating himself of 1000 meter (potential energy), by propelling himself at 500 km/h (kinetic energy) or by increasing his temperature of 3°C (thermal energy).

That being said, the basic premise of energy storage consists of saving an amount of energy generated at one time to use it at another time. For electrical energy, the art of ‘storing’ is particularly difficult because electricity cannot be stored itself at any scale. Physically, electricity is not considered as a source of energy, but is better described as a vector for energy transportation. Although it is possible to store the electrical energy under electrostatic form in a capacitor, the storage capacity remains limited. In fact, to store large-scale electrical energy, the generated electricity is rather converted into another form of energy that is more appropriate and realistic to store.¹⁸ As an example, charging a battery converts an amount of electrical energy into chemical energy that be later transformed back into electrical energy in order to produce an electrical work. Given the principle that the energy is always conserved (1st law of thermodynamics), energy storage sounds to be natural. So, why is it so challenging to store energy?

To answer to this question and understand the challenges addressed by the energy storage and conversion, the notion of ‘the quality’ of the energy needs to be introduced. To put it simple, the total energy of a system can be divided in two different categories: the energy that is available to do work (‘free energy’ or ‘exergy’) and the energy condemned to leave the system as dissipative heat (‘useless energy’).¹⁶ The latter is related to the concept of entropy (S), that is a measure of the quality of the energy. Although the quantity of energy cannot be destroyed (1st law of thermodynamics), its quality can. Indeed, the 2nd law of thermodynamics states that the quality of the energy degrades spontaneously, and the entropy of an isolated system can only increase. Let’s imagine that all the free energy of the system would be converted into work, the total entropy of the system would remain unchanged. However, the system is unavoidably subject to irreversibility converting the free energy into heat (entropy generation), due to dissipative processes (friction, turbulences). Although the conversion of thermal energy into useful work is thermodynamically possible (e.g. internal combustion engine), the Nature always exerts an ‘energy tax’ that need to be paid by the surrounding as heat towards a cold sink, resulting in an increase of universe entropy.¹⁶

Those laws are the foundation of all the processes occurring in nature and are primordial to

understand and improve the efficiency of processes related to energy storage and energy conversion.

1.2.2 A technological approach

A wide range of electrical energy storage systems exists for stationary electrical energy storage and each technology has specific features that are suitable for various applications, in which the entire conventional electricity grid can be valued from the bulk generation to the customer service.^{8–13,18–20} Today, overproduction of electrical energy is mainly absorbed by pump-hydro storage (PHS) plants, which stand for about 99% of the world electric storage capacity (ca. 3% of global energy generation capacity). Although the system demonstrates high power and capacity ratings, good cycle stability and long lifetime, the major drawbacks of PHS are the lack of available geological site for the installation and the high capital cost requirement.⁸ With the increase of storage capacity need and the decentralisation of the electrical production, alternative systems are necessary. The various technologies are classified according to the nature of the storing energy and the field of application into the electrical grid that will depend on technical aspects such as power rating, discharging time, storage duration, self-discharge, energy and power density, life time or capital cost (Figure 1.2).

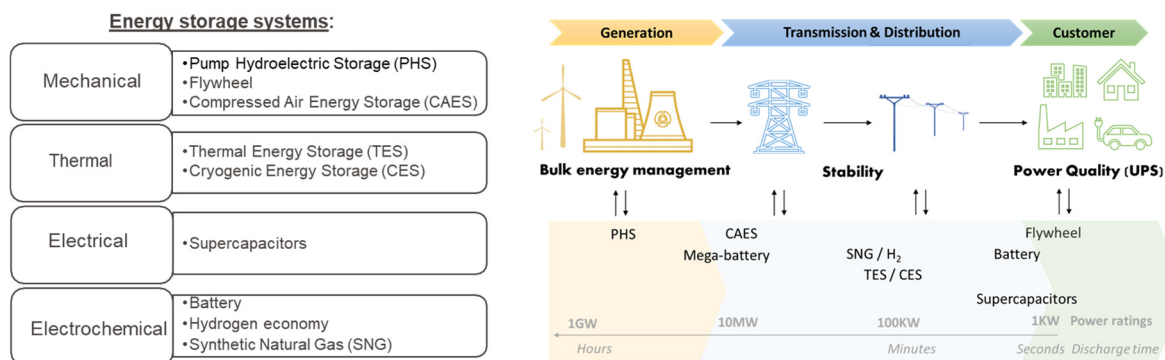


Figure 1.2 Main electric energy storage systems classified according to the physical nature of the storage and the field of application into the electrical grid.

1.1.1.1 Mechanical energy storage

Mechanical energy storage systems convert electrical energy into mechanical energy either as potential energy or kinetic energy. The most common systems are pumped hydroelectric storage (PHS), compressed air energy storage (CAES) and flywheel energy storage (FES).

Pumped hydroelectric storage (PHS): The method takes advantage of two water reservoirs installed at two different elevations. During off-peak hours, the surplus of electrical energy is converted into potential energy by pumping the water from the lower to the upper reservoir. The stored potential energy is converted back to electricity by powering a turbine with generator (turbine unit) during peak hours. Typical efficiencies of the system is generally comprised between 70 to 80%.^{8,22}



Figure 1.3 Pumped hydroelectric storage power plant of Nant de Drance in the canton of Valais in Switzerland interconnecting the Vieux Emosson (2225 m) and the Emosson (1930 m) water reservoirs. The storage capacity of the plant is about 20 GWh with a plant power of 900 MW.²³

Compressed Air Energy Storage (CAES): The system converts electrical energy in mechanical energy by compressing air and stores it within either underground or above-ground storage reservoirs. When the power grid needs to be supplied, the compressed gas is successively heated (by heat recuperation or burning of fossil fuels) and expanded into power turbines. As for pumped hydroelectric storage system, CAES installations has a large capacity and power rating, but required very specific topological conditions. Typical efficiency is usually range between 40 and 75%.^{8,24}

Flywheel Energy Storage (FES): Flywheels store energy in a massive rotating cylinder (kinetic energy). The speed of the rotor is regulated by transferring electricity through a motor-generator system. Wind shear and energy loss are reduced using bearings and placing the system under high vacuum environment. Flywheels enable high power density, high efficiency (~90%) and long lifetime, but have low capacity and high self-discharge.^{18,20}

1.1.1.2 Electrical and magnetic energy storage

Electric and magnetic energy storage systems store directly electrical energy in either an electric field or a magnetic field. The most common systems are electric double layer supercapacitors (EDLS) (electric energy storage) and superconducting magnetic energy storage (SMES) (magnetic energy storage).

Electric double layer supercapacitor (EDLS): Usually, a capacitor is made of two electrical conductors separated by a thin layer of dielectric material. The electrical energy is stored in the electric field formed between the two metallic plates. Instead of the common dielectric layer, supercapacitors are composed of an electrolyte solution and a porous membrane separating the two electrical conductors. The supercapacitor arrangement increases significantly the power and energy density of the system compared to conventional capacitors. The main advantages are fast charging/discharging time, long life-time and high efficiency (~90%). However, the technology is limited for large-scale energy storage due to high self-discharge and low energy capacity.^{25–27}

Superconducting magnetic energy storage (SMES): The system stores the energy in the magnetic field induced by the flow of a direct current in a superconducting coil. The system needs to be maintained below the superconducting critical temperature of the coil material using a cooling system. Although the technology suffers from economic issues, it offers several advantages including fast charging/discharging time, high efficiency (~97%) and high power output.^{8,13,28,29}

1.1.1.3 Thermal energy storage

Thermal energy storage systems convert electrical energy in the form of thermal energy by utilizing either sensible heat, latent heat, or sorption heat of a medium.

Sensible heat storage: Sensible heat is the heat exchanged by a system in which a change of temperature occurs. The method consists of heating up an appropriate medium (with relatively high specific heat capacity) in order to increase its temperature without going through phase or structure change. The heat is then extracted back to produce steam and power turbines. Typical materials used are solid (*e.g.* ground, granite, concrete...), liquid (*e.g.* water, oil...) or molten salts. The efficiency may vary from 50 to 90%.^{13,26,30}

Latent heat storage: Latent heat is the heat exchanged by a system during phase transition (constant-temperature process). Latent heat storage uses phase change materials (PCMs) as storage medium. The advantage of the technology is to reach high energy density and efficient heat transfer (constant temperature) with system efficiency at 50-75%.^{13,30}

Thermo-chemical sorption storage: The system relies on a thermodynamic cycle, where a hot source is employed to heat up an adsorbent (*e.g.* zeolite or silica gel) and to vaporize the working fluid (*e.g.* water) from the adsorbent medium. Then, the working fluid is condensed at lower temperature, the heat of condensation is withdrawn from the system and the working fluid is stored (charging process). For the discharge step, the working fluid is heat up and the resulting vapor adsorbs on the adsorbent releasing heat at high temperature (heat of adsorption). Although the system achieves efficiency (75-100%) and energy density higher than others thermal storage systems, the technology requires more complex design.^{13,30}

1.1.1.4 Electrochemical and chemical energy storage

Electrochemical and chemical energy storage devices store electrical energy in the form of chemical energy (E_{ch}) by means of conversion reactions. The conversion processes take place in an electrochemical cell that can either generates electricity from electrochemical potential (galvanic cell) or converts electrical energy in the form of chemical energy (electrolytic cell). Galvanic cells include primary cells (non-rechargeable batteries, *e.g.* Volta's pile, Daniell cell, alkaline...), secondary cells (rechargeable batteries, *e.g.* lead-acid, lithium-ion...) and tertiary cells (fuel cells, *e.g.* alkaline, polymer electrolyte membrane...). Commonly, an electrochemical cell is separated in two electrode compartments (half-cell) that are interconnected externally by an electrical circuit (electron conductor) and internally by an electrolyte (ion conductor).^{10,11,31} The electrolyte acts as an ion conductor between the two

electrodes in order to guarantee the electroneutrality of the cell. Besides, the main role of the electrodes is to supply the surface at which redox reactions occur. By definition, the cathode refers to the electrode at which reduction occurs, while the anode is the electrode at which the oxidation occurs.³¹

Fuel cell differs from batteries in the sense that it generates electricity from a chemical fuel fed from external storage tank while battery generates electrical energy from the chemical energy of the embedded active substance.³² In general, the term “electrochemical energy storage” is employed for the pseudocapacitors and the batteries systems, while “chemical energy storage” envelops all technologies that store the electrical energy in a chemical fuel *via* electrolyser/fuel cell combination.

Electrochemical pseudocapacitor: Unlike electric double layer capacitors that store energy in the form of electrostatic energy, electrochemical pseudocapacitors store it in the form of ionic charge *via* fast and reversible electron charge-transfer processes (faradaic) such as redox reactions, electrosorption or intercalation between the electrode and the electrolyte. The main difference with batteries is that it involves only very fast sequence of reversible processes.^{27,33,34} Note that we speak about hybrid supercapacitor when the device results from the combination of the electric double-layer supercapacitor and pseudocapacitor systems.

Battery energy storage system: Besides portable electronic devices and transportation applications, batteries have also drawn increasing interest for large scale applications thanks to numerous advantages including high conversion efficiency, good reactivity and geographical independence.^{10,35,36} Batteries are electrochemical energy storage devices that convert electrical energy in the form of electrochemical potential through reversible redox reactions of two distinct redox couples (Ox_1/Red_1 et Ox_2/Red_2). Upon the charge of the battery, electrical work is injected to drive an oxidation reaction at the positive electrode and reduction reaction at the negative electrode. During the discharge, the reverse reactions are spontaneously taking place while connecting the two electrodes to an external load, releasing the chemical energy onto electrical work. The cell voltage of a battery cell (E_{cell}) is given by the difference between the electrode potential of the cathode and the anode reactions:

$$E_{\text{cell}} = E_{\text{cathode}} - E_{\text{anode}} = -\frac{\Delta_r G}{nF} \quad (\text{Eq. 1.2})$$

where $\Delta_r G$ is the Gibbs energy delivered by the overall redox reaction exchanging n electrons

and F is the Faraday constant (*i.e.* the charge of a mole of electrons, $96485 \text{ C} \cdot \text{mol}^{-1}$).

Conventionally, the electrodes of a battery are assigned according to the mode of discharge, so the anode refers to the negative electrode and the cathode refers to the positive electrode, although reverse reactions occur during the charge. Usually, single cells are arranged in series to reach the desired voltage, which forms a stack. Note that primary batteries are not considered for power grid application, so in this thesis the term battery will refer to secondary batteries.³⁷

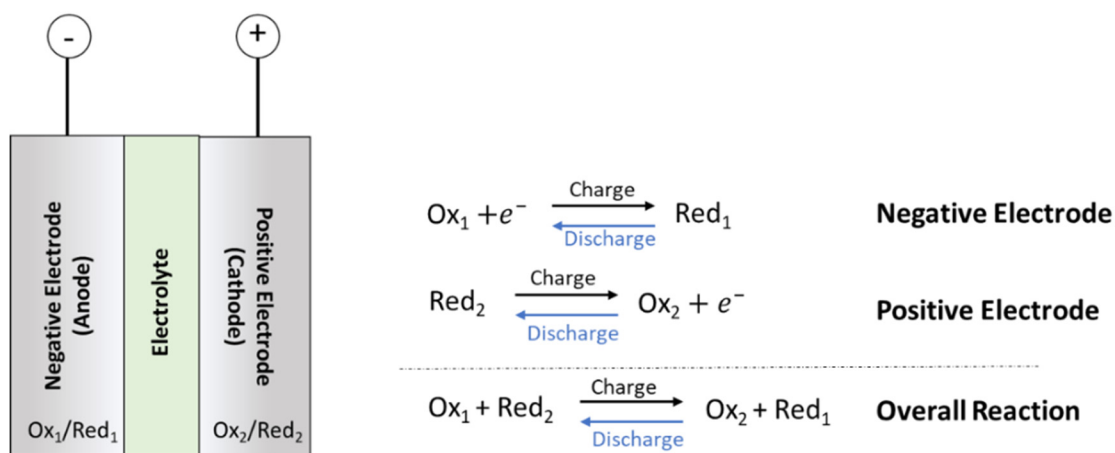


Figure 1.4 Simplified schematic of the working principle of a rechargeable battery with the charge/discharge reactions occurring at the anode and the cathode.

The amount of energy stored and the rate at which the energy can be extracted from the battery are given by the energy density ($\text{Wh} \cdot \text{L}^{-1}$) and the power density ($\text{W} \cdot \text{L}^{-1}$) of the system, and are directly linked by the thermodynamic and kinetics properties dictated by the choice of chemistry and materials composing the battery.¹⁸ In this regard, numerous battery chemistries were developed with various characteristics and performances serving a wide range of application.^{29,35,38} The main technologies for large-scale energy storage are discussed in Section 1.3.

Chemical fuels: In general, chemical fuels offer several advantages in terms of energy density and ease of storage and transportation. In this context, converting excess of renewable electricity into a chemical fuel (*e.g.* electrolysis) which can be stored and used subsequently for electricity generation (*e.g.* fuel cell) or other energy generation is of great interest. Several chemical compound are currently been considered including hydrogen, methane, ammonia, hydrocarbons and methanol.³⁹ Among them, hydrogen is believed to be a realistic energy carrier vector able to store and provide energy to all the sectors of economy. A renewable and

carbon-free energy system based on hydrogen energy is often called “hydrogen economy” and is described more in detail in Section 1.4.^{39–41}

1.3 Stationary battery for large-scale energy storage

For grid-scale application, the energy and power density matter less than for transportation and mobile applications and features such as the reliability, the safety, and the durability of the system are favored.⁴² The main battery technologies considered for utility-scale storage are described below and their main characteristics are summarized in Table 1.2.

1.3.1 Conventional secondary batteries

- *Lithium-ion*: The development of battery systems has been often driven by high energy density considerations. For this purpose, Li is strongly attractive due to the fact it is the most electropositive element in the periodic table ($\text{Li}/\text{Li}^+ = -3.04$ vs. SHE) and the lightest metal ($6.94 \text{ g}\cdot\text{mol}^{-1}$).³¹ In this context, since the first commercialization in 1990s, Li-ion batteries have become one of the most important technologies, leading the global market of batteries, especially for portable electronic devices.¹¹ Lithium-ion batteries rely on redox intercalation processes where the cathode and the anode reversibly exchange Li^+ ions. To do it, the technology employs intercalation materials. The anode is usually made of carbonaceous materials (*e.g.* graphite) and numerous different types of lithium metal oxide (*e.g.* LiCoO_2 , LiMn_2O_4 ...) or olivines (*e.g.* LiFePO_4 ...) can be used at the cathode. The electrolyte is made up of lithium salts (*e.g.* LiPF_6) dissolved in an organic solvent (*e.g.* ethylene carbonate, dimethyl carbonate,...).³⁷ Although the lithium-ion batteries dominate the portable electronic devices market, improvements in terms of lifetime, cost reduction and safety management are critical to expand into large-scale electrical grid applications.^{11,18}

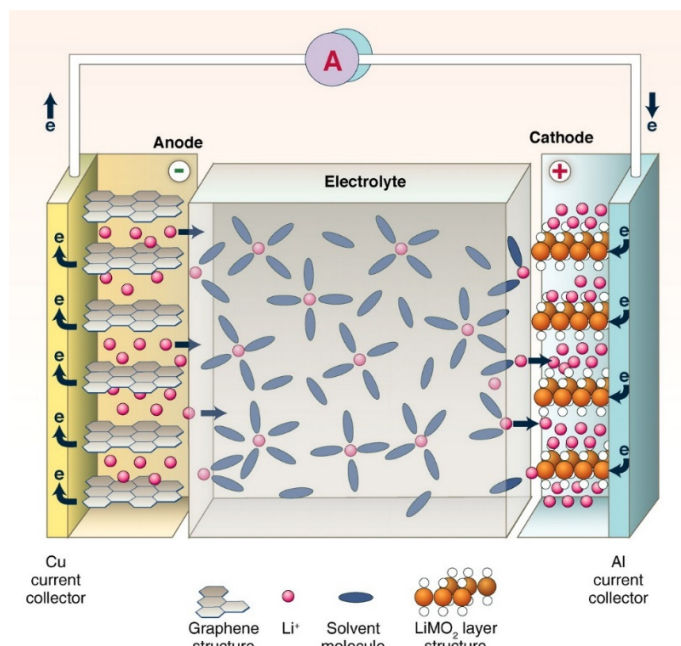


Figure 1.5 Schematic of a lithium-ion battery. During the charge, Li^+ ions are removed or deintercalated from the positive electrode (e.g. layered oxide compound) and inserted or intercalated into the negative electrode (e.g. graphitic layers). Reverse processes occurs during discharge.³⁵

- *Lead acid:* Invented in 1859, lead-acid battery is a very mature technology. Typically, the battery cell is made of PbO_2 anode and a Pb cathode that are immersed in a solution of concentrated sulfuric acid. Different kind of lead-acid battery has been developed including the flooding battery, the valve-regulated lead–acid battery and gelled/absorbed electrolyte-based lead acid battery.^{11,37}
- *Sodium-based:* Among the sodium-based batteries, sodium-sulfur batteries (NaS) and sodium-nickel-chloride (ZEBRA cells) employed molten salt as anode and cathode with a solid beta alumina ceramic electrolyte, that allows the transport of sodium ions between the two electrodes. NaS system consists of molten sodium at the negative electrode and molten sulfur at the positive electrode, while sodium-nickel-chloride cell employs a metal halide cathode (NiCl_2).^{11,43} Besides molten salts technologies, the development of sodium-ion batteries is growing. Similarly, to Li-ion technology, the batteries involves intercalations processes of Na^+ ions between the cathode and the anode during charging/discharging process, using the same types of porous conductive polymer materials. To-date, significant efforts are made for the development of reliable active material with several cathode materials reported including layer-structured transition metal oxides, polyanionic-type compounds, prussian blue analogues, and organic-based materials.^{44,45} Owing to the superior safety, the economic benefits from

abundant sodium resources, Na-ion battery is a promising alternative to lithium-ion battery for large-scale energy storage.

- Nickel-based:** Nickel-Cadmium (NiCd) is another mature battery technology (>100 years). Typically, the system is made of a nickel hydroxide cathode, a cadmium hydroxide anode, a separator and an alkaline electrolyte. The system is limited due to the toxicity of cadmium and the so-called “memory effect” (tendency of the system to lose capacity in case of repeated partial discharge). To address those concerns, nickel-metal hydride battery (NiMH) was proposed as an alternative by using a hydrogen-absorbing alloy (MH) anode instead of cadmium (e.g. AB5-type [LaCePrNdNiCoMnAl], A2B7-type [LaCePrNdMgNiCoMnAlZr], or AB2-type [VTiZrNiCrCoMnAlSn] metal hydride active materials).^{11,29,38}

1.3.2 Redox flow battery

Redox flow batteries (RFBs) have drawn great attention by providing valuable opportunities for stationary applications such as flexibility, durability and safety.^{46,47} While conventional secondary batteries store energy within the electrode structure, flow batteries carry the charge in two distinct liquid electrolytes containing soluble redox species (posolyte and negolyte) located in separated external tanks (Figure 1.6).³⁵ During the battery operations, the two electrolytes are pumped from the external containers to the electrochemical cell where reduction and oxidation reactions take place on the respective electrode surface. The electrochemical cell is assembled with an ion exchange membrane to separate the positive and the negative half-cell compartments and maintain the electroneutrality of the flow cell.^{10,35,48}

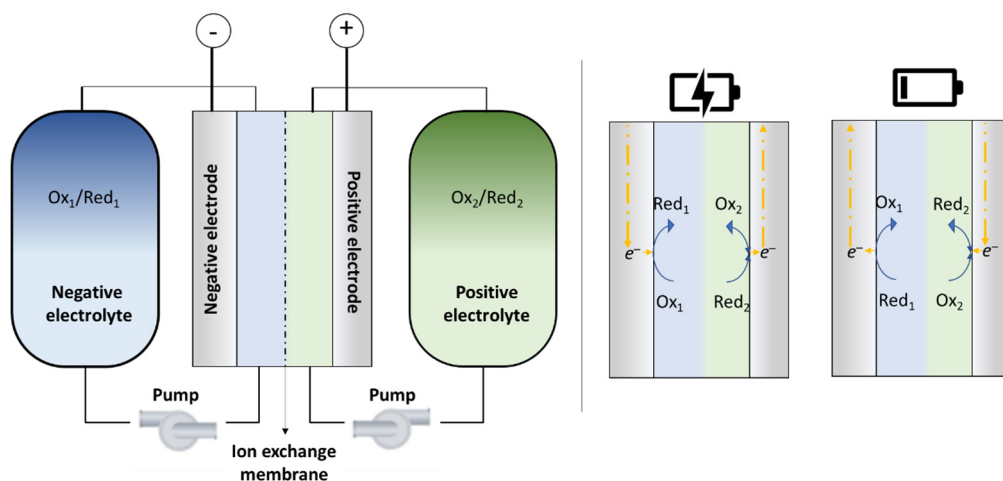


Figure 1.6 Schematic of a redox flow battery.

The unique design of flow batteries offers several advantages for large-scale energy storage:

Flexibility: The structure of redox flow batteries enables to decouple power and capacity, whilst offering considerable flexibility and modularity for large-scale energy storage applications. In fact, the energy storage capacity of the system can be tuned by varying the volume of electrolytes while the power is a matter of the electrode surface available.⁴⁶ This contrasts with the conventional batteries in which the energy is directly stored in the electrodes.

Lifetime and stability: Flow batteries may operate for more than 10 years ($> 10^4$ 000 cycles). In contrast to other batteries, the “inert” role of electrodes during the charge-transfer reactions prevents the system from advanced electrodes degradations due to phase or morphology transformations.³⁵ Therefore, the battery lifetime relies more on the degradation of auxiliaries, such as pump or cell components that can be readily replaced. Moreover, the flow batteries are less sensitive to depth charge or discharge.⁴⁶

Safety: In addition, RFBs are not exposed to thermal runaway risk, which can be a major hurdle in lithium-based batteries.^{46,49,50}

In spite of the advantages described above, RFB's suffer from low energy density ($< 30 \text{ Wh} \cdot \text{L}^{-1}$) as compared to other battery technologies due to solubility limitation of redox active species and the stability potential window of the solvent, especially for aqueous system that is constrained by hydrogen evolution reaction (HER) and oxygen evolution reactions (OER).¹¹

The choice of redox-active material has an important impact on the performance of the flow battery by influencing the kinetics, the viscosity of the electrolyte and the capacity of the system. Upon the recent development of RFB, a wide range of metal-based redox couples dissolved in aqueous and non-aqueous electrolytes has been investigated. The most common are summarized in Table 1.1.^{46,47,49,51,52} More recently, an increasing number of electrolytes based on organic molecules was reported (*e.g.* TEMPO, anthraquinone, viologen derivatives, ferrocene derivatives...).^{53–55} Organic molecules can provide several advantages in terms of solubility, reversibility and cost. However, chemical degradation is responsible for most of the capacity fading of organic-based RFB's.⁵⁵

Table 1.1 Summary of the main inorganic redox couples investigated for the development of redox flow batteries.

Redox Species	Redox Potential / V vs. SHE
Zn ²⁺ /Zn	−0.76
VCl ₃ /VCl ₂	−0.58
Cr ³⁺ /Cr ²⁺	−0.41
S ₄ ^{2−} /S ₂ ^{2−}	−0.27
V ³⁺ /V ²⁺	−0.26
Pb ²⁺ /Pb	−0.13
Ti ⁴⁺ /Ti ³⁺	0.04
Fe ³⁺ /Fe ²⁺	0.77
Br [−] /ClBr ₂ [−]	0.80
VO ₂ ⁺ /VO ²⁺	1.00
Br ₂ /Br [−]	1.09
O ₂ /H ₂ O	1.23
Cl ₂ /Cl [−]	1.36
Mn ³⁺ /Mn ²⁺	1.51
Ce ⁴⁺ /Ce ³⁺	1.67

To-date, some successful RFB technologies have been developed and received industrial investments towards commercialization for grid-scale storage applications including all-vanadium,⁵⁶ zinc-bromine,⁵⁷ polysulphide/bromine⁵⁸ and iron/chromium⁵⁹ redox flow batteries. Among them, the all-vanadium redox flow battery (VRFB) received the greatest interest and is the most widely commercialized RFB.^{18,46,48,56,60,61} The main advantage of the technology is to employ a single metal suppressing cross-contamination concerns, with V³⁺/V²⁺ ($E^0 = -0.26$ V vs. SHE) redox couple on the negative side and VO₂⁺/VO²⁺ ($E^0 = 1.00$ V vs. SHE) on the positive side (Figure 1.7).⁶¹ A typical VRFB operates between −5 and 40°C in a sulfuric acid electrolyte containing ca. 1.6 M of the vanadium redox species.⁵⁶ The round-trip energy efficiency was demonstrated to vary from 70% to 90% with an energy density of about 20-30 Wh·L^{−1} (*i.e.* 25-35 Wh·kg^{−1}).^{62,63} During battery operations, the following charging and discharging reactions take place on carbon felt electrodes.^{60,64}

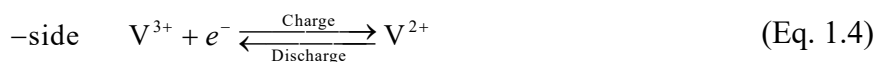
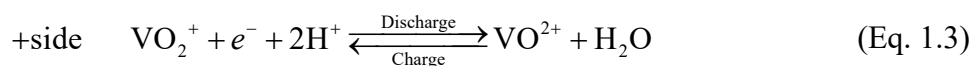


Table 1.2 Comparison of the technical characteristics of the main battery energy storage systems considered for large-scale energy storage.^{11,18,19,38,42,65–70}

Type	Chemical reactions at anode and cathode	Operating temperature /°C	Energy density /Wh·L ⁻¹	Power density /W·L ⁻¹	Cell potential / V	Cycle efficiency / %	Cycle lifetime	Advantages	Disadvantages
Li-ion	$\text{Li}_n\text{C} \rightleftharpoons \text{C} + n\text{Li}^+ + ne^-$ $\text{Li}_{1-n}\text{XXO}_2 + n\text{Li}^+ + ne^- \rightleftharpoons \text{LiXXO}_2$	-25-40	300-750	1500-10'000	3.6-4.2	90-97	1000-10'000	High power and energy density High efficiency	Thermal runaway risk Sophisticated BMS
Lead-acid	$\text{Pb} + \text{SO}_4^{2-} \rightleftharpoons \text{PbSO}_4 + 2e^-$ $\text{PbO}_2 + \text{SO}_4^{2-} + 4\text{H}^+ + 2e^- \rightleftharpoons \text{PbSO}_4 + 2\text{H}_2\text{O}$	-40-60	25-90	10-400	~2.1	70-90	200-2000	Mature Low cost	Limited life-cycle Low power and energy density
Nickel-cadmium	$\text{Cd} + 2\text{OH}^- \rightleftharpoons \text{Cd}(\text{OH})_2 + 2e^-$ $2\text{NiOOH} + 2\text{H}_2\text{O} + 2e^- \rightleftharpoons 2\text{Ni}(\text{OH})_2 + 2\text{OH}^-$	-40-60	50-150	80-600	~1.3	60-70	2000-3000	Mature	Toxicity of cadmium Low power and energy density “Memory effect”
Nickel-metal hydride	$\text{MH} + \text{OH}^- \rightleftharpoons \text{M} + \text{H}_2\text{O} + e^-$ $\text{NiOOH} + \text{H}_2\text{O} + e^- \rightleftharpoons \text{Ni}(\text{OH})_2 + \text{OH}^-$	-30-75	140-300	10-600	~1.3	50-80	300-3000	Mature Less toxic than Ni-Cd	Low power and energy density Limited life-cycle
Sodium-sulfur	$2\text{Na} \rightleftharpoons 2\text{Na}^+ + 2e^-$ $x\text{S} + 2\text{Na}^+ + 2e^- \rightleftharpoons \text{Na}_2\text{S}_x$	300-350	150-300	150-230	~2	75-90	2500-5000	High energy density Good lifetime Low cost	Thermal management Safety issues
Sodium-nickel-chloride (ZEBRA)	$2\text{Na} \rightleftharpoons 2\text{Na}^+ + 2e^-$ $\text{NiCl}_2 + 2\text{Na}^+ + 2e^- \rightleftharpoons \text{Ni} + 2\text{NaCl}$	270-300	150-200	220-300	~2.6	80-85	2000-3000	High energy density Good lifetime Low cost	Thermal management Capacity fading
All-vanadium RFB	$\text{V}^{2+} \rightleftharpoons \text{V}^{3+} + e^-$ $\text{VO}_2^+ + 2\text{H}^+ + e^- \rightleftharpoons \text{VO}^{2+} + \text{H}_2\text{O}$	10-40	10-30	0.5-2	~1.3	60-90	>10'000	High flexibility Good lifetime High safety	Low power and energy density

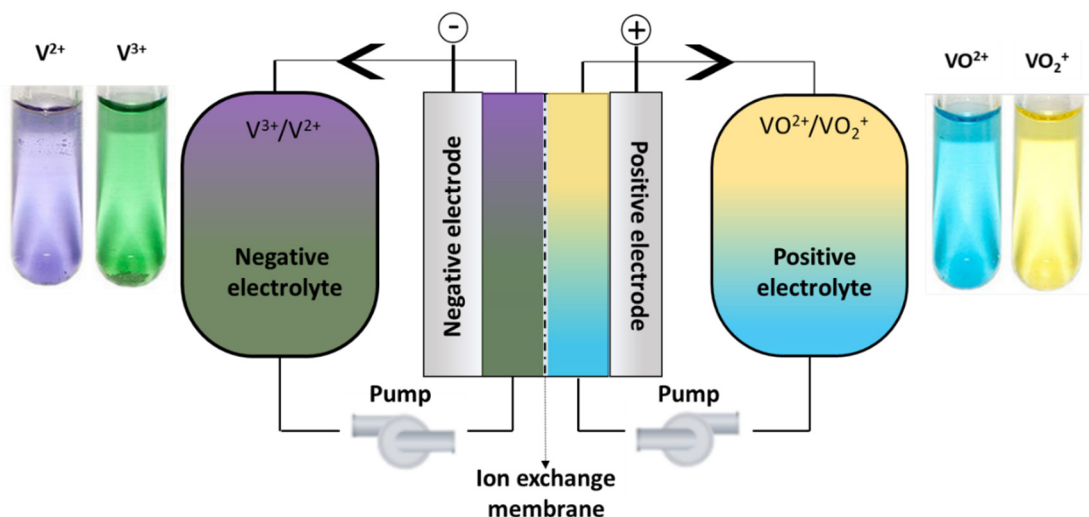


Figure 1.7 Schematic of an all-vanadium redox flow battery.

1.4 Hydrogen economy

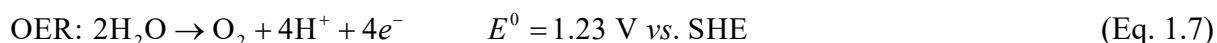
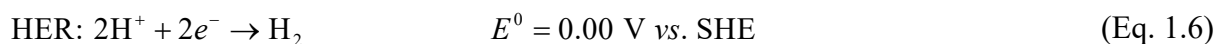
The relatively high gravimetric energy density of hydrogen of $142 \text{ MJ}\cdot\text{kg}^{-1}$ (higher heating value, HHV) make it an ideal candidate for energy storage and carbon-free energy carrier.¹⁸ In this context, the hydrogen economy is the economic model in which hydrogen is used as a sustainable energy vector for the purpose of various energy sectors including transportation, heat and industry (Figure 1.8). The major challenge of the model is the tremendous investments that are necessary to adapt the infrastructure including hydrogen production, storage, distribution and end-use conversion.⁷¹

Today, hydrogen gas is essentially used as a primary feedstock for the chemical industry (*e.g.* the synthesis of ammonia,⁷² the refining of fossil fuels⁷³ or metals,⁷⁴ the treatment of different materials going from semiconductors to glass⁷⁵ and others). While hydrogen element represents 75% of the universe mass, the presence of hydrogen gas (H_2) is rare in the Earth's atmosphere (1 ppm)⁷⁶. The nonexistence of any direct H_2 source on Earth makes its extraction impossible and consequently the synthesis of this molecule needs to be achieved on an industrial scale in a way to be used for a mass production of many components. About 50 million tonnes of hydrogen gas are produced every year corresponding to about 2% of the world's primary energy consumption.^{76,77} Today, 95% of the production of hydrogen relies on the use of fossil fuels, in particular steam reforming of methane (SMR) according to the synthetic pathways described in (Eq. 1.5). The resulting hydrogen produced is denoted as “grey” and is responsible for the

release of 830 Mt of CO₂ in the atmosphere per year. Note that the resulting hydrogen is denoted as ‘‘blue’’ in case of CO₂ capture.^{76,78,79}



For the development of a sustainable ‘‘hydrogen economy’’, the hydrogen gas is rather produced by water electrolysis with energy input generated by renewable sources.^{76,80,81} The hydrogen gas generated is usually denoted as ‘‘green’’. Note that the label ‘‘low-carbon’’ of Certifhy¹ is obtained in case the electricity used emits less than 80 g CO₂·kWh⁻¹. The splitting of water using electricity is as old as electrochemistry and relies on two half-reactions, namely the oxygen evolution reaction (OER) and the hydrogen evolution reaction (HER):



Water splitting is a highly energy intensive process. Thermodynamically, the electrolytic process requires a cell voltage greater than the theoretical standard potential of the water electrolysis cell (1.23 V). However, the dissociation of water into hydrogen and oxygen is an endothermic process ($\Delta_r H^0 = 286 \text{ kJ} \cdot \text{mol}^{-1}$ at room temperature) yielding to the thermoneutral potential of 1.48 V. Moreover, a high energy potential barrier is present in order to break water bond, which requires the use of catalysts for HER and OER to improve the kinetics of the reactions. In practice, the external potential applied to the electrolytic cell is greater with value up to 2V, depending on the type of electrolyzers. Today, only 4 % of the hydrogen gas is produced by water electrolysis, mainly for application requiring high purity hydrogen (*e.g.* electronics industry, fuel cell vehicles...).^{72,76} Three main technologies are considered today as scalable systems for electrolytic hydrogen production:

- Alkaline electrolyser is the most mature technology with reasonable efficiency (62-82% with respect to HHV), in which water splitting occurs at the surface of two electrodes immersed in an alkaline electrolyte (*e.g.* 20-30% KOH).^{18,82,83} The operating

¹ <https://www.certifhy.eu>

temperature is usually 60-80°C. The alkaline environment favoured the kinetics of OER affording the use of less precious electrocatalysts such as nickel. The main disadvantages related to the alkali electrolyzers stem from the caustic environment affecting the durability of cell components and the low current density limiting the production rate.⁸⁴⁻⁸⁶

- Proton exchange membrane (PEM) electrolyser is a more recent technology that uses a solid proton-conducting polymer as electrolyte. Similarly, to alkaline electrolyser, PEM operates at 60-80°C. The technology offers greater energy efficiency (65-82% with respect to HHV), a lower gas crossover, a more compact design, and higher production rates. However, the system requires more expensive components including noble-based electrocatalysts (*e.g.* Pt/C, IrO₂...), bipolar plates electrode and current collectors.^{18,82-84,87}
- Solid oxide electrolysis cell (SOEC) operates at temperature of 700-900°C where steam electrolysis can be achieved. The system uses ceramic electrolyte such as proton-conducting solid oxide (*e.g.* yttria-doped barium zirconate or cerate) or an oxide-ion conducting solid oxide electrolyte (*e.g.* yttria-stabilized zirconia or gadolinia doped ceria) to allow the selective mobility of H⁺ and O²⁻ through the ceramic membrane, respectively.¹⁸ Due to elevated temperature, the system achieves higher efficiency (>90%) by improving thermodynamics, kinetics and transport rates. The major challenges of the technology consist to minimize the complexity of design and to improve the lifetime of the cell materials at elevated temperatures.⁸⁸

After the electrolysis of water, hydrogen can be stored as a compressed gas in pressurized vessels (25-40 g·L⁻¹ at 350-700 bar), as a liquid in insulated vessel (70 g·L⁻¹), in a liquid organic hydrogen carrier *via* hydrogenation process or in a metal hydride or metal organic framework (MOF) *via* absorption process.²⁶

Regarding usage, hydrogen can be converted back into electricity using fuel cells. Various type of fuel cells exists including polymer electrolyte membrane fuel cell, alkaline fuel cell, phosphoric acid fuel cell, molten carbonate fuel cell and solid oxide fuel cell.¹⁸ Although the resulting round-trip efficiency is low for power-to-power application (30-50%), the hydrogen energy carrier can achieve very long term energy storage without self-discharge and can be

scalable to very large energy capacity. In a more general view, the generated hydrogen can also be further used for other usage including heating sector or industrial applications.²⁶

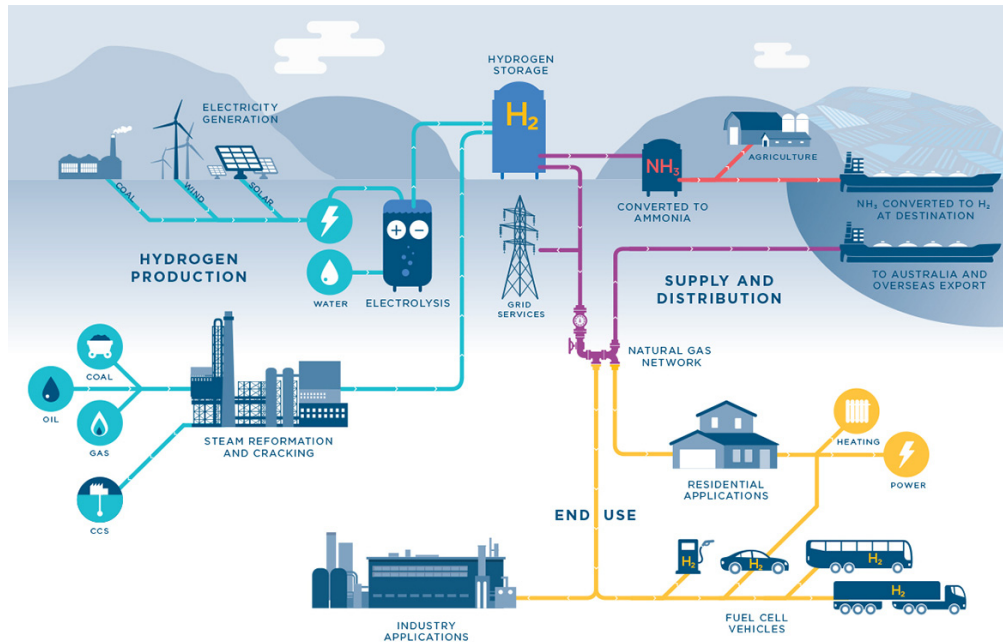


Figure 1.8 Hydrogen economy in which hydrogen is used as the main energy carrier and vector.⁸⁹

1.5 Electromobilis demonstrator

1.5.1 General layout

In 2014, the demonstration site Electromobilis was built in Martigny (Figure 1.9).^{90–95} This experimental platform aims at highlighting the reliability of electrochemical energy storage solutions for large-scale energy storage. The main research focused on redox flow battery and hydrogen technologies in order to determine their reliability for promoting the integration of renewable energy (*e.g.* solar, wind) and electrical mobility such as BEVs and FCEVs in the conventional electrical grid. Here are the main electrochemical devices installed on-site (Figure 1.10):

- An all-vanadium redox flow battery of 10 kW/40 kWh to play the role of power buffer between solar production (10 kW) and the electricity demand of the building.
- An all-vanadium redox flow battery of 200 kW/400 kWh that acts as a power buffer between the electrical grid and battery electric vehicles.

- A complete system for hydrogen including production by electrolysis (alkaline electrolyser 50 kW), purification and compression (up to 700 bar) and refuelling station for fuel-cell electric vehicles.



Figure 1.9 Illustration of the demonstration site Electromobilis, EPFL © LEPA, 2016.

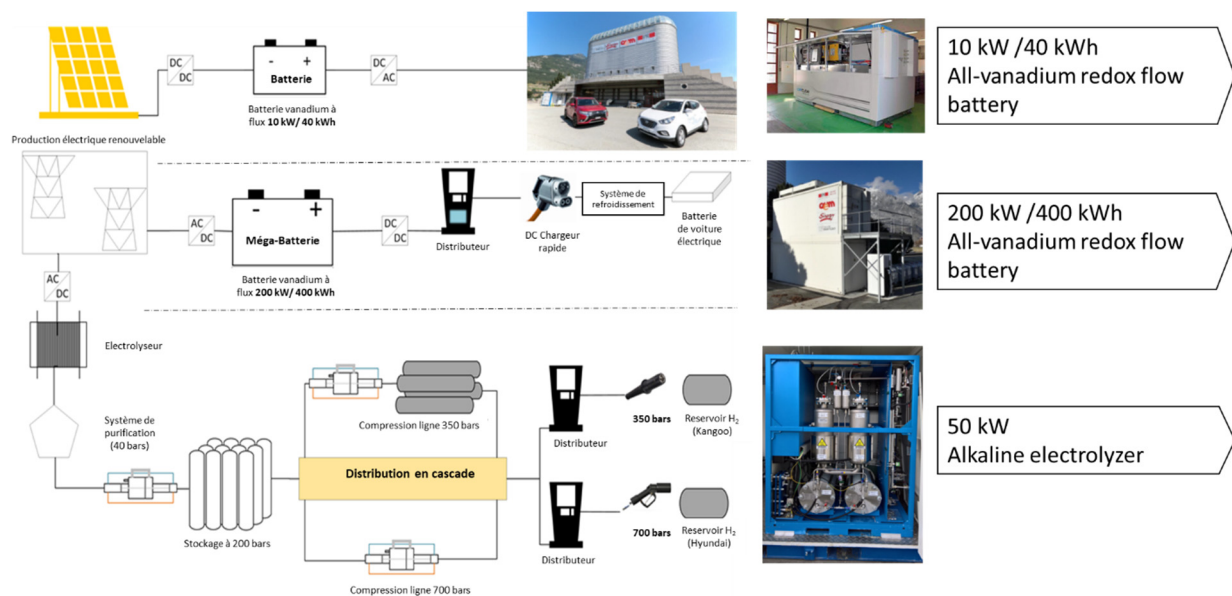


Figure 1.10 Overview of the mains installations on the demonstration site Electromobilis, EPFL.

1.5.2 Redox flow battery operation

Redox flow batteries were purchased from Gildemeister energy storage GmbH, Austria. The 10 kW/40 kWh and 200 kW/400 kWh were respectively referenced as CellCube FB 10-40 and CellCube FB 200-400.

The 200 kW/400 kWh VRFB shown in Figure 1.11 included 4 modules of 20 electrochemical stacks (upper container) and two electrolyte double walled tanks containing 26 m³ of 1.6 M vanadium sulfate electrolyte in concentrated (2M) sulfuric acid (lower container). Each stack was designed with 27 bipolar cells in series and end-of-stack copper current collector. The single cell was composed of graphitic felts electrodes (28 cm x 19.5 cm x 0.46 cm), anionic exchange membrane and graphite bipolar plates. All the stacks were individually connected to the main DC line (650-750 V) with a DC/DC convertor to afford individual stack decoupling. The battery was powered by the 400 VAC 50 Hz network using an AC/DC rectifier and was connected to a fast DC charger for battery electric vehicle.



Figure 1.11 Illustration of the 200 kW / 400 kWh all-vanadium redox flow battery installed on the demonstration site Electromobilis, EPFL © LEPA, 2016.

The characterization of the 200 kW / 400 kWh RFB revealed overall energy efficiencies at maximum of 60%. The performances were largely impacted by a non-optimized battery management system and the auxiliary power electronics (centrifugal pump, AC/DC convertors, DC/DC convertors, cooling system...) contributing to up to 24% of energy losses.⁹⁴

In the framework of the demonstrator, Ligen *et al.* reported a robust methodology to assess the relevance of local battery energy storage implementation to reduce the required grid tie for multi-stall electric vehicle charging stations.⁹²

Unfortunately, the extended operations of the two batteries led to leakages of electrolyte from the stacks causing irreversible damages. After disassembling the damaged stacks, the failures were attributed to the corrosion on the positive half-cell compartment involving corrosion of carbon electrodes and bipolar plates (cracks formation) compromising the impermeability of the bipolar separators. As a result, the electrolyte leached on the copper current collector until complete dissolution. In addition, the resulting electrolyte contamination with copper was observed to be deleterious for the battery operation. In fact, the dissolved copper was able to plate on the negative compartment enhancing drastically the rate of parasitic hydrogen evolution reaction, yielding to irreversible imbalance of electrolyte and complete failure of the redox flow battery. In order to recover the electrolyte, we developed a purification procedure on-site. A pilot-installation was built on the demonstration site and the contaminated electrolytes were successfully recovered. The analysis of the failure and the purification procedure are presented in detail in chapter II. On the basis of these investigations and issues, measures and improvements were undertaken on the battery management system (BMS) to improve the system performances and avoid premature failures.

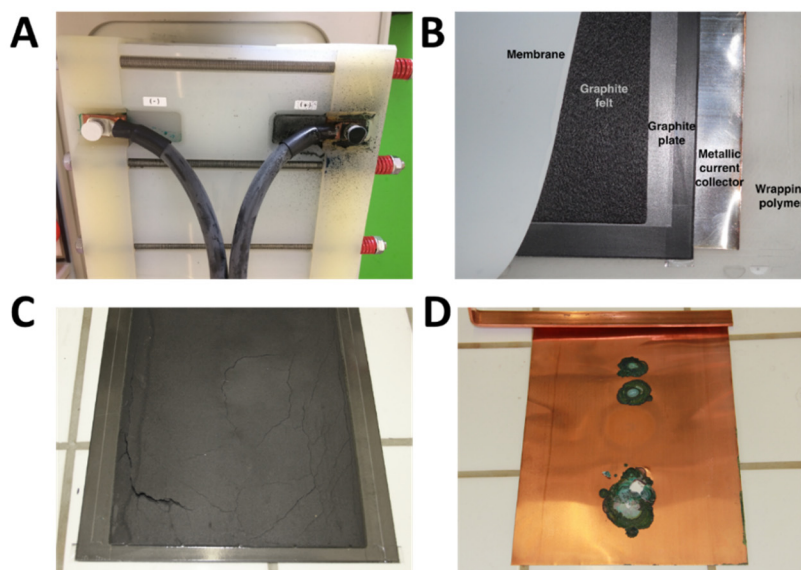


Figure 1.12 Illustration of the stack degradation observed in the all-vanadium redox flow battery installed in Electromobilis; (A) Electrolyte leakage of the stack (B) Components of the stack (C) Cracks observed on a carbon bipolar plate (D) Corrosion observed on a copper current collector.

1.5.3 Hydrogen infrastructure and operation

The hydrogen refuelling station consisted of several infrastructures:

- The production unit: The hydrogen was produced on-site by water splitting from an alkaline electrolyser (McPhy Energy, McLyzer 10-10 50 kW) composed of 2 electrolysis stacks (115 cells) of 25 kW, achieving a nominal production of 850 g of H₂ per hour. Note that the balance of plant (BOP), gas management and control system were redesigned for research purposes. The electrolyser was operated at a pressure of 10 bar. Energy consumption of 5.8 kWh·Nm⁻³ (DC) and 6.4 kWh·Nm⁻³ (AC with auxiliaries) were obtained.⁹⁵
- The purification unit: After the electrolysis, the hydrogen stream was sent to a purification process including a scrubber for particle and KOH removal, a deoxygenation catalytic reactor, coalescing filter and vacuum assisted pressure swing adsorption (VPSA) unit (working at 40 bar) for water removal. The resulting hydrogen outlet stream was compatible with ISO 14687:2019 standard.⁹⁶
- The compression unit and station unit: For the compression, commercial hydrogen gas boosters (Maximator) were used. A first compression step (Maximator DLE-15-2) between the outlet of the purification unit at 40 bar and the bulk storage at 200 bar was performed. Then, the hydrogen gas was compressed between the bulk storage at 200 bar and two pressure level cascades at 500 bar (Maximator DLE-35-2) and 700 bar (Maximator DLE-75-2). The refuelling station was designed to refill the Swiss Hydrogen Kangoo at 350 bar and a Hyundai ix35 Fuel Cell at 700 bar.⁹⁷

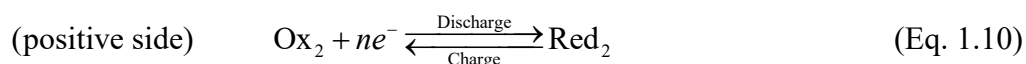
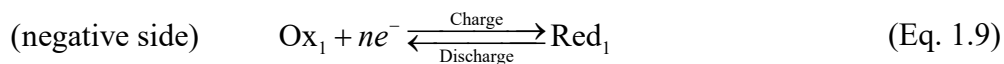
1.6 Redox dual-flow battery

1.6.1 Concept

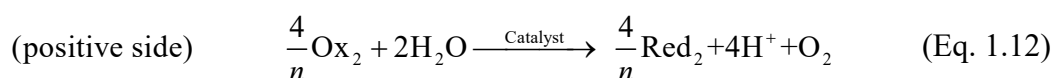
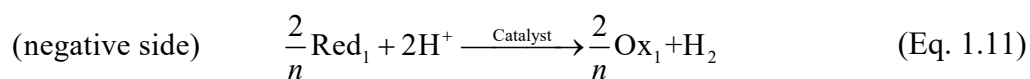
In the framework of the Electromobilis demonstrator, Amstutz *et al.* introduced the concept of “dual-circuit redox flow battery” or “redox dual-flow battery” (RDFB). This system differs from a conventional redox flow battery (RFB) by including a secondary platform for energy storage, in which the charged electrolytes can be chemically discharged *via* redox-catalytic water splitting, converting power to renewable hydrogen (Figure 1.13-A). The energy stored

within the hydrogen carrier can be further converted back into electrical energy using fuel cells (*e.g.* stationary or vehicles), or used for other industrial processes.⁹⁸

Upon conventional battery mode, electricity can be electrochemically stored by charging and discharging the positive and the negative electrolytes according to the following reactions:



As an alternative, the charged electrolytes can be pumped through external catalytic bed reactors (out of the electrochemical cell), where they will respectively act as electron mediators (donor and acceptor) to carry out hydrogen evolution reaction (HER) and redox-mediated oxygen evolution reaction (OER) over appropriate redox electrocatalysts.^{99,100}



Considering a full conversion for the redox-mediated reaction, the production of hydrogen consumes an equal number of protons than the production of oxygen generates, consuming only water during the chemical process.

An important prerequisite for the redox dual-flow system is the choice of both suitable redox-mediators and redox electrocatalysts. Obviously, in order to compete with the performance of conventional RFB, the redox-mediators must satisfy several requirements in terms of reversibility, solubility and stability. In addition, the standard potential of the selected redox couples is a key success factor of the feasibility of the RDFB. Indeed, it is critical that the mediators can address optimally the two different modes of discharge. In the first instance, the potential of the redox couples must be in the water stability range under the battery mode conditions (*e.g.* carbon electrodes) in order to avoid undesired HER and OER in the electrochemical cell. On the other hand, the thermodynamic potential of the positive and negative redox couples must be sufficient to drive respectively redox-mediated OER and HER under the chemical discharge mode over the appropriated redox electrocatalysts.

As shown in Figure 1.13-B, the redox-mediated HER and OER involve two simultaneous electron transfer reactions at the surface of the redox electrocatalytic particles, that are conductive floating particles that facilitate the electron transfer by playing the role of electrons shuttles between the two redox couples.

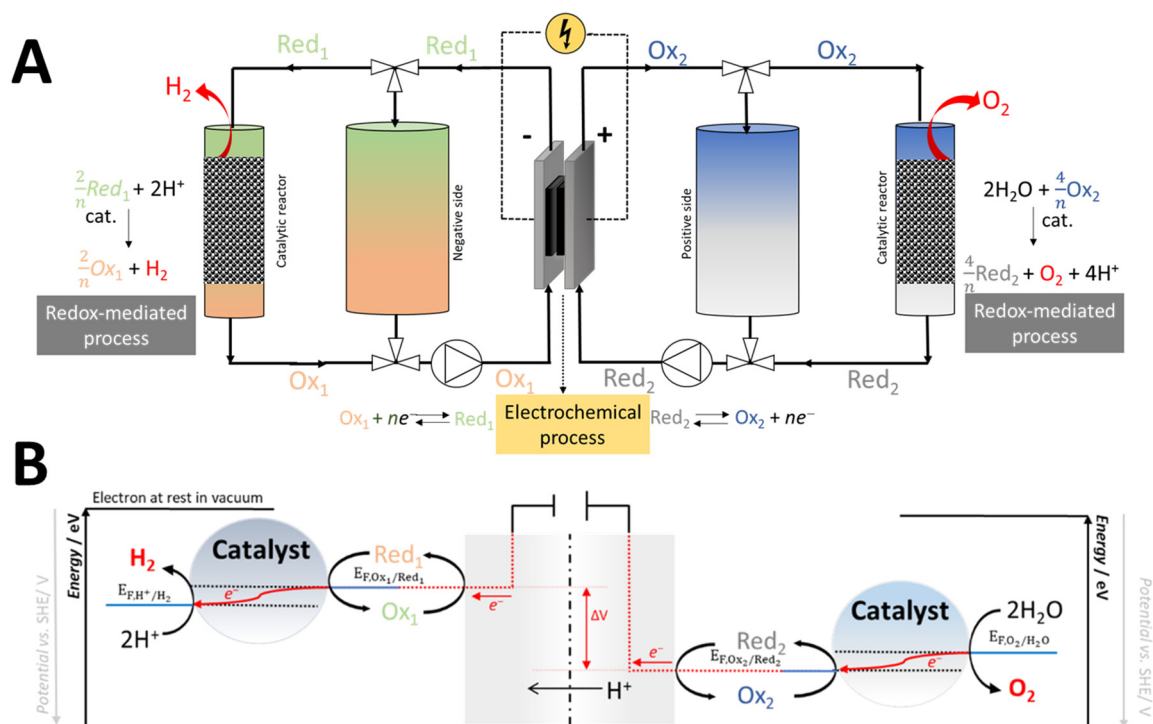


Figure 1.13 (A) General schematic of the redox dual-flow battery (B) Energy diagram of the redox catalytic HER and OER *via* redox mediators.

During the redox-mediated HER, the electrons are supplied by the oxidation of Red_1 and drawn by the reduction of protons.¹⁰⁰ Similarly, during the redox-mediated OER, the electrons are supplied by the oxidation of water and drawn by the reduction of Ox_2 . Note that in the absence of redox electrocatalysts, although thermodynamically favorable, the direct homogenous electron transfer reactions of (Eq. 1.11) and (Eq. 1.12) are thermodynamically possible but kinetically limited. The contact of the redox mediators with the redox electrocatalysts favors kinetically the electron-transfer processes. As a result, the electrochemical potentials of the electron (work necessary to bring a mole of electrons from the vacuum) or Fermi levels of the electron of the redox electrocatalyst and the redox mediator equilibrate. At equilibrium, the Fermi level of the electron in the redox electrocatalysis will be imposed by the rates of the two electron-transfer reactions on the electrocatalyst surface, by equilibrating close to the Fermi level of the faster redox couple.¹⁰¹

1.6.2 Advantages

By combining electrochemical energy storage with renewable hydrogen production, the dual-circuit redox flow battery offers several advantages in the field of large-scale energy storage:

Energy capacity: The RDFB can store energy beyond the capacity of the conventional RFB ($15\text{--}40\text{ Wh}\cdot\text{L}^{-1}$) owing to the higher specific capacity of the hydrogen energy carrier ($870\text{--}1300\text{ Wh}\cdot\text{L}^{-1}$ at storing pressure ranging from 350–750 bar, lower heating value (LHV)).¹⁰² The design of the system enables to capture and store the electrical energy surplus exceeding the storage capacity of the redox flow battery in the form of hydrogen. The generated hydrogen can be stored and used later, freeing up storage space in the battery itself.

Flexibility: The RDFB offers great operation flexibility by providing both distributed electricity storage and on-demand hydrogen production. Such a hybridization is of great interest for emerging grid infrastructures, including charging service station for both fast charging of electric vehicles and hydrogen refilling of fuel-cell vehicles, especially when the electricity is generated from intermittent sources such as solar and wind. The integration of energy storage solutions provides several benefits to the stations such as peak shaving and load buffering, minimizing the grid power constraints.

Decoupling HER and OER: In conventional electrolyzers (*e.g.* alkaline and polymer electrolyte membrane technologies), HER and OER occur simultaneously at the two electrodes separated by an ion exchange membrane or a diaphragm.^{99,100} The resulting O_2 and H_2 recombination is a major issue of the conventional technologies involving material degradation (formation of $\text{OH}\cdot$ radicals), safety concerns and need for complementary purification unit. Redox-mediated water electrolysis gives the opportunity to decouple OER and HER in time and in space. The strategy of decoupled water splitting was first reported in 2013 by Symes and Cronin using the polyoxometalate phosphomolybdic acid ($\text{H}_3\text{PMo}_{12}\text{O}_{40}$) as a redox mediator able to store reversibly the protons and the electrons generated during the oxygen generation step to liberate them later in another compartment in order to carry on the hydrogen generation step.¹⁰³ Recently, several water splitting systems have been proposed to decouple the generation of oxygen and hydrogen.^{104–108} Additionally, the redox mediation enables to carry on the gas evolving reactions away from conventional electrodes, mitigating mass transport and conductivity limitation arising from bubbles formation at the electrode-electrolyte interface.

This offers the opportunity to design three-dimensional (3D) catalytic bed reactor using less active/cheaper redox electrocatalysts.

Electrolyte rebalancing: A major hurdle with redox flow batteries is to control imbalance between the two half-cell electrolytes (see chapter II). Several processes such as membrane electrolyte crossover and undesired side reactions can lead to electrolyte imbalance. While volume electrolyte imbalance can be mitigated by electrolytes remixing, the imbalance causing deviation of the average oxidation state (AOS) is more demanding and requires advanced chemical or electrochemical rebalancing methods. With this in mind, the RDFB offers the opportunity to control individually the state-of-charge (SOC) of each half-cell electrolyte through redox-mediated processes, facilitating electrolyte state-of-charge rebalancing management.⁹²

1.6.3 State-of-the-art

In 2013, Amstutz *et al.* patented the concept of the dual-flow circuit redox flow battery.¹⁰⁹ The system was first studied with a vanadium-cerium redox flow battery module (Figure 1.14-A), employing V^{3+}/V^{2+} ($E^0 = -0.26$ V vs. SHE) and Ce^{4+}/Ce^{3+} ($E^0 = +1.44$ V vs. SHE) redox couples in sulfuric acid as negative and positive redox mediators, respectively.⁹⁹ Upon operation, the electrolyte could be electrochemically charged and discharged on graphite felt electrodes in the flow cell or chemically discharged in external catalytic beds. Redox-mediated HER was performed over Mo_2C redox electrocatalysts, while redox-mediated OER was carried on RuO_2 or IrO_2 . Even though the system was successfully demonstrated with chemical discharge at high conversion yield, limitations were observed from the use of cerium mediator on the positive side, especially in terms of solubility, corrosion and degradation.⁹⁹

As an alternative approach, the concept of dual-circuit redox was applied to a conventional all-vanadium RFB. Given that the standard potential of VO_2^+/VO^{2+} redox couple (1.00 V vs. SHE) is lower than that of the OER reaction (1.23 V vs. SHE), it is thermodynamically impossible to drive spontaneously the chemical discharge. As the positive discharge is critical during hydrogen production to maintain the balance of the electrolytes SOC and the protons in the battery, it is critical to bypass the chemical discharge of the positive electrolyte. Peljo *et al.* reported different strategies consisting of discharging the positive electrolyte electrochemically in an external unit using $V(V)/SO_2$ (Figure 1.14-B) or $V(V)/H_2S$ fuel cell (Figure 1.14-C).¹¹⁰ Even though those systems have the advantage to produce valuable products (H_2SO_4 or $S(s)$),

the resulting efficiency, the additional capital cost of electrochemical unit and the need for separation unit limit the economic benefit. More recently, Piwek *et al.* reported a similar approach by implementing a V(V)/O₂ fuel cell (Figure 1.14-D).¹¹¹

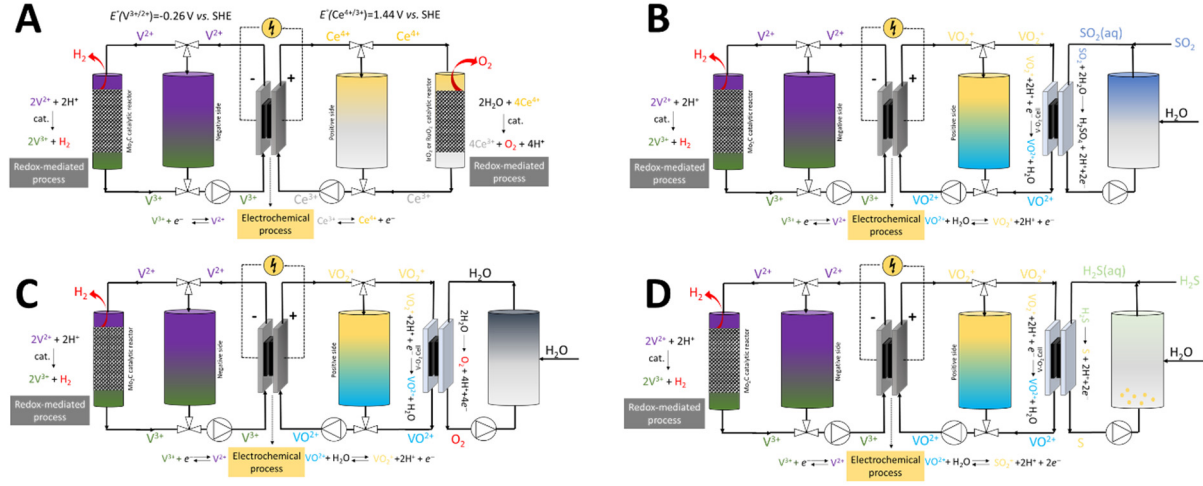
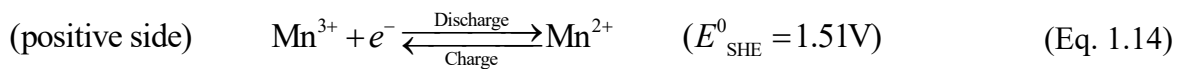


Figure 1.14 General schematic of developed redox dual-flow systems: (A) vanadium-cerium redox dual-flow battery (B) vanadium-vanadium redox dual-flow battery using an additional V(V)/SO₂ fuel cell (C) vanadium-vanadium redox dual-flow battery using an additional V(V)/H₂S fuel cell (D) vanadium-vanadium redox dual-flow battery using an additional V(V)/O₂ fuel cell.

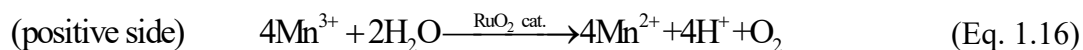
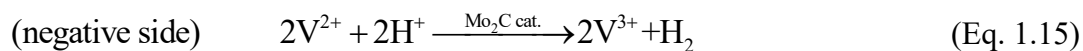
1.7 Challenges and objectives of the thesis

In this general context, the objective of this thesis is to develop a novel redox dual-flow battery system, that can reliably afford both electrical energy storage and hydrogen production. As shown on Figure 1.15, the proposed system consists of a novel and eco-friendly vanadium-manganese flow cell with Mn³⁺/Mn²⁺ (1.51 V vs. SHE) and V³⁺/V²⁺ (−0.26 V vs. SHE) as positive and negative redox-mediators, respectively.

Upon battery mode, the electrolytes can be charged and discharged electrochemically according to the following redox reactions:



Upon water electrolysis mode, the positive electrolyte and the negative electrolyte can be discharged through redox-mediated HER and OER in external Mo₂C-based and RuO₂-based catalytic reactors:



Chapter II differs from the other chapters in the sense that is not directly dedicated to the development of the redox dual-flow battery, but presents in detail the failure analysis of the commercial all-vanadium redox flow battery installed on the demonstrator site of Electromobilis. Nevertheless, the study serves to acquire an industrial vision of the remaining challenges required by redox flow battery systems and provides additional motivation for the development of redox dual-flow battery. The chapter highlights the degradation scenarios and assesses the principle consequences resulting from the failure including copper-contamination of the electrolytes. A remedial strategy is proposed with the development of a purification method on-site to recover the electrolyte and bring back the battery to operation.

Chapter III is devoted to the stabilization of the manganese electrolyte composing the redox dual-flow system to decrease the formation of MnO₂, which is a major hurdle in vanadium-manganese redox flow battery.

Chapter IV presents a comprehensive kinetic study of the vanadium-mediated hydrogen evolution production over Mo₂C redox electrocatalyst. From a mechanistic reaction pathway, a kinetic rate law is established. The process model is implemented in a semi-batch reactor configuration to highlight the optimal parameter to carry out the reaction in an efficient way for a given demand in hydrogen.

Chapter V concerns the design of the catalytic reactors by proposing a fast and simple method for the fabrication of Mo₂C-based electrocatalysts on a carbon substrate by photonic flash synthesis.

Chapter VI is dedicated to the design and the assembly of a prototype at laboratory scale. It demonstrates the proof-of-concept and presents the performances of the vanadium-manganese

redox dual-flow system.

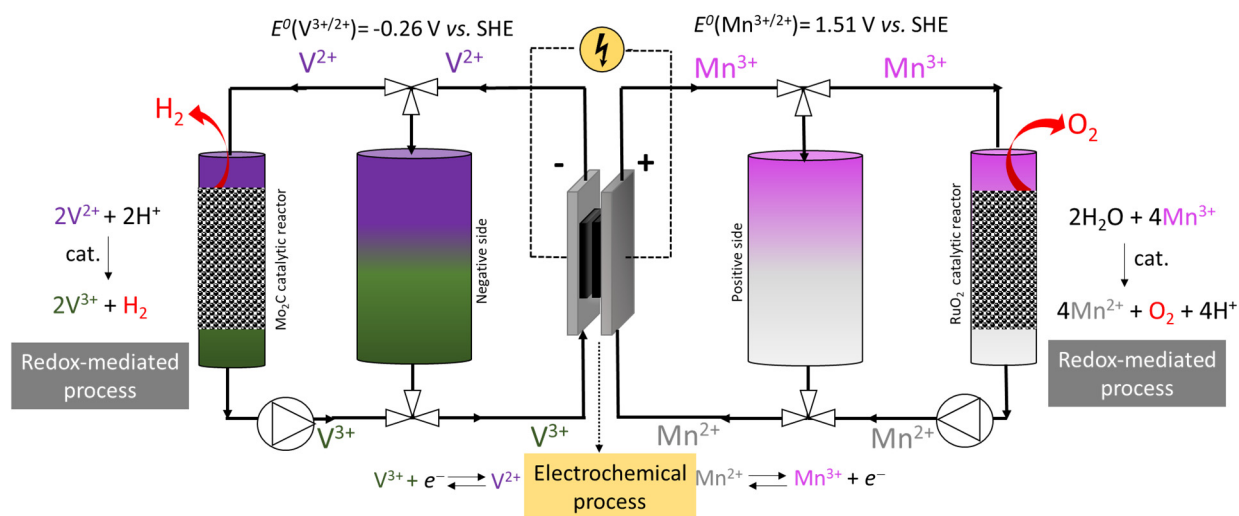


Figure 1.15 General schematic of the vanadium-manganese dual-flow battery developed in this thesis.

References

- (1) World gross electricity production, by source, 2018 – Charts – Data & Statistics <https://www.iea.org/data-and-statistics/charts/world-gross-electricity-production-by-source-2018> (accessed 2020 -10 -06).
- (2) Grande Dixence SA | <https://www.alpiq.com/power-generation/hydropower-plants/storage-power-plants/grande-dixence> (accessed 2021 -08 -05).
- (3) Masson-Delmotte, V.; Zhai, P.; Pörtner, H.-O.; Roberts, D.; Skea, J.; Shukla, P. R.; Pirani, A.; Moufouma-Okia, W.; Péan, C.; Pidcock, R.; Connors, S.; Matthews, J. B. R.; Chen, Y.; Zhou, X.; Gomis, M. I.; Lonnoy, E.; Maycock, T.; Tignor, M.; Waterfield, T. IPCC, 2018: Summary for Policymakers. In: Global Warming of 1.5°C. An IPCC Special Report on the Impacts of Global Warming of 1.5°C above Pre-Industrial Levels and Related Global Greenhouse Gas Emission Pathways, in the Context of Strengthening the Global Response to the Threat of Climate Change, Sustainable Development, and Efforts to Eradicate Poverty. World Meteorological Organization, Geneva, Switzerland.
- (4) Baker, J. N.; Collinson, A. Electrical Energy Storage at the Turn of the Millennium. *Power Eng. J.* **1999**, *13* (3), 107–112. <https://doi.org/10.1049/pe:19990301>.
- (5) DETEC, F. D. of the E., Transport, Energy and Communications. Energy Strategy 2050 <https://www.uvek.admin.ch/uvek/en/home/energie/energiestrategie-2050.html> (accessed 2020 -12 -18).
- (6) Panwar, N. L.; Kaushik, S. C.; Kothari, S. Role of Renewable Energy Sources in Environmental Protection: A Review. *Renew. Sustain. Energy Rev.* **2011**, *15* (3), 1513–1524. <https://doi.org/10.1016/j.rser.2010.11.037>.
- (7) Huber, M.; Dimkova, D.; Hamacher, T. Integration of Wind and Solar Power in Europe: Assessment of Flexibility Requirements. *Energy* **2014**, *69*, 236–246. <https://doi.org/10.1016/j.energy.2014.02.109>.
- (8) Zhao, H.; Wu, Q.; Hu, S.; Xu, H.; Rasmussen, C. N. Review of Energy Storage System for Wind Power Integration Support. *Appl. Energy* **2015**, *137*, 545–553. <https://doi.org/10.1016/j.apenergy.2014.04.103>.
- (9) Electric Energy Storage Technology Options: A White Paper Primer on Applications, Costs, and Benefits. 170.
- (10) Divya, K. C.; Østergaard, J. Battery Energy Storage Technology for Power Systems—An Overview. *Electr. Power Syst. Res.* **2009**, *79* (4), 511–520. <https://doi.org/10.1016/j.epsr.2008.09.017>.
- (11) Chen, H.; Cong, T. N.; Yang, W.; Tan, C.; Li, Y.; Ding, Y. Progress in Electrical Energy Storage System: A Critical Review. *Prog. Nat. Sci.* **2009**, *19* (3), 291–312. <https://doi.org/10.1016/j.pnsc.2008.07.014>.
- (12) Vazquez, S.; Lukic, S. M.; Galvan, E.; Franquelo, L. G.; Carrasco, J. M. Energy Storage Systems for Transport and Grid Applications. *IEEE Trans. Ind. Electron.* **2010**, *57* (12), 3881–3895. <https://doi.org/10.1109/TIE.2010.2076414>.
- (13) Hannan, M. A.; Hoque, M. M.; Mohamed, A.; Ayob, A. Review of Energy Storage Systems for Electric Vehicle Applications: Issues and Challenges. *Renew. Sustain. Energy Rev.* **2017**, *69*, 771–789. <https://doi.org/10.1016/j.rser.2016.11.171>.
- (14) MJR's Marine Energy Storage Solutions. *MJR Power & Automation*, 2018.
- (15) Clausius, R. Ueber Die Bewegende Kraft Der Wärme Und Die Gesetze, Welche Sich Daraus Für Die Wärmelehre Selbst Ableiten Lassen. *Ann. Phys.* **1850**, *155* (4), 500–524. <https://doi.org/10.1002/andp.18501550403>.
- (16) Atkins, P. *Four Laws That Drive the Universe*; OUP Oxford, 2007.

- (17) Struchtrup, H. Introduction: Why Thermodynamics? In *Thermodynamics and Energy Conversion*; Struchtrup, H., Ed.; Springer: Berlin, Heidelberg, 2014; pp 1–9. https://doi.org/10.1007/978-3-662-43715-5_1.
- (18) Gür, T. M. Review of Electrical Energy Storage Technologies, Materials and Systems: Challenges and Prospects for Large-Scale Grid Storage. *Energy Environ. Sci.* **2018**, *11* (10), 2696–2767. <https://doi.org/10.1039/C8EE01419A>.
- (19) Luo, X.; Wang, J.; Dooner, M.; Clarke, J. Overview of Current Development in Electrical Energy Storage Technologies and the Application Potential in Power System Operation. *Appl. Energy* **2015**, *137*, 511–536. <https://doi.org/10.1016/j.apenergy.2014.09.081>.
- (20) Hemmati, R.; Saboori, H. Short-Term Bulk Energy Storage System Scheduling for Load Leveling in Unit Commitment: Modeling, Optimization, and Sensitivity Analysis. *J. Adv. Res.* **2016**, *7* (3), 360–372. <https://doi.org/10.1016/j.jare.2016.02.002>.
- (21) Electrical Energy Storage, White Paper. IEC Market Strategy Board.
- (22) Rehman, S.; Al-Hadhrami, L. M.; Alam, Md. M. Pumped Hydro Energy Storage System: A Technological Review. *Renew. Sustain. Energy Rev.* **2015**, *44*, 586–598. <https://doi.org/10.1016/j.rser.2014.12.040>.
- (23) Kolb, S. Les défis techniques de Nant de Drance <https://www.bulletin.ch/fr/news-detail/les-defis-techniques-de-nant-de-drance.html> (accessed 2021 -08 -05).
- (24) Budt, M.; Wolf, D.; Span, R.; Yan, J. A Review on Compressed Air Energy Storage: Basic Principles, Past Milestones and Recent Developments. *Appl. Energy* **2016**, *170*, 250–268. <https://doi.org/10.1016/j.apenergy.2016.02.108>.
- (25) Koochi-Fayegh, S.; Rosen, M. A. A Review of Energy Storage Types, Applications and Recent Developments. *J. Energy Storage* **2020**, *27*, 101047. <https://doi.org/10.1016/j.est.2019.101047>.
- (26) Gallo, A. B.; Simões-Moreira, J. R.; Costa, H. K. M.; Santos, M. M.; Moutinho dos Santos, E. Energy Storage in the Energy Transition Context: A Technology Review. *Renew. Sustain. Energy Rev.* **2016**, *65*, 800–822. <https://doi.org/10.1016/j.rser.2016.07.028>.
- (27) Zhou, L.; Li, C.; Liu, X.; Zhu, Y.; Wu, Y.; van Ree, T. 7 - Metal Oxides in Supercapacitors. In *Metal Oxides in Energy Technologies*; Wu, Y., Ed.; Metal Oxides; Elsevier, 2018; pp 169–203. <https://doi.org/10.1016/B978-0-12-811167-3.00007-9>.
- (28) G, V. S. V.; Madichetty, S. Application of Superconducting Magnetic Energy Storage in Electrical Power and Energy Systems: A Review. *Int. J. Energy Res.* **2018**, *42* (2), 358–368. <https://doi.org/10.1002/er.3773>.
- (29) Soloveichik, G. L. Battery Technologies for Large-Scale Stationary Energy Storage. *Annu. Rev. Chem. Biomol. Eng.* **2011**, *2* (1), 503–527. <https://doi.org/10.1146/annurev-chembioeng-061010-114116>.
- (30) Sarbu, I.; Sebarchievici, C. A Comprehensive Review of Thermal Energy Storage. *Sustainability* **2018**, *10* (1), 191. <https://doi.org/10.3390/su10010191>.
- (31) Passerini, S.; Bresser, D.; Moretti, A.; Varzi, A. *Batteries: Present and Future Energy Storage Challenges*, Wiley.; 2020; Vol. 1.
- (32) Krishan, O.; Suhag, S. An Updated Review of Energy Storage Systems: Classification and Applications in Distributed Generation Power Systems Incorporating Renewable Energy Resources. *Int. J. Energy Res.* **2019**, *43* (12), 6171–6210. <https://doi.org/10.1002/er.4285>.
- (33) Abbas, Q.; Mirzaeian, M.; Hunt, M. R. C.; Hall, P.; Raza, R. Current State and Future Prospects for Electrochemical Energy Storage and Conversion Systems. *Energies* **2020**, *13* (21), 5847. <https://doi.org/10.3390/en13215847>.
- (34) Hossain, E.; Faruque, H. M. R.; Sunny, M. S. H.; Mohammad, N.; Nawar, N. A Comprehensive Review on Energy Storage Systems: Types, Comparison, Current

- Scenario, Applications, Barriers, and Potential Solutions, Policies, and Future Prospects. *Energies* **2020**, *13* (14), 3651. <https://doi.org/10.3390/en13143651>.
- (35) Dunn, B.; Kamath, H.; Tarascon, J.-M. Electrical Energy Storage for the Grid: A Battery of Choices. *Science* **2011**, *334* (6058), 928–935. <https://doi.org/10.1126/science.1212741>.
- (36) Yang, Y.; Bremner, S.; Menictas, C.; Kay, M. Battery Energy Storage System Size Determination in Renewable Energy Systems: A Review. *Renew. Sustain. Energy Rev.* **2018**, *91*, 109–125. <https://doi.org/10.1016/j.rser.2018.03.047>.
- (37) Batteries: Present and Future Energy Storage Challenges, 2 Volume Set | Wiley <https://www.wiley.com/en-us/Batteries%3A+Present+and+Future+Energy+Storage+Challenges%2C+2+Volume+Set-p-9783527345762> (accessed 2021 -08 -09).
- (38) Fan, X.; Liu, B.; Liu, J.; Ding, J.; Han, X.; Deng, Y.; Lv, X.; Xie, Y.; Chen, B.; Hu, W.; Zhong, C. Battery Technologies for Grid-Level Large-Scale Electrical Energy Storage. *Trans. Tianjin Univ.* **2020**, *26* (2), 92–103. <https://doi.org/10.1007/s12209-019-00231-w>.
- (39) Aneke, M.; Wang, M. Energy Storage Technologies and Real Life Applications – A State of the Art Review. *Appl. Energy* **2016**, *179*, 350–377. <https://doi.org/10.1016/j.apenergy.2016.06.097>.
- (40) Bockris, J. O. M. The Hydrogen Economy: Its History. *Int. J. Hydrog. Energy* **2013**, *38* (6), 2579–2588. <https://doi.org/10.1016/j.ijhydene.2012.12.026>.
- (41) Zhang, F.; Zhao, P.; Niu, M.; Maddy, J. The Survey of Key Technologies in Hydrogen Energy Storage. *Int. J. Hydrog. Energy* **2016**, *41* (33), 14535–14552. <https://doi.org/10.1016/j.ijhydene.2016.05.293>.
- (42) Yang, Z.; Zhang, J.; Kintner-Meyer, M. C. W.; Lu, X.; Choi, D.; Lemmon, J. P.; Liu, J. Electrochemical Energy Storage for Green Grid. *Chem. Rev.* **2011**, *111* (5), 3577–3613. <https://doi.org/10.1021/cr100290v>.
- (43) Benato, R.; Cosciani, N.; Crugnola, G.; Dambone Sessa, S.; Lodi, G.; Parmeggiani, C.; Todeschini, M. Sodium Nickel Chloride Battery Technology for Large-Scale Stationary Storage in the High Voltage Network. *J. Power Sources* **2015**, *293*, 127–136. <https://doi.org/10.1016/j.jpowsour.2015.05.037>.
- (44) Deng, J.; Luo, W.-B.; Chou, S.-L.; Liu, H.-K.; Dou, S.-X. Sodium-Ion Batteries: From Academic Research to Practical Commercialization. *Adv. Energy Mater.* **2018**, *8* (4), 1701428. <https://doi.org/10.1002/aenm.201701428>.
- (45) Fang, Y.; Xiao, L.; Chen, Z.; Ai, X.; Cao, Y.; Yang, H. Recent Advances in Sodium-Ion Battery Materials. *Electrochem. Energy Rev.* **2018**, *1* (3), 294–323. <https://doi.org/10.1007/s41918-018-0008-x>.
- (46) Weber, A. Z.; Mench, M. M.; Meyers, J. P.; Ross, P. N.; Gostick, J. T.; Liu, Q. Redox Flow Batteries: A Review. *J. Appl. Electrochem.* **2011**, *41* (10), 1137. <https://doi.org/10.1007/s10800-011-0348-2>.
- (47) Alotto, P.; Guarnieri, M.; Moro, F. Redox Flow Batteries for the Storage of Renewable Energy: A Review. *Renew. Sustain. Energy Rev.* **2014**, *29*, 325–335. <https://doi.org/10.1016/j.rser.2013.08.001>.
- (48) Reynard, D.; Dennison, C. R.; Battistel, A.; Girault, H. H. Efficiency Improvement of an All-Vanadium Redox Flow Battery by Harvesting Low-Grade Heat. *J. Power Sources* **2018**, *390*, 30–37. <https://doi.org/10.1016/j.jpowsour.2018.03.074>.
- (49) Soloveichik, G. L. Flow Batteries: Current Status and Trends. *Chem. Rev.* **2015**, *115* (20), 11533–11558. <https://doi.org/10.1021/cr500720t>.

- (50) Ponce de León, C.; Frías-Ferrer, A.; González-García, J.; Szánto, D. A.; Walsh, F. C. Redox Flow Cells for Energy Conversion. *J. Power Sources* **2006**, *160* (1), 716–732. <https://doi.org/10.1016/j.jpowsour.2006.02.095>.
- (51) Gentil, S.; Reynard, D.; Girault, H. H. Aqueous Organic and Redox-Mediated Redox Flow Batteries: A Review. *Curr. Opin. Electrochem.* **2020**, *21*, 7–13. <https://doi.org/10.1016/j.coelec.2019.12.006>.
- (52) Pan, F.; Wang, Q. Redox Species of Redox Flow Batteries: A Review. *Molecules* **2015**, *20* (11), 20499–20517. <https://doi.org/10.3390/molecules201119711>.
- (53) Singh, V.; Kim, S.; Kang, J.; Byon, H. R. Aqueous Organic Redox Flow Batteries. *Nano Res.* **2019**, *12* (9), 1988–2001. <https://doi.org/10.1007/s12274-019-2355-2>.
- (54) Leung, P.; Shah, A. A.; Sanz, L.; Flox, C.; Morante, J. R.; Xu, Q.; Mohamed, M. R.; Ponce de León, C.; Walsh, F. C. Recent Developments in Organic Redox Flow Batteries: A Critical Review. *J. Power Sources* **2017**, *360*, 243–283. <https://doi.org/10.1016/j.jpowsour.2017.05.057>.
- (55) Kwabi, D. G.; Ji, Y.; Aziz, M. J. Electrolyte Lifetime in Aqueous Organic Redox Flow Batteries: A Critical Review. *Chem. Rev.* **2020**, *120* (14), 6467–6489. <https://doi.org/10.1021/acs.chemrev.9b00599>.
- (56) Skyllas-Kazacos, M.; Cao, L.; Kazacos, M.; Kausar, N.; Mousa, A. Vanadium Electrolyte Studies for the Vanadium Redox Battery—A Review. *ChemSusChem* **2016**, *9* (13), 1521–1543. <https://doi.org/10.1002/cssc.201600102>.
- (57) Wu, M. C.; Zhao, T. S.; Jiang, H. R.; Zeng, Y. K.; Ren, Y. X. High-Performance Zinc Bromine Flow Battery via Improved Design of Electrolyte and Electrode. *J. Power Sources* **2017**, *355*, 62–68. <https://doi.org/10.1016/j.jpowsour.2017.04.058>.
- (58) Zhang, S.; Guo, W.; Yang, F.; Zheng, P.; Qiao, R.; Li, Z. Recent Progress in Polysulfide Redox-Flow Batteries. *Batter. Supercaps* **2019**, *2* (7), 627–637. <https://doi.org/10.1002/batt.201900056>.
- (59) Zeng, Y. K.; Zhou, X. L.; An, L.; Wei, L.; Zhao, T. S. A High-Performance Flow-Field Structured Iron-Chromium Redox Flow Battery. *J. Power Sources* **2016**, *324*, 738–744. <https://doi.org/10.1016/j.jpowsour.2016.05.138>.
- (60) Parasuraman, A.; Lim, T. M.; Menictas, C.; Skyllas-Kazacos, M. Review of Material Research and Development for Vanadium Redox Flow Battery Applications. *Electrochimica Acta* **2013**, *101*, 27–40. <https://doi.org/10.1016/j.electacta.2012.09.067>.
- (61) Rychcik, M.; Skyllas-Kazacos, M. Characteristics of a New All-Vanadium Redox Flow Battery. *J. Power Sources* **1988**, *22* (1), 59–67. [https://doi.org/10.1016/0378-7753\(88\)80005-3](https://doi.org/10.1016/0378-7753(88)80005-3).
- (62) Ding, C.; Zhang, H.; Li, X.; Liu, T.; Xing, F. Vanadium Flow Battery for Energy Storage: Prospects and Challenges. *J. Phys. Chem. Lett.* **2013**, *4* (8), 1281–1294. <https://doi.org/10.1021/jz4001032>.
- (63) Skyllas-Kazacos, M.; Chakrabarti, M. H.; Hajimolana, S. A.; Mjalli, F. S.; Saleem, M. Progress in Flow Battery Research and Development. *J. Electrochem. Soc.* **2011**, *158* (8), R55–R79. <https://doi.org/10.1149/1.3599565>.
- (64) Kear, G.; Shah, A. A.; Walsh, F. C. Development of the All-Vanadium Redox Flow Battery for Energy Storage: A Review of Technological, Financial and Policy Aspects. *Int. J. Energy Res.* **2012**, *36* (11), 1105–1120. <https://doi.org/10.1002/er.1863>.
- (65) Poullikkas, A. A Comparative Overview of Large-Scale Battery Systems for Electricity Storage. *Renew. Sustain. Energy Rev.* **2013**, *27*, 778–788. <https://doi.org/10.1016/j.rser.2013.07.017>.
- (66) Bullich-Massagué, E.; Cifuentes-García, F.-J.; Glenney-Crende, I.; Cheah-Mañé, M.; Aragüés-Peñalba, M.; Díaz-González, F.; Gomis-Bellmunt, O. A Review of Energy

- Storage Technologies for Large Scale Photovoltaic Power Plants. *Appl. Energy* **2020**, 274, 115213. <https://doi.org/10.1016/j.apenergy.2020.115213>.
- (67) Zhang, C.; Wei, Y.-L.; Cao, P.-F.; Lin, M.-C. Energy Storage System: Current Studies on Batteries and Power Condition System. *Renew. Sustain. Energy Rev.* **2018**, 82, 3091–3106. <https://doi.org/10.1016/j.rser.2017.10.030>.
- (68) Hameer, S.; Niekerk, J. L. van. A Review of Large-Scale Electrical Energy Storage. *Int. J. Energy Res.* **2015**, 39 (9), 1179–1195. <https://doi.org/10.1002/er.3294>.
- (69) Menictas, C.; Skyllas-Kazacos, M.; Lim, T. M. *Advances in Batteries for Medium and Large-Scale Energy Storage: Types and Applications*; Elsevier, 2014.
- (70) Sabihuddin, S.; Kiprakis, A. E.; Mueller, M. A Numerical and Graphical Review of Energy Storage Technologies. *Energies* **2015**, 8 (1), 172–216. <https://doi.org/10.3390/en8010172>.
- (71) Moreno-Benito, M.; Agnolucci, P.; Papageorgiou, L. G. Towards a Sustainable Hydrogen Economy: Optimisation-Based Framework for Hydrogen Infrastructure Development. *Comput. Chem. Eng.* **2017**, 102, 110–127. <https://doi.org/10.1016/j.compchemeng.2016.08.005>.
- (72) Lattin, W. C.; Utgikar, V. P. Transition to Hydrogen Economy in the United States: A 2006 Status Report. *Int. J. Hydrog. Energy* **2007**, 32 (15), 3230–3237. <https://doi.org/10.1016/j.ijhydene.2007.02.004>.
- (73) Mueller-Langer, F.; Tzimas, E.; Kaltschmitt, M.; Peteves, S. Techno-Economic Assessment of Hydrogen Production Processes for the Hydrogen Economy for the Short and Medium Term. *Int. J. Hydrog. Energy* **2007**, 32 (16), 3797–3810. <https://doi.org/10.1016/j.ijhydene.2007.05.027>.
- (74) Eliaz, N.; Eliezer, D.; Olson, D. L. Hydrogen-Assisted Processing of Materials. *Mater. Sci. Eng. A* **2000**, 289 (1), 41–53. [https://doi.org/10.1016/S0921-5093\(00\)00906-0](https://doi.org/10.1016/S0921-5093(00)00906-0).
- (75) Ramachandran, R.; Menon, R. K. An Overview of Industrial Uses of Hydrogen. *Int. J. Hydrog. Energy* **1998**, 23 (7), 593–598. [https://doi.org/10.1016/S0360-3199\(97\)00112-2](https://doi.org/10.1016/S0360-3199(97)00112-2).
- (76) Armaroli, N.; Balzani, V. The Hydrogen Issue. *ChemSusChem* **2011**, 4 (1), 21–36. <https://doi.org/10.1002/cssc.201000182>.
- (77) Olah, G. A.; Goepfert, A.; Prakash, G. K. S. *Beyond Oil and Gas: The Methanol Economy*; John Wiley & Sons, 2018.
- (78) Hydrogen - Fuels & Technologies <https://www.iea.org/fuels-and-technologies/hydrogen> (accessed 2020 -02 -10).
- (79) Ohi, J. Hydrogen Energy Cycle: An Overview. *J. Mater. Res.* **2005**, 20 (12), 3180–3187. <https://doi.org/10.1557/jmr.2005.0408>.
- (80) Rausch, B.; Symes, M. D.; Chisholm, G.; Cronin, L. Decoupled Catalytic Hydrogen Evolution from a Molecular Metal Oxide Redox Mediator in Water Splitting. *Science* **2014**, 345 (6202), 1326–1330. <https://doi.org/10.1126/science.1257443>.
- (81) Noh, H.; Kung, C.-W.; Otake, K.; Peters, A. W.; Li, Z.; Liao, Y.; Gong, X.; Farha, O. K.; Hupp, J. T. Redox-Mediator-Assisted Electrocatalytic Hydrogen Evolution from Water by a Molybdenum Sulfide-Functionalized Metal–Organic Framework. *ACS Catal.* **2018**, 8 (10), 9848–9858. <https://doi.org/10.1021/acscatal.8b02921>.
- (82) Zeng, K.; Zhang, D. Recent Progress in Alkaline Water Electrolysis for Hydrogen Production and Applications. *Prog. Energy Combust. Sci.* **2010**, 36 (3), 307–326. <https://doi.org/10.1016/j.pecs.2009.11.002>.
- (83) Holladay, J. D.; Hu, J.; King, D. L.; Wang, Y. An Overview of Hydrogen Production Technologies. *Catal. Today* **2009**, 139 (4), 244–260. <https://doi.org/10.1016/j.cattod.2008.08.039>.

- (84) Bessarabov, D.; Wang, H.; Li, H.; Zhao, N. *PEM Electrolysis for Hydrogen Production: Principles and Applications*; CRC Press, 2016.
- (85) Amstutz, V.; Toghiani, K. E.; Powlesland, F.; Vrubel, H.; Comninellis, C.; Hu, X.; Girault, H. H. Renewable Hydrogen Generation from a Dual-Circuit Redox Flow Battery. *Energy Environ. Sci.* **2014**, 7 (7), 2350–2358. <https://doi.org/10.1039/C4EE00098F>.
- (86) Hu, W. Electrocatalytic Properties of New Electrocatalysts for Hydrogen Evolution in Alkaline Water Electrolysis. *Int. J. Hydrog. Energy* **2000**, 25 (2), 111–118. [https://doi.org/10.1016/S0360-3199\(99\)00024-5](https://doi.org/10.1016/S0360-3199(99)00024-5).
- (87) Carmo, M.; Fritz, D. L.; Mergel, J.; Stolten, D. A Comprehensive Review on PEM Water Electrolysis. *Int. J. Hydrog. Energy* **2013**, 38 (12), 4901–4934. <https://doi.org/10.1016/j.ijhydene.2013.01.151>.
- (88) Rashid, M. M.; Mesfer, M. K. A.; Naseem, H.; Danish, M. Hydrogen Production by Water Electrolysis: A Review of Alkaline Water Electrolysis, PEM Water Electrolysis and High Temperature Water Electrolysis.
- (89) Australia - A National Hydrogen Strategy: Shaping Possibilities For Australia's Hydrogen Economy. | Conventus Law <https://www.conventuslaw.com/report/australia-a-national-hydrogen-strategy-shaping/> (accessed 2021 -08 -16).
- (90) Ligen, Y.; Vrubel, H.; Girault, H.; Ligen, Y.; Vrubel, H.; Girault, H. H. Mobility from Renewable Electricity: Infrastructure Comparison for Battery and Hydrogen Fuel Cell Vehicles. *World Electr. Veh. J.* **2018**, 9 (1), 3. <https://doi.org/10.3390/wevj9010003>.
- (91) Ligen, Y.; Vrubel, H.; Girault, H. Energy Efficient Hydrogen Drying and Purification for Fuel Cell Vehicles. *Int. J. Hydrog. Energy* **2020**. <https://doi.org/10.1016/j.ijhydene.2020.02.035>.
- (92) Ligen, Y.; Vrubel, H.; Girault, H. Local Energy Storage and Stochastic Modeling for Ultrafast Charging Stations. *Energies* **2019**, 12 (10), 1986. <https://doi.org/10.3390/en12101986>.
- (93) Reynard, D.; Vrubel, H.; Dennison, C. R.; Battistel, A.; Girault, H. On-Site Purification of Copper-Contaminated Vanadium Electrolytes Using a Vanadium Redox Flow Battery. *ChemSusChem* 0 (ja). <https://doi.org/10.1002/cssc.201802895>.
- (94) Bryans, D.; Amstutz, V.; Girault, H. H.; Berlouis, L. E. A. Characterisation of a 200 KW/400 KWh Vanadium Redox Flow Battery. *Batteries* **2018**, 4 (4), 54. <https://doi.org/10.3390/batteries4040054>.
- (95) Ligen, Y.; Girault, H.; Rager, J. Combined Service Station for Battery Electric & Hydrogen Fuel Cell Vehicles - Final Report. Swiss Federal Office for Energy 2018.
- (96) Ligen, Y.; Vrubel, H.; Girault, H. Energy Efficient Hydrogen Drying and Purification for Fuel Cell Vehicles. *Int. J. Hydrog. Energy* **2020**, 45 (18), 10639–10647. <https://doi.org/10.1016/j.ijhydene.2020.02.035>.
- (97) Ligen, Y.; Vrubel, H.; Arlettaz, J.; Girault, H. Experimental Correlations and Integration of Gas Boosters in a Hydrogen Refueling Station. *Int. J. Hydrog. Energy* **2020**, 45 (33), 16663–16671. <https://doi.org/10.1016/j.ijhydene.2020.04.162>.
- (98) Dennison, C. R.; Vrubel, H.; Amstutz, V.; Peljo, P.; Toghiani, K. E.; Girault, H. H. Redox Flow Batteries, Hydrogen and Distributed Storage. *Chimia* **2015**, 69 (12), 753–758. <https://doi.org/10.2533/chimia.2015.753>.
- (99) Amstutz, V.; Toghiani, K. E.; Powlesland, F.; Vrubel, H.; Comninellis, C.; Hu, X.; Girault, H. H. Renewable Hydrogen Generation from a Dual-Circuit Redox Flow Battery. *Energy Environ. Sci.* **2014**, 7 (7), 2350–2358. <https://doi.org/10.1039/C4EE00098F>.
- (100) Reynard, D.; Bolik-Coulon, G.; Maye, S.; Girault, H. H. Hydrogen Production on Demand by Redox-Mediated Electrocatalysis: A Kinetic Study. *Chem. Eng. J.* **2020**, 126721. <https://doi.org/10.1016/j.cej.2020.126721>.

-
- (101) Peljo, P.; Scanlon, M. D.; Olaya, A. J.; Rivier, L.; Smirnov, E.; Girault, H. H. Redox Electrocatalysis of Floating Nanoparticles: Determining Electrocatalytic Properties without the Influence of Solid Supports. *J. Phys. Chem. Lett.* **2017**, *8* (15), 3564–3575. <https://doi.org/10.1021/acs.jpcclett.7b00685>.
- (102) Ligen, Y. Electrochemical systems for hydrogen fuel cell and battery electric vehicle infrastructure <https://infoscience.epfl.ch/record/282095> (accessed 2021 -06 -25). <https://doi.org/10.5075/epfl-thesis-7916>.
- (103) Symes, M. D.; Cronin, L. Decoupling Hydrogen and Oxygen Evolution during Electrolytic Water Splitting Using an Electron-Coupled-Proton Buffer. *Nat. Chem.* **2013**, *5* (5), 403–409. <https://doi.org/10.1038/nchem.1621>.
- (104) Dotan, H.; Landman, A.; Sheehan, S. W.; Malviya, K. D.; Shter, G. E.; Grave, D. A.; Arzi, Z.; Yehudai, N.; Halabi, M.; Gal, N.; Hadari, N.; Cohen, C.; Rothschild, A.; Grader, G. S. Decoupled Hydrogen and Oxygen Evolution by a Two-Step Electrochemical–Chemical Cycle for Efficient Overall Water Splitting. *Nat. Energy* **2019**, *4* (9), 786–795. <https://doi.org/10.1038/s41560-019-0462-7>.
- (105) Huang, J.; Wang, Y. Efficient Renewable-to-Hydrogen Conversion via Decoupled Electrochemical Water Splitting. *Cell Rep. Phys. Sci.* **2020**, *1* (8), 100138. <https://doi.org/10.1016/j.xcrp.2020.100138>.
- (106) McHugh, P. J.; Stergiou, A. D.; Symes, M. D. Decoupled Electrochemical Water Splitting: From Fundamentals to Applications. *Adv. Energy Mater.* *n/a* (n/a), 2002453. <https://doi.org/10.1002/aenm.202002453>.
- (107) Wallace, A. G.; Symes, M. D. Decoupling Strategies in Electrochemical Water Splitting and Beyond. *Joule* **2018**, *2* (8), 1390–1395. <https://doi.org/10.1016/j.joule.2018.06.011>.
- (108) Zhang, F.; Wang, Q. Redox-Mediated Water Splitting for Decoupled H₂ Production. *ACS Mater. Lett.* **2021**, *3* (5), 641–651. <https://doi.org/10.1021/acsmaterialslett.1c00074>.
- (109) Amstutz, V.; Toghiani, K. E.; Comninellis, C.; Girault, H. H. Redox Flow Battery for Hydrogen Generation. US9543609B2, January 10, 2017.
- (110) Peljo, P.; Vrabel, H.; Amstutz, V.; Pandard, J.; Morgado, J.; Santasalo-Aarnio, A.; Lloyd, D.; Gumy, F.; Dennison, C. R.; Toghiani, K. E.; Girault, H. H. All-Vanadium Dual Circuit Redox Flow Battery for Renewable Hydrogen Generation and Desulfurisation. *Green Chem.* **2016**, *18* (6), 1785–1797. <https://doi.org/10.1039/C5GC02196K>.
- (111) Piwek, J.; Dennison, C. R.; Frackowiak, E.; Girault, H.; Battistel, A. Vanadium-Oxygen Cell for Positive Electrolyte Discharge in Dual-Circuit Vanadium Redox Flow Battery. *J. Power Sources* **2019**, *439*, 227075. <https://doi.org/10.1016/j.jpowsour.2019.227075>.

CHAPTER II

Failure analysis and purification strategy of copper-contaminated vanadium electrolytes

The results presented in this chapter are adapted with permission from D. Reynard, H. Vrubel, C. R. Dennison, A. Battistel, H. Girault, On-Site Purification of Copper-Contaminated Vanadium Electrolytes by using a Vanadium Redox Flow Battery, ChemSusChem 2019, 12, 1222. DOI: 10.1002/cssc.201802895 © 2019 Wiley-VCH Verlag GmbH & Co. KGaA, Weinheim.

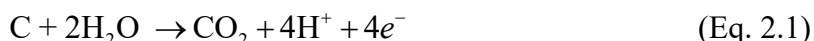
Abstract

Carbon corrosion and cracks through graphite bipolar plates were observed on several stacks of a commercial vanadium redox flow system (10 kW/ 40 kWh) enabling the electrolyte to leach the copper current collectors and contaminating the entire electrolyte solution with copper. First, a detailed analysis of the failure is conducted to understand the circumstances of the incident. The deleterious effects of copper contaminants on the operation of a VRFB are highlighted. To tackle the problems related to copper pollution, a simple, eco-friendly and cost-effective procedure to identify copper contamination and to purify the electrolyte is developed on-site. The process described is successfully used to purify on-site 6000 L of vanadium electrolyte ($\text{VO}_2^+/\text{VO}^{2+}$ mixture) to levels below 1 ppm.

This chapter differs from the others because is not directly related to the development of the redox dual-flow battery, but it deals with the operational failure of a commercial vanadium redox flow battery (10 kW/ 40 kWh) installed in the framework of the demonstration site Electromobilis. The failure revealed the need for improvement in the field of engineering, diagnosis and control strategy and failures remedial action to avoid premature degradation and to meet with robust performances over long-term operation. This incident motivated the development of the redox dual-flow battery system proposed in this thesis.

2.1 Introduction

In order to be competitive on the market of large-scale energy systems, VRFB technology needs to address several challenges. A lot of effort has been dedicated to increase the performances, but reports on the long-term stability of the VRFB remain often confidential with few publications addressing this issue.¹⁻³ It is widely accepted that VRFBs have a long lifetime because electrodes are not subjected to physical degradation due to morphology changes upon charge/discharge cycles and because the redox species cannot be depleted.⁴ On the other hand, carbon electrodes, particularly those on the positive side, may be subjected to anodic corrosion, which drastically reduces the battery lifetime. In recent years, Liu *et al.* studied the corrosion behaviour of the positive side electrode.⁵ They have observed that CO₂ gas evolution is triggered at an anodic polarization potential above 1.85 V vs. SHE at 20°C.



Generally, a VRFB operates at cell voltage below 1.60 V, which, because of the negative potential of the negative side, maintains the electrode potential of the anode below 1.85 V vs. SHE to prevent corrosion. However, Liu *et al.* reported that the threshold potential for carbon corrosion shifts negatively with an increase of temperature, polarization time, and concentration of functional groups like COOH and C=O at the electrode surface.⁵ In a commercial battery, only the cell voltage and the open circuit voltage are usually monitored, but not the individual electrode potentials. Therefore, we proposed two scenarios in which the corrosion rate of the electrode can seriously increase:

Scenario A - Imbalance of the electrolyte: An operating VRFB may present several processes that lead to electrolyte imbalance and consequent capacity loss.^{3,6,7} These include:

- Crossover of vanadium ions through the membrane
- Volumetric transfer of electrolyte resulting of the differential pressure drop
- Oxidation of V^{2+} by air on the negative side
- Parasitic gassing side reactions: hydrogen evolution reaction (HER) at the negative electrode and oxygen evolution reaction (OER) on the positive

Among these processes, air oxidation of V^{2+} and hydrogen evolution on the negative side will shift positively the potential of both sides.^{2,3,5-7} In this particular case, the average oxidation state (AOS) is shifted and the electrolyte needs to be rebalanced by chemical or electrochemical processes to ensure that the amount of reduced species on the negative electrolyte matches the amount of oxidized species on the positive electrolyte ($AOS=3.5$, $[V^{2+}]=[VO_2^+]$). In commercial systems, the state-of-charge (SOC) is usually calculated by measuring the open circuit voltage (OCV) using the Nernst equation (Figure 2.1). The Nernst equation (Eq. 2.2) relates the electrode potential at equilibrium (E) to the standard electrode potential (E°). Considering the half-cell reaction $xOx + ne^- \rightleftharpoons yRed$, it is expressed as follows:

$$E = E^\circ + \frac{RT}{nF} \ln \left(\frac{a_{ox}^x}{a_{red}^y} \right) \quad (\text{Eq. 2.2})$$

where R is the ideal gas constant, T is the temperature, F is the Faraday constant and a_{ox} and a_{red} are the chemical activities for the oxidized and reduced species.

Then, with the assumption that the electrolyte is properly balanced, the SOC is calculated using (Eq. 2.3):

$$SOC = \frac{e^{\frac{nF}{2RT}(E_{OCV} - E_{OCV}^\circ - C)}}{1 + e^{\frac{nF}{2RT}(E_{OCV} - E_{OCV}^\circ - C)}} \quad (\text{Eq. 2.3})$$

where C is the correction factor for the activity of protons.

In the absence of a method to detect the electrolyte imbalance in real-time, the battery management system cannot operate properly and the positive electrolyte is exposed to overcharging risks, reaching highly oxidative potential values and triggering electrode

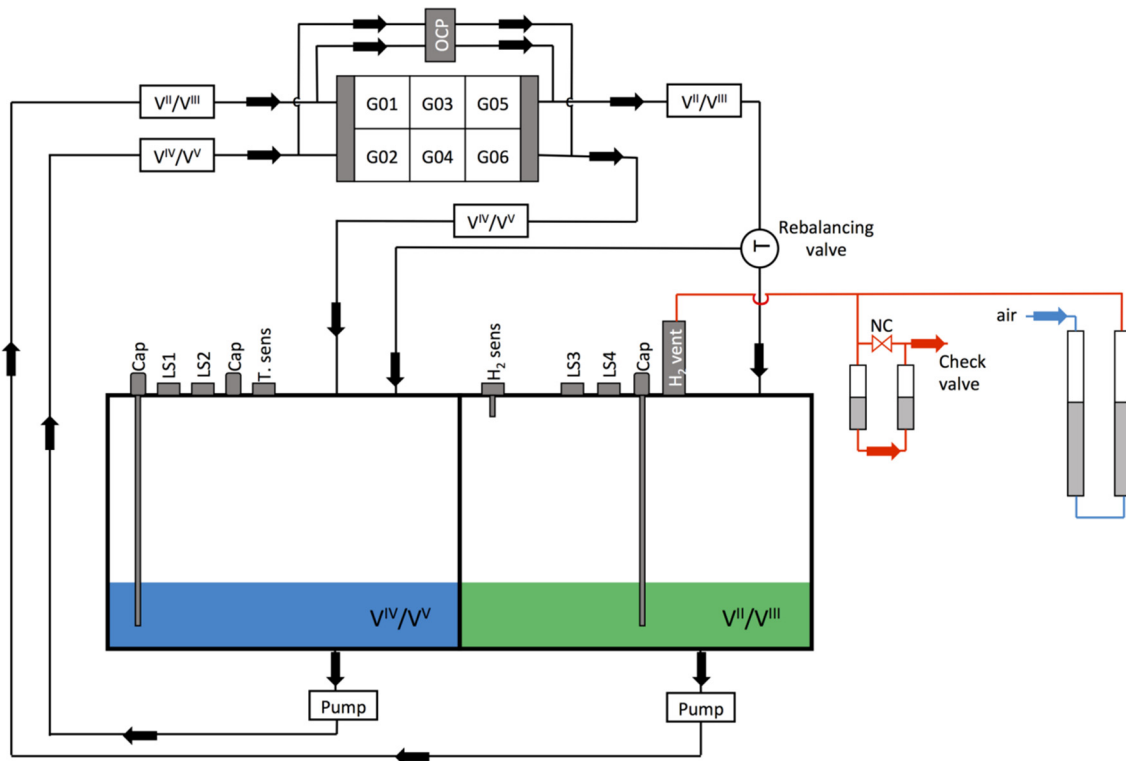
corrosion.^{2,5,7-9}

Figure 2.1 General description of the 10/40 CellCube pipelines.¹⁰

Scenario B - Local rise of temperature and potential: A VRFB stack is an assembly of single cells (porous carbon | membrane | porous carbon) connected electrically in series with bipolar plates. The conductive electrolyte is sent through the porous carbon electrodes of each compartment cell from a common manifold. This electrolyte network surrounding the electrodes at different potentials induces leakage (shunt) currents resulting in power losses. These losses may lead to higher temperatures and potential spots that can trigger gas evolution and electrode degradation.^{11,12} The local differences in conductivity of the carbon composite bipolar plates, if those are not homogenous in thickness or composition, can also contribute to these phenomena. As the roughness of a bipolar plate is increased with chemical and mechanical degradation, the process can easily escalate.¹²

In the framework of the demonstrator (see Chapter I, Section 1.5), a commercial all-vanadium RFB (10 kW/40 kWh) was installed in Martigny, Switzerland.^{13,14} After 3 years of operation, advanced corrosion of the carbon electrodes and bipolar plates was observed, as shown on Figure 2.2. Spectrophotometric analysis of the electrolyte indicated an imbalance of 20%

between the positive electrolyte and the negative electrolyte ($\text{AOS}=3.7$)¹⁵, supporting the Scenario A proposed above.

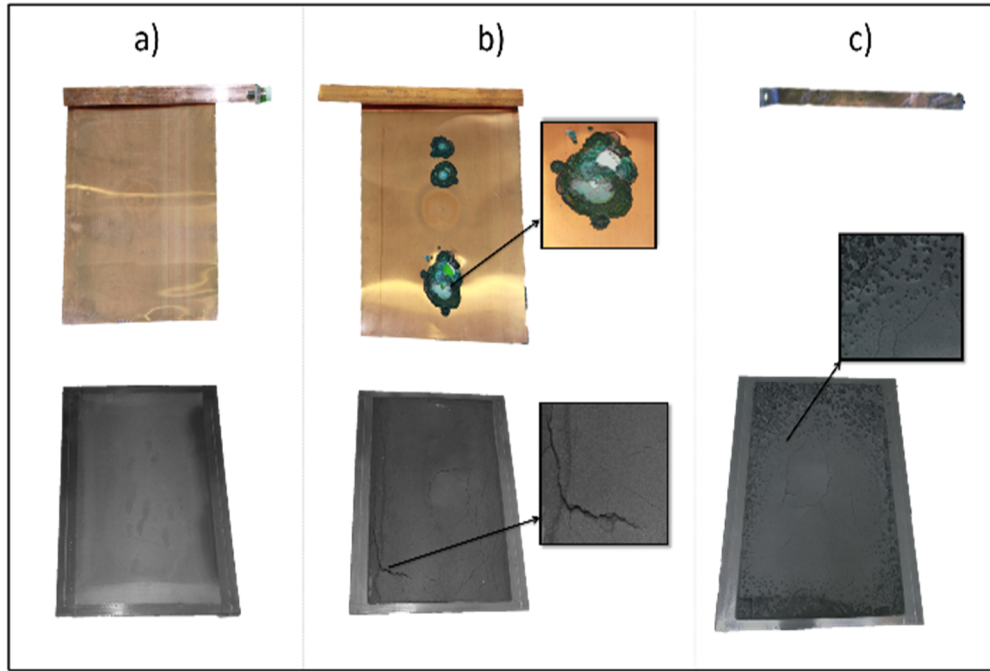


Figure 2.2 Photos of copper current collector and bipolar plate of a VRFB stack: (a) No corrosion (b) Marked corrosion (c) Complete corrosion.

The presence of cracks on the terminal bipolar plate used as an electrical contact to a current collector allowed a direct connection between the positive electrolyte and the copper current collector (Figure 2.3). Dissolution of copper progressed causing a total failure of the stack. It was found that Cu^{2+} could migrate from the positive to the negative electrolyte, through electrolyte levels rebalancing and/or membrane crossover.

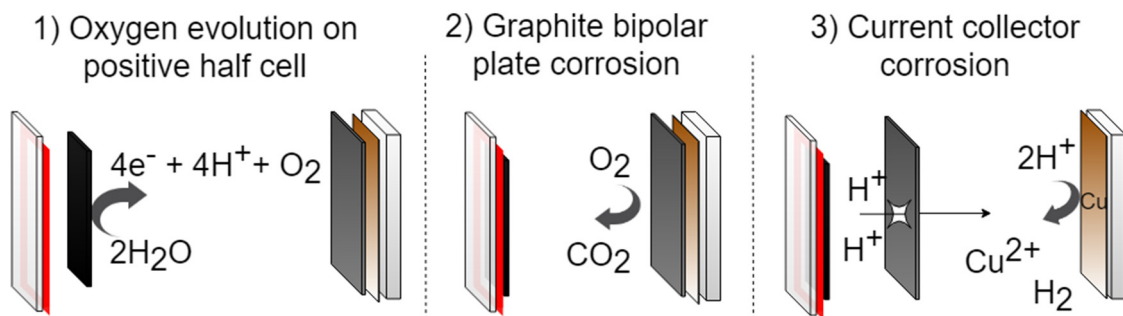


Figure 2.3 Proposed corrosion process occurring on the positive half-cell.

Precipitation of metallic copper on the negative electrode favoured parasitic hydrogen evolution reaction (HER) and accelerated the oxidation state imbalance between the two redox electrolytes, inducing a negative feedback loop.

In this chapter, the effect of copper on the behaviour of VRFB operation was examined to evaluate the risks of operating the battery with copper contaminated electrolytes. A semi-quantitative colorimetric procedure to estimate the concentration of copper within the vanadium electrolyte was developed to allow on-site diagnostic. A simple cost-effective method based on electroplating was developed for on-site treatment of large amounts of copper contaminated vanadium electrolyte (1.6 M $\text{VO}^{2+}/\text{V}^{3+}$, 2 M H_2SO_4 , 50 mM H_3PO_4).

2.2 Experimental Section

2.2.1 Chemicals

1,5-Diphenylthiocarbazone - Dithizone (DTZ, $\geq 99\%$), dichloromethane (CH_2Cl_2 , $\geq 99,9\%$), Copper(II) sulphate pentahydrate ($\text{CuSO}_4 \cdot 5\text{H}_2\text{O}$, $\geq 99\%$), sodium phosphate tribasic dodecahydrate ($\text{Na}_3\text{PO}_4 \cdot 12\text{H}_2\text{O}$, $\geq 98\%$), and sulfuric acid (H_2SO_4 , 95-98%) were purchased from Sigma Aldrich and used without further purification. Dithizone-dichloromethane (DTZ- CH_2Cl_2) solution ($20 \text{ mg} \cdot \text{L}^{-1}$) was prepared and stored in a fridge under inert atmosphere to minimize degradation. A commercial vanadium electrolyte composed of an aqueous solution of 1.6 M V(III)/ 1.6 M V(IV) (ca. 50:50), 2 M sulfuric acid (H_2SO_4), and 50 mM H_3PO_4 was purchased from (Reactana) and used without further purification.

2.2.2 Instrumentation

The pH measurements were performed using a freshly calibrated Mettler Toledo FiveEasy Plus pH meter with a glass electrode. ICP-MS analyses were performed in a PerkinElmer Nexion 300D using an external calibration method. UV-vis measurements were performed with an Ocean Optics USB2000+ spectrometer. Electrochemical experiments were performed with an Autolab Potentiostat (PGSTAT204) or with a Biologic HCP-1005 (100A booster) for single-cell experiments. SEM images were performed with a Teneo SEM (FEI, USA) equipped with a Schottky field emission gun. Secondary electron detection was achieved with an Everhart-Thornley detector and an in-lens detector.

2.2.3 Determination of Cu^{2+}

Dithizone method: 2 mL of the electrolyte solution was diluted with 2 mL of distilled water. The pH of the solution was adjusted to 1.4 by addition of 1.6 g of $\text{Na}_3\text{PO}_4 \cdot 12\text{H}_2\text{O}$. After complete dissolution, 2 mL of the DTZ- CH_2Cl_2 solution ($20 \text{ mg} \cdot \text{L}^{-1}$) was added. The copper was extracted by shaking the mixture alternatively 15 seconds by hand and 45 seconds by vortex for 5 minutes. The organic phase was then carefully transferred to a 1 mm quartz cuvette for UV-vis measurement or to a vial for colorimetric estimation (Figure 2.8). The detailed procedure is shown in Figure 2.4

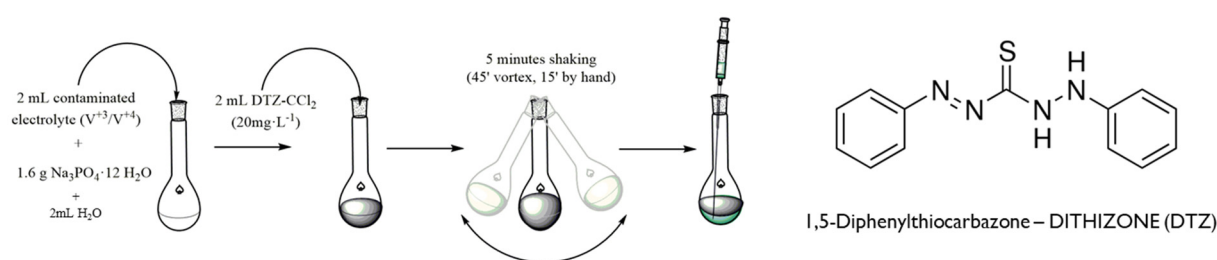


Figure 2.4 Detailed experimental procedure for the determination of copper using the dithizone methodology and molecular structure of the dithizone colorimetric agent.

ICP-MS: For selected samples, exact copper concentration was also determined by ICP-MS.

2.2.4 Anodic stripping voltammetry

Anodic stripping analysis (ASV) was performed in a 3-electrode set-up with a carbon felt working electrode (SGL GFD 5), an $\text{Ag}|\text{AgCl}$ (*vs.* sat. KCl) reference electrode, and a carbon felt counter electrode. A magnetic stirrer was used to agitate the solution. The measurement was performed in three steps: (1) Pre-cleaning of the working electrode at 1.2 V during 20 s; (2) Chronoamperometric plating during 400 s at a given deposition potential (E_p); (3) Stripping by linear sweep voltammetry from E_p to 1.2 V at a scan rate of $0.1 \text{ V} \cdot \text{s}^{-1}$.

2.2.5 Single-cell measurements

All the experiments were performed with a single-cell of identical construction to the stacks present in the commercial VRFB (Figure 2.5-A). The carbon felt electrodes (SGL GFD 5) and the copper current collectors have a geometric surface area of ca. 550 cm^2 . The membrane is of anion exchange type (Fumatech 375-PP). The electrolyte levels were stabilized by joining the two reservoirs *via* a thin siphon tube. The system was gas-tight and connected to a pressure

sensor (MPX5010DP) to monitor eventual gas production (Calibration curve available in Appendix II-1). The electrolyte was pumped with a peristaltic pump (Minipuls 3, Gilson) through flexible PTFE tubing.

2.2.6 Scale-up

The purification system was built using a commercial VRFB stack of 27 electrochemical cells (Figure 2.5-B). A retention tray, containing the stacks and the OCV cell, was fixed onto an aluminum framework. Vanadium electrolyte was circulated into rigid PVC and flexible PE tubes using pressure controlled centrifugal pumps. A container of 1 m³ was used to contain the contaminated electrolyte. The stack was powered by a 1.2 kW DC power supply (TTi QPX 1200SP). The system was controlled by a Siemens based automation control system (Simatic S7-1200).

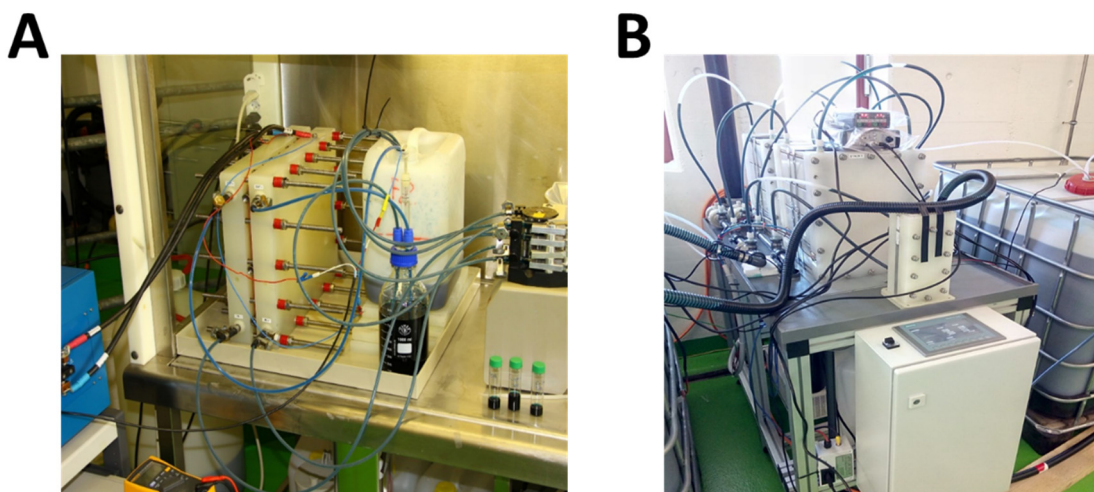


Figure 2.5 (A) Image of the single flow cell set-up used for the electrolyte purification (B) Image of the purification system that was developed on-site using 27 cells stacks and 1000 L reservoirs.

2.3 Results and Discussion

2.3.1 Effect of copper on VRFB operation

Since it is difficult to estimate the process in which soluble copper ions migrate from the positive electrolyte to form copper particles in the negative side, the effect of copper presence in the vanadium electrolyte was studied by adding known amounts of copper directly into a commercial vanadium electrolyte (50% V³⁺, 50% VO²⁺) before the pre-charge step. No

noticeable precipitation of copper happens in this solution. Different amounts of copper sulfate were added to the negative electrolyte (0, 50, 100 and 200 mg of Cu) and three charge/discharge cycles were recorded after each pre-charge step between 20% and 85% SOC. The cycles were performed with 500 mL of commercial electrolyte at each side corresponding to a total copper concentration of 0, 50, 100 and 200 ppm ($\text{mg}\cdot\text{L}^{-1}$) (0, 0.79, 1.57, 3.15 mM).

This range corresponds to the expected concentrations for the dissolution of one or more current collectors in a 40 kWh battery (one copper current collector weighs ca. 250 g). Figure 2.6 shows the resulting voltage and the corresponding volumetric hydrogen production during charge/discharge cycles. Without copper, no hydrogen evolution was observed. The hydrogen production increased with the increased amounts of copper leading to a capacity loss of up to 0.15% after three cycles. The trend of the hydrogen evolution rate with the concentration of copper and the detailed hydrogen evolution parameters are shown in Figure 2.7 and Table 2.1.

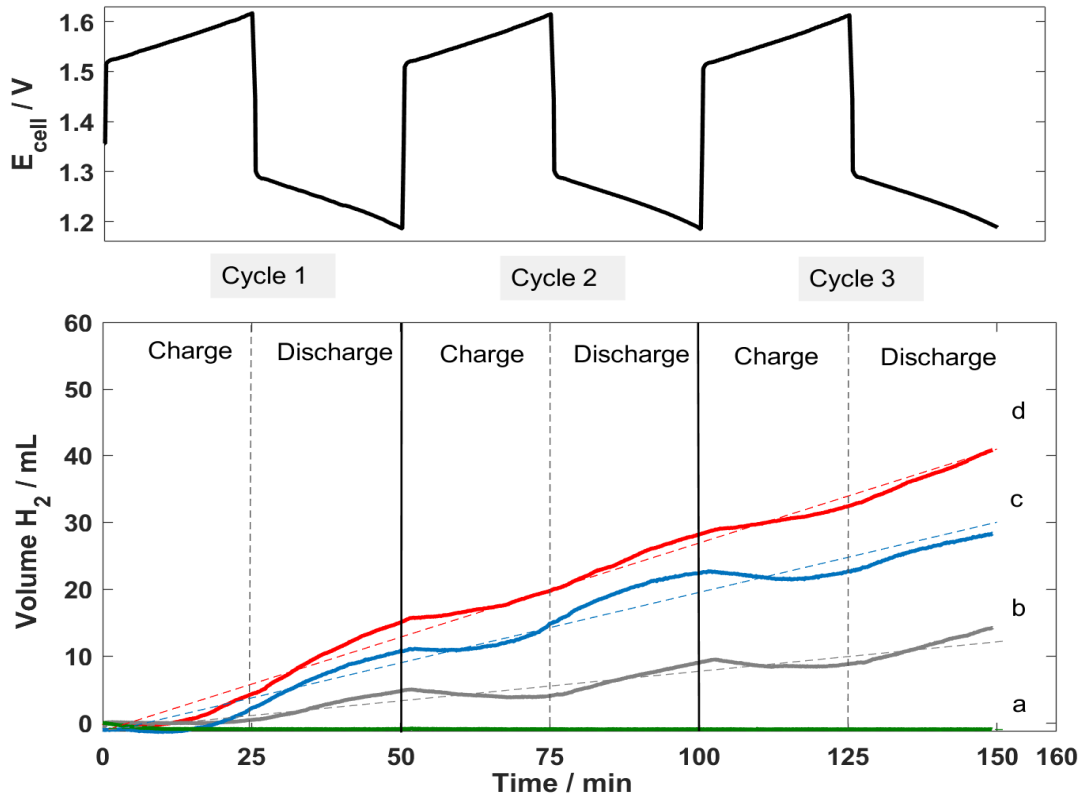


Figure 2.6 Cell voltage profile and volumetric hydrogen production of the VRFB operating between 20 and 85 % SOC at a current density of $50 \text{ mA}\cdot\text{cm}^{-2}$ for different concentrations of copper (a) zero ppm Cu (b) 50 ppm Cu (c) 100 ppm Cu (d) 200 ppm Cu.

Although Wei *et al.* had described a kinetic improvement for the $\text{V}^{3+}/\text{V}^{2+}$ couple on copper decorated carbon felt electrodes,¹⁶ our results show its deleterious effect on the performance of

the VRFB due to continuous hydrogen evolution and irreversible capacity loss. It is, hence, necessary to purify the electrolyte to return the battery to operating conditions.

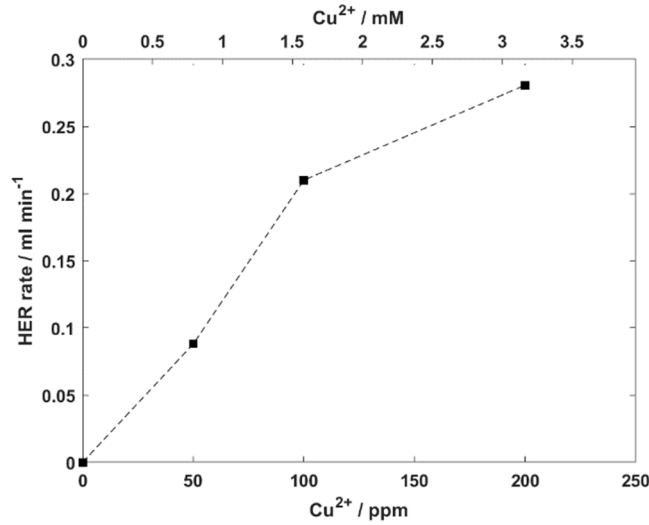


Figure 2.7 Average volumetric hydrogen evolution rate as a function of the amount of copper.

Table 2.1 Summary of hydrogen evolution parameters for each cycle of VRFB operating between 20 and 85 % SOC at a current density of $50 \text{ mA} \cdot \text{cm}^{-2}$ in presence of different amounts of copper within the negative side.

Copper content / mg		0	50	100	200
Volumetric Hydrogen	Cycle 1	0	4.9	10.8	15.3
	Cycle 2	0	4.4	11.7	13.2
Production / mL	Cycle 3	0	5.0	5.8	12.3
Capacity loss / %		0	0.05	0.10	0.15
Average flow rate / $\text{ml} \cdot \text{min}^{-1}$		0	0.088	0.210	0.281

2.3.2 Copper determination

In case of a stack failure, it is interesting to be able to assess the integrity of the current collector and the purity of the electrolyte.

Although instrumental techniques like Inductively Coupled Plasma-Optical Emission Spectroscopy (ICP-OES), Inductively Coupled Plasma Mass Spectrometry (ICP-MS) and Atomic Absorption Spectroscopy (AAS) can easily detect the presence of copper and other

metals in the electrolyte, they are not always available on-site. Colorimetric techniques are cheap, reliable, fast and portable instruments are commercially available.

Dithizone (DTZ) is a widely used reagent for the determination of trace heavy metal ions with which it forms highly coloured water insoluble complexes. Liquid-liquid extraction of copper from vanadium electrolyte can be accomplished with the use of an appropriate solvent at a controlled pH value.

CCl_4 has been widely used as organic solvent for liquid-liquid extraction, in part due to the fast kinetic of complexation. The use of CCl_4 has abruptly declined since the Montreal Protocol in reason of its high ozone-depleting potential and acute toxicity. Since then, dichloromethane was found to be a useful alternative to CCl_4 . A.M. Kiwan reported that CH_2Cl_2 even increased with the sensitivity of DTZ towards Cu^{2+} .¹⁷ However, DTZ- CH_2Cl_2 exhibits lower extraction power compared to carbon tetrachloride solutions.^{17–19}

DTZ reacts with copper to form two chelate complexes: purple primary copper(II) dithizonate with a Cu:DTZ ratio of 1:2 and brown-yellow secondary copper dithizonate, with a Cu:DTZ ratio of 1:1. Both complexes can exist in equilibrium depending on the medium conditions.^{20–22} As shown in Figure 2.8, the solution of DTZ- CH_2Cl_2 (ca. $20 \text{ mg} \cdot \text{L}^{-1}$) displays two absorption maxima at 442 nm and 608 nm, with absorbance of 0.537 and 1.075 respectively (for 1 cm optical path). The chelating agent was found to be stable at least two weeks if kept under nitrogen and at 4°C . Primary copper dithizonate and secondary copper dithizonate showed absorption maxima at 529 and at 443 nm, respectively. Degradation of dithizone, observable as diminishing of its characteristic peaks in the UV-vis, was noticed in presence of oxygen and VO_2^+ solutions, probably due to redox reactions. To overcome this problem, determination of copper was carried out in a $\text{VO}^{2+}/\text{V}^{3+}$ solution obtained by mixing equal amounts of the positive and negative electrolytes. The mixed solution was more reliable in terms of pH, vanadium concentration, and state of charge than a sample taken from the negative or positive electrolyte.

For the analysis, the electrolyte was first buffered at a pH value of 1.4 to achieve an optimal complexation, while still preventing vanadium(III) hydroxide formation. At this pH value, gold, platinum, silver, mercury, bismuth and stannous tin have to be considered as possible interferences.¹⁹ Due to the slow kinetics, the efficiency of complexation of copper in CH_2Cl_2 -DTZ is highly dependent on the extraction conditions (time and mixing of phases). Preliminary experiments showed that acceptable reproducibility was achieved within 5 minutes, although total conversion may take more than 30 minutes. Under the present experimental conditions,

the copper concentration was estimated based on the following color scale (Figure 2.8): 0-1 ppm green, 2 ppm purple-black, 3-4 ppm pink, 5-10 ppm pink-orange, >10 ppm yellow.^{17–22}

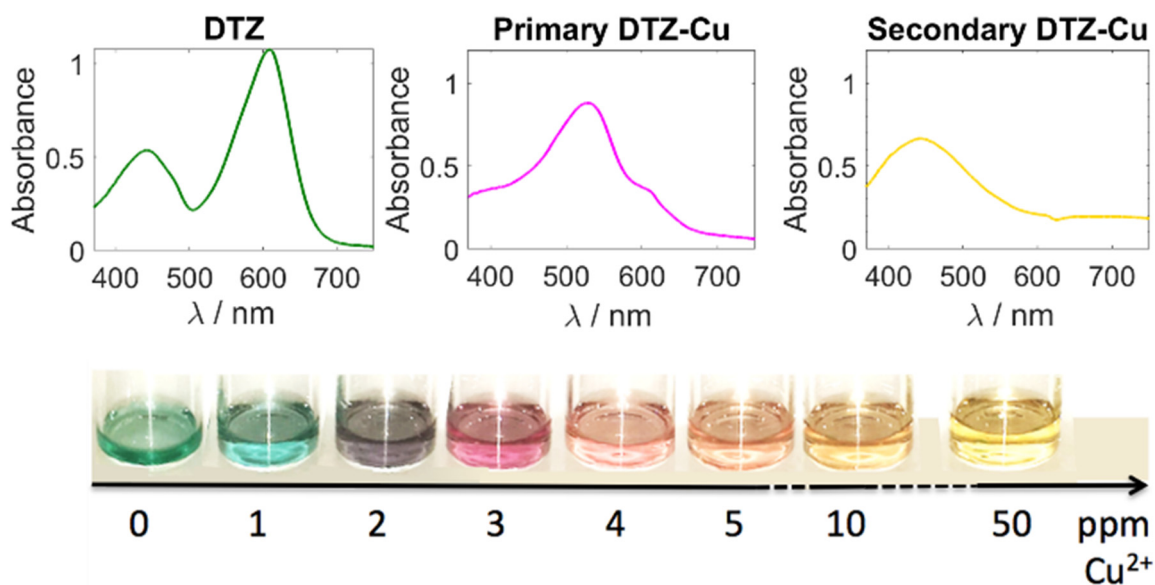
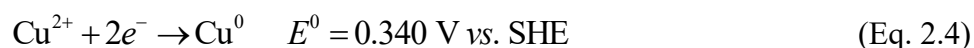


Figure 2.8 UV-vis spectra of DTZ-CH₂Cl₂ solution: purple primary copper(II) dithizonate (Cu:DTZ ratio of 1:2) and brown-yellow secondary copper dithizonate (Cu:DTZ ratio of 1:1) and colorimetric scale to estimate copper concentration.

2.3.3 Purification strategy

While addition of copper salts to V³⁺/V²⁺ results in immediate precipitation of metallic copper particles, we observed that most of the copper had plated on the carbon felt electrodes during the pre-charge step carried on the single-cell experiments described earlier.

One strategy to regenerate the electrolyte after copper contamination is to plate out copper cations present in the electrolyte onto an electrode surface according to the following reaction:²³



A practical approach is to use a commercial VRFB stack for performing this reaction. To study the viability of the process, copper electroplating in vanadium electrolyte on carbon felt was first examined. Optimal parameters of deposition were determined using anodic stripping voltammetry (ASV) of a mixture of vanadium electrolyte and copper sulphate (5 ppm on Cu) as described in the experimental section.^{23–27} The plating of copper was performed at different potentials in the range of –20 mV to –140 mV vs. SHE. The stripping peak current magnitude was used to quantify the rate of electrodeposition.

Figure 2.9-A shows the recorded current during the chronoamperometric plating of a vanadium solution containing 5 ppm of copper at different deposition potential. As expected, the magnitude of the current increases with the increase of the deposition potential. Note that the current signal includes both copper and vanadium reduction. Thus, the stripping current magnitude was used to determine the rate of copper deposition. Figure 2.9-B shows the stripping waves of copper oxidation which is located close to the equilibrium potential for Cu^{2+}/Cu . The stripping current magnitude increases with the increase of the deposition overpotential. The deposition started from potentials below -60 mV and the stripping current increased steeply from -60 mV to -100 mV. The stripping peaks for potentials below -100 mV suggested a diffusion limited process. Thus, to minimize energy losses, we considered the optimal plating potential as ca. -100 mV vs. SHE.

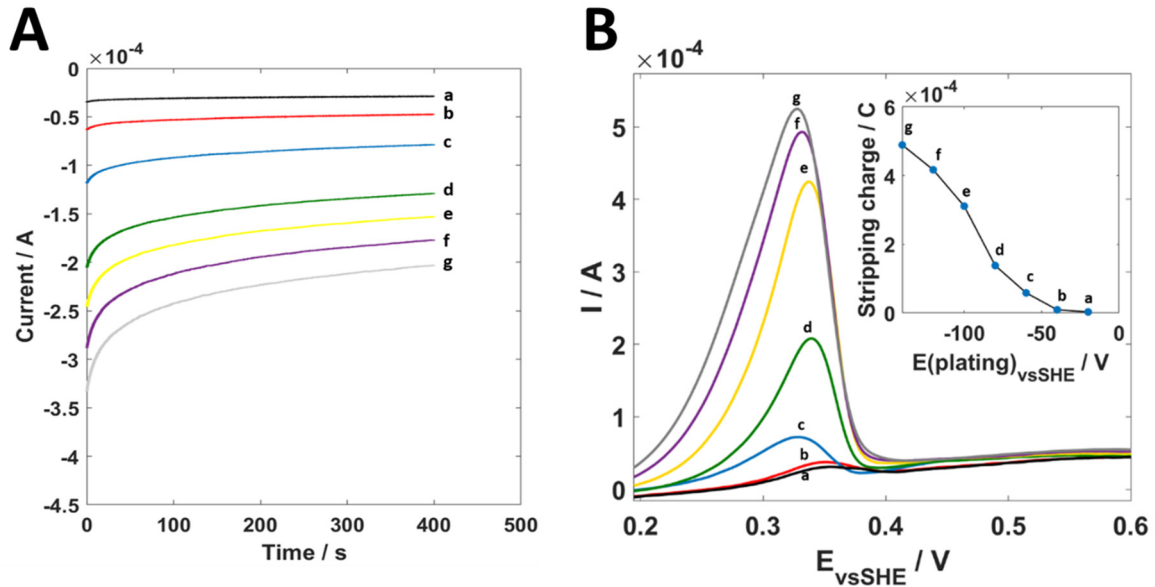


Figure 2.9 (A) Current vs. time plot of chronoamperometric plating during 400s on carbon felt of a vanadium electrolyte mixture containing 5 ppm of Cu^{2+} at different deposition potentials (a) -20 mV (b) -40 mV (c) -60 mV (d) -80 mV (e) -100 mV (f) -120 mV (g) -140 mV. (B) Resulting anodic stripping voltammograms. Inset plot: stripping charge in function of the plating potential.

These results confirmed that a commercial VRFB stack could be used to purify large quantities of $\text{VO}^{2+}/\text{V}^{3+}$ electrolyte solution using electroplating and that regeneration of the stack can be achieved. The purification setup proposed here is composed by a commercial VRFB stack with both positive and negative compartments fed by the same reservoir containing the copper contaminated $\text{VO}^{2+}/\text{V}^{3+}$ electrolyte. The stack is powered at constant potential enough to ensure copper reduction at the negative side. The outlets of the stacks were then mixed back into the initial contaminated electrolyte reservoir to keep the same initial solution potential, and thus

avoid parasitic HER. A scheme of the installation is depicted in Figure 2.10. Alongside the purification, the qualitative dithizone method was used to evaluate the copper concentration. At the end of the purification, the copper was removed from the stack by flushing it with an oxidative solution.

To test the system, a single-cell experiment was assembled to optimize the parameters. The purification process was performed with 3 L of vanadium electrolyte ($\text{VO}^{2+}/\text{V}^{3+}$ ca. 60:40) containing ca. 50 ppm of copper.

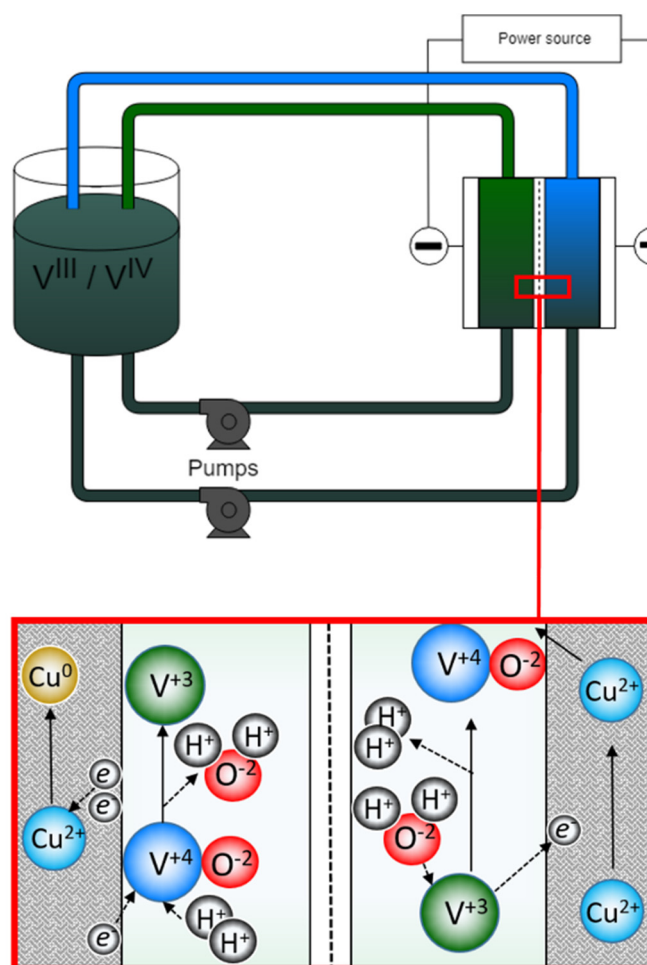


Figure 2.10 Schematic of the purification process developed to remove copper from the vanadium electrolyte. Here V^{4+} means $\text{V}(\text{V})$.

The purification process was performed in a three-electrode setup by adding a reference electrode into the main reservoir. Based on the results of ASV, three potentials were chosen: -80 mV, -100 mV, and -120 mV. After each experiment, the negative carbon felt electrode was cleaned by flushing solution of $\text{VO}^{2+}/\text{V}^{3+}$ ($E^\circ = 0.34$ V vs. SHE), without external power, for 10 minutes. Samples were taken on the outlet of the negative side and used for the determination of copper concentration by ICP-MS.

Table 2.2 summarizes the obtained results. At -80 mV, the removal efficiency reached 97.7% after the first 5 minutes and 100% after 10 minutes. At -100 mV and -120 mV, 100% removal efficiency was attained already after the first 5 minutes. No hydrogen evolution was observed during the experiments.

To evaluate the capacity of the purification process, the experiment at -100 mV was repeated with 400 mL of heavily contaminated copper electrolyte ($1\text{g of Cu} - 2500\text{ mg}\cdot\text{L}^{-1}$). The pressure on the closed system was monitored to detect parasitic HER.

After 1 hour of purification, no copper could be detected in the reservoir (dithizone qualitative analysis gave a green color). Despite of the large quantities of copper present on the carbon felt, no hydrogen evolution was recorded, indicating the importance to keep the potential of the solution constant and close to the standard equilibrium potential of $\text{VO}^{2+}/\text{V}^{3+}$ ($E^\circ=0.34\text{ V vs. SHE}$).

Table 2.2 Copper concentration at the outlet of the negative side at various time of the purification.

Purification	$E_{\text{vs SHE}} / \text{V}$	Negative outlet copper concentration /ppm			
		$C_{0\text{min}}$	$C_{5\text{min}}$	$C_{10\text{min}}$	$C_{30\text{min}}$
1	-0.080	49.75	1.15	No trace	No trace
2	-0.100	49.8	No trace	No trace	No trace
3	-0.120	47.8	No trace	No trace	No trace

After the experiment, the morphology of the negative carbon felt electrode was studied by SEM. Figure 2.11-a shows the morphology of the carbon felt electrode before and Figure 2.11-b and Figure 2.11-c show the carbon felt after the purification. It was observed that most of the copper was plated directly at the inlet of the single-cell. Indeed, Figure 2.11-b shows clearly a copper deposit layer that covered most of the carbon felt surface. As shown in Figure 2.11-c, only few traces of copper were observed close to the outlet, indicating that large amounts of copper can be removed even by a single cell. Finally, Figure 2.11-d confirms that copper can be efficiently removed by soaking the electrode in $\text{VO}^{2+}/\text{V}^{3+}$ electrolyte for ca. 30 minutes. The experiment was repeated and the regenerated electrode was tested in a conventional VRFB equipped with

a pressure sensor. No hydrogen evolution was observed when the battery operated between 20 and 85% SOC.

Note that a second strategy was investigated in order to purify the copper-contaminated electrolyte (Appendix II-2). Although the approach achieved promising results, it presented several drawbacks in terms of reliability and safety for large-scale purification compared to the method presented in this section.

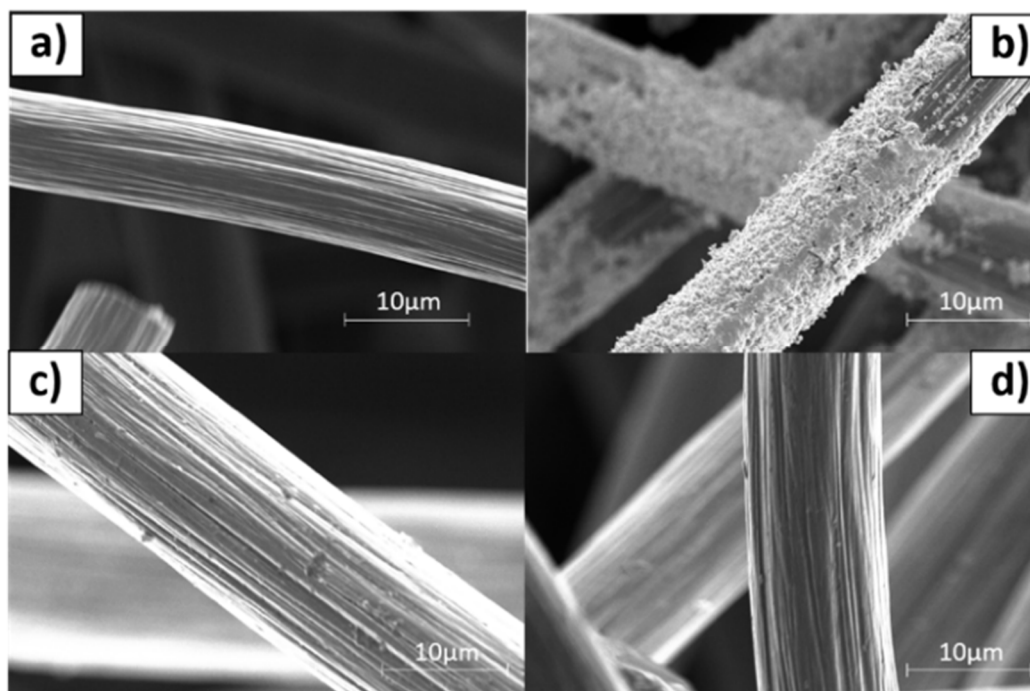


Figure 2.11 SEM images of (a) fresh carbon felt, (b) carbon felt sample close to the inlet and (c) carbon felt sample close to the outlet of the single-cell (d) and carbon felt sample after regeneration.

2.3.4 Scale-up and demonstration

The system described in Figure 2.10 was built on-site, using a 27-cell stack and 1000 L reservoir. The stack was powered at a constant potential of 29 V to ensure a negative potential of at least -100 mV *vs.* SHE. Initially, a 100 L of contaminated electrolyte containing about ca. 40 ppm of Cu^{2+} was used. The electrolyte was cycled at a flow rate value of about $3 \text{ L} \cdot \text{min}^{-1}$ for each side. Samples were taken from both negative outlet and reservoir and used for the determination of copper by ICP-MS. The evolution of copper concentrations with time is shown in Figure 2.12. The electrolyte was successfully purified after 6 hours of operation and reached a final copper concentration of 58 ± 2 ppb.

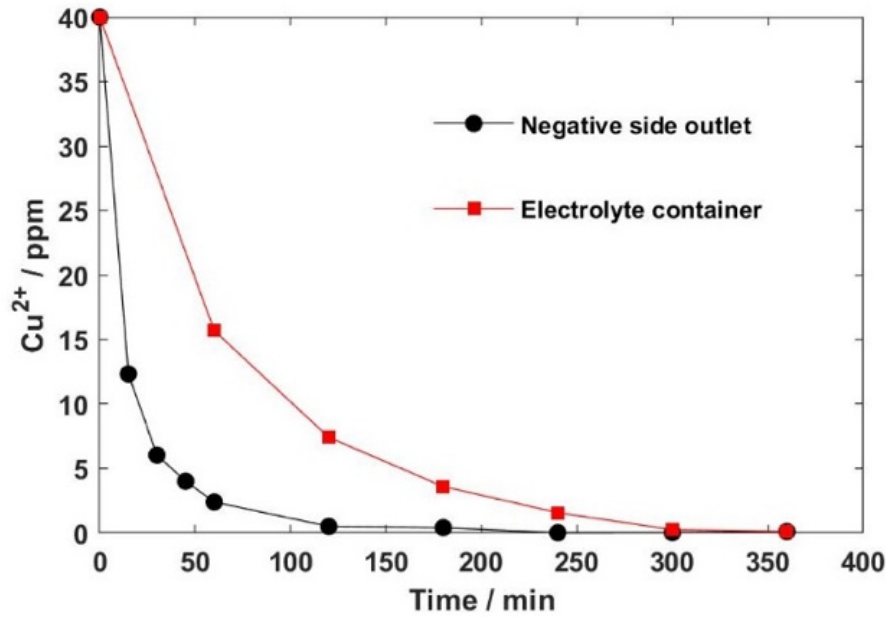


Figure 2.12 Evolution of copper concentration (ICP-MS) of the negative side outlet and the container electrolyte with time of purification.

The same procedure was applied to purify a total amount of 6 m³ of contaminated electrolyte. We needed less than 30 L of electrolyte to wash the stack after use and we assume that the same stack can be used to purify easily 100 m³. The cost of the operation is dominated by the price of the stack and the disposal of the sacrificial electrolyte washing solution. As we concentrate the copper contaminants in less than 30 L of electrolyte, the price of the purification represents only a fraction of what would have been necessary to buy a fresh electrolyte and dispose of the contaminated one (6000 L).² Furthermore, disposing highly acidic solutions of heavy metals requires large amounts of other chemicals and it is neither an environmental friendly practice nor wise in the guise of natural abundance of vanadium ores.

2.4 Conclusion

In this chapter, we report the dramatic consequences of advanced carbon corrosion on an all-vanadium redox flow battery. A commercial VRFB system (10kW/40kWh) was taken as a case study. For some yet unclear reasons, the battery underwent advanced carbon corrosion of the positive side leading to stack leakage and system failure after 3 years of use. Because of the deterioration of the carbon felt and the bipolar plates, the electrolyte reached the copper current collector dissolving it. Thus, in addition to the stack damages, the electrolyte was polluted with copper.

Here, we highlight the deleterious effect of copper on the performance of a VRFB. It was observed that metallic copper improved the parasitic HER on the negative side. To tackle the problems related to copper pollution, a purification process was developed in order to treat large quantities of electrolyte. A classical VRFB stack was used to plate out the copper removing it from the solution. The optimal cathode potential for deposition onto carbon felt was determined to be -100 mV vs. SHE . The process described here was successfully used to purify 6000 L of vanadium electrolyte ($\text{VO}^{2+}/\text{V}^{3+}$ mixture). Moreover, the stack could be regenerated after the purification. The on-site purification was demonstrated to be simple, eco-friendly and cost-effective.

On the basis of the above, significant efforts should be done to improve battery management system (BMS) by developing reliable monitoring and operation strategies in order to guarantee a continuous control on the performances and the health of the battery. In this regard, the redox dual-flow battery is attractive because it enables the individual control of the state-of-charge of each electrolyte, which mitigate the risk arising from electrolyte imbalance.

References

- (1) Parasuraman, A.; Lim, T. M.; Menictas, C.; Skyllas-Kazacos, M. Review of Material Research and Development for Vanadium Redox Flow Battery Applications. *Electrochimica Acta* **2013**, *101*, 27–40. <https://doi.org/10.1016/j.electacta.2012.09.067>.
- (2) Kear, G.; Shah, A. A.; Walsh, F. C. Development of the All-Vanadium Redox Flow Battery for Energy Storage: A Review of Technological, Financial and Policy Aspects. *International Journal of Energy Research* **2012**, *36* (11), 1105–1120. <https://doi.org/10.1002/er.1863>.
- (3) Nolte, O.; A. Volodin, I.; Stolze, C.; D. Hager, M.; S. Schubert, U. Trust Is Good, Control Is Better: A Review on Monitoring and Characterization Techniques for Flow Battery Electrolytes. *Materials Horizons* **2021**. <https://doi.org/10.1039/D0MH01632B>.
- (4) Skyllas-Kazacos, M.; Chakrabarti, M. H.; Hajimolana, S. A.; Mjalli, F. S.; Saleem, M. Progress in Flow Battery Research and Development. *J. Electrochem. Soc.* **2011**, *158* (8), R55–R79. <https://doi.org/10.1149/1.3599565>.
- (5) Liu, H.; Xu, Q.; Yan, C.; Qiao, Y. Corrosion Behavior of a Positive Graphite Electrode in Vanadium Redox Flow Battery. *Electrochimica Acta* **2011**, *56* (24), 8783–8790. <https://doi.org/10.1016/j.electacta.2011.07.083>.
- (6) Schweiss, R.; Pritzl, A.; Meiser, C. Parasitic Hydrogen Evolution at Different Carbon Fiber Electrodes in Vanadium Redox Flow Batteries. *J. Electrochem. Soc.* **2016**, *163* (9), A2089–A2094. <https://doi.org/10.1149/2.1281609jes>.
- (7) Skyllas-Kazacos, M.; Kazacos, M. State of Charge Monitoring Methods for Vanadium Redox Flow Battery Control. *Journal of Power Sources* **2011**, *196* (20), 8822–8827. <https://doi.org/10.1016/j.jpowsour.2011.06.080>.
- (8) Wei, L.; Zhao, T. S.; Xu, Q.; Zhou, X. L.; Zhang, Z. H. In-Situ Investigation of Hydrogen Evolution Behavior in Vanadium Redox Flow Batteries. *Applied Energy* **2017**, *190*, 1112–1118. <https://doi.org/10.1016/j.apenergy.2017.01.039>.
- (9) Satola, B.; Komsijska, L.; Wittstock, G. Corrosion of Graphite-Polypropylene Current Collectors during Overcharging in Negative and Positive Vanadium Redox Flow Battery Half-Cell Electrolytes. *J. Electrochem. Soc.* **2018**, *165* (5), A963–A969. <https://doi.org/10.1149/2.0921805jes>.
- (10) Amstutz, V. Redox Flow Battery and Indirect Water Electrolysis. 270.
- (11) Darling, R. M.; Shiau, H.-S.; Weber, A. Z.; Perry, M. L. The Relationship between Shunt Currents and Edge Corrosion in Flow Batteries. *J. Electrochem. Soc.* **2017**, *164* (11), E3081–E3091. <https://doi.org/10.1149/2.0081711jes>.
- (12) Tang, A.; McCann, J.; Bao, J.; Skyllas-Kazacos, M. Investigation of the Effect of Shunt Current on Battery Efficiency and Stack Temperature in Vanadium Redox Flow Battery. *Journal of Power Sources* **2013**, *242*, 349–356. <https://doi.org/10.1016/j.jpowsour.2013.05.079>.
- (13) Ligen, Y.; Vrubel, H.; Girault, H.; Ligen, Y.; Vrubel, H.; Girault, H. H. Mobility from Renewable Electricity: Infrastructure Comparison for Battery and Hydrogen Fuel Cell Vehicles. *World Electric Vehicle Journal* **2018**, *9* (1), 3. <https://doi.org/10.3390/wevj9010003>.
- (14) Dennison, C. R.; Vrubel, H.; Amstutz, V.; Peljo, P.; Toghiani, K. E.; Girault, H. H. Redox Flow Batteries, Hydrogen and Distributed Storage. *Chimia (Aarau)* **2015**, *69* (12), 753–758. <https://doi.org/10.2533/chimia.2015.753>.
- (15) Roznyatovskaya, N.; Herr, T.; Küttinger, M.; Fühl, M.; Noack, J.; Pinkwart, K.; Tübke, J. Detection of Capacity Imbalance in Vanadium Electrolyte and Its Electrochemical Regeneration for All-Vanadium Redox-Flow Batteries. *Journal of Power Sources* **2016**, *302*, 79–83. <https://doi.org/10.1016/j.jpowsour.2015.10.021>.

- (16) Wei, L.; Zhao, T. S.; Zeng, L.; Zhou, X. L.; Zeng, Y. K. Copper Nanoparticle-Deposited Graphite Felt Electrodes for All Vanadium Redox Flow Batteries. *Applied Energy* **2016**, *180*, 386–391. <https://doi.org/10.1016/j.apenergy.2016.07.134>.
- (17) Kiwan, A. M. Use of Dichloromethane with Dithizone as an Alternative Solvent to Carbon Tetrachloride Restricted by Montreal Protocol. *Talanta* **1997**, *44* (5), 947–950. [https://doi.org/10.1016/S0039-9140\(96\)02135-2](https://doi.org/10.1016/S0039-9140(96)02135-2).
- (18) Bendix, G.; Grabenstetter, D. Dithizone Method for Rapid Determination of Copper. *Ind. Eng. Chem. Anal. Ed.* **1943**, *15* (10), 649–652. <https://doi.org/10.1021/i560122a019>.
- (19) Wei, G.-T.; Yang, Z.; Chen, C.-J. Room Temperature Ionic Liquid as a Novel Medium for Liquid/Liquid Extraction of Metal Ions. *Analytica Chimica Acta* **2003**, *488* (2), 183–192. [https://doi.org/10.1016/S0003-2670\(03\)00660-3](https://doi.org/10.1016/S0003-2670(03)00660-3).
- (20) Rice, C. R.; Faulkner, R. A.; Jewsbury, R. A.; Bullock, S.; Dunmore, R. A Structural Study of Dithizone Coordination Chemistry. *CrystEngComm* **2017**, *19* (25), 3414–3419. <https://doi.org/10.1039/C7CE00580F>.
- (21) Irving, H. M. N. H.; Kiwan, A. M. Studies with Dithizone: Part XXV. Secondary Copper(II) Dithizonate. *Analytica Chimica Acta* **1971**, *56* (3), 435–446. [https://doi.org/10.1016/S0003-2670\(01\)80933-8](https://doi.org/10.1016/S0003-2670(01)80933-8).
- (22) Freiser, B. S.; Freiser, Henry. Nature of the Enol or Secondary Series of Diphenylthiocarbazone Chelates. *Anal. Chem.* **1970**, *42* (2), 305–306. <https://doi.org/10.1021/ac60284a021>.
- (23) Grujicic, D.; Pesic, B. Electrodeposition of Copper: The Nucleation Mechanisms. *Electrochimica Acta* **2002**, *47* (18), 2901–2912. [https://doi.org/10.1016/S0013-4686\(02\)00161-5](https://doi.org/10.1016/S0013-4686(02)00161-5).
- (24) Zhou, X. J.; Harmer, A. J.; Heinig, N. F.; Leung, K. T. Parametric Study on Electrochemical Deposition of Copper Nanoparticles on an Ultrathin Polypyrrole Film Deposited on a Gold Film Electrode. *Langmuir* **2004**, *20* (12), 5109–5113. <https://doi.org/10.1021/la0497301>.
- (25) Dai, X.; Nekrassova, O.; Hyde, M. E.; Compton, R. G. Anodic Stripping Voltammetry of Arsenic(III) Using Gold Nanoparticle-Modified Electrodes. *Analytical Chemistry* **2004**, *76* (19), 5924–5929. <https://doi.org/10.1021/ac049232x>.
- (26) Agra-Gutiérrez, C.; Hardcastle, J. L.; Ball, J. C.; Compton, R. G. Anodic Stripping Voltammetry of Copper at Insonated Glassy Carbon-Based Electrodes: Application to the Determination of Copper in Beer. *The Analyst* **1999**, *124* (7), 1053–1057. <https://doi.org/10.1039/a902974e>.
- (27) Takeuchi, R. M.; Santos, A. L.; Padilha, P. M.; Stradiotto, N. R. Copper Determination in Ethanol Fuel by Differential Pulse Anodic Stripping Voltammetry at a Solid Paraffin-Based Carbon Paste Electrode Modified with 2-Aminothiazole Organofunctionalized Silica. *Talanta* **2007**, *71* (2), 771–777. <https://doi.org/10.1016/j.talanta.2006.05.035>.

Appendix II

Appendix II-1: Pressure sensor calibration

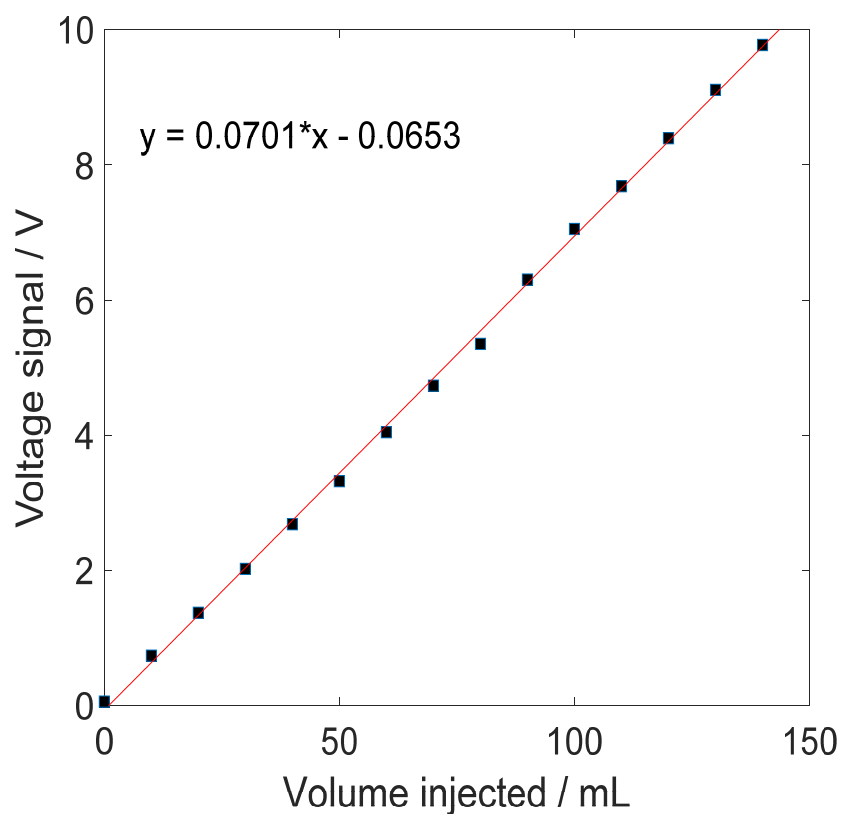


Figure A2.1 Calibration curve of the pressure sensor (MPX501DP). It was used to convert the voltage signal of the pressure sensor into the volume of hydrogen produced. The plot was performed by injecting air with a syringe in the range of 0 to 140 mL. The gas was assumed to be ideal and the solubility constant along the change of pressure.

Appendix II-2: Additional purification strategy

Besides the purification method described in the manuscript, a second approach was investigated for the electrolyte purification. The method consisted of a commercial VRFB stack with positive and negative compartments fed by two reservoirs containing cleaned and copper contaminated V^{3+}/VO^{2+} electrolyte, respectively. The stack was powered at constant potential enough to ensure copper reduction at the negative side until the desired copper concentration. At the end of the purification, the positive and the negative electrolyte were mixed back into a third reservoir to restore the initial solution potential. The copper was removed from the stack by applying an oxidative potential or by flushing an oxidative solution.

Although the process was found to remove copper in an efficient way, the process showed several drawbacks for large-scale purification. Since the SOC of the negative electrolyte and the amount of metallic copper plated increased during the operations, HER was promoted within the progress of the purification. This was problematic because it led to electrolyte imbalance between the positive and the negative electrolyte. In addition, the process had the disadvantage to employ large amount of clean electrolyte that may lead to additional purification cost. The mixing of V^{2+} and VO_2^+ is highly exothermic and must be performed with caution.

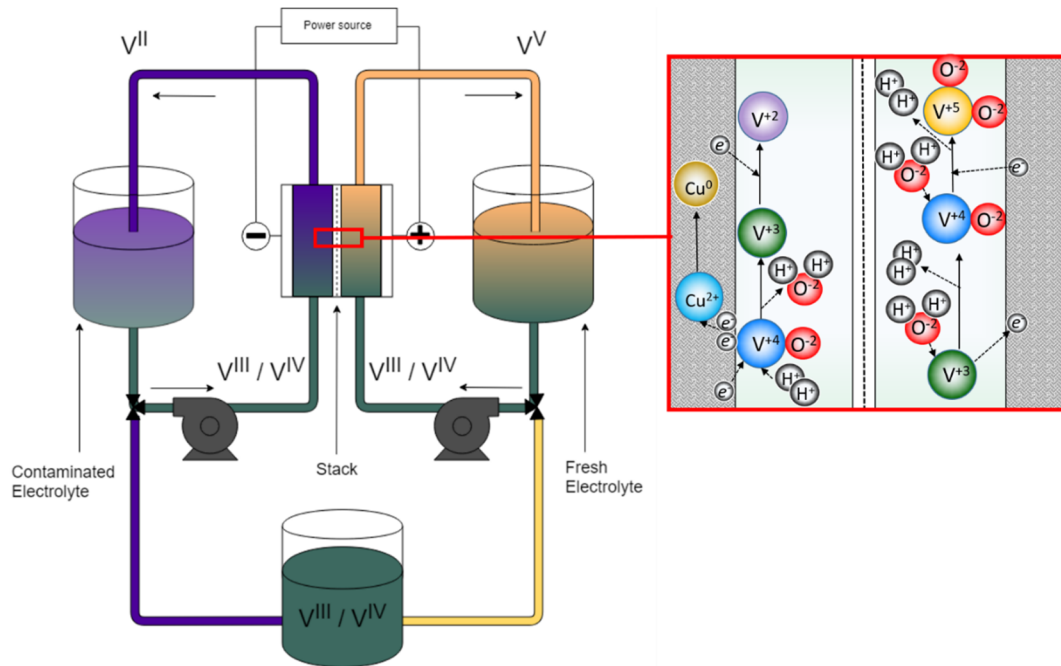
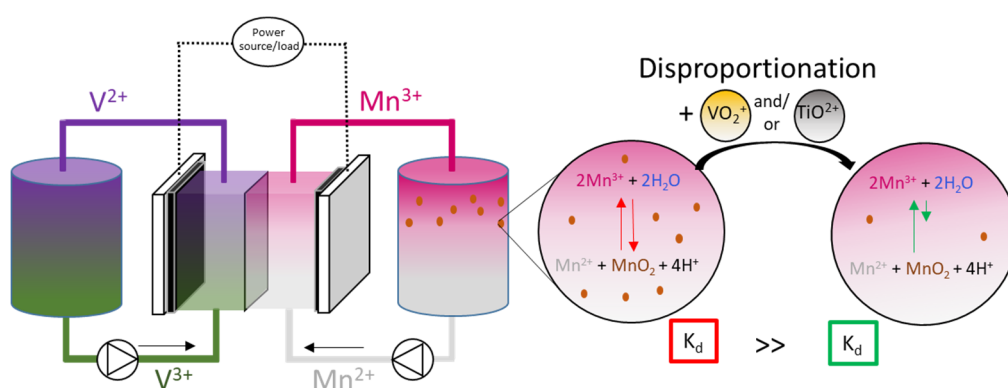


Figure A2.2 Schematic of an additional purification process developed to remove copper from the vanadium electrolyte. Here V^{4+} and V^{5+} means V(IV) and V(V), respectively.

CHAPTER III

Stabilization of manganese electrolyte ($\text{Mn}^{3+}/\text{Mn}^{2+}$)

The results presented in this chapter are adapted with permission from D. Reynard, S. Maye, P. Peljo, V. Chanda, H. H. Girault, S. Gentil, Vanadium–Manganese Redox Flow Battery: Study of Mn(III) Disproportionation in the Presence of Other Metallic Ions, Chem. Eur. J. 2020, 26, 7250, DOI:10.1002/chem.202000340 © 2020 Wiley-VCH Verlag GmbH & Co. KGaA, Weinheim.

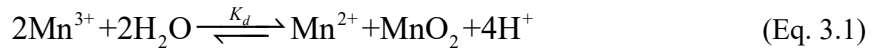


Abstract

The $\text{Mn}^{3+}/\text{Mn}^{2+}$ redox couple with a standard potential of +1.51 V vs. SHE has drawn interest for the design of vanadium-manganese redox dual-flow battery (RFB). However, Mn^{3+} disproportionation leads to a loss of capacity, an increase of pressure drop and electrode passivation due to the formation of MnO_2 during battery cycling. In this chapter, the influence of TiO^{2+} or/and VO_2^+ on Mn^{3+} stability in acidic conditions is studied, by formulating 4 different electrolytes at equimolar ratios (Mn, Mn:Ti, Mn:V, Mn:V:Ti). Voltametric studies reveal an EC_i process for Mn^{2+} oxidation responsible for the electrode passivation. SEM and XPS analysis demonstrate that the nature and the morphology of the passivating oxides layer strongly rely on the electrolyte composition. Spectroelectrochemistry highlights the stabilization effect of TiO^{2+} and VO_2^+ on Mn^{3+} . At a comparable pH, the amount of Mn^{3+} lost through disproportionation is decreased by a factor of 2.5 in the presence of TiO^{2+} or/and VO_2^+ . VO_2^+ is an efficient substitute to TiO^{2+} in order to stabilize Mn^{3+} electrolyte for redox flow battery applications.

3.1 Introduction

Manganese, the 12th most abundant element on earth, is a transition metal found in ores, in combination with iron, and mainly extracted in South Africa. Among the most common oxidation states (II, III, IV, V and VII), Mn(II) (Mn²⁺) is the most stable. Higher oxidation states are strong oxidizing agents such as permanganate (VII; MnO₄⁻) or manganate anions (VI, MnO₄²⁻), or known catalysts for water oxidation (IV, MnO₂).¹ The high standard redox potential of the Mn³⁺/Mn²⁺ couple (+ 1.51 V vs. SHE) has attracted interest for the investigation of V/Mn RFB.²⁻⁴ In this configuration, a standard cell voltage of 1.77 V ($E_{cell}^{\circ} = E_{Mn^{3+}/Mn^{2+}}^{\circ} - E_{V^{3+}/V^{2+}}^{\circ}$) is expected. As compared to the all-vanadium RFB,^{5,6} the main interest comes from higher energy densities, accounting for a 500 mV higher cell potential. However, cycling performances and battery lifetime remain limited by the instability of Mn³⁺ in solution, which is disproportionated to Mn²⁺ and MnO₂ (Eq. 3.1):



The formation of MnO₂ particles leads to a reduced mass transport, a higher pressure drop, electrode passivation and irreversible decays in the RFB capacity and power.⁴ To minimize the issues related to disproportionation reactions, higher sulfuric acid concentrations up to 6 M and/or addition of TiO₂²⁺ to the manganese electrolytes were shown to stabilize Mn³⁺. Hence, the equilibrium of the disproportionation reaction was displaced and the morphology of the manganese oxide particles modified.⁷⁻⁹ Tokuda *et al.* demonstrated by X-ray diffraction and X-ray absorption that formation of Ti-SO₄ bonds in an electrolyte composed of MnSO₄ and TiOSO₄ favors H⁺ dissociation from H₂SO₄ and consequently promotes the dissolution of MnO₂(s) particles with a decrease of the pH.¹⁰ Recently, a hydrogen/manganese hybrid redox flow battery has demonstrated interesting results maintaining 75% of energy efficiency over 160 cycles at low Mn²⁺ and TiO₂²⁺ concentrations to prevent MnO₂ formation (0.2 M). However, electrolytes rebalancing was performed every 5 cycles to maintain stable performances.¹¹ Till today, the disproportionation reaction of Mn³⁺ is not well understood and limits applications of manganese electrolyte in RFBs. Several mechanisms were discussed in the literature to describe the oxidation of Mn²⁺.^{3,12-15} Generally, a E₁C₁E₂ mechanism (*e.g.* – electron transfer, irreversible

chemical reaction, electron transfer) is considered. The first step consists of the electrochemical oxidation of Mn²⁺ (E₁ - (Eq. 3.2)):



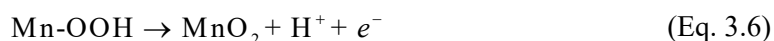
Then, it was reported that the mechanism for the disproportionation of Mn³⁺ can differ according to the local proton concentration. In fact, at low pH, Mn³⁺ disproportionates into Mn²⁺ and MnO₂ in an irreversible chemical reaction (C_i - (Eq. 3.3) and (Eq. 3.4)).¹³



At higher pH, Mn³⁺ could also go through a hydrolysis step to form an oxy-hydroxide intermediate (Eq. 3.5):¹³⁻¹⁷



In this particular case, Mn-OOH can then further be oxidized to MnO₂ through a second electrochemical step (E₂ - (Eq. 3.6)):¹³⁻¹⁷



Those reactions ((Eq. 3.4) and (Eq. 3.6)) may lead to a chemical and/or electrochemical passivation of the electrode surface.¹³⁻¹⁷ The deposition of MnO₂ was described as a nucleation and growth process by Huang *et al.* on graphite electrodes.¹⁶

Herein, we present a characterization of various Mn²⁺ electrolytes in the presence of TiO₂⁺ and introduced for the first time VO₂⁺ as a stabilizing agent. Four different electrolytes were studied in high acidic conditions (5 M H₂SO₄) at equimolar ratios: Mn²⁺, Mn²⁺:TiO₂⁺, Mn²⁺:VO₂⁺ and Mn²⁺:VO₂⁺:TiO₂⁺. Voltammetry was performed in both static and hydrodynamic conditions in order to elucidate the chemical and electrochemical processes associated with the Mn²⁺ oxidation at the electrode surface. The formation of oxide layers was investigated on both carbon felt and glassy carbon electrodes at low and high acidic concentrations. SEM combined with XPS analyses were used to investigate the morphology and the chemical nature of the oxide. The disproportionation reaction occurring in the bulk was monitored by spectroelectrochemistry, XPS and SEM.

3.2 Experimental section

3.2.1 Materials and methods

Manganese sulfate monohydrate ($\text{MnSO}_4 \cdot \text{H}_2\text{O}$, > 99%), titanium oxysulfate solution (TiOSO_4 , ~15 wt. % in dilute sulfuric acid, 99.99% trace metals basis, Sigma-Aldrich), vanadium pentoxide (V_2O_5 , > 99.6%) and sulfuric acid (H_2SO_4 , 95-97 %) were purchased from Sigma Aldrich and used without further purification. Four different electrolytes were prepared in 5 M H_2SO_4 : 0.1 M Mn, 0.1 M Mn:V (1:1), 0.1 M Mn:Ti (1:1), and 0.1 M Mn:V:Ti (1:1:1). Solutions containing vanadium were sonicated and stirred for 2 hours in order to dissolve V_2O_5 . For iodometry, anhydrous potassium iodide (KI, 99%) was purchased from Sigma Aldrich and $\text{Na}_2\text{S}_2\text{O}_3$ sodium thiosulfate pentahydrated (> 99.5%, Fluka) and starch from potatoes ($(\text{C}_6\text{H}_{10}\text{O}_5)_n$) were purchased from Fluka. Electrochemical experiments were conducted with an Autolab PGSTAT204 (Metrohm) or a Biologic SP-300 potentiostat. Scanning electron microscopy images were performed with a Teneo SEM (FEI, USA) equipped with a Schottky field emission gun. UV/Vis measurements were performed with an Agilent 8453 spectrophotometer. X-ray photoelectron spectroscopy (XPS) was conducted with a VersaProbe II from Physical Electronics.

3.2.2 Electrochemical characterization

Electrochemical experiments were performed in a 3-electrode setup with a glassy carbon rotating disk electrode (RDE, Metrohm, 0.196 cm^2), an $\text{Ag}|\text{AgCl}$ (KCl sat.) reference electrode, and a platinum counter electrode. The working electrode was polished before each experiment with $1 \mu\text{m}$ silica polishing solution and immersed in an aqueous solution of isopropanol (50%) in an ultrasound bath for 30 minutes. Static cyclic voltammetry was performed between 0.2 to 2 V vs. SHE at scan rates ranging from 0.005 to $5 \text{ V} \cdot \text{s}^{-1}$. Dynamic linear sweep voltammetry was performed with a RDE from 0.2 to 2.5 V vs. SHE at a scan rate of $0.01 \text{ V} \cdot \text{s}^{-1}$ and various rotation speeds ranging from 200 to 2500 rpm.

3.2.3 Spectroelectrochemistry

The oxidation reaction of Mn^{2+} to Mn^{3+} was monitored by UV-visible spectrophotometry at wavelengths around 500 nm for various electrolyte solutions in 5 M H_2SO_4 : 0.1 M Mn, 0.1 M Mn:V (1:1), 0.1 M Mn:Ti (1:1), and 0.1 M Mn:V:Ti (1:1:1). The electrolysis was performed in

a H-shape electrochemical cell (H-cell) at +1.8 V vs. Ag|AgCl (KCl sat.) with a carbon felt working electrode (anode), a carbon felt counter electrode (cathode) and an Ag|AgCl (KCl sat.) reference electrode placed within the anodic compartment. The H-cell included a glass frit separator. The anodic and cathodic compartments contained 25 mL of 100 mM Mn²⁺ sulfate solution and 40 mL of 150 mM VO₂⁺ sulfate solution in 5 M H₂SO₄, respectively. The concentration of Mn³⁺ along the electrolysis process was monitored by UV-visible spectrophotometry at fixed wavelengths according to the electrolyte composition: $\lambda_{\text{Mn}^{3+}}(\text{Mn}) = 490 \text{ nm}$, $\lambda_{\text{Mn}^{3+}}(\text{Mn:Ti}) = 517 \text{ nm}$, $\lambda_{\text{Mn}^{3+}}(\text{Mn:V}) = 500 \text{ nm}$, $\lambda_{\text{Mn}^{3+}}(\text{Mn:V:Ti}) = 506 \text{ nm}$. The electrolyte was sampled every 5 minutes from the bulk solution of the positive side using syringe equipped with a 25 mm Yeti HPLC filter (0.22 μm PTFE membrane) to remove the suspended MnO₂ particles. UV-vis spectra background caused by the remaining MnO₂ particles was normalized at 700 nm. The molar absorption coefficient (ϵ) of Mn³⁺ in each electrolyte was calculated using a Beer-Lambert relation:

$$A = \epsilon lc \quad (\text{Eq. 3.7})$$

where A is the absorbance, l is the length of the optical path and c is the concentration of the attenuating species.

The exact concentration of Mn³⁺ was determined by iodometric titration. The detailed procedure of iodometry for each electrolyte is detailed in the section 3.2.5.

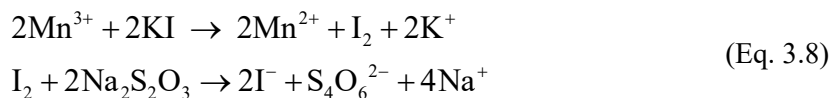
3.2.4 Study of manganese oxide formation

The formation of oxides was studied for the various electrolytes. Chronoamperometry experiments were performed in a 3-electrode set-up with different carbon working electrodes (carbon felt and flat glassy carbon), a platinum counter electrode, and an Ag|AgCl (KCl 3M) reference electrode. H-cell electrolysis of Mn²⁺ was performed at potential value of +1.8 V vs. SHE for 30 minutes. Experiments were conducted twice. Four electrolytes in 50 mM sulfuric acid solution were studied: 10 mM Mn, 10 mM Mn:V (1:1), 10 mM Mn:Ti (1:1), and 10 mM Mn:V:Ti (1:1:1). Scanning electron microscopy (FEI SEM Teneo) of the electro-grafted layers deposited onto carbon felt and glassy carbon electrodes were imaged at 3-5kV, 0.4-0.25nA with lower in-lens, in-column and Everhard-Thronley secondary electron detectors (ETD). Chemical composition of the oxide layers deposited onto the glassy carbon working electrodes were

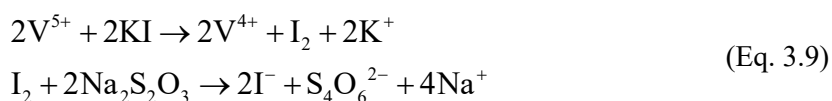
analysed by XPS. The spectra were calibrated with the C-C bound of the adventitious carbon contamination at 284.8 eV.

3.2.5 Iodometry for Mn³⁺ titration

The main titration reaction is described below (Eq. 3.8):



The reduction of I₂ by S₂O₃²⁻ has a potential of 0.456 V (vs. SHE). The secondary titration reaction is described below (Eq. 3.9):



According to the different redox potentials of the electroactive species (Table 3.1) which compose the analytes, only Mn³⁺ and V₂O₅ should be reduced by the iodide. Consequently, a blank experiment was carried out before the Mn²⁺ solution bulk electrolysis for the solutions containing V₂O₅. This blank allows to quantify the amount of V₂O₅ and to calculate the real Mn³⁺ concentration without the influence of the VO₂⁺ on the volumetric analysis.

Table 3.1 Standard potentials of the electroactive redox couples during iodometric titration.

Redox Couple	E^0 / V
Mn ²⁺ /Mn	-1.185
TiO ₂ / Ti ²⁺	-0.502
S ₂ O ₃ ²⁻ /S ₄ O ₆ ²⁻	0.08
VO ²⁺ /V ³⁺	0.337
I ₂ /I ⁻	0.536
VO ₂ ⁺ / VO ²⁺	0.991
Mn ³⁺ /Mn ²⁺	1.542

Between 5 and 10 mL of the pink Mn³⁺ analyte was titrated by following the previous redox reactions. The indicator, a 20 g·L⁻¹ starch (starch from potatoes, (C₆H₁₀O₅)_n, Fluka) solution, was added for the volumetric analysis (around 5-10 drops). An excess of KI (potassium iodide, anhydrous, free-flowing, Redis-Dri(TM), ReagentPlus, 99%, Sigma-Aldrich) reduced the Mn³⁺ and produced iodine which complexes with starch to give a dark purple color. Iodine was

quantitatively reduced back to iodide by a 0.1 (or 0.05) M $\text{Na}_2\text{S}_2\text{O}_3$ solution (sodium thiosulfate pentahydrated, analytical grade, >99.5%, Fluka). At the end of the analysis, Mn^{2+} solution was transparent.

Standards and solutions were made of $\text{MnSO}_4 \cdot \text{H}_2\text{O}$ (manganese(II) sulfate monohydrate, ReagentPlus, >99%, Sigma-Aldrich), TiOSO_4 (titanium⁴⁺ oxysulfate solution, ~15 wt. % in dilute sulfuric acid, 99.99% trace metals basis, Sigma-Aldrich), V_2O_5 (vanadium(V) oxide, >99.6% trace metal basis, Sigma-Aldrich) and H_2SO_4 (sulfuric acid, 95-98 % for analysis, Merck):

- Standard 1: aqueous solution of 0.05 M V_2O_5 and 1 M H_2SO_4 ;
- Standard 2: aqueous solution of 0.05 M V_2O_5 and 5 M H_2SO_4 ;
- Solution 1: aqueous solution of 0.1 M Mn^{2+} and 5 M H_2SO_4 ;
- Solution 2: aqueous solution of 0.1 M Mn^{2+} , 0.1 M TiOSO_4 and 5 M H_2SO_4 ;
- Solution 3: aqueous solution of 0.1 M Mn^{2+} , 0.05 M V_2O_5 and 5 M H_2SO_4 ;
- Solution 4: aqueous solution of 0.1 M Mn^{2+} , 0.1 M TiOSO_4 , 0.05 M V_2O_5 and 5 M H_2SO_4 .

The bulk electrolysis of the Mn^{2+} to the Mn^{3+} was achieved with a simple two electrode set-up with carbon felt electrodes and a potential between 2 - 2.5 V. This redox titration method seemed to be interesting also for the quantification of VO_2^+ in a redox flow battery. The state of charge could be determined by iodometry specifically for the positive side as the iodide can only reduce VO_2^+ among the different oxidation state of vanadium.

3.3 Results and discussion

3.3.1 Electrochemical study of electrolytes

Electrochemical characterizations of the four electrolytes at equimolar ratio in 5M H_2SO_4 (Mn, Mn:Ti, Mn:V and Mn:V:Ti) were performed by cyclic voltammetry (CV) at $0.01 \text{ V} \cdot \text{s}^{-1}$ (Figure 3.1 A-C) and $1 \text{ V} \cdot \text{s}^{-1}$ (Figure 3.1 B-D).

As shown in Figure 3.1-A for the Mn electrolyte, only one anodic peak at +1.72 V vs. SHE was observed and corresponds to the oxidation of Mn^{2+} into Mn^{3+} , (E_1 -(Eq. 3.2)). In these high acidic conditions (5M H_2SO_4), the electrochemical reaction E_2 was not observed, indicating that Mn^{3+} disproportionates in purely chemical process ((Eq. 3.3) and (Eq. 3.4)). Another reason to

claim the absence of E₂ was the low kinetic of Mn-OOH oxidation (Eq. 3.6). In fact, Petitpierre *et al.*³² detected the anodic peak corresponding to E₂ only at temperature above 40°C.

In the cathodic region, two reduction peaks were observed at +1.51 and +1.12 V for Mn. The former peak (+1.51 V *vs.* SHE) was attributed to the one electron reduction of Mn³⁺ to Mn²⁺ (E₁). As Mn³⁺ was consumed through the chemical step (C_i - (Eq. 3.3) and (Eq. 3.4)), the peak intensity was considerably lower than for the forward peak. At higher scan rates (Figure 3.1-B, 1 V·s⁻¹), this peak intensity increased slightly. This effect is characteristic of EC_i processes as the irreversible chemical reaction has less time to occur, and so larger amount of Mn³⁺ was reduced back at the electrode with less passivation. At the beginning of the reverse scan, an anodic shoulder could be observed at +1.87 V *vs.* SHE and was induced by the increasing concentration of Mn²⁺ in the diffusion layer. This rise of concentration comes from the chemical disproportionation reaction of Mn³⁺ (Eq. 3.3).

The second cathodic peak (+1.12 V *vs.* SHE) was assigned to the reduction of MnO₂ to Mn²⁺ (Eq. 3.10).



For Mn:Ti, a similar shape for the CVs was recorded in Figure 3.1-A and Figure 3.1-B. The peak attributed to (Eq. 3.10) was shifted by 30 mV towards cathodic potentials (+1.09 V *vs.* SHE) and the intensity was lower than for the pure Mn electrolyte. This suggests an influence of TiO²⁺ on the chemical reaction rate ((Eq. 3.3) and (Eq. 3.4)), that may decrease the formation of MnO₂. Furthermore, the shoulder at the beginning of the reverse scan (+1.87 V *vs.* SHE) exhibited a lower anodic current because of a lower rate of disproportionation. We hypothesize that a dinuclear complex was formed in between TiO²⁺ and Mn³⁺, protecting it from disproportionation. However, no clear spectroscopic signature was reported so far.¹¹

In the presence of vanadium (Figure 3.1-C), additional reversible oxidation and reduction peaks were observed at an apparent standard potential of +1.1 V *vs.* SHE attributed to one electron reduction of VO₂⁺ to VO²⁺. The large peak-to-peak potential difference (Figure 3.1-D) is due to the slow kinetics of VO₂⁺/VO²⁺ redox couples.¹⁸ Mn³⁺/Mn²⁺ electrochemical reduction was observed at an apparent redox potential of +1.57 V *vs.* SHE (Figure 3.1-C). The peak-to-peak potential difference was found to be 20 mV smaller in the presence of vanadium ($\Delta E = 210$ mV for Mn and Mn:Ti ; $\Delta E = 190$ mV for Mn:V and Mn:V:Ti), suggesting a better reversibility. It

is worth mentioning that the reduction peak potential value was taken at the foot of the wave in all the cases. As compared to Mn and Mn:Ti, the 2-electron reduction of MnO_2 to Mn^{2+} (Eq. 3.10) was not clearly visible because of the overlapping of the VO_2^+ to VO^{2+} reduction peak.

At $1 \text{ V} \cdot \text{s}^{-1}$, a reduction peak was observed at $+1.5 \text{ V}$ vs. SHE (Figure 3.1-D), accounting for a slower electrode passivation and more favorable electrochemical reduction of Mn^{3+} to Mn^{2+} . Note that no shoulder around $+1.87 \text{ V}$ vs. SHE was observed for the pure VO_2^+ electrolyte. This confirms that the origin of the shoulder was due to the sudden increase of Mn^{2+} concentration following the disproportionation reaction.

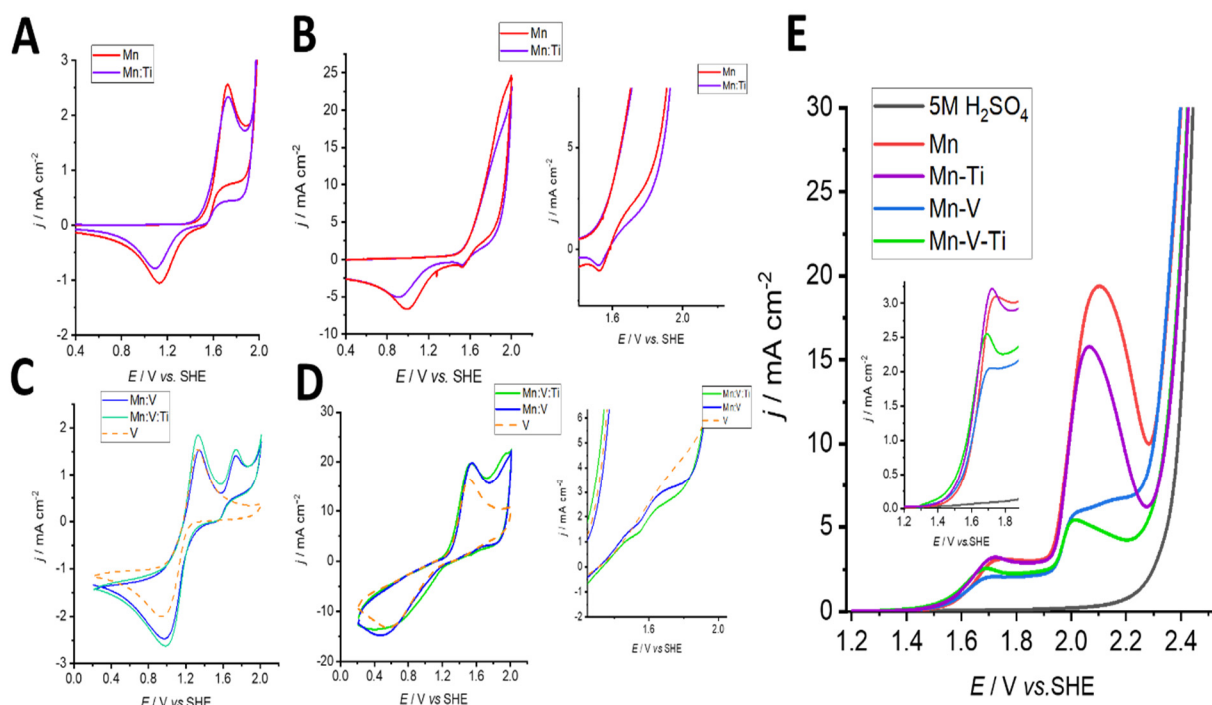


Figure 3.1 iR -corrected cyclic voltammetry of 100 mM (1:1:1) of the different electrolytes: (A-B) Mn and Mn:Ti, (C-D) Mn:V:Ti and Mn:V performed at $10 \text{ mV} \cdot \text{s}^{-1}$ (left chart) and $1 \text{ V} \cdot \text{s}^{-1}$ (right chart) in 5 M H_2SO_4 as supporting electrolyte. (E) Linear sweep voltammetry of the different electrolyte 5 M H_2SO_4 , 100 mM Mn, 100 mM Mn:Ti (1:1), 100 mM Mn:V (1:1) and 100 mM Mn:V:Ti (1:1:1) performed using a glassy-carbon RDE at 1000 rpm and $10 \text{ mV} \cdot \text{s}^{-1}$. The inset shows a zoom of LSV for anodic process at $+1.5 \text{ V}$ vs. SHE.

Rotating-disk electrode (RDE) experiments were carried out for each electrolyte between $+1$ to $+1.8 \text{ V}$ vs. SHE at $10 \text{ mV} \cdot \text{s}^{-1}$. The passivation of the electrode by MnO_2 insulating layer prevents the observation of a conventional sigmoidal current. The diffusion coefficient of each electrolyte was calculated using the Koutecky-Levich equation:

$$\frac{1}{i_m} = \frac{1}{i_k} + \frac{1}{0.62nFAD^{2/3}\omega^{1/2}\nu^{-1/6}C_0} \quad (\text{Eq. 3.11})$$

where i_m is the measured current (A), i_k is the kinetic current (A), n is the number of electrons, F the Faraday constant ($\text{C}\cdot\text{mol}^{-1}$), A the geometric area of the working electrode (0.196 cm^2), D the diffusion coefficient ($\text{cm}^2\cdot\text{s}^{-1}$), ω the angular rotation rate of the electrode ($\text{rad}\cdot\text{s}^{-1}$), ν is the kinematic viscosity ($\text{cm}^2\cdot\text{s}^{-1}$) and C_0 is the concentration of the analyte ($\text{mol}\cdot\text{cm}^{-3}$). The kinematic viscosity ($0.0153\text{-}0.0155 \text{ cm}^2\cdot\text{s}^{-1}$) was calculated from the ratio of the dynamic viscosity (μ) over the density (ρ). The dynamic viscosity of 5 M H_2SO_4 at 298K is $2.02\cdot 10^{-3}$ cP and was considered as constant with the addition of the different redox species. The density was calculated by weighing 1 mL of each electrolyte as a triplicate.

Diffusion coefficients of Mn^{2+} into the different electrolytes were calculated to be $1.18\cdot 10^{-6} \text{ cm}^2\cdot\text{s}^{-1}$ for Mn electrolyte, which is in good agreement with previous studies.^{18,19} In the case of Mn:V, Mn:V:Ti and Mn:Ti electrolytes, the diffusions coefficients were respectively found to be $3.68\cdot 10^{-7} \text{ cm}^2\cdot\text{s}^{-1}$, $1.64\cdot 10^{-7} \text{ cm}^2\cdot\text{s}^{-1}$, $1.66\cdot 10^{-7} \text{ cm}^2\cdot\text{s}^{-1}$. The RDE voltammograms and Koutecky-Levich plots are shown in Appendix III-1. The calculated diffusion coefficients are summarized in Table 3.2:

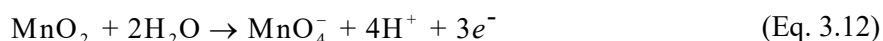
Table 3.2 Diffusion coefficients calculated using the Koutecky-Levich equation for each electrolyte.

Electrolytes	Mn ²⁺ diffusion coefficient ($\text{cm}^2 \text{ s}^{-1}$)
100 mM Mn	$1.18\cdot 10^{-6}$
100 mM Mn-Ti	$1.66\cdot 10^{-7}$
100 mM Mn-V	$3.68\cdot 10^{-7}$
100 mM Mn-V-Ti	$1.64\cdot 10^{-7}$

As the diffusion coefficient depends on $1/a$ (with a being the ionic radius), the lower order of magnitude observed in the presence of other metallic ions suggests the formation of a complex between those transition metals. According to the electronic structure of d orbitals of Mn^{3+} (d^4) and the absence of d electrons for TiO^{2+} and VO_2^+ , direct metal-metal bonding is not possible.

We anticipate that an oxo-bridge might be responsible for any dinuclear cluster formation, as suggested by Tokuda *et al.*¹⁰

Linear sweep voltammetry was then performed at 1000 rpm up to +2.5 V *vs.* SHE (Figure 3.1-E). The inset at +1.5 V *vs.* SHE shows the oxidation of Mn²⁺ for the various electrolytes, which corresponds to the E₁C_i mechanisms described previously ((Eq. 3.3) and (Eq. 3.5)). No current plateau was observed due to electrode passivation by MnO₂, which tends to decrease the current. At + 1.9 V *vs.* SHE, we observed oxidation peaks at different intensities with the following trend: Mn>Mn:Ti>Mn:V>Mn:V:Ti, This oxidation process was attributed to the oxidation of deposited MnO₂ into the permanganate anion, as shown in (Eq. 3.12):



The peak current correlated directly to the quantity of MnO₂ deposited after the E₁C_i mechanism. In the presence of vanadium or/and titanium, peak currents were significantly decreased as compared to Mn. This observation suggests a possible complexation between Mn³⁺ and the different cations, reducing significantly the formation of MnO₂. Finally, the oxidation of the electrolyte to O₂ was observed from + 2.3 V *vs.* SHE, as shown by the sharp increase in anodic current without diffusion limitation. These electrochemical characterizations demonstrates a significant influence of VO₂⁺ and TiO₂²⁺ cations on the disproportionation reaction of Mn³⁺.

3.3.2 Surface analysis of electrografted oxide layers

To study further the stabilizing role of TiO₂²⁺ and/or VO₂⁺ on the disproportionation process, we investigated the morphology and the chemical nature of the passivating layer formed at the electrode surface using Scanning Electron Microscopy (SEM) and X-ray Photoelectron Spectroscopy (XPS). The electrodeposition was performed at +1.8 V *vs.* SHE onto carbon felt and glassy carbon electrodes for each electrolyte in 5 M H₂SO₄. Only few traces of oxide layers were observed by SEM. XPS measurements did not give reliable results due to high signal-to-noise ratio in reason of the low amount of material.

To promote the formation of passivating layers, the sulfuric acid concentration was decreased to 50 mM to move the equilibrium of the disproportionation equilibrium (Eq. 3.1) towards MnO_2 formation and lower the solubility of oxides particles. For the Mn electrolyte, the carbon fibers were totally covered by MnO_2 flakes with an estimated thickness of 500 nm. The addition of titanium or vanadium reduced considerably the formation of MnO_2 , lowering the thickness of the oxide layer below 100 nm (Figure 3.2).

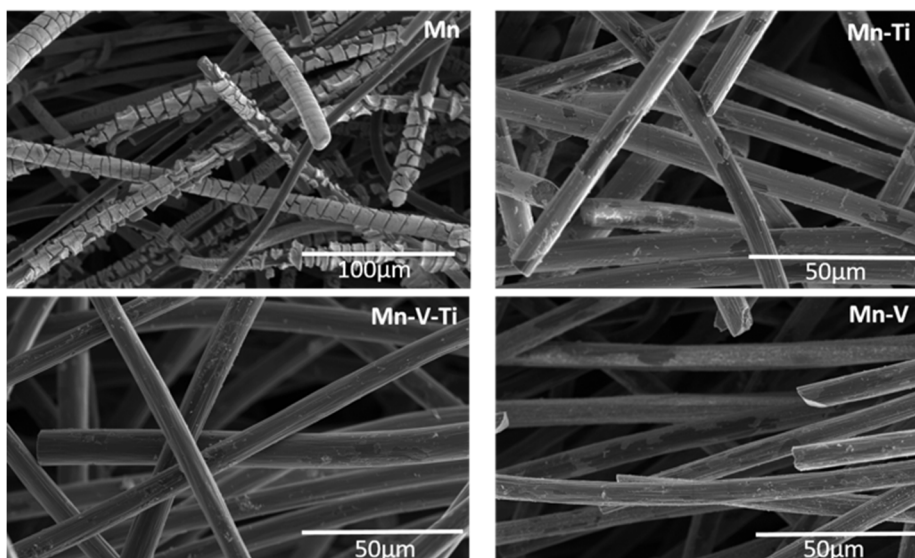


Figure 3.2 SEM images of electrodeposited oxide layers on carbon felt electrodes for Mn, Mn:Ti, Mn:V, and Mn:V:Ti electrolytes (3kV, 0.4 nA).

The same experiments on planar glassy carbon electrodes were performed and the resulting SEM pictures are shown in Figure 3.3. The deposition of MnO_2 in the presence of Mn created a thick layer in which cracks were observed. Cactus-like particles above 1 μm of diameter (inset, Figure 3.3) were observed as aggregates over the entire electrode surface, suggesting a nucleation/growth process. In the presence of TiO^{2+} , the amount of deposited oxide layer was reduced. The fluctuating contrast was attributed to variation in chemical composition, suggesting that the passivating layers are thin and do not cover the entire GC sublayers. Interestingly, Mn:V and Mn:V:Ti exhibited oxide layers with different structures, in which a rough surface and particles aggregation were observed on the whole electrode. This suggests another nucleation/growth mechanisms at the electrode surface along with the presence of different oxide species as compared to Mn and Mn:Ti electrolytes.

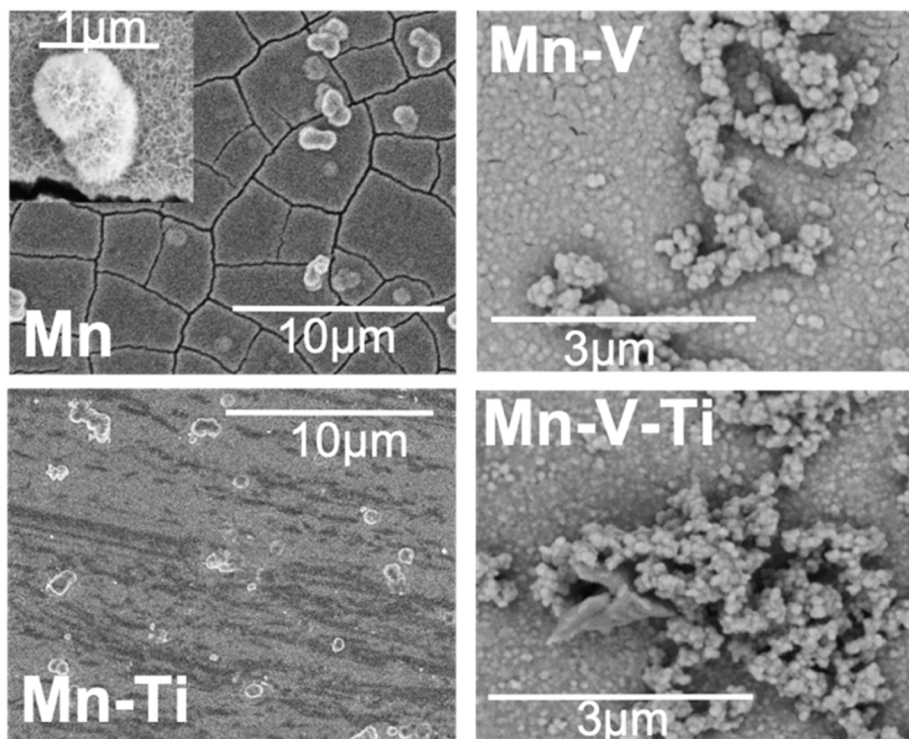


Figure 3.3 SEM images of electrodeposited manganese oxide layers on glassy carbon electrodes, obtained after electrolysis at +1.8 V vs. SHE, for Mn, Mn:Ti, Mn:V and Mn:V:Ti electrolytes (3kV, 25 pA). The inset on Mn shows the nuclei aggregates on the whole electrode surface.

To determine the chemical nature of the oxide layers observed by SEM, XPS was performed (Figure 3.4). The relative atomic concentrations (at.%) obtained at 50 mM H_2SO_4 for oxide layers-modified glassy carbon electrodes are reported in the Table 3.3. Binding energies of 642.37 and 654.11 eV were attributed respectively to $\text{Mn}2p_{3/2}$ and $\text{Mn}2p_{1/2}$ orbitals (Figure 3.4-A– Mn and Mn:Ti). Splitting energy of 4.7 eV, obtained for $\text{Mn}3s$ orbitals, correlates with the presence of MnO_2 (Figure 3.4-D).²⁰ This was in good agreement with the proposed EC_i mechanism that demonstrates electrode passivation by MnO_2 . For Mn:Ti, MnO_2 was also detected on the electrode surface (Figure 3.4-A and Figure 3.4-D). Additionally, a symmetric peak shape of $\text{Ti}2p$ orbitals at 458.24 and 463.88 eV, along with a splitting energy of 5.7 eV, were attributed to TiO_2 layers (Figure 3.4-C), accounting for +4 oxidation states. Thus, the passivating layer was a mixture of MnO_2 and TiO_2 , with relative atomic concentrations of 90 at.% of Mn and 10 at.% of Ti (Table 3.3). The presence of TiO_2 may not be a product of the Mn^{2+} - TiO^{2+} oxidation process, discussed in the previous section (Figure 3.1). TiO_2 was likely formed due to an excess of TiO^{2+} that could have been oxidized by the change of acidity of the

surface while preparing the samples for SEM and XPS. This suggests that Mn:Ti ratio is not optimal and could be adjusted.

Interestingly, with the presence of vanadium (Mn:V and Mn:Ti:V), no trace of MnO_2 was detected on the surface of the passivating layer. However, a satellite peak at 648 eV was observed in between $\text{Mn}2p_{1/2}$ and $\text{Mn}2p_{3/2}$ orbitals, which corresponds to the presence of MnO (Figure 3.4-B). This was confirmed by a splitting energy of 5.9 eV in between Mn3s orbitals (Figure 3.4-E), accounting for an oxidation state of +2.²¹ Furthermore, analysis of V2p orbitals resulted in asymmetric peaks at 517.02 and 524.52 eV, that are assigned to $2p_{3/2}$ and $2p_{1/2}$ orbitals, respectively. Splitting energy was found to be equal to 7.4 eV, suggesting the presence of V_2O_5 particles.²² In the case of Mn:V:Ti, TiO_2 oxide particles were additionally detected, after calculation of the splitting energy in between Ti2p orbitals (Figure 3.4-C).

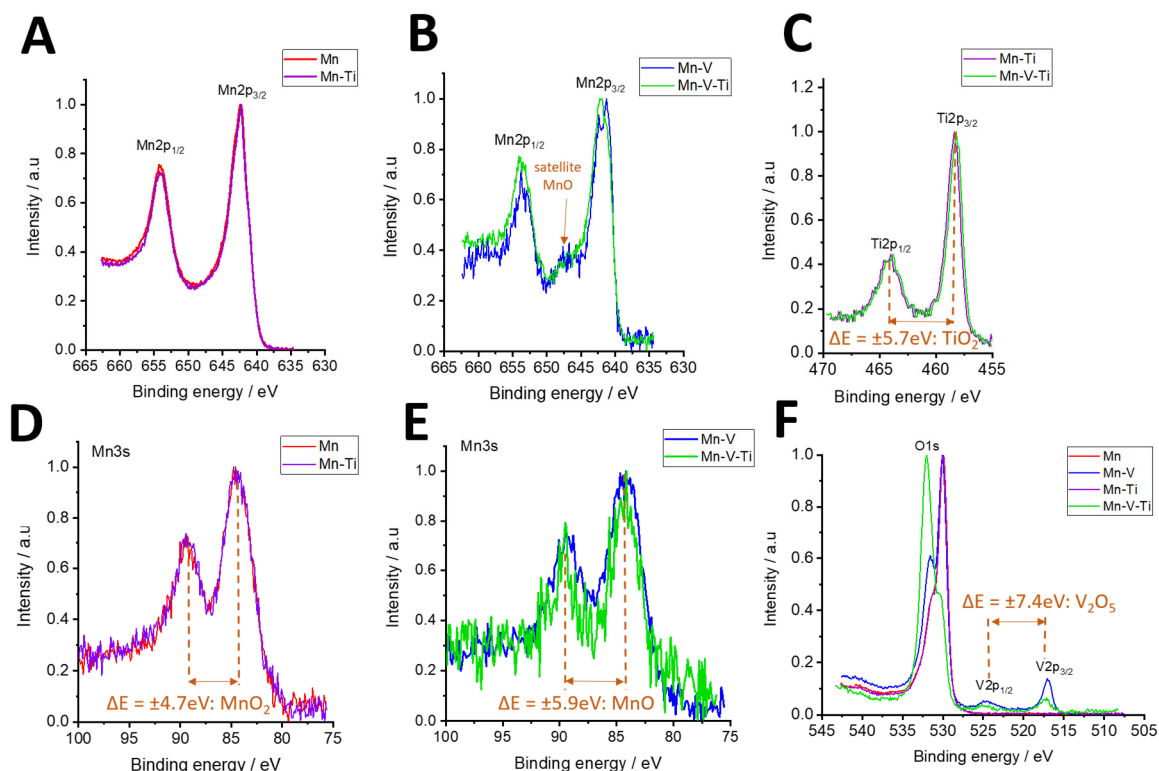


Figure 3.4 XPS spectra of the electrodeposited manganese oxide layers on glassy carbon electrode for Mn 2p orbitals (A and B), Mn3s orbitals (D and E), Ti 2p orbitals (C) and V2p, O1s orbitals (F). The energy splitting interaction in between orbitals is reported on graph C to F.

For Mn:V, relative atomic concentrations of Mn and V were respectively measured to 89% and 11% (Table 3.3). The same explanation as for TiO_2 presence can be proposed for V_2O_5 detection, suggesting that Mn:V ratio is not ideal. For Mn:V:Ti, 47 at. % of Mn, 15 at. % of V

and 37 at.% of Ti were calculated. The higher relative atomic concentration of Ti in the case of Mn:V:Ti compared to the Mn:Ti electrolyte suggests that V may have more affinity in complexing Mn. However, it is worth mentioning that the relative atomic concentrations are quantitative, but it describes a specific region (where the XPS beam scanned the sample) and the results can vary according to the heterogeneity of the passivated layer.

The presence of MnO with vanadium additives was not well understood and seemed to be formed only at the electrode surface. We hypothesize that VO_2^+ influences the chemistry at the electrode surface due to an interaction with Mn^{2+} . Although no traces of MnO_2 particles was detected by XPS at the electrode surface, we found them directly in the bulk, as depicted in Figure 3.5. This suggests that the EC_i process previously described for the oxidation of Mn^{2+} still occurs in presence of vanadium. Additionally, the peak attributed to MnO_2 oxidation (Eq. 3.12) was observed for each electrolyte (Figure 3.1-E), although this oxidation peak was smaller in the presence of vanadium. The shape of the latter anodic signal differed while adding or not vanadium.

Without VO_2^+ , a peak comparable to a stripping was recorded, highlighting the presence of a deposited layer of MnO_2 on the electrode surface. When VO_2^+ was added, a signal closer to a plateau was observed, which could describe a diffusion-controlled oxidation due to the MnO_2 particles in suspension.

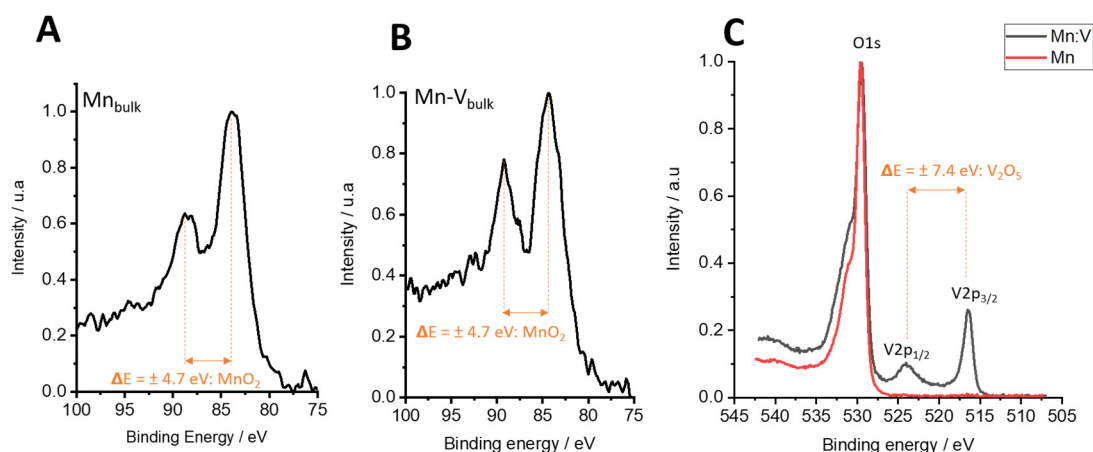


Figure 3.5 XPS spectrum of particles formed in the bulk after electrolysis of 100 mM of MnSO_4 and 100 mM of MnSO_4 + 50 mM V_2O_5 in 50 mM H_2SO_4 at +1.8V vs. SHE. In the region 100-75 eV, Mn3s orbital spectrum gives an energy splitting of 4.7 eV corresponding to MnO_2 . In the region 525-510 eV, orbitals corresponding to $\text{V}2p_{1/2}$ and $\text{V}2p_{3/2}$ were found for Mn:V with an energy splitting of 7.4 eV attributed to V_2O_5 . The relative atomic concentrations were found to be 25 at.% of Mn and 75 at.% of V for the particles formed into the Mn:V electrolyte.

Table 3.3 XPS relative atomic concentrations for oxide layers-modified glassy carbon electrodes formed in 50 mM H_2SO_4 as supporting electrolyte.

	Mn	Mn:Ti	Mn:V	Mn:V:Ti
Mn (at.%)	100	90	89	47
V (at.%)	-	-	11	15
Ti (at.%)	-	10	-	37

3.3.3 Study of Mn^{3+} disproportionation in solution by spectroelectrochemistry

Electrochemical investigations and oxide layers structural analysis were useful to address the electrochemical and chemical insights occurring for each electrolyte. Nevertheless, no clear conclusion could be made regarding the Mn^{3+} stability in solution by studying only the EC_i mechanism. In order to evaluate the stabilizing role of vanadium and titanium in preventing Mn^{3+} from disproportionation, spectroelectrochemical studies were performed at high acidic concentrations.

As shown on the UV-visible spectrum of Figure 3.6-A, the maximum absorption peak of Mn^{3+} in 5 M H_2SO_4 occurs at 490 nm, which is in accordance with values reported in literature.²³ After titanium and/or vanadium addition, maximum absorption peaks of Mn^{3+} were shifted above 500 nm suggesting chemical interactions between those cations, as already reported.²⁴ The following values were observed: : $\lambda_{\text{Mn}^{3+}}(\text{Mn}) = 490 \text{ nm}$, $\lambda_{\text{Mn}^{3+}}(\text{Mn:Ti}) = 517 \text{ nm}$, $\lambda_{\text{Mn}^{3+}}(\text{Mn:V}) = 500 \text{ nm}$, $\lambda_{\text{Mn}^{3+}}(\text{Mn:V:Ti}) = 506 \text{ nm}$.

As the absorbance of Mn^{3+} varies according to the nature of the electrolyte, it was necessary to determine the molar absorption extinction coefficient of Mn^{3+} ($\epsilon_{\text{Mn(III)}}$, λ_{max}) for each solution (Appendix III-2). To calculate those values, various solutions of Mn^{3+} were prepared by the electrochemical oxidation of 0.1 M Mn^{2+} solutions in 5 M H_2SO_4 . The exact concentration of Mn^{3+} was confirmed by iodometric titration. Finally, the extinction coefficient values were calculated using Lambert-Beer law: $\epsilon_{\text{Mn}^{3+}}(\text{Mn}) (490\text{nm}) = 108.3 \text{ L}\cdot\text{mol}^{-1}\cdot\text{cm}^{-1}$, $\epsilon_{\text{Mn}^{3+}}(\text{Mn:Ti}) (517\text{nm}) = 65.8 \text{ L}\cdot\text{mol}^{-1}\cdot\text{cm}^{-1}$, $\epsilon_{\text{Mn}^{3+}}(\text{Mn:V}) (500\text{nm}) = 84.52 \text{ L}\cdot\text{mol}^{-1}\cdot\text{cm}^{-1}$, $\epsilon_{\text{Mn}^{3+}}(\text{Mn-V-Ti}) (506\text{nm}) = 52.35 \text{ L}\cdot\text{mol}^{-1}\cdot\text{cm}^{-1}$.

To evaluate the disproportionation equilibrium (Eq. 3.1) for each electrolyte, solutions of Mn^{2+} in 5 M H_2SO_4 were electrolysed at +1.8 V vs. SHE, and the concentration of Mn^{3+} was monitored by UV-vis spectroscopy (Appendix III-3). Figure 3.6-B shows the resulting concentration of Mn^{3+} as a function of the amount of charge injected in the solution during the electrolysis. The black dotted line follows the ideal scenario in which no disproportionation would occur. In this case, the maximal concentration of Mn^{3+} (equivalent to the initial concentration of Mn^{2+}) would be reached after injecting exactly 241 C (e.g. – considering 25 mL of a 0.1 M Mn^{2+} solution in 5 M H_2SO_4). Any deviation below this line results from the disproportionation reaction of Mn^{3+} (Eq. 3.1) or/and other potential side reactions.

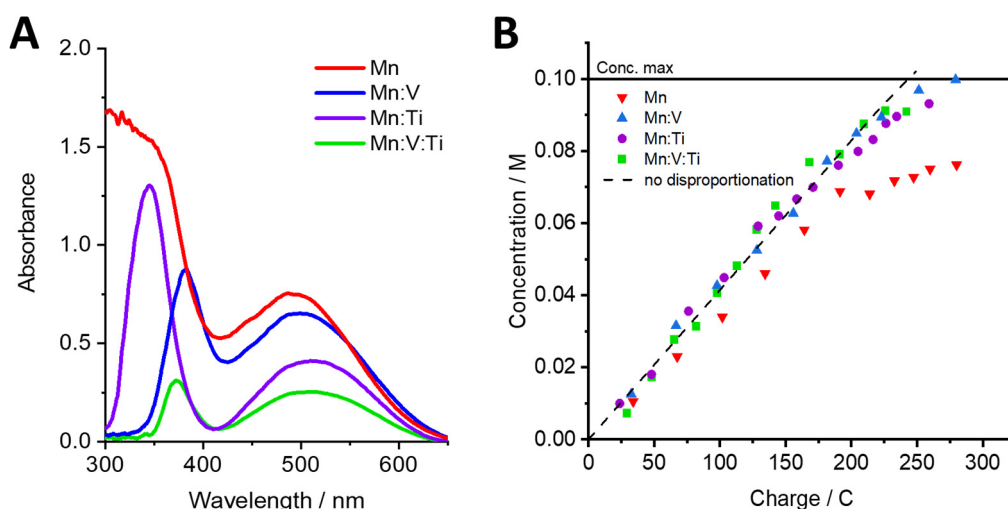


Figure 3.6 UV-visible spectra for 100 mM Mn^{3+} , 100 mM $\text{Mn}^{3+}\text{-TiO}^{2+}$ (1:1), 100 mM $\text{Mn}^{3+}\text{-VO}_2^+$, 100 mM $\text{Mn}^{3+}\text{-TiO}^{2+}\text{-VO}_2^+$ (1:1:1) (left) Concentration of Mn^{3+} measured by iodometric titration as a function of the amount of charge injected during the electrolysis at +1.8V vs. SHE of 40 mL of a solution of Mn^{2+} in 5 M H_2SO_4 .

Without any other metal ions, the deviation was very significant and Mn^{3+} concentration reached a threshold value around 0.075 M. At this concentration, the rate of disproportionation (Eq. 3.1) was equivalent to the rate of Mn^{3+} formation (Eq. 3.2), maintaining the concentration of Mn^{3+} constant. This indicates that 25 % of Mn^{3+} produced by electrolysis was involved in the disproportionation process. When TiO^{2+} or/and VO_2^+ were added in the electrolyte, Mn^{3+} concentration values above 0.09 M were reached, resulting in a net shift of the equilibrium towards Mn^{3+} and confirming the stabilizing effect of TiO^{2+} and VO_2^+ additives. In this case, less than 10% of Mn^{3+} disproportionated. No additional improvement in terms of stabilization was observed by combining the two additives. The main results are reported in Table 3.4.

Table 3.4 Summary of values obtained after spectroelectrochemistry for the different electrolytes in 5 M H_2SO_4 .

	Mn	Mn:Ti	Mn:V	Mn:V:Ti
$\lambda \setminus \text{nm}$	490	517	500	506
$\varepsilon_{\text{Mn}^{3+}} \setminus \text{M}^{-1} \cdot \text{cm}^{-1}$	108.3	65.8	84.5	52.4
$c_{\text{Mn}^{3+},\text{eq}} \setminus \text{M}$	≈ 0.075	>0.090	>0.090	>0.090

For the first time, VO_2^+ was demonstrated as an excellent stabilizing agent for Mn^{3+} in acidic conditions. Indeed, vanadium was shown to be as efficient as TiO^{2+} to reduce Mn^{3+} disproportionation.

3.4 Conclusion

In this chapter, we investigated the stabilization of Mn^{3+} towards irreversible disproportionation to Mn^{2+} and MnO_2 with either TiO^{2+} or/and VO_2^+ at equimolar ratio in acidic conditions. Electrochemical characterizations highlighted the EC_i mechanism occurring during the oxidation of Mn^{2+} and resulting in electrode passivation. Hydrodynamic linear sweep voltammetry was performed for Mn, Mn:Ti, Mn:V and Mn:V:Ti, and the diffusion coefficients of Mn^{2+} were respectively calculated to $1.18 \cdot 10^{-6} \text{ cm}^2 \cdot \text{s}^{-1}$, $1.66 \cdot 10^{-7} \text{ cm}^2 \cdot \text{s}^{-1}$, $3.68 \cdot 10^{-7} \text{ cm}^2 \cdot \text{s}^{-1}$, $1.64 \cdot 10^{-7} \text{ cm}^2 \cdot \text{s}^{-1}$. SEM and XPS experiments were performed to further study the chemical nature and the morphology of the passivating layer at the electrode. To promote the formation of the passivating layer, the experiments were performed at low acidic concentrations. A net decrease in the thickness of the oxide layer was observed with the presence of TiO^{2+} or/and VO_2^+ . Surprisingly, in the presence of VO_2^+ , MnO particles unlike MnO_2 were detected by XPS, suggesting a different chemistry at the electrode surface. However, traces of MnO_2 was still detected in the bulk. Additionally, TiO_2 and V_2O_5 was respectively detected in presence of Ti^{4+} and VO_2^+ and might be formed due to an excess of metal ions that could have been oxidized by the change of acidity of the surface.

Spectroelectrochemical analyses were performed for each electrolyte formulation. Without additives, the concentration of Mn^{3+} reached a threshold value of 0.075 M. In the presence of VO_2^+ and TiO^{2+} , the threshold concentration increased to a value beyond 0.09 M to onset the disproportionation, confirming the efficient stabilization of Mn^{3+} . Furthermore, the different

wavelengths corresponding to the maximum absorbance of Mn^{3+} between each electrolyte suggested a complexation of Mn^{3+} with TiO^{2+} and/or VO_2^+ *via* possible oxo-bridge.

Overall, VO_2^+ was observed to enhance the stability of Mn^{3+} as compared to TiO^{2+} , which is of high interest for the development of the vanadium-manganese redox dual-flow battery applications. In fact, Mn:V electrolyte could be used instead of Mn:Ti as the positive side of the Mn-V RFB, minimizing crossover issues and economical aspects. The stabilization of the Mn^{3+} would decrease the MnO_2 particles formation and minimize pressure drop, electrode passivation, capacity loss.

References

- (1) Colli, A. N.; Peljo, P.; Girault, H. H. High Energy Density $\text{MnO}_4^-/\text{MnO}_4^{2-}$ Redox Couple for Alkaline Redox Flow Batteries. *Chemical Communications* **2016**, 52 (97), 14039–14042. <https://doi.org/10.1039/C6CC08070G>.
- (2) He, Z.; Jin, G.; Gao, C.; Chen, Y.; Han, H.; Liu, J. A New Redox Flow Battery of High Energy Density with V/Mn Hybrid Redox Couples. *Journal of Renewable and Sustainable Energy* **2014**, 6 (5), 053124. <https://doi.org/10.1063/1.4898368>.
- (3) Xue, F.-Q.; Wang, Y.-L.; Wang, W.-H.; Wang, X.-D. Investigation on the Electrode Process of the Mn(II)/Mn(III) Couple in Redox Flow Battery. *Electrochimica Acta* **2008**, 53 (22), 6636–6642. <https://doi.org/10.1016/j.electacta.2008.04.040>.
- (4) Lee, H. J.; Park, S.; Kim, H. Analysis of the Effect of MnO_2 Precipitation on the Performance of a Vanadium/Manganese Redox Flow Battery. *Journal of The Electrochemical Society* **2018**, 165 (5), A952–A956. <https://doi.org/10.1149/2.0881805jes>.
- (5) Reynard, D.; Dennison, C. R.; Battistel, A.; Girault, H. H. Efficiency Improvement of an All-Vanadium Redox Flow Battery by Harvesting Low-Grade Heat. *Journal of Power Sources* **2018**, 390, 30–37. <https://doi.org/10.1016/j.jpowsour.2018.03.074>.
- (6) Reynard, D.; Vrabel, H.; Dennison, C. R.; Battistel, A.; Girault, H. On-Site Purification of Copper-Contaminated Vanadium Electrolytes by Using a Vanadium Redox Flow Battery. *ChemSusChem* **2019**, 12 (6), 1222–1228. <https://doi.org/10.1002/cssc.201802895>.
- (7) Kaku, H.; Dong, Y.-R.; Hanafusa, K.; Moriuchi, K.; Shigematsu, T. Effect of Ti(IV) Ion on Mn(III) Stability in Ti/Mn Electrolyte for Redox Flow Battery. *ECS Transactions* **2016**, 72 (10), 1–9. <https://doi.org/10.1149/07210.0001ecst>.
- (8) Dong, Y.-R.; Kawagoe, Y.; Itou, K.; Kaku, H.; Hanafusa, K.; Moriuchi, K.; Shigematsu, T. Improved Performance of Ti/Mn Redox Flow Battery by Thermally Treated Carbon Paper Electrodes. *ECS Transactions* **2017**, 75 (18), 27–35. <https://doi.org/10.1149/07518.0027ecst>.
- (9) Dong, Y.-R.; Kaku, H.; Hanafusa, K.; Moriuchi, K.; Shigematsu, T. A Novel Titanium/Manganese Redox Flow Battery. *ECS Transactions* **2015**, 69 (18), 59–67. <https://doi.org/10.1149/06918.0059ecst>.
- (10) Tokuda, K.; Iihara, J.; Saito, Y.; Masuno, A.; Inoue, H. Structural Analysis of Sulfuric Acid Solutions Containing Ti and Mn Using X-Ray Diffraction, x-Ray Absorption Fine Structure, and Molecular Dynamics Simulation. *The Journal of Chemical Physics* **2018**, 149 (1), 014503. <https://doi.org/10.1063/1.5024950>.
- (11) Rubio-Garcia, J.; Kucernak, A.; Zhao, D.; Li, D.; Fahy, K.; Yufit, V.; Brandon, N.; Gomez-Gonzalez, M. Hydrogen/Manganese Hybrid Redox Flow Battery. *Journal of Physics: Energy* **2018**, 1 (1), 015006. <https://doi.org/10.1088/2515-7655/aaee17>.
- (12) Nijjer, S.; Thonstad, J.; Haarberg, G. M. Oxidation of Manganese(II) and Reduction of Manganese Dioxide in Sulphuric Acid. *Electrochimica Acta* **2000**, 46 (2–3), 395–399. [https://doi.org/10.1016/S0013-4686\(00\)00597-1](https://doi.org/10.1016/S0013-4686(00)00597-1).
- (13) Clarke, C. J.; Browning, G. J.; Donne, S. W. An RDE and RRDE Study into the Electrodeposition of Manganese Dioxide. *Electrochimica Acta* **2006**, 51 (26), 5773–5784. <https://doi.org/10.1016/j.electacta.2006.03.013>.
- (14) Kao, W.-H.; Weibel, V. J. Electrochemical Oxidation of Manganese(II) at a Platinum Electrode. *Journal of Applied Electrochemistry* **1992**, 22 (1), 21–27. <https://doi.org/10.1007/BF01093007>.

-
- (15) Petitpierre, J.-Ph.; Comninellis, Ch.; Plattner, E. Oxydation Du MnSO_4 en dioxyde de manganese dans H_2SO_4 30%. *Electrochimica Acta* **1990**, 35 (1), 281–287. [https://doi.org/10.1016/0013-4686\(90\)85071-T](https://doi.org/10.1016/0013-4686(90)85071-T).
- (16) Huang, W.; Li, J.; Xu, Y. Nucleation/Growth Mechanisms and Morphological Evolution of Porous MnO_2 Coating Deposited on Graphite for Supercapacitor. *Materials* **2017**, 10 (10), 1205. <https://doi.org/10.3390/ma10101205>.
- (17) Moyer, L. *Advanced Inorganic Chemistry*; World Technologies: S.l., 2014.
- (18) Lawton, J.; Tiano, S.; Donnelly, D.; Flanagan, S.; Arruda, T. The Effect of Sulfuric Acid Concentration on the Physical and Electrochemical Properties of Vanadyl Solutions. *Batteries* **2018**, 4 (3), 40. <https://doi.org/10.3390/batteries4030040>.
- (19) Gorlin, Y.; Chung, C.-J.; Nordlund, D.; Clemens, B. M.; Jaramillo, T. F. Mn_3O_4 Supported on Glassy Carbon: An Active Non-Precious Metal Catalyst for the Oxygen Reduction Reaction. *ACS Catalysis* **2012**, 2 (12), 2687–2694. <https://doi.org/10.1021/cs3004352>.
- (20) Biesinger, M. C.; Payne, B. P.; Grosvenor, A. P.; Lau, L. W. M.; Gerson, A. R.; Smart, R. St. C. Resolving Surface Chemical States in XPS Analysis of First Row Transition Metals, Oxides and Hydroxides: Cr, Mn, Fe, Co and Ni. *Applied Surface Science* **2011**, 257 (7), 2717–2730. <https://doi.org/10.1016/j.apsusc.2010.10.051>.
- (21) Di Castro, V.; Polzonetti, G. XPS Study of MnO Oxidation. *Journal of Electron Spectroscopy and Related Phenomena* **1989**, 48 (1), 117–123. [https://doi.org/10.1016/0368-2048\(89\)80009-X](https://doi.org/10.1016/0368-2048(89)80009-X).
- (22) Biesinger, M. C.; Lau, L. W. M.; Gerson, A. R.; Smart, R. St. C. Resolving Surface Chemical States in XPS Analysis of First Row Transition Metals, Oxides and Hydroxides: Sc, Ti, V, Cu and Zn. *Applied Surface Science* **2010**, 257 (3), 887–898. <https://doi.org/10.1016/j.apsusc.2010.07.086>.
- (23) Maiti, K.; Sen, P. K.; Barik, A. K.; Pal, B. Influence of Microheterogeneous Environments of Sodium Dodecyl Sulfate on the Kinetics of Oxidation of L -Serine by Chloro and Chlorohydroxo Complexes of Gold(III). *J. Phys. Chem. A* **2018**, 122 (24), 5270–5282. <https://doi.org/10.1021/acs.jpca.8b02409>.
- (24) Selim, R. G.; Lingane, J. J. Coulometric Titration with Higher Oxidation States of Manganese. *Analytica Chimica Acta* **1959**, 21, 536–544. [https://doi.org/10.1016/0003-2670\(59\)80233-6](https://doi.org/10.1016/0003-2670(59)80233-6).

Appendix III

Appendix III-1: Koutecky-Levich analysis

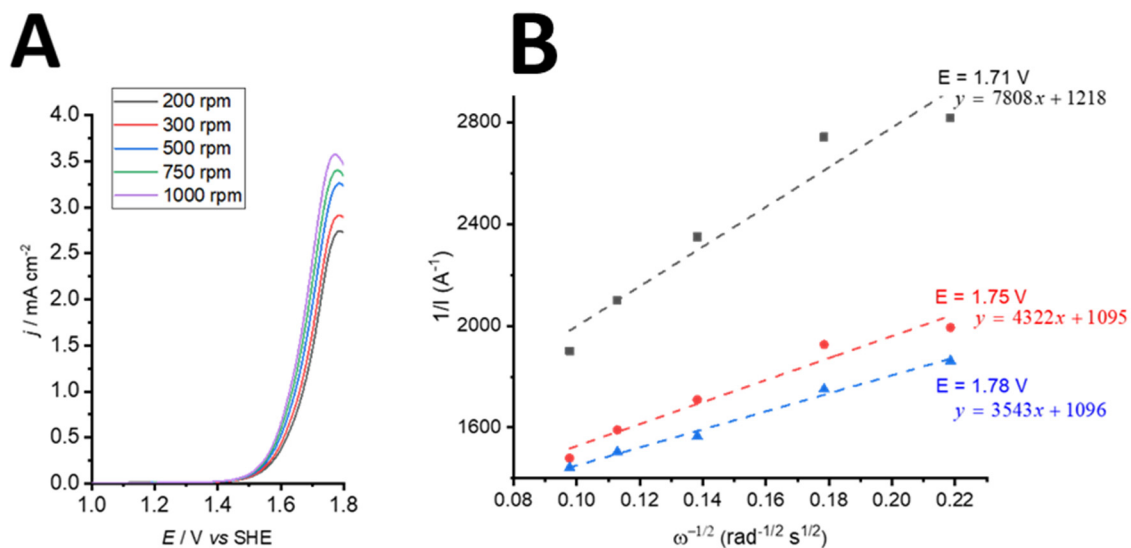


Figure A3.1 Linear sweep voltammetry of 100 mM Mn in 5 M H_2SO_4 performed at $10 \text{ mV} \cdot \text{s}^{-1}$ and different rotation rates using a glassy carbon rotating-disk electrode and corresponding Koutecky-Levich plots at different potential values.

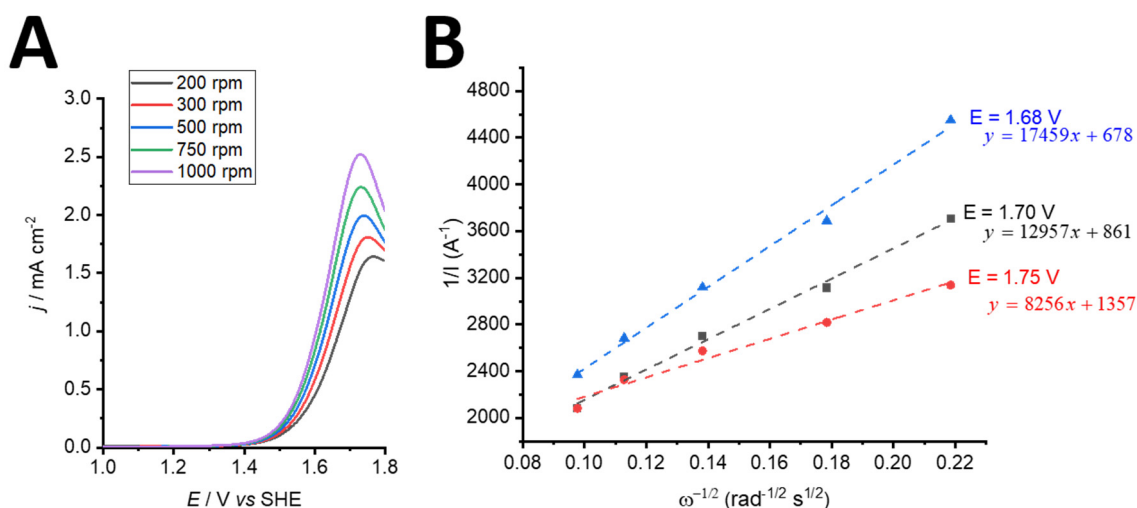


Figure A3.2 Linear sweep voltammetry of 100 mM Mn:Ti in 5 M H_2SO_4 performed at $10 \text{ mV} \cdot \text{s}^{-1}$ and different rotation rates using a glassy carbon rotating-disk electrode and corresponding Koutecky-Levich plots at different potential values.

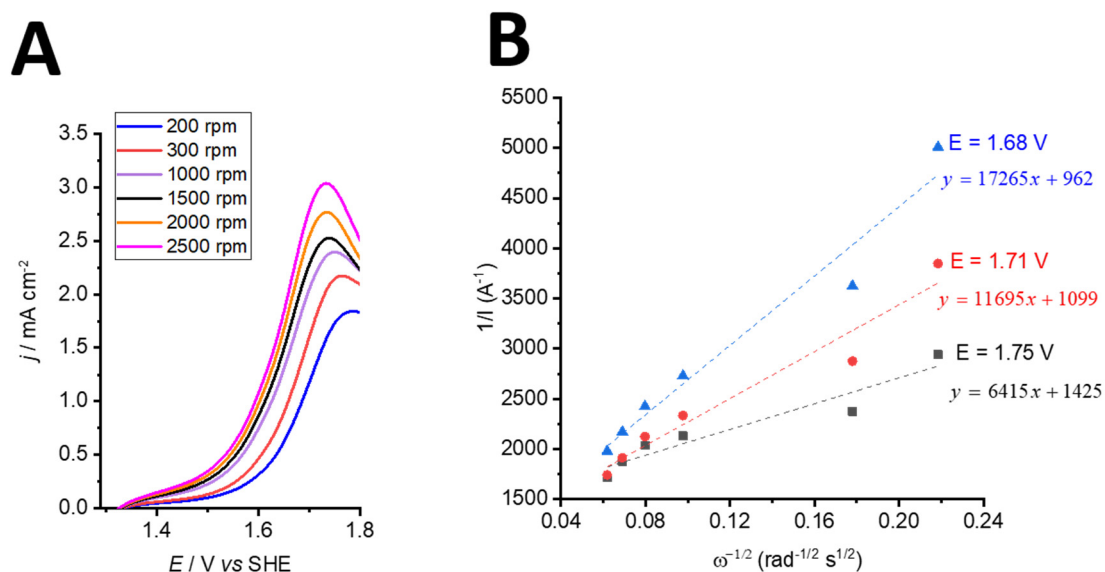


Figure A3.3 Linear sweep voltammetry of 100 mM Mn:V in 5 M H_2SO_4 performed at $10 \text{ mV}\cdot\text{s}^{-1}$ and different rotation rates using a glassy carbon rotating-disk electrode and corresponding Koutecky-Levich plots at different potential values.

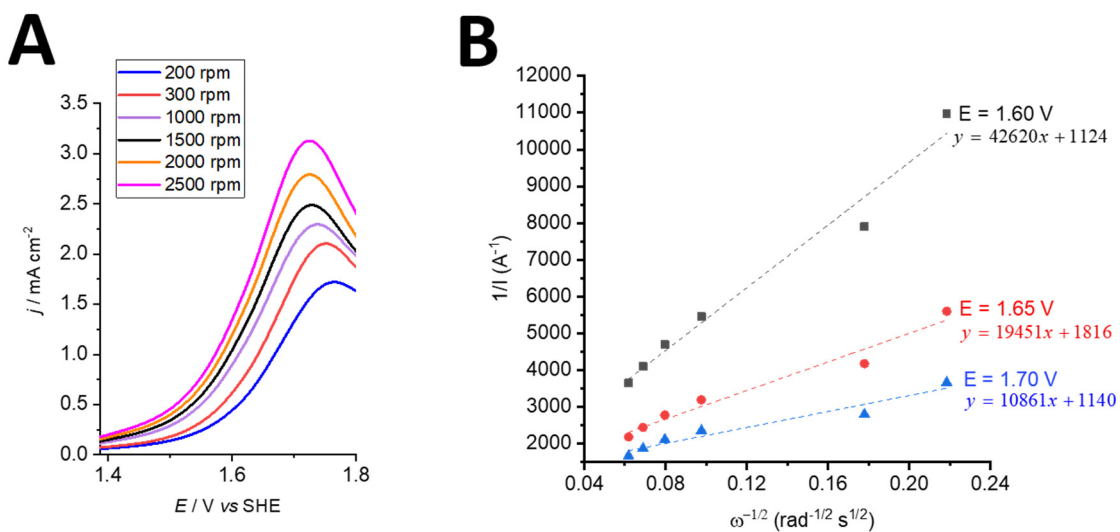


Figure A3.4 Linear sweep voltammetry of 100 mM Mn:V:Ti in 5 M H_2SO_4 performed at $10 \text{ mV}\cdot\text{s}^{-1}$ and different rotation rates using a glassy carbon rotating-disk electrode and corresponding Koutecky-Levich plots at different potential values.

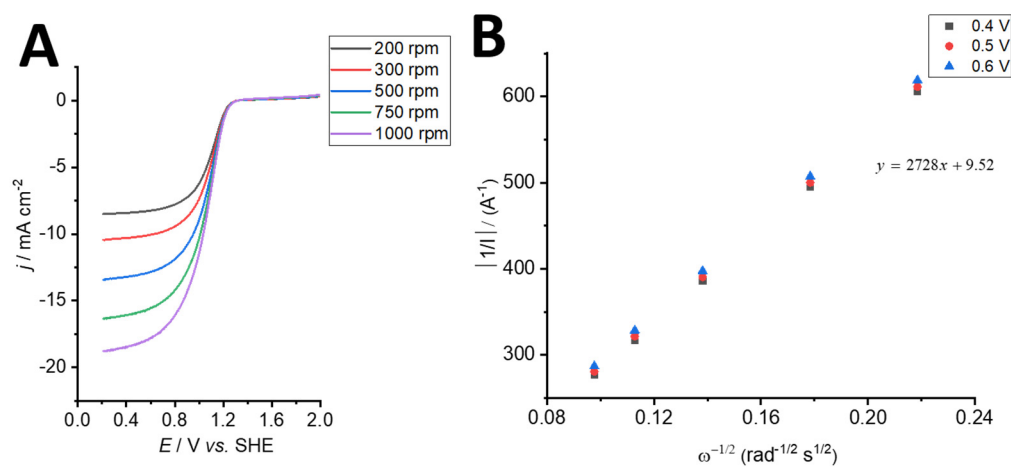


Figure A3.5 Linear sweep voltammetry of 100 mM V in 5 M H_2SO_4 performed at $10 \text{ mV} \cdot \text{s}^{-1}$ and different rotation rates using a glassy carbon rotating-disk electrode and corresponding Koutecky-Levich plots at different potential values.

Appendix III-2: Determination of molar absorption extinction coefficient of Mn^{3+}

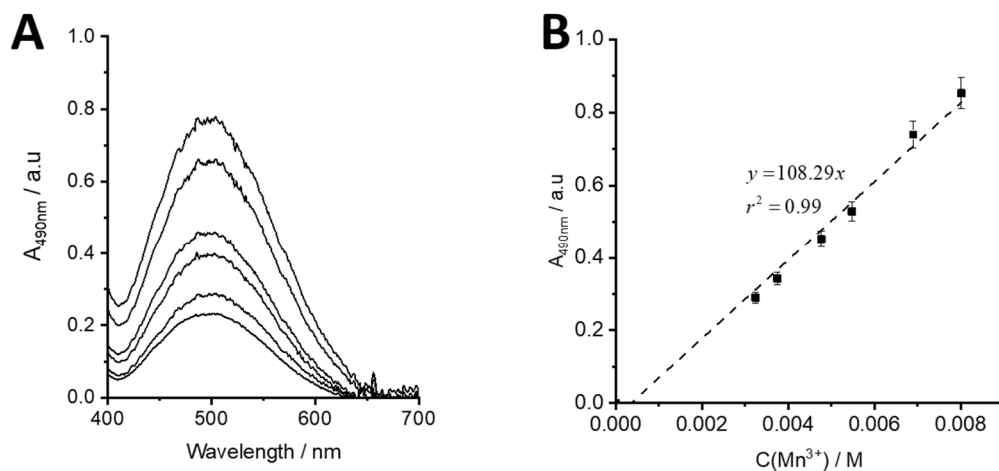


Figure A3.6 UV-vis spectra of Mn^{3+} solutions obtained by bulk-electrolysis of 100 mM MnSO_4 in 5 M H_2SO_4 and evolution of the absorbance at the maximum absorption peak of Mn^{3+} (relative to the electrolyte formulation) as a function of the concentration of Mn^{3+} , determined by iodometry.

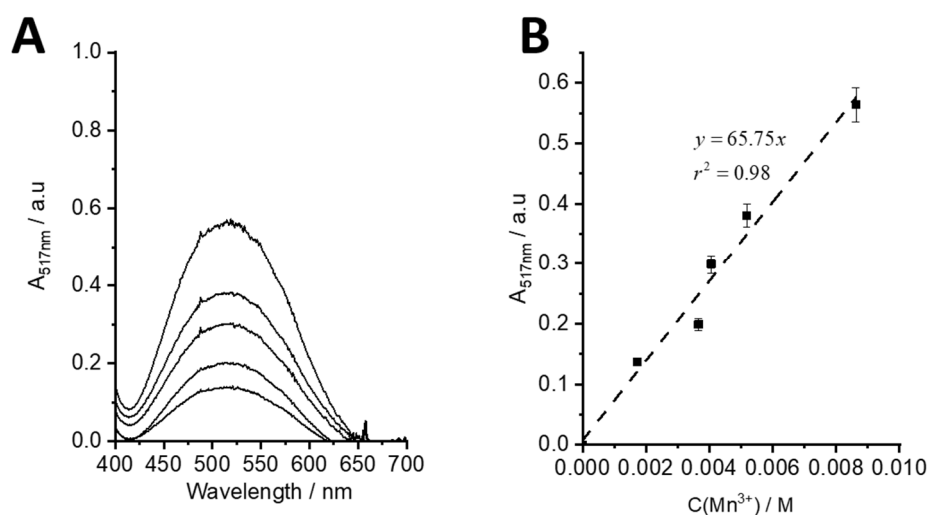


Figure A3.7 UV-vis spectra of Mn^{3+} - TiO^{2+} solutions obtained after bulk-electrolysis of 100 mM MnSO_4 + 100 mM TiOSO_4 solutions in 5 M H_2SO_4 and evolution of the absorbance at the maximum absorption peak of Mn^{3+} - TiO^{2+} (relative to the electrolyte formulation) as a function of the concentration of Mn^{3+} , determined by iodometry.

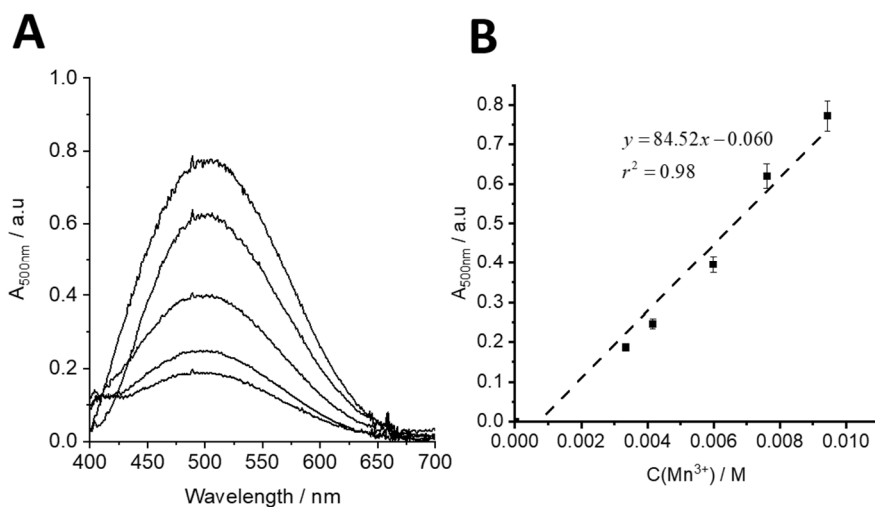


Figure A3.8 UV-vis spectra of Mn:V solutions obtained after bulk-electrolysis of 100 mM MnSO_4 + 50 mM V_2O_5 solutions in 5 M H_2SO_4 and evolution of the absorbance at the maximum absorption peak of $\text{Mn}^{3+}:\text{VO}_2^+$ (relative to the electrolyte formulation) as a function of the concentration of Mn^{3+} , determined by iodometry.

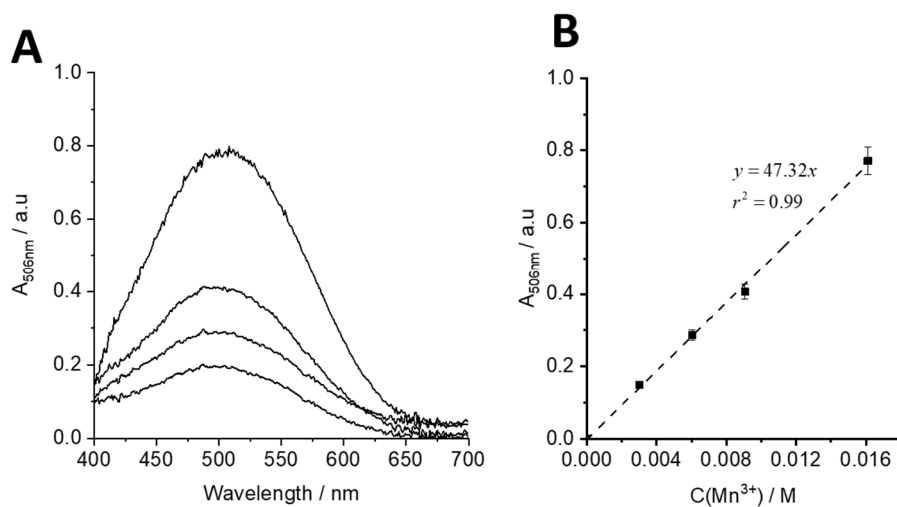


Figure A3.9 UV-vis spectra of Mn:V:Ti solutions obtained after bulk-electrolysis of 100 mM MnSO_4 + 50 mM V_2O_5 + 100 mM TiOSO_4 solutions in 5 M H_2SO_4 and evolution of the absorbance at the maximum absorption peak of $\text{Mn}^{3+}:\text{TiO}^{2+}:\text{VO}_2^+$ (relative to the electrolyte formulation) as a function of the concentration of Mn^{3+} , determined by iodometry.

Appendix III-3: UV-vis of spectroelectrochemical analysis

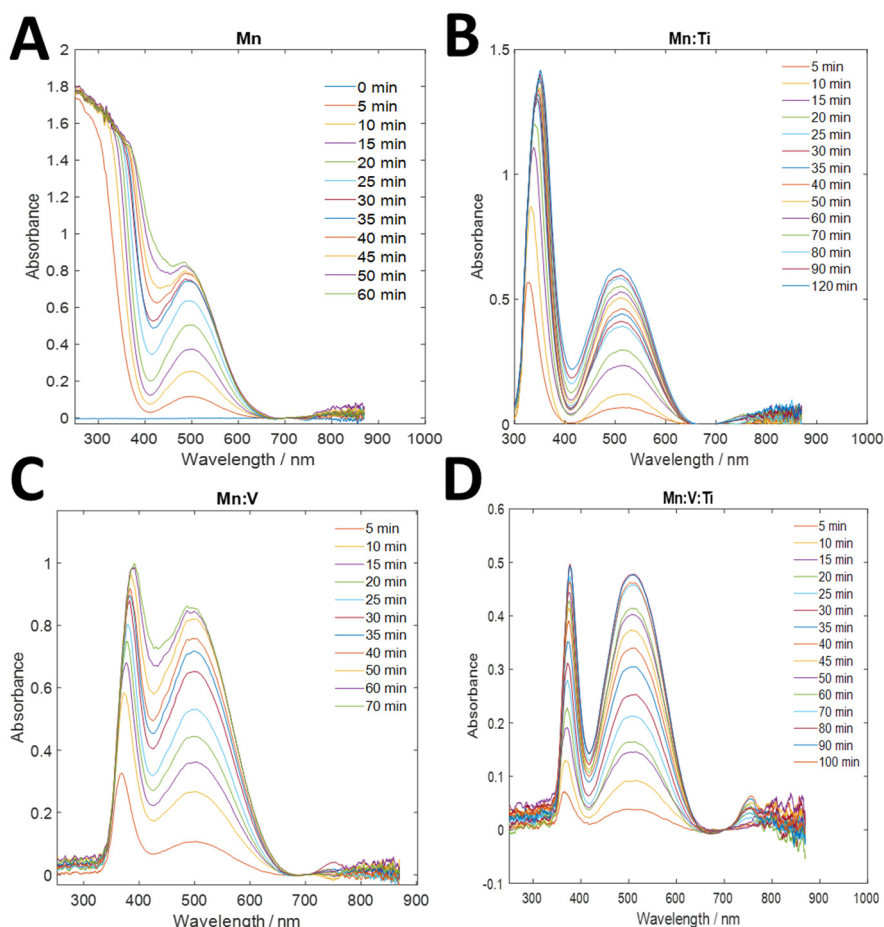
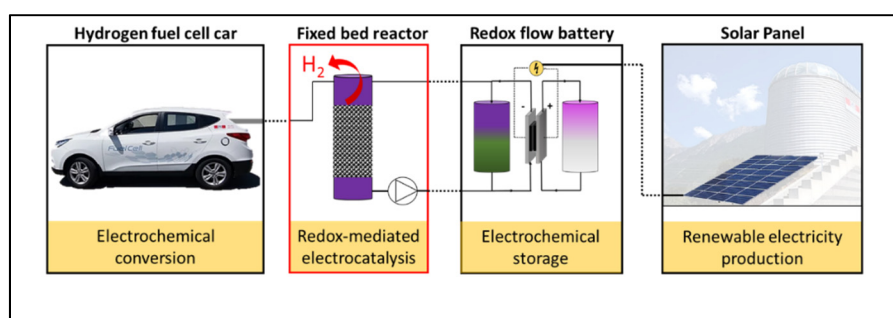


Figure A3.10 UV-vis spectra of Mn electrolyte along the time of the electrolysis at +1.8V vs. SHE of 40 mL of a solution of (A) 100 mM Mn^{3+} , (B) 100 mM Mn^{3+} - TiO^{2+} (1:1), (C) 100 mM Mn^{3+} - VO_2^+ (1:1), (D) 100 mM Mn^{3+} - TiO^{2+} - VO_2^+ (1:1:1) in 5 M H_2SO_4 (The background signal due to turbidity of the solution was removed at 700 nm).

CHAPTER IV

Kinetic model of redox-mediated hydrogen production

The results presented in this chapter are adapted with permission from D. Reynard, G. Bolik-Coulon, S. Maye, H. H. Girault, Hydrogen production on demand by redox-mediated electrocatalysis: A kinetic study Chemical Engineering Journal, 2020, 126721, DOI: 10.1016/j.cej.2020.126721, © 2020 The Authors. Published by Elsevier B.V. This is an open access article under the CC BY license.



Abstract

In this chapter, the vanadium-mediated hydrogen evolution over low-cost Mo_2C electrocatalyst of the proposed redox dual-flow battery is studied through the development of a reaction kinetics model. Based on a proposed mechanistic reaction scheme, a kinetic rate law is established as a function of the concentration of V^{2+} , the state-of-charge of the vanadium electrolyte from a vanadium redox flow battery and the amount of available catalytic sites on solid Mo_2C . Kinetic experiments in transient conditions reveals a first-order dependence on both the concentration of V^{2+} and the concentration of catalytic active sites and a power law with an exponential factor of 0.57 is measured on the molar ratio $\text{V}^{2+}/\text{V}^{3+}$, *i.e.* on the electrochemical driving force generated on the Mo_2C particles. The kinetic rate law is validated by studying the rate of reaction in steady-state conditions using a specially developed rotating ring-disk device (RRD) methodology. The kinetic model is demonstrated to be a useful tool to predict the hydrogen production *via* the chemical oxidation of V^{2+} over Mo_2C at low pH ($>1\text{ M H}_2\text{SO}_4$). For a perspective, the model is implemented in a semi-batch reactor. The simulations highlight the optimal state-of-charge (SOC) to carry out the reaction in an efficient way for a given demand in hydrogen.

4.1 Introduction

In the proposed vanadium-manganese redox dual-flow system, the negative and the positive charged redox species of a V-Mn RFB (*e.g.* negative side V^{3+}/V^{2+} , positive side Mn^{3+}/Mn^{2+}) can be employed as redox mediators (electron donor or acceptor) for respectively performing proton reduction and water oxidation.^{14,21,22} The reactions do not occur at the electrode surface, but are carried out in outer reservoirs on the surface of an appropriate solid electrocatalyst to increase the rate of the electron transfer reactions. Upon operation, the redox-mediated hydrogen evolution reaction is carried out over a molybdenum carbide (β - Mo_2C) electrocatalytic bed without the need of an additional energy input (spontaneous reaction). The resulting hydrogen evolution reaction is given by the following equation:



In order to use low-cost (precious-metal free) electrocatalysts for the proton reduction in acidic conditions, molybdenum-based electrocatalysts have been widely considered. Among these catalysts, MoS_2 was considered as a good alternative electrocatalyst to Pt-group towards HER.^{26–29} More recently, Vrubel and Hu investigated the use of a commercial molybdenum carbides (β - Mo_2C , hexagonal form) and have shown an even better stability and activity towards HER.³⁰ In the present work, a similar commercial molybdenum carbide (in the form of microparticles of 1 to 5 μm) was used as it was reported to be stable and active towards HER in both acidic and alkaline media.^{14,22,30} Peljo *et al.* operated the redox dual-flow battery at pilot scale with the same commercial Mo_2C catalyst (Figure 4.1) for more than six months without observable changes in activity.²³ The use of a low-cost catalyst is of particular interest in order to propose a system with high accessibility for industrial applications.

To control the production flow rate of hydrogen, it is necessary to understand the kinetic behind the vanadium-mediated process for HER. Previous studies revealed that the rate of electrocatalytic mediated-electron transfer depends on various parameters such as the availability of catalyst sites, the redox potential of the mediator solution and the reactants concentration.^{10,20} However, no clear determination of the kinetic rate law was established. In this chapter, we performed a complete kinetic and mechanistic study of the hydrogen evolution reaction *via* the chemical oxidation of V^{2+} over a commercial Mo_2C (β -form, hcp structure)^{22,30} by redox electrocatalysis. First, a kinetic rate law was established according to an assumed reaction mechanism. From this, the exponential factor associated to each kinetic parameter was

determined by hydrogen flow measurements. The proposed rate law was corroborated using an adapted rotating ring-disk device (RRD) technique that enables the study of the reaction at steady-state conditions and also a full characterisation of the redox electrocatalyst. Furthermore, a conversion study was performed to further confirm and enlarge the range of validity of the kinetic model. Finally, the developed kinetic model was implemented to simulate the process in a semi-batch reactor.

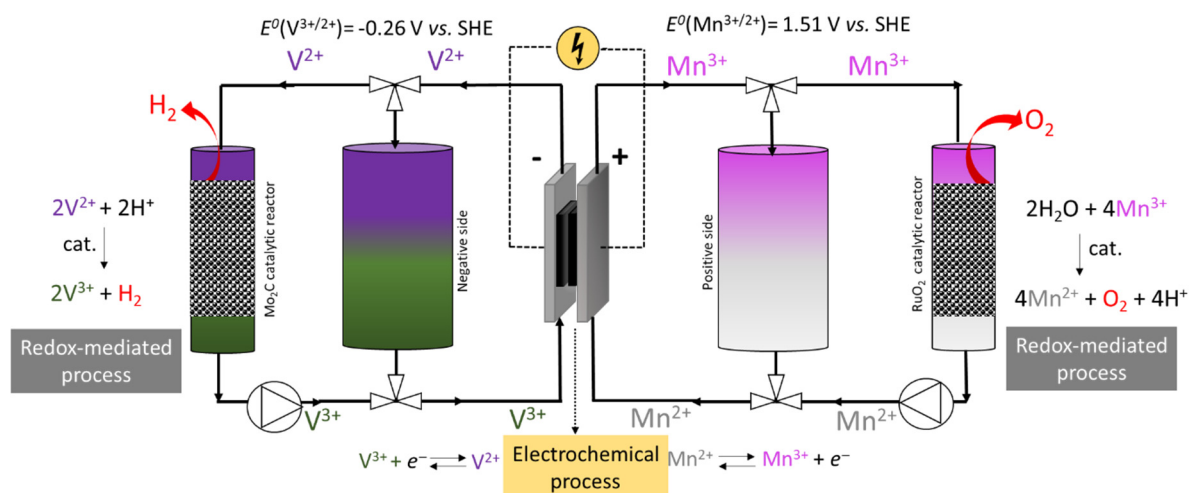


Figure 4.1 Schematic of a dual-circuit redox flow battery with V^{3+}/V^{2+} redox couple as redox mediators to perform proton reduction.

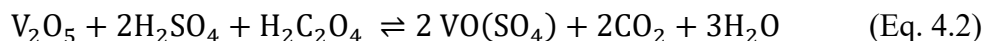
4.2 Experimental method

4.2.1 Chemicals

Dimethylformamide (DMF, 99.5%) was purchased from Roth and dried on 4 Å molecular sieves. Sulfuric acid (H_2SO_4 , 95-97%) was purchased from Merck and used without further purification. Nafion (20% w/w in EtOH) was purchased from Ion Power (D2020 Alcohol based 1000 EW) and used without further purification. Molybdenum carbide (Mo_2C , 99%, β -form, hcp structure^{22,30}), oxalic acid ($H_2C_2O_4$, 98%), hydrazine monohydrate ($N_2H_4 \cdot H_2O$, 64-65%), and vanadium oxide (V_2O_5 , 99.6%) were purchased from Sigma Aldrich and used without further purification.

4.2.2 Electrolyte synthesis

1.5 M of VO(SO₄) electrolyte solution in 2 M H₂SO₄ was synthesized *via* the chemical reduction of vanadium pentoxide by oxalic acid:



To prepare 500 mL of vanadium electrolyte, 68.25 g of V₂O₅ were placed in a triple-neck round-bottom flask and mixed with 100 mL of distilled water. 73.5 g of sulfuric acid were slowly added and the mixture was refluxed (115°C). 33.75 g of H₂C₂O₄ were carefully added (formation of a thick foam due to CO₂ production). To complete the reduction of V₂O₅, few drops of an aqueous solution of hydrazine (10% v/v) were slowly added. At the end of the reaction, the mixture was cooled down and filtered on ceramic. The solution was finally completed with distilled water. The obtained 1.5 M VO²⁺ solution was then electrolysed in a single-flow cell to prepare solution of 1.5 M V(II) (negative side) and 1.5 M VO₂⁺ (positive side) in 2 M H₂SO₄. Initially, 1 L of 1.5 M VO²⁺ was disposed within two reservoirs and the electrolytes were circulated through the cell with a peristaltic pump (Minipuls 3, Gilson), where oxidation and reduction respectively occur on the positive and the negative side. The electrolysis was performed at a constant cell potential of 1.6 V. The flow-cell was made of carbon felt electrodes (SGL GFD 5) and copper current collectors with a geometric surface area of around 550 cm². The membrane was of anion-exchange type (Fumatech 375-PP). These solutions were used for the preparation of all the other vanadium electrolytes.

4.2.3 Instrumentation

Electrochemical experiments were performed with an Autolab potentiostat PGSTAT204 (Metrohm) and with an Autolab bipotentiostat PGSTAT302N (Metrohm) while using the RRD device. A Biologic HCP-1005 (100A booster) was used for the electrolysis of the vanadium electrolyte. Hydrogen flows were recorded with a high-precision hydrogen thermal mass flow meter (Red-y smart meter GSM, ±1% accuracy) purchased from Vögtlin Instruments. SEM images were performed with a Teneo SEM (FEI, USA) equipped with a Schottky field emission gun. Secondary electron detection was carried out with an Everhart–Thornley detector and an in-lens detector. Optical imaging was conducted with a Keyence model VK-8710 Color 3D laser scanning microscopy. UV-vis measurements were performed with an Ocean Optics FLAME-S spectrometer.

4.2.4 Mo₂C film preparation

The RRD device consisted of a rotating ring-disk electrode (purchased from Metrohm) including a glassy-carbon disk and a platinum ring (disk diameter = 5 mm, gap between disk and ring = 0.375 mm, ring thickness = 0.375 mm, theoretical collection efficiency = 24.9%, thread = M4, shaft material: PEEK). The RRD electrode was first mechanically polished with 1 and 0.05 μm aluminium oxide (Al_2O_3 , 1.0 μm , purchased from Buehler) on 8'' microcloth PSA 10/PK (Buehler) and sonicated for 3 minutes in a solution of water:isopropanol (50:50). For the preparation of the Mo₂C film, 6 μL of an ink of the electrocatalyst in *N,N*-dimethylformamide (30 $\text{mg}\cdot\text{L}^{-1}$) was dropcasted on the glassy carbon of the GC-Pt RRD device (Glassy Carbon-Platinum Rotating Ring Disk) at a spinning rate of 300 rpm (catalyst loading of 5.97 $\text{mg}\cdot\text{cm}^{-2}$). The solvent was then evaporated at 10 mbar for 3 minutes. A 4 mm diameter circular pattern was used to avoid leak of the catalyst ink on the platinum ring. To enhance the stability, the Mo₂C film was covered with 25 μL of a solution of Nafion (2% wt in dry ethanol), evaporated at 10 mbar for 3 minutes.

An electrochemical benchmarking protocol was followed to characterize the Mo₂C film, especially the surface area, the catalytic activity and the stability of the film.³²

4.2.5 Kinetic study in transient conditions

To determine the dependence of the overall rate of the hydrogen generation reaction with the state-of-charge of the vanadium redox electrolyte, the concentration of V^{2+} and the amount of electrocatalyst, the chemical oxidation of various electrolyte solutions (Appendix IV-1) was studied by monitoring the hydrogen production flow. The chemical oxidations were performed in a 100 mL stirred-chemical reactor (Schott bottle) connected with PVDF tubing to a hydrogen flowmeter (5 $\text{mL}\cdot\text{min}^{-1}$ and 648 $\text{mL}\cdot\text{min}^{-1}$). The rate of reaction was measured according to:

$$r = \frac{dn_{\text{H}_2}}{dt} = \frac{\rho \dot{V}_{\text{H}_2}}{M_{\text{H}_2}} \quad (\text{Eq. 4.3})$$

where ρ is the volumetric mass density of hydrogen ($\text{g}\cdot\text{L}^{-1}$), \dot{V}_{H_2} is the volumetric flow of hydrogen ($\text{mol}\cdot\text{L}^{-1}$), and M_{H_2} is the molar mass of hydrogen ($\text{g}\cdot\text{mol}^{-1}$). For every experiment, the system was first purged with hydrogen and the sealing of the apparatus was checked with a gas leak detector. The catalyst powder was first well-dispersed in 2 M aqueous H_2SO_4 . The reaction was triggered by adding the vanadium electrolyte. The chemical reactor was kept under

stirring using a magnet (500 rpm). For the conversion study, 50 mL of V^{2+}/V^{3+} (1.44 M in 2 M H_2SO_4 , SOC= 85%) were oxidized on 25 ± 1 mg of molybdenum carbide mesh (powder ≤ 45 μm). To monitor the state of charge of the solution, samples were collected during the chemical oxidation and analysed by UV-vis spectroscopy in a 1 mm quartz cuvette. A filter (Xtra H-PTFE-20/25 purchased from Chromafil, 20 μm pore size) was used for the sampling to remove particles of Mo_2C . The UV-vis calibration curve was performed for absorbance (A) at wavelength (λ) of 400 nm for 1.44 M V^{2+}/V^{3+} in 2 M H_2SO_4 electrolyte solutions (SOC ranging from 20% to 100%). The background was adjusted using the isosbestic point at $\lambda = 725$ nm ($A=0.25$) (Appendix IV-2).

4.2.6 Kinetic study in steady-state conditions

All the RRD kinetic experiments at steady-state conditions were performed in an inert atmosphere at 20°C. The collection efficiency of H_2 produced on the disk and collected on the ring was determined electrochemically with the GC-Pt RRD (covered with a Nafion layer 25 μL of 2% wt in dry ethanol) in a solution of 2 M aqueous H_2SO_4 at rotating speed of 2000 rpm. Chronoamperometry experiments were performed at different potentials comprised between -0.24 V and -0.29 V vs. SHE, while linear sweep voltammetry was performed at the ring from 0.1 V to 1.2 V vs. SHE with a scan rate of 50 $mV \cdot s^{-1}$. The anodic current at 0.2 V vs. SHE was plotted as a function of the resulting cathodic current on the disk, with the slope indicating the collection efficiency.

The rate of reaction (Eq. 4.1) was studied for various vanadium solutions in 2 M H_2SO_4 : 150 mM V^{2+}/V^{3+} (15%, 25%, 35%, 45%, 55%, 65%, 75), 300 mM V^{2+}/V^{3+} (15%, 25%, 35%, 45%, 55%). After purging the electrolyte with Argon, the Mo_2C film RRD was immersed at a rotation rate of 2000 rpm and the platinum was linearly polarized from -0.1 V to 1 V vs. Ag|AgCl (sat. KCl) with a scan rate of 50 $mV \cdot s^{-1}$. Blank measurements were performed using the GC-Pt RRD electrode covered with Nafion to quantify the background signal due to V^{2+} oxidation on the platinum ring. The dependence of protons on the reaction was also evaluated by studying the reaction rate for 300 mM V^{2+}/V^{3+} (SOC= 35%) in various concentrations of H_2SO_4 (1000 mM, 1500 mM, 2000 mM).

4.3 Theoretical basis

In a redox-mediated process (Eq. 4.1), two distinct electron transfer reactions take place on a solid electrocatalyst particle, here the oxidation of V^{2+} (Eq. 4.4) and the reduction of protons (Eq. 4.5),²² and the role of the solid electrocatalysts is to cope with the different number of electrons for the two half-reactions:



where $k_{cat,a}$ is the rate constant of the anodic half-cell reaction and $k_{cat,c}$ is the rate constant of the cathodic half-cell reaction. Both half-cell reactions occur simultaneously and the electrocatalyst plays the role of a conductor of electrons that are supplied by the oxidation of V^{2+} and drawn by the reduction of the protons.

According to this reaction scheme, the rate law of the reaction of interest (Eq. 4.1) would be governed by the slowest step between the two half-cell reactions (rate-determining step). In terms of energy levels, the driving force of the mediated-electron transfer is set by the difference of the Fermi levels between the electrocatalytic material and that of the limiting redox couple determined by the Nernst equation. As shown in Figure 4.2, if the two-half reactions occur at different rates, the Fermi level of the catalyst particles equilibrates with the Fermi level of the electron in solution for the fastest redox couple.

As both half-reactions occur in the same potential range ($E_{V^{3+}/V^{2+}}^0 = -0.26$ V vs. SHE, $E_{H^{+}/H_2}^0 = 0$ V vs. SHE) on the Mo_2C electrocatalyst, it is difficult to isolate the kinetic parameters for each half-reaction using classical electrochemical methodologies (*e.g.* Butler-Volmer).

Considering the large excess of protons (due to the low solubility and stability of V^{2+} and V^{3+} redox species at low pH³³) composing the commercial vanadium electrolyte (~ 1.6 M V in 2M H_2SO_4) and the high activity of Mo_2C for HER³⁰, we assume that the half-reaction of V^{2+} oxidation is the rate-determining step and the mediated electron transfer follows the reaction scheme described in Figure 4.2-B. In other words, the overall reaction (Eq. 4.1) is pseudo-first order with respect to V^{2+} . Indeed, the oxidation of V^{2+} involves quite a solvent re-organization energy slowing down the electron transfer rate.

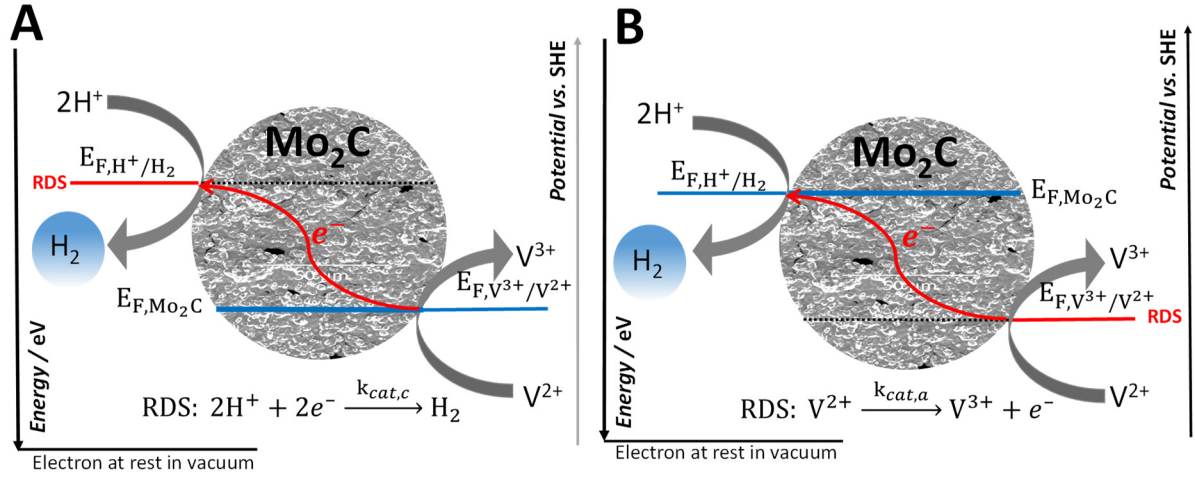


Figure 4.2 Fermi levels for the vanadium-assisted hydrogen evolution diagram over Mo₂C catalyst. (A) The proton reduction is the rate determining step, the Fermi level in the particle is fixed by the Nernst potential of V^{3+}/V^{2+} couple. (B) The oxidation of V^{2+} is the rate determining step, the Fermi level in the particle is fixed by the Fermi level of the electron in solution for the proton hydrogen reaction, *i.e.* by the Nernst potential of the proton/hydrogen reaction. Please note the axis for energy, lower energy on top, higher energy below.

Thereafter, the oxidation of V^{2+} (Eq. 4.4) is postulated to occur according to the following elementary steps:³⁴



where $*$ represents the catalytic active sites on the Mo₂C particles, k_1 , k_{-1} , k_2 are respectively the kinetic rate constants of the adsorption step, the desorption step and the electrochemical half-cell reaction of the adsorbed reactant (oxidation of $V^{2+,*}$). We assume that the adsorption equilibrium constant of H^+ remains constant due to the excess of protons in solution and the low solubility of H_2 (no accumulation). Thereby, the rate law of the reaction of interest (Eq. 4.1) is governed by the kinetic of the oxidation of V^{2+} at the catalytic surface (unimolecular surface reaction).^{34,35}

$$v_{cat,a} = k_2 \theta_{V^{2+}} [*] \quad (\text{Eq. 4.8})$$

Where $v_{cat,a}$ is the overall reaction rate, $\theta_{V^{2+}}$ is the fractional surface coverage (fraction of occupied sites = $[V^{2+,*}]/[*]$) and $[*]$ is the concentration of all active sites (occupied or not). Furthermore, the irreversible one-electron redox process of (Eq. 4.7) (oxidation of $V^{2+,*}$) is governed by the Butler-Volmer model and k_2 can be written as follows.^{36,37}

$$k_2 = k_2^0 e^{\frac{\alpha F(E-E_{eq})}{RT}} \quad (\text{Eq. 4.9})$$

where k_2^0 is the pre-exponential factor, α is the dimensionless charge transfer coefficient of the anodic reaction for the redox couple V^{3+}/V^{2+} , F is the Faraday constant ($96485 \text{ C}\cdot\text{mol}^{-1}$), R is the ideal gas constant ($8.314 \text{ J}\cdot\text{mol}^{-1}\cdot\text{K}^{-1}$), T is the temperature (K) and $E-E_{eq}$ is the overpotential (η) given by the difference between the Fermi level of the electrons in the electrocatalyst and the Fermi level of the electrons in solution associated to the redox couple V^{3+}/V^{2+} (*i.e.* Nernst potential). The overpotential generated at the electrocatalyst surface in (Eq. 4.9) is then the difference between the catalyst particle Fermi level (close to the equilibrium potential of H^+/H_2 , E_{H^+/H_2}) and the equilibrium potential generated by the redox couple V^{3+}/V^{2+} in solution:

$$E - E_{eq} \approx E_{H^+/H_2} - E_{V^{3+}/V^{2+}}^\circ - \frac{RT}{F} \ln \frac{[V^{3+}]}{[V^{2+}]} \quad (\text{Eq. 4.10})$$

where $[V^{2+}]$ and $[V^{3+}]$ are the molar concentrations of V^{2+} and V^{3+} ($\text{mol}\cdot\text{L}^{-1}$).

All in all, the Mo_2C microparticles behave as an electrode for which the potential is chemically set close to 0 V, and onto which V^{2+} is oxidized. (Eq. 4.10) is a key equation that reflects the importance of the redox-mediator potential in the kinetics. By analogy, the redox-mediator acts as a “liquid electrode” by accepting or giving electrons (electron donor in this particular case). By regrouping all the terms that are independent of the state-of-charge ($\text{SOC} = [V^{2+}]/([V^{2+}]+[V^{3+}])$) of the solution, in the pre-exponential factor (k_2^0), we can express k_2 as follows:

$$k_2 = k_2^0 e^{\frac{-\alpha F}{RT} \left(E_{V^{3+}/V^{2+}}^\circ - E_{\text{RHE}} + \frac{RT}{F} \ln \frac{[V^{3+}]}{[V^{2+}]} \right)} = A \left(\frac{[V^{2+}]}{[V^{3+}]} \right)^\alpha = A \left(\frac{\text{SOC}}{1-\text{SOC}} \right)^\alpha \quad (\text{Eq. 4.11})$$

where A is a kinetic factor that is temperature-dependent.

Then, if we apply the steady-state approximation to the intermediate $V^{2+,*}$, we have:

$$\frac{d[V^{2+,*}]}{dt} = 0 = k_1[V^{2+}][*](1-\theta_{V^{2+}}) - k_2\theta_{V^{2+}}[*] - k_{-1}\theta_{V^{2+}}[*] \quad (\text{Eq. 4.12})$$

$$\theta_{V^{2+}} = \frac{k_1[V^{2+}]}{k_1[V^{2+}] + k_{-1} + k_2} \quad (\text{Eq. 4.13})$$

From this point, we can then distinguish two cases:

1) **Limiting step: redox reaction of the adsorbed reactant** ($k_2 \ll k_1[V^{2+}], k_{-1}$)

$$v_{cat,a} \approx k' [V^{2+}]^\gamma [*] \quad \text{with} \quad \begin{cases} \gamma=1, k' = \frac{k_1}{k_{-1}} k_2 \text{ (low } [V^{2+}]) \\ \gamma=0, k' = k_2 \text{ (high } [V^{2+}]) \end{cases} \quad (\text{Eq. 4.14})$$

2) **Limiting step: adsorption/desorption** ($k_2 \gg k_1[V^{2+}], k_{-1}$)

$$v_{cat,a} \approx k' [V^{2+}]^\gamma [*] \quad \text{with} \quad k' = k_1, \gamma = 1 \quad (\text{Eq. 4.15})$$

Herein, we assume that the state-of-charge of the electrolyte would influence the kinetics of the overall rate of reaction (Eq. 4.1) and thus the rate law has to be governed by the oxidation of the adsorbed V^{2+} (Eq. 4.7). From the expression of k_2 described in (Eq. 4.11), the general rate law governing the reaction of interest (Eq. 4.1) can be expressed as follow:

$$v_{rxn} = k_{cat} \left(\frac{\text{SOC}}{1 - \text{SOC}} \right)^\alpha [V^{2+}]^\gamma [*] \quad (\text{Eq. 4.16})$$

Where k_{cat} is the reaction rate constant of redox-mediated process (Eq. 4.1) and γ is the associated reaction order with respect to $[V^{2+}]$.

4.4 Results and discussion

4.4.1 Kinetic experiments in transient conditions

A classical method to determine the kinetic parameters of the rate law consists in measuring the reaction rate by varying one kinetic parameter while keeping the others in large excess. At low pH, if the oxidation of V^{2+} is the rate-determining step, the kinetic of the overall reaction should be sensitive to the SOC of the vanadium electrolyte, the concentration of V^{2+} and the electrocatalyst load. Thus, the rate of reaction (v_{rxn}) was studied as a function of each kinetic parameters to determine the respective orders of reaction. The chemical oxidation of various V^{2+}/V^{3+} solutions in 2 M H_2SO_4 over Mo_2C were carried out in a stirred-tank reactor at room temperature by monitoring the hydrogen production with a flowmeter. The electrolytes were formulated in a way to maintain the same volume at the expense of the total vanadium concentration in order to ensure, within the reactor, both constant stirring and headspace (Appendix IV-1). The reactor was purged with hydrogen gas before triggering the reaction in the bulk. The initial flow rate was considered to calculate the various reaction orders. Figure

4.3 shows the dependence of the overall rate of reaction (Eq. 4.1) as a function of the concentration of V^{2+} (Figure 4.3-A), the SOC (Figure 4.3-B) and the mass of catalyst (Figure 4.3-C). The recorded hydrogen flowrate profiles along the chemical oxidation are available in the Appendix IV-1.

To determine the dependence of the overall rate on V^{2+} concentration, several electrolytes were prepared (0.025-0.50 M V^{2+} , 0.025-0.5 M V^{3+} , 2 M H_2SO_4) and chemically oxidized over 50 ± 1 mg of Mo_2C . In order to minimize the variation of the initial equilibrium potential of the electrolytes, the solutions were prepared by maintaining the state-of-charge at 0.5 ($[V^{2+}]=[V^{3+}]$). As shown in Figure 4.3-A, an apparent reaction order of $\gamma \approx 1$ was observed, which is the order expected for a one-electron transfer reaction with respect to the interfacial concentration of the adsorbed reactant ($V^{2+,*}$). The first-order dependence of overall reaction rate on V^{2+} is in agreement with the kinetic rate law proposed in (Eq. 4.16), with a dependence of k_{rxn} on the adsorption/desorption equilibrium. Then, the sensitivity of the reaction rate with the state-of-charge of the solution was evaluated by studying the chemical discharges over 50 ± 1 mg of Mo_2C electrocatalyst of various electrolyte solutions (0.15 M V^{2+} , 0.015-1.35 M V^{3+} , 2 M H_2SO_4) at SOC ranging from 20 to 90%. As shown in Figure 4.3-B, an apparent kinetic factor of $\alpha \approx 0.57$ was observed. The value is very close to the charge transfer coefficient reported in the literature³⁸ consolidating the hypothesis that the mediated electron transfer process is driven by the difference between the Fermi level of the Mo_2C electrocatalytic particles and that of the limiting redox couple potential V^{2+}/V^{3+} . Finally, the chemical oxidations of vanadium electrolyte solutions (0.375 M V^{2+} , 0.375 M V^{3+} , 2 M H_2SO_4) on various load of electrocatalyst ranging from 3 to 50 mg were carried out. As shown in Figure 4.3-C, an apparent exponential factor of 1 was extracted from the experimental data as predicted by the kinetic rate law. The results obtained under transient conditions reveal that the kinetic of the reaction (Eq. 4.1) fits well with the reaction scheme described in the kinetic model section.

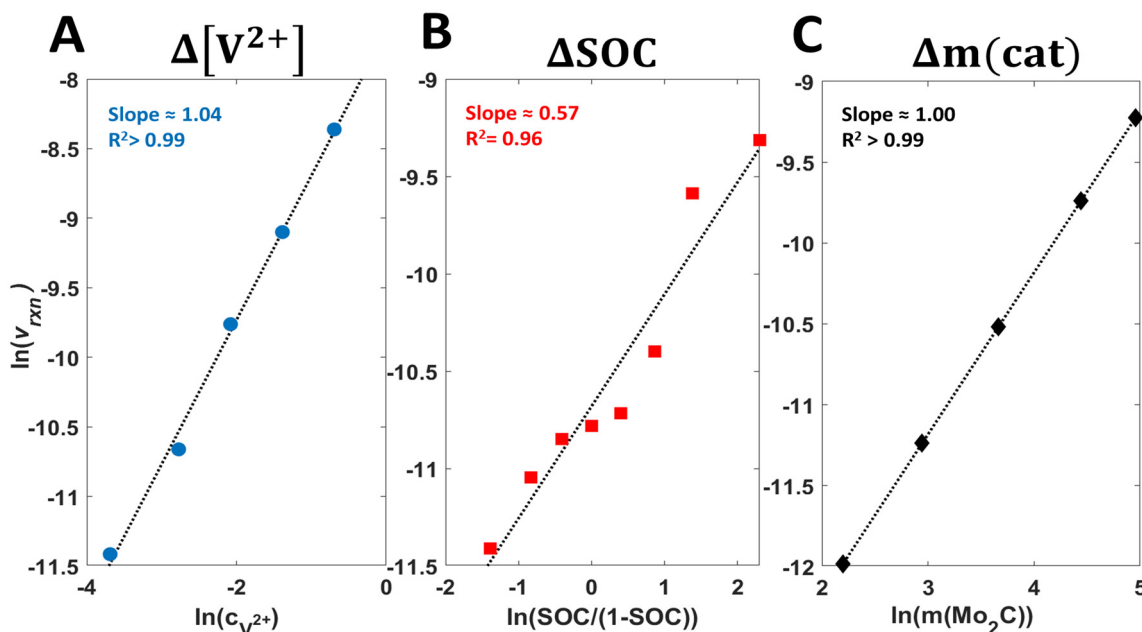


Figure 4.3 Dependence of the overall rate of reaction as a function of the kinetic parameters: (A) $\ln(v_{\text{rxn}})$ vs. $\ln(c_{V^{2+}})$ plot (B) $\ln(v_{\text{rxn}})$ vs. $\ln(\text{SOC}/(1-\text{SOC}))$ (C) $\ln(v_{\text{rxn}})$ vs. $\ln(m(\text{Mo}_2\text{C}))$. The slopes indicate the respective orders of reaction.

4.4.2 Kinetic experiments in steady-state conditions

4.4.2.1 Description of the RRD method

To validate the results obtained under transient conditions, we have developed a method using a rotating ring disk device to study the kinetic of the mediated electron transfer reaction in steady-state conditions under diffusion-controlled regime.

The approach consists in preparing a Mo_2C film-Pt RRD device by drop casting a catalyst ink on a commercial polished glassy carbon disk RRD electrode, **but not connected to a potentiostat** (Figure 4.5). It is important to notice that in the film, the Mo_2C microparticles do not need to be in electrical contact to each other, as each microparticle acts as an electrocatalyst. Next, we covered the Mo_2C film with a Nafion layer to enhance the short-term stability of the electrocatalytic surface. The Nafion layer was observed to be homogeneous with a thickness of $\sim 1.5 \mu\text{m}$. As depicted in Figure 4.4, while the bare electrode or the Mo_2C film is covered with a thin pure Nafion layer (where the diffusion layer of reacting species is smaller than that in the solutions), we keep a steady-state diffusion-controlled current with the thickness of the diffusion layer equal to the thickness of the membrane layer.³⁰

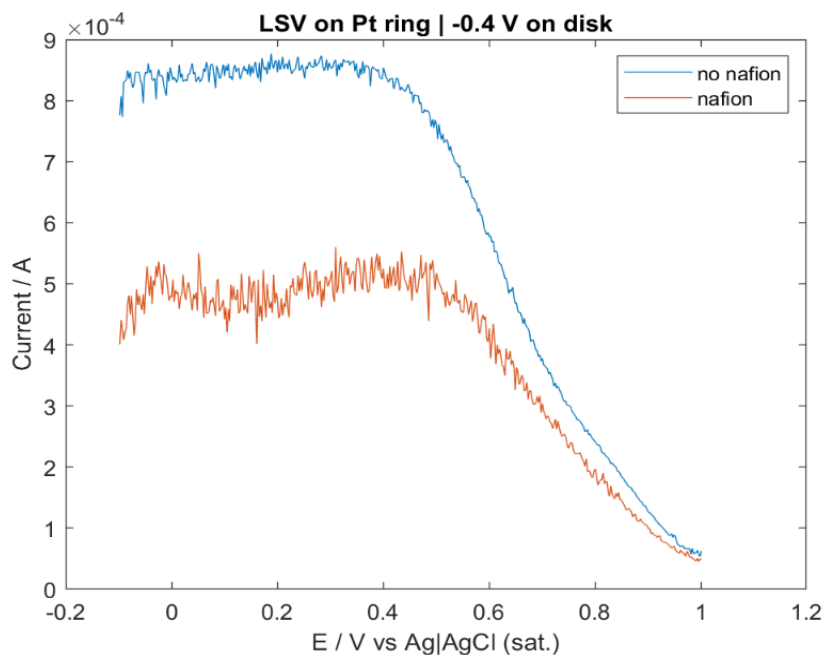
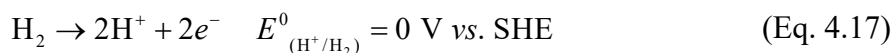


Figure 4.4 Linear sweep voltammetry between -0.2 to 1 V *vs.* Ag|AgCl (sat. KCl) on the ring while the disk potential is kept at -0.4 V *vs.* Ag|AgCl (sat. KCl) in presence and without Nafion.

The Mo₂C film-Pt RRD device is then immersed in the vanadium electrolyte (redox-mediator) to spontaneously trigger the mediated-electron transfer in the Mo₂C film. Under rotation, the hydrogen produced (Eq. 4.1) is circulated in a laminar flow from the electrocatalytic film to the platinum ring, where the potential is swept from 0.1 V to 1.2 V *vs.* SHE to oxidize back the hydrogen generated from the disk:



The resulting anodic signal at 0.2 V *vs.* SHE can be analysed to quantify the overall rate of the reaction occurring in the film according to the following equation:

$$v_{rxn} = \frac{I_{ring}}{n \cdot F \cdot CE} \quad (\text{Eq. 4.18})$$

where I_{ring} is the anodic current recorded on the ring at 0.2 V *vs.* SHE (A), n is the number of electrons involved in the electrochemical reaction, F is the Faraday constant ($96,485 \text{ C} \cdot \text{mol}^{-1}$) and CE is the experimental collection efficiency of the RRD device. The background current generated by the simultaneous V^{2+} oxidation on the ring was subtracted by carrying out blank experiments in the same conditions in the absence of the electrocatalyst. The interest of the method is to evaluate the kinetic of the mediated electron process under well-established steady-

state conditions and a constant catalytic activity in a controlled-diffusion regime. This improves considerably the control on the mass-transfer and kinetic parameters of the reaction. Furthermore, the activity, the surface and the stability of the electrocatalyst film can be precisely determined using electrochemical voltammetry.

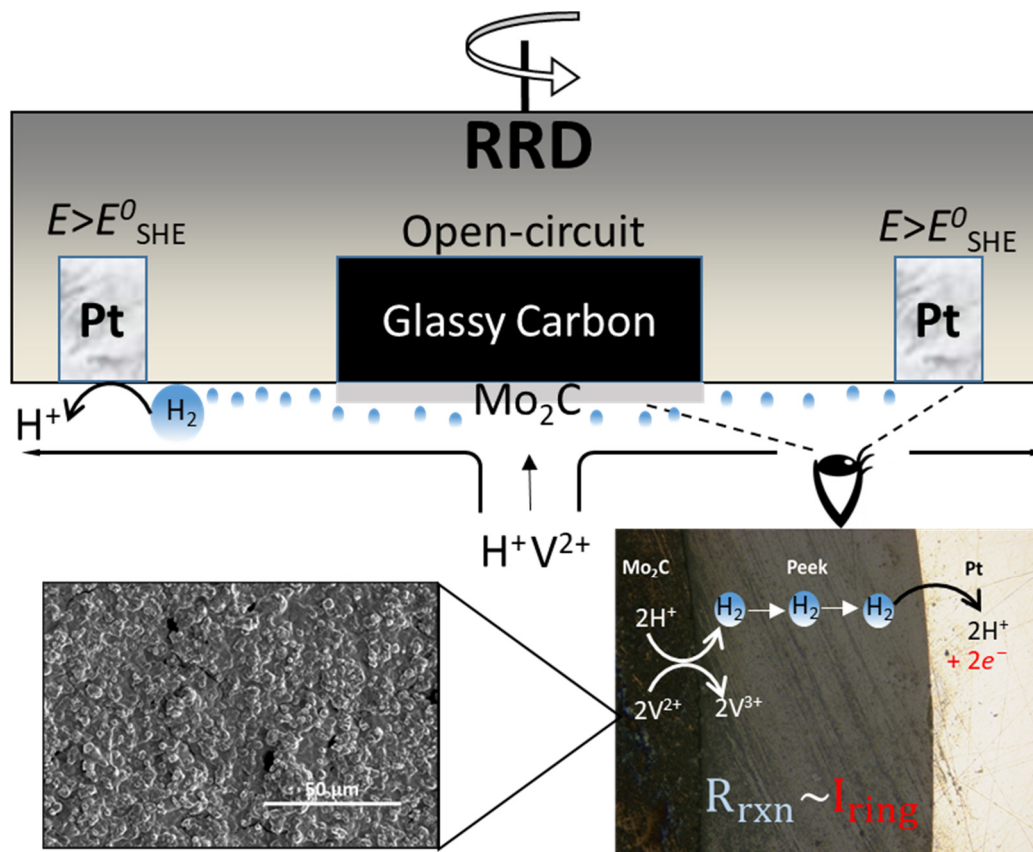


Figure 4.5 Schematic of the rotating ring disk device methodology used to study the kinetic of heterogeneous catalytic mediated-electron process at steady-state conditions.

4.4.2.2 Electrochemical characterization of Mo₂C film

Discrepancies of the activity of Mo₂C electrocatalyst towards HER were reported in the literature because of different catalyst sources and/or method preparation.^{39–41} In this chapter, a benchmarking protocol was followed to characterize the Mo₂C film, especially the surface area, the catalytic activity and the stability of the electrode.⁴² As comparison, the electrocatalytic performance of the Pt and the GC electrodes were also investigated. All the measurements were performed in a three-electrode cell set-up equipped with the working electrodes (GC, Pt or Mo₂C film), an Ag|AgCl (sat. KCl) reference electrode and a carbon felt counter electrode. The analyte was purged with Argon for 30 minutes prior to each set of experiments to remove

dissolved oxygen. All the experiments were carried out in aqueous acidic media (1M aqueous H_2SO_4 , pH=0) at a rotation rate of 2000 rpm.

The electrode surface area was estimated from the electrochemical double-layer capacitance (C_{dl}) and the specific capacitance of the electrode (C_s):

$$\text{Surface area} \approx \frac{C_{dl}}{C_s} \quad (\text{Eq. 4.19})$$

The double-layer capacitance of the catalytic surface was estimated using cyclic voltammetry (CV). Based on the CV measurements, the electrochemical capacitance was calculated from the dependence between the scan-rate and the non-faradaic current associated to the double-layer charging according to the following equation:

$$I_{nf} = \nu \cdot C_{dl} \quad (\text{Eq. 4.20})$$

where I_{nf} is the non-faradaic current (A) and ν is the scan rate ($\text{V} \cdot \text{s}^{-1}$).

Surface area

The surface area of each electrode was determined by carrying out cyclic voltammetry (CV) in a 0.1 V potential window centered on the open-circuit potential (OCP) (non-faradaic region). The CVs were conducted at 500 rpm for seven different scan rates: $0.05 \text{ V} \cdot \text{s}^{-1}$, $0.10 \text{ V} \cdot \text{s}^{-1}$, $0.20 \text{ V} \cdot \text{s}^{-1}$, $0.30 \text{ V} \cdot \text{s}^{-1}$, $0.40 \text{ V} \cdot \text{s}^{-1}$, $0.50 \text{ V} \cdot \text{s}^{-1}$, $0.60 \text{ V} \cdot \text{s}^{-1}$. The working electrode was held at each starting potential for 15 s before beginning a linear sweep polarization (LSV). The cyclic voltammograms were performed in the vicinity of the open-circuit potential for the GC, the Pt and the Mo_2C film electrodes and the resulting non-faradaic currents at the OCP value were plotted as a function of the scan rate (Figure 4.6), with the slopes revealing the double layer capacitance. The electrochemical double layer capacitance was measured to be $4.25 \mu\text{F}$ for the glassy carbon electrode, $3.77 \mu\text{F}$ for the Pt electrode and $20.7 \mu\text{F}$ for the Mo_2C film electrode. Using $C_s = 0.035 \text{ mF} \cdot \text{cm}^{-2}$ as a general specific capacitance in $1\text{M H}_2\text{SO}_4$,⁴² we estimated the catalytic surface area to 0.11, 0.12 and 0.59 cm^2 for the Pt, GC, and Mo_2C film electrodes, respectively. The surface area measured for the Mo_2C film was significantly larger due to the high porosity of the drop casted surface.

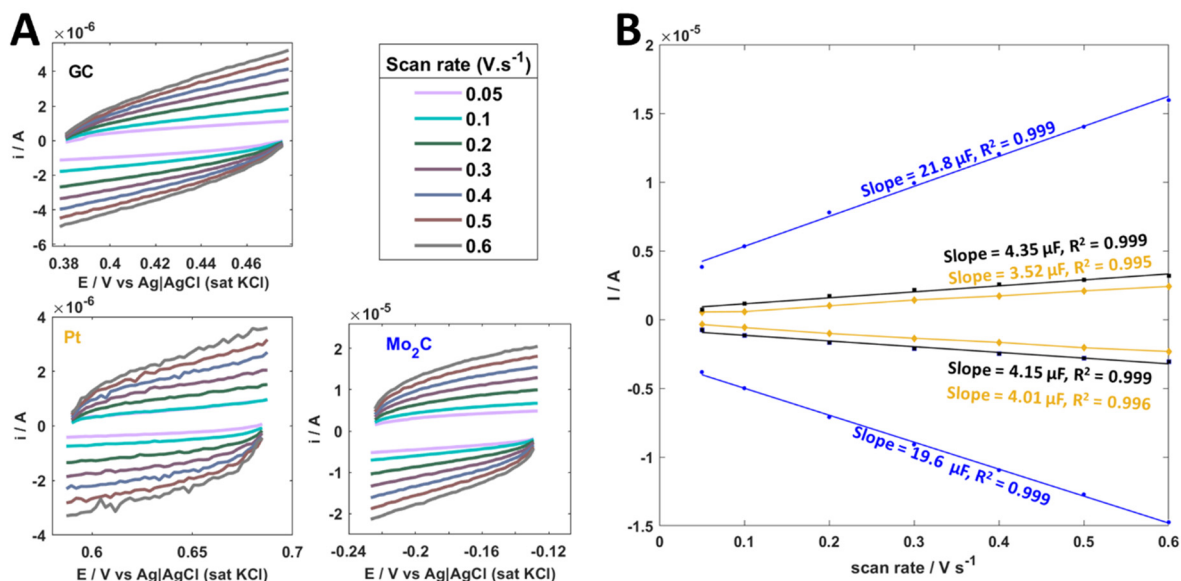


Figure 4.6 (A) Cyclic voltammograms at scan-rate comprised between 0.05 to 0.6 V·s⁻¹ in the following potential range: [OCP – 0.05 V, OCP + 0.05 V]. (B) Plots of the non-faradaic current measured at the OCP in function of the scan-rate for glassy carbon (black), platinum (yellow) and Mo₂C film (blue).

Mo₂C film catalytic activity

The catalytic activity of the Mo₂C film, Pt and GC electrodes towards HER was investigated in 1 M H₂SO₄ by LSV-based and EIS-based Tafel slopes analysis. Figure 4.7-A and Figure 4.7-C compare the polarization curves (LSV, scan rate of 0.005 V·s⁻¹) and the corresponding Tafel slopes for each electrocatalytic surface. In agreement with previous reports, Pt and GC electrode respectively exhibited polarization curve with onset overpotential of ~ 0 mV and ~ – 400 mV and a Tafel slope around 35 mV·dec⁻¹ and 169 mV·dec⁻¹.^{43,44} After drop-casting the commercial Mo₂C (β-form, hcp structure) on the glassy carbon disc (negligible activity towards HER in the vanadium solution), the onset potential was lowered to ~ –150 mV and a Tafel slope around 93 mV·dec⁻¹ was measured. Previous studies on Mo₂C electrocatalyst reported Tafel slope varying from 55 mV·dec⁻¹ to 120 mV·dec⁻¹, suggesting that hydrogen evolution on Mo₂C goes through a Volmer-Heyrovsky mechanism with the rate determining step that can be either the Volmer step or the Heyrovsky step.^{30,45–49} L. Ma *et al.* believes that the discrepancy between the reported Tafel slope for Mo₂C is related to the size of the catalytic particles that can differ substantially according to the electrode preparation.⁴⁷ To corroborate those results, electrochemical impedance spectroscopy (EIS) was performed for each electrode from 100 kHz to 1 Hz at selected potentials in the onset potential region of the studied electrode with a single modulated AC potential of 10 mV. Experimental data was fitted with the software Matlab™ (version

R2018a). Figure 4.7-B shows the recorded Nyquist plot for each electrode. In the case of GC and Pt, the Nyquist plot revealed the presence of a single semi-circle for each overpotential. A two-time constant model including a resistance R_s (representing the resistance between the reference and the working electrode) in series with a parallel constant phase element-resistance (CPE-R) representing the charge transfer resistance of the studied chemical reaction (HER) was used to fit the experimental data (Figure 4.8-A). For the Mo₂C film, the presence of a second semi-circle at high frequencies was observed, probably accounting for the surface porosity of the electrode. In this particular case, an additional CPE-R was used to build the equivalent circuit (Figure 4.8-B) for the fitting. The mass transfer resistance was neglected as we carried out the experiments in a dynamic mode. Interestingly, an inductive loop was observed at low frequencies on the Nyquist plot for the GC and the Mo₂C electrodes. This suggests that HER is going through Heyrovsky-Volmer mechanism with Heyrovsky step competing with Volmer step as the RDS.⁵⁰ The Tafel slopes were extracted by plotting the overpotential as a function of $\log(R_{ct}^{-1})$ (Figure 4.7-D) and were comparable to the values measured from the polarization curves, confirming the reasonable electrocatalytic activity of the Mo₂C film electrode toward HER.

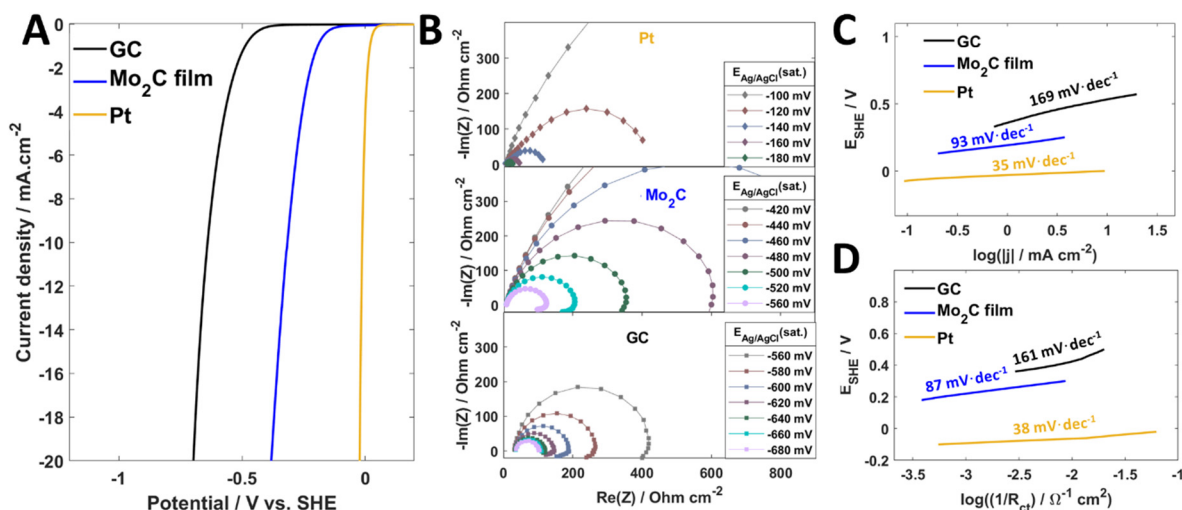


Figure 4.7 (A) Polarization curves in 1 M H₂SO₄ for GC (black), Pt (yellow) and Mo₂C film (blue) at a scan rate of 5 mV·s⁻¹ and a rotation speed of 3000 rpm. The reported potentials are corrected for the iR -drop. (B) Nyquist plot resulting from EIS experiments at selected overpotential and frequency ranging from 100 kHz to 100 mHz for each electrode at a rotation speed of 3000 rpm (C) Tafel slopes measured from LSV experiments (D) Tafel slopes measured from EIS experiments.

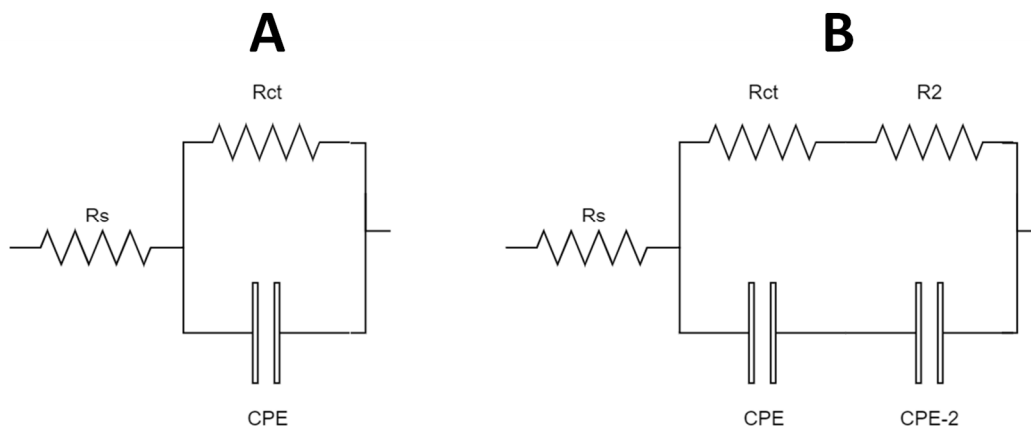


Figure 4.8 Equivalent circuits used for fitting the EIS data. (A) One CPE model used for Pt and GC electrode (B) two CPE model used for Mo₂C electrode.

Mo₂C film stability

Finally, the short-term stability of the catalyst layer against bubbles formation was examined by studying the evolution of the surface area (from CV) along successive 15 minutes controlled-potential electrolysis at -0.2 V *vs.* SHE for 900 s. Figure 4.9 shows the resulting surface area values after five successive chronoamperometries. Without Nafion, the catalytic surface was observed to drop by a factor of 1.5 after the first controlled-current electrolysis and stabilized at surface area twice smaller than initially. While the electrode was covered with Nafion layer, no significant decrease of the surface area was observed along the experiments. The measured surface area varied within 15%, which we believe is a consequence of the bubbles trapped in the Nafion layer. Table 4.1 compares the surface area and the catalytic performance for the Pt, GC and Mo₂C film electrodes.

Table 4.1 Summary of the catalytic parameters for Pt, GC and Mo₂C film electrodes investigated in 1 M H₂SO₄.

	Geometrical Surface Area /cm ²	Surface area (CV) /cm ²	η_{onset} /mV	$\eta_{10\text{mA}\cdot\text{cm}^{-2}}$ /mV	Tafel slope /mV·dec ⁻¹ (LSV)	Tafel slope /mV·dec ⁻¹ (EIS)
Pt	0.20	0.11	≈ 0	12	35	38
GC	0.20	0.12	≈ 400	640	169	161
Mo₂C film (β-form)	0.20	0.59	≈ 150	310	93	87

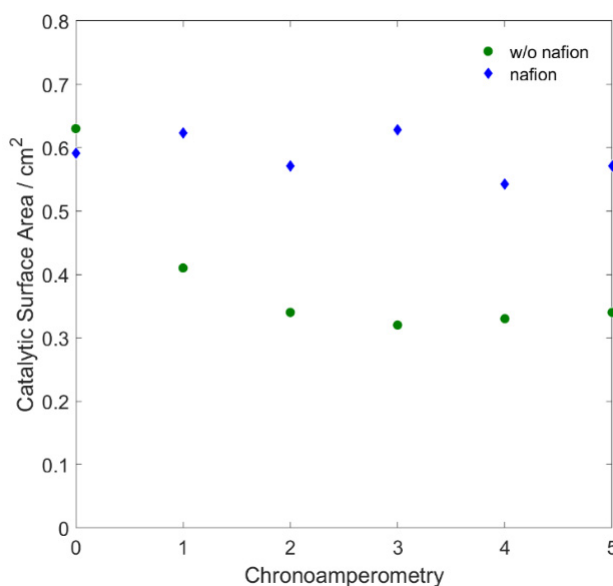


Figure 4.9 Surface area values after successive chronoamperometries for 15 minutes at controlled-potential electrolysis of -0.4 V vs. Ag|AgCl (sat. KCl) with and without Nafion.

4.4.2.3 Kinetic study

Steady-state RRD kinetic experiments were carried out on two different sets of vanadium electrolyte solutions in 2 M H_2SO_4 : 150 mM $\text{V}^{2+}/\text{V}^{3+}$ (15%, 25%, 35%, 45%, 55%, 65%, and 75%), 300 mM $\text{V}^{2+}/\text{V}^{3+}$ (15%, 25%, 35%, 45%, and 55%). We prepared and characterized the Mo_2C film before every experiment to ensure the performance and the stability of the catalytic layer following an electrochemical benchmarking protocol.³² The collection efficiency was measured to about 8% compared to a maximum theoretical value of 24.9% (Appendix IV-2). The difference between the experimental and the theoretical collection efficiency was due to the presence of Nafion hindering an optimal flow from the disk to the ring (*e.g.* bubble fouling). For every solution, blank measurements were performed using a GC-Pt (Glassy Carbon-Platinum) RRD device with the disc covered with Nafion but in the absence of Mo_2C in order to subtract the background signal due to V^{2+} oxidation on the platinum ring. All the anodic LSV recorded on the ring are available in Figure 4.10.

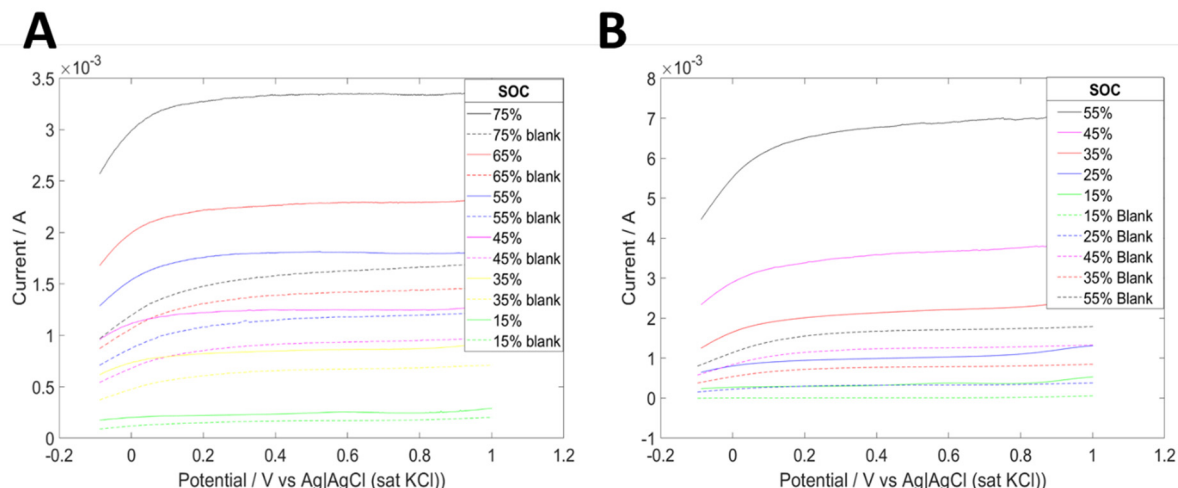


Figure 4.10 Recorded LSV on the ring during RRD measurements for solution of (A) 150 mM V^{2+}/V^{3+} solution and (B) 300 mM V^{2+}/V^{3+} solution.

The resulting rates of reaction were measured using (Eq. 4.18) for each electrolyte solution and are shown in Figure 4.11 as a function of both the concentration of V^{2+} and the state-of-charge of the electrolyte. An apparent kinetic constant, k_{app} , was calculated using the proposed kinetic law with the exponential factors previously found,

$$v_{rxn} = k_{app} \left(\frac{SOC}{1 - SOC} \right)^{0.57} [V^{2+}] \quad (\text{Eq. 4.21})$$

and was found to be $4.56 \cdot 10^{-7} \text{ L} \cdot \text{s}^{-1}$ for 150 mM V^{3+}/V^{2+} solutions and $1.48 \cdot 10^{-6} \text{ L} \cdot \text{s}^{-1}$ for the 300 mM V^{3+}/V^{2+} solutions. The experimental variations may result from changes in rheological properties between two sets of experiments that may affect the collection efficiency. Since it was not possible to evaluate CE in presence of V^{2+} , the one measured in 2 M H_2SO_4 was considered for all the calculations.

To compare the experimental data, we drew in the Figure 4.11 the mathematical representation of the kinetic rate law (Eq. 4.16). In this model estimation, we used the kinetic parameters found with the transient experiments ($\alpha = 0.57$, $\gamma = 1$) and an average value of the apparent kinetic rate constant was considered ($\overline{k_{app}} = 9.69 \cdot 10^{-7} \text{ L} \cdot \text{s}^{-1}$) to normalize the experimental data and correct the uncertainty on the collection efficiency. Figure 4.11 illustrates the good agreement of the model predictions with the RRD experimental data and demonstrates the applicability of the rate law established in this chapter governing the kinetic of the redox-mediated hydrogen production (Eq. 4.1).

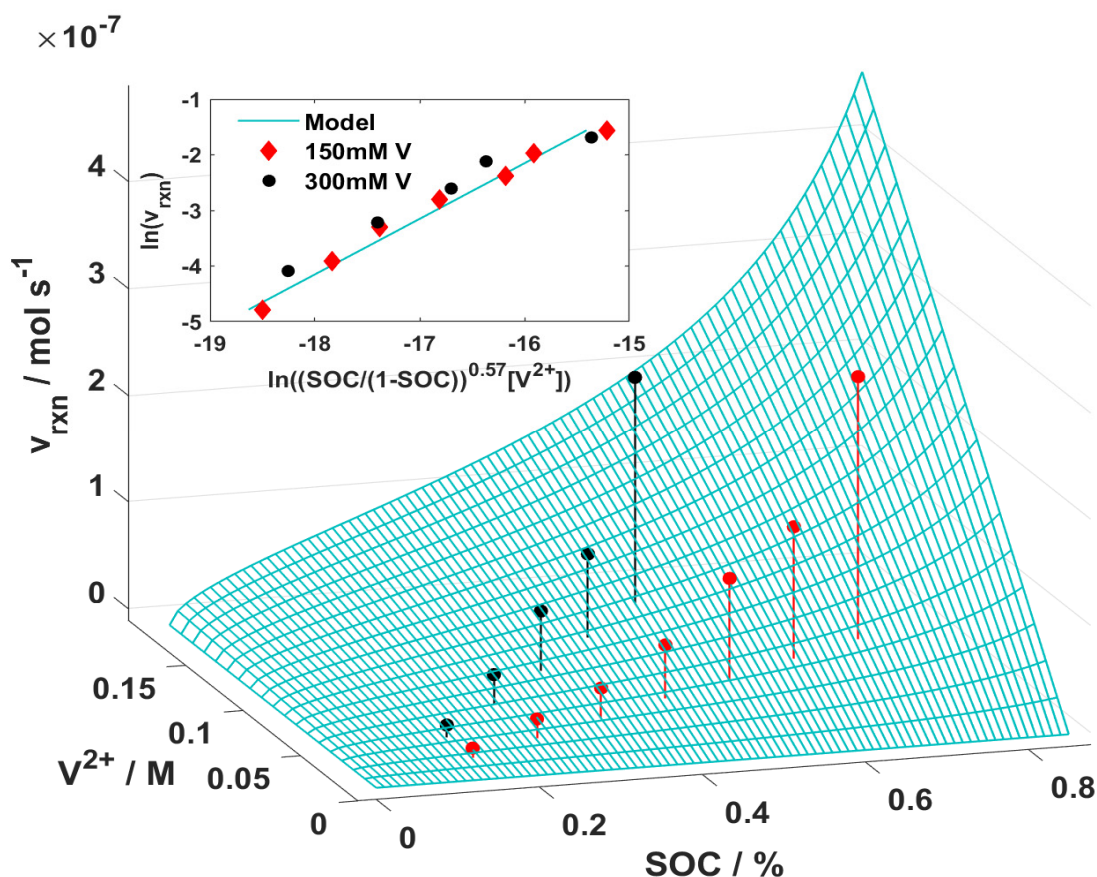


Figure 4.11 Overall rate of reaction as a function of the concentration of V^{2+} and the state-of-charge of the vanadium electrolyte. (Blue grid) Mathematical predictions of the proposed model $v_{\text{rxn}} = 9.69 \cdot 10^{-7} \left(\frac{\text{SOC}}{1-\text{SOC}} \right)^{0.57} [\text{V}^{2+}]$ (Red stem) Experimental data for 150 mM $\text{V}^{2+}/\text{V}^{3+}$ electrolyte solutions (2 M H_2SO_4) (Black stem) Experimental data for 300 mM $\text{V}^{2+}/\text{V}^{3+}$ electrolyte solutions (2 M H_2SO_4). (Inset plot) Plot of the natural logarithm of v_{rxn} as a function of the natural logarithm of $\left(\frac{\text{SOC}}{1-\text{SOC}} \right)^{0.57} [\text{V}^{2+}]$.

Furthermore, Figure 4.12 reveals that the concentration of H^+ does not affect the overall rate of reaction at sulfuric concentration above 1M. This confirms that the oxidation of V^{2+} is the rate determining step of the mediated electron process in this range of protons concentration.

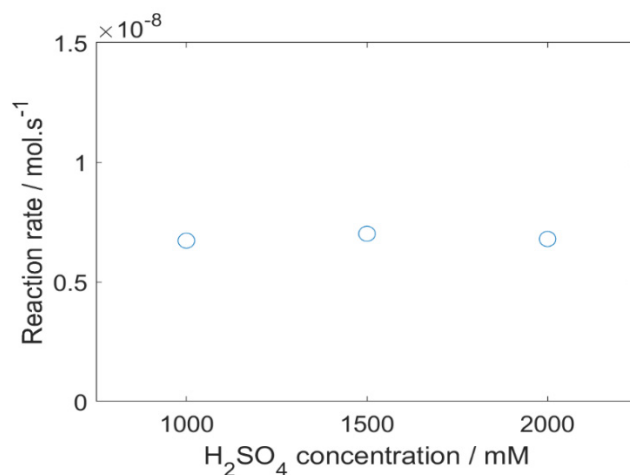


Figure 4.12 Overall rate of reaction measured during the chemical discharge of 300 mM V^{2+}/V^{3+} (SOC= 35%) in various concentrations of H_2SO_4 (1000 mM, 1500 mM, 2000 mM).

4.4.3 Conversion study

In order to confirm the proposed kinetic rate law and to extend the validity range of the model, a conversion study was performed by discharging 1.44 M V^{3+}/V^{2+} (SOC = 85%) electrolyte solution in 2 M H_2SO_4 over 25 ± 1 mg Mo_2C . The reaction was studied by monitoring the flowrate of H_2 produced (flowmeter) and the state-of-charge of the electrolyte (UV-vis). The variation of the protons concentration along the reaction was not considered. The production of hydrogen was recorded during 35 minutes before the detection limit ($5 \text{ mL} \cdot \text{min}^{-1}$) was reached (Figure 4.13-A) and the electrolyte state-of-charge was measured to about 20% (Figure 4.13-A). The UV-vis calibration curve is available in Appendix IV-2.

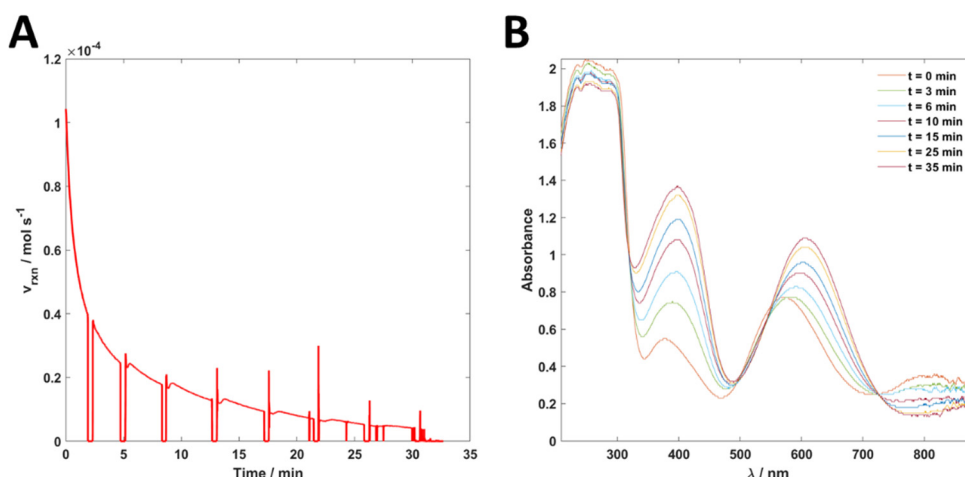


Figure 4.13 (A) Recorded rate of reaction during the conversion study using the flowmeter (B) UV-vis spectra of the sample take throughout the reaction of the conversion study.

Figure 4.14-A shows the experimental rates of reaction as a function of the SOC and the concentration of V^{2+} . The model-predicted rates of reaction were plotted using equation (Eq. 4.21). Figure 4.14-B illustrates the evolution of V^{2+} concentration throughout the reaction. To plot the model-predicted evolution of V^{2+} concentration during the reaction, the following differential equation was solved:

$$v_{\text{rxn}} = -\frac{1}{2} \frac{\partial n_{V^{2+}}}{\partial t} = k_{\text{app}} \left(\frac{n_{V^{2+}}}{n_{V^{\text{tot}}} - n_{V^{2+}}} \right)^{0.57} \left(\frac{n_{V^{2+}}}{V} \right) \quad (\text{Eq. 4.22})$$

The volume of the reactor was considered to remain constant during the reaction ($V=50$ mL). The apparent kinetic rate constant, k_{app} , was calculated to $2.23 \cdot 10^{-5} \text{ L} \cdot \text{s}^{-1}$ by fitting to the first recorded experimental data (at $t=3$ min). The net increase of the measured apparent kinetic rate constant (compared to the values measured for RRD experiments) is due to a change of the electrocatalytic surface. In absence of the Nafion layer, the surface diffusion of reactants increases resulting in an increase of the apparent kinetic rate constant. The good agreement between the kinetic model and the experimental data corroborates the rate law suggested in this chapter, in which the kinetics is governed by the rate of the oxidation of the adsorbed V^{2+} on Mo_2C .

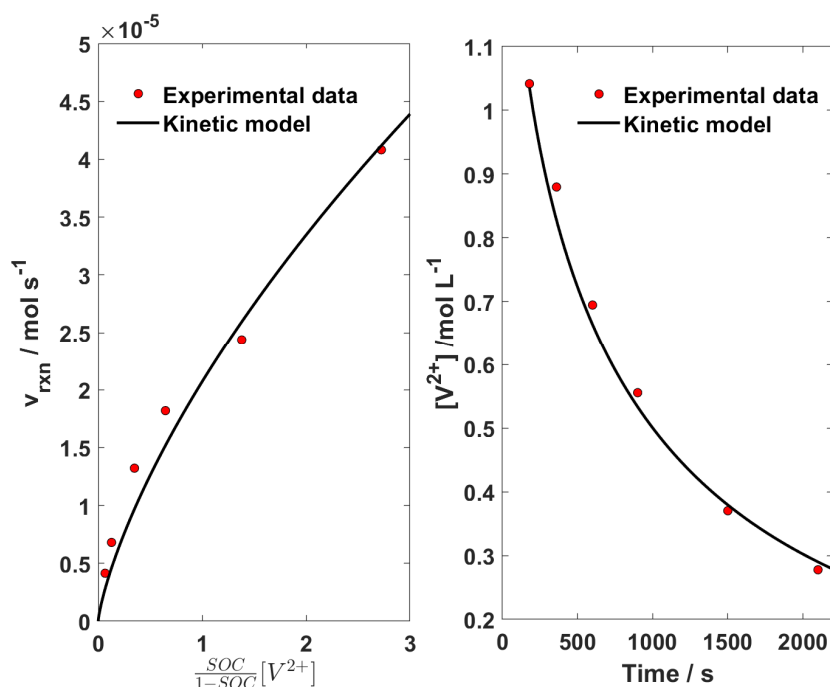


Figure 4.14 (A) Plot of overall reaction rate as a function of $\left(\frac{\text{SOC}}{1-\text{SOC}} \right) [V^{2+}]$ (B) Plot of the concentration of V^{2+} as a function of the reaction time. (Black line) Mathematical predictions from the established kinetic model (Red dot) Experimental data.

4.4.4 Model prediction for the production of hydrogen in a semi-batch reactor

The kinetic model was used to predict the production of hydrogen and determine the optimal conditions to discharge 1 L of a commercial vanadium electrolyte (1.6 M V^{3+}/V^{2+} , 2 M H_2SO_4). The process simulations were conducted in an isothermal semi-batch heterogeneous reactor (1 L) for the chemical discharge of the electrolyte. The reactor includes an outlet for extracting hydrogen flow in order to keep the pressure constant (Figure 4.15-A). The load of electrocatalyst was fixed at 0.1% w/v and the reaction was conducted at 20°C and 1 bar. At the end of the discharge, the electrolyte was flowed through an electrolyser unit where the electrolyte was charged back at a constant current of 20 A (Figure 4.15-A). On the basis of the previous experiments, the kinetic parameters implemented in the simulation were $\alpha = 0.57$, $\gamma = 1$ and $k_{app} = 8.91 \cdot 10^{-4} \text{ L} \cdot \text{s}^{-1}$ (for 1g of electrocatalyst). The process simulations were performed with Matlab™ (version R2018a).

Figure 4.15-B predicts the time profile for the hydrogen generated in a semi-batch reactor for different initial SOC's comprised between 0.2 to 0.9. As expected, the production rate of hydrogen increases with the increase of SOC. Since the amount of V^{2+} fed to the reactor is larger at higher SOC, the total amount of hydrogen produced for a given conversion increases. The energy required to charge back the electrolyte is then proportional to the amount of V^{3+} that need to be reduced back, and thus to the time of electrolysis. Consequently, it becomes relevant to evaluate the optimal SOC to complete efficiently the reaction in terms of time and energy consumption. Figure 4.15-C compares the cycle time (discharge + charge) for various hydrogen demand ranging from 0.1 to 0.6 mol per cycle as a function of the initial SOC of the electrolyte. For a given hydrogen demand per cycle, the discharging time depends on the initial SOC of the electrolyte, but the charging time remains constant. The results of the simulation show that the cycle time decreases when the reaction is conducted at high SOC's for a given hydrogen demand. Each curve reveals a vertical asymptote corresponding to the minimum value of initial SOC required to enable the generation of the desired amount of hydrogen. Interestingly, a threshold value for the initial SOC can be extracted at the maximum curvature of the curve. Below this value, the process becomes time-consuming and not optimal for an efficient production of hydrogen.

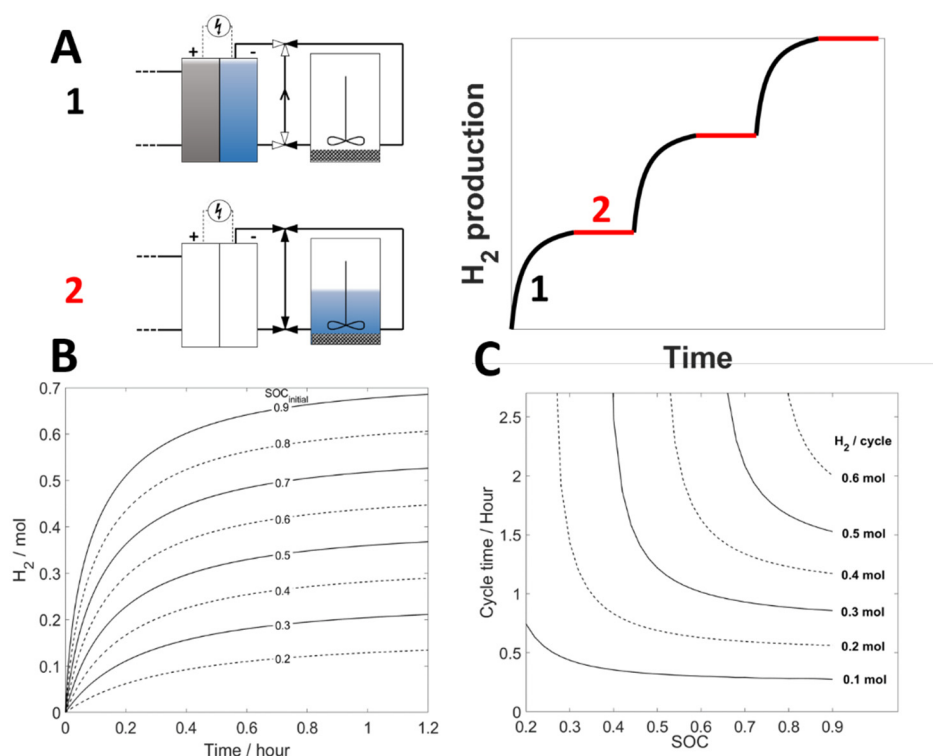


Figure 4.15 A. Schematic of the process used for the simulations including a heterogeneous semibatch reactor (1) to carry out the chemical discharge and an electrochemical cell (20 A), (2) to electrolyse back the electrolyte. B. Predictions of the time profile for the produced hydrogen during the discharge of various electrolyte (1.6 M V^{3+}/V^{2+} , 2 M H_2SO_4) with SOC ranging from 0.2 to 0.9. C. Predictions of the cycle time (charge + discharge) as a function of the initial SOC of the electrolyte for various demand in hydrogen per cycle.

4.5 Conclusion

The reaction kinetics of the hydrogen evolution reaction through the chemical oxidation of V^{2+} on a commercial Mo_2C (β -form, hcp structure)^{22,30} electrocatalyst was studied. Considering that the overall rate of reaction was determined by the rate of the oxidation of the adsorbed V^{2+} onto V^{3+} on the electrocatalyst, we established a kinetic rate law depending on the state-of-charge of the vanadium electrolyte, the concentration of V^{2+} and the amount of catalytic site. The corresponding reaction orders were determined by examining the dependence of the overall rate of reaction while varying one kinetic parameter and keeping the others in excess. A first order dependence was observed on the concentration of V^{2+} and on the catalyst load. Then, we determined an exponential factor of 0.57 on the ratio V^{2+}/V^{3+} , which is in accordance with the expected charge transfer coefficient of the redox couple V^{3+}/V^{2+} .

In order to validate the proposed kinetic model, measurements of the reaction rates at steady-state conditions were carried out using an adapted RRD method. The approach consists in immersing a rotating Mo₂C film deposited on a non-electrically connected glassy carbon disc - Pt ring electrode in the vanadium electrolyte in a dynamic mode. The resulting hydrogen produced is flowed radially and oxidized back on the platinum ring. The overall rate of reaction is related to the recorded signal and depends on the collection efficiency of the apparatus. The Mo₂C film-Pt device was prepared by drop casting a catalyst ink on a commercial GC-Pt RRD and recovering the electrically isolated disc with a Nafion layer. The Mo₂C film was fully characterized by studying the stability, the activity and the electrochemical active surface area of the catalytic layer by electrochemical measurements. The kinetic experiments were carried out for 150 mM and 300 mM V³⁺/V²⁺ electrolyte solutions in 2 M H₂SO₄ at SOC ranging from 15 to 75%. The apparent kinetic rate constant was adjusted to $9.69 \cdot 10^{-7} \text{ L} \cdot \text{s}^{-1}$ to fit the experimental data. A good agreement was observed between the model-predicted and experimentally measured rates of reaction.

To further validate the kinetic model, the chemical oxidation of a 1.44 M V²⁺/V³⁺ in 2 M H₂SO₄ was completed in a stirred tank reactor. The reaction was followed by monitoring both the hydrogen flowrate and the SOC of the bulk electrolyte during the reaction. The strong agreement between the model and the experimental data suggests that the kinetic model proposed in this chapter is an efficient tool to predict the kinetic of the vanadium-assisted hydrogen evolution on Mo₂C catalyst in high acidic conditions. Finally, process simulations were performed for an isothermal semi-batch reactor. The results of the simulations emphasize the optimal SOC to discharge efficiently the electrolyte for various demands in hydrogen. The ability to control the hydrogen production and to optimize the charging and discharging time is important for the reliability of the redox dual-flow battery to deal with the fluctuating nature of the electrical grid.

References

- (1) Lattin, W. C.; Utgikar, V. P. Transition to Hydrogen Economy in the United States: A 2006 Status Report. *International Journal of Hydrogen Energy* **2007**, 32 (15), 3230–3237. <https://doi.org/10.1016/j.ijhydene.2007.02.004>.
- (2) Mueller-Langer, F.; Tzimas, E.; Kaltschmitt, M.; Peteves, S. Techno-Economic Assessment of Hydrogen Production Processes for the Hydrogen Economy for the Short and Medium Term. *International Journal of Hydrogen Energy* **2007**, 32 (16), 3797–3810. <https://doi.org/10.1016/j.ijhydene.2007.05.027>.
- (3) Eliaz, N.; Eliezer, D.; Olson, D. L. Hydrogen-Assisted Processing of Materials. *Materials Science and Engineering: A* **2000**, 289 (1), 41–53. [https://doi.org/10.1016/S0921-5093\(00\)00906-0](https://doi.org/10.1016/S0921-5093(00)00906-0).
- (4) Ramachandran, R.; Menon, R. K. An Overview of Industrial Uses of Hydrogen. *International Journal of Hydrogen Energy* **1998**, 23 (7), 593–598. [https://doi.org/10.1016/S0360-3199\(97\)00112-2](https://doi.org/10.1016/S0360-3199(97)00112-2).
- (5) Armaroli, N.; Balzani, V. The Hydrogen Issue. *ChemSusChem* **2011**, 4 (1), 21–36. <https://doi.org/10.1002/cssc.201000182>.
- (6) Olah, G. A.; Goepfert, A.; Prakash, G. K. S. *Beyond Oil and Gas: The Methanol Economy*; John Wiley & Sons, 2018.
- (7) Hydrogen - Fuels & Technologies <https://www.iea.org/fuels-and-technologies/hydrogen> (accessed 2020 -02 -10).
- (8) Ohi, J. Hydrogen Energy Cycle: An Overview. *Journal of Materials Research* **2005**, 20 (12), 3180–3187. <https://doi.org/10.1557/jmr.2005.0408>.
- (9) Rausch, B.; Symes, M. D.; Chisholm, G.; Cronin, L. Decoupled Catalytic Hydrogen Evolution from a Molecular Metal Oxide Redox Mediator in Water Splitting. *Science* **2014**, 345 (6202), 1326–1330. <https://doi.org/10.1126/science.1257443>.
- (10) Noh, H.; Kung, C.-W.; Otake, K.; Peters, A. W.; Li, Z.; Liao, Y.; Gong, X.; Farha, O. K.; Hupp, J. T. Redox-Mediator-Assisted Electrocatalytic Hydrogen Evolution from Water by a Molybdenum Sulfide-Functionalized Metal–Organic Framework. *ACS Catal.* **2018**, 8 (10), 9848–9858. <https://doi.org/10.1021/acscatal.8b02921>.
- (11) Zeng, K.; Zhang, D. Recent Progress in Alkaline Water Electrolysis for Hydrogen Production and Applications. *Progress in Energy and Combustion Science* **2010**, 36 (3), 307–326. <https://doi.org/10.1016/j.pecs.2009.11.002>.
- (12) Bessarabov, D.; Wang, H.; Li, H.; Zhao, N. *PEM Electrolysis for Hydrogen Production: Principles and Applications*; CRC Press, 2016.
- (13) Holladay, J. D.; Hu, J.; King, D. L.; Wang, Y. An Overview of Hydrogen Production Technologies. *Catalysis Today* **2009**, 139 (4), 244–260. <https://doi.org/10.1016/j.cattod.2008.08.039>.
- (14) Amstutz, V.; Toghiani, K. E.; Powlesland, F.; Vrubel, H.; Comninellis, C.; Hu, X.; Girault, H. H. Renewable Hydrogen Generation from a Dual-Circuit Redox Flow Battery. *Energy Environ. Sci.* **2014**, 7 (7), 2350–2358. <https://doi.org/10.1039/C4EE00098F>.
- (15) Hu, W. Electrocatalytic Properties of New Electrocatalysts for Hydrogen Evolution in Alkaline Water Electrolysis. *International Journal of Hydrogen Energy* **2000**, 25 (2), 111–118. [https://doi.org/10.1016/S0360-3199\(99\)00024-5](https://doi.org/10.1016/S0360-3199(99)00024-5).
- (16) Carmo, M.; Fritz, D. L.; Mergel, J.; Stolten, D. A Comprehensive Review on PEM Water Electrolysis. *International Journal of Hydrogen Energy* **2013**, 38 (12), 4901–4934. <https://doi.org/10.1016/j.ijhydene.2013.01.151>.
- (17) Ligen, Y.; Vrubel, H.; Girault, H. Energy Efficient Hydrogen Drying and Purification for Fuel Cell Vehicles. *International Journal of Hydrogen Energy* **2020**. <https://doi.org/10.1016/j.ijhydene.2020.02.035>.

- (18) Bloor, L. G.; Solarska, R.; Bienkowski, K.; Kulesza, P. J.; Augustynski, J.; Symes, M. D.; Cronin, L. Solar-Driven Water Oxidation and Decoupled Hydrogen Production Mediated by an Electron-Coupled-Proton Buffer. *J. Am. Chem. Soc.* **2016**, *138* (21), 6707–6710. <https://doi.org/10.1021/jacs.6b03187>.
- (19) Symes, M. D.; Cronin, L. Decoupling Hydrogen and Oxygen Evolution during Electrolytic Water Splitting Using an Electron-Coupled-Proton Buffer. *Nature Chem* **2013**, *5* (5), 403–409. <https://doi.org/10.1038/nchem.1621>.
- (20) Rausch, B.; Symes, M. D.; Cronin, L. A Bio-Inspired, Small Molecule Electron-Coupled-Proton Buffer for Decoupling the Half-Reactions of Electrolytic Water Splitting. *J. Am. Chem. Soc.* **2013**, *135* (37), 13656–13659. <https://doi.org/10.1021/ja4071893>.
- (21) Amstutz, V.; Toghiani, K. E.; Comninellis, C.; Girault, H. H. EOS Holding (Switzerland), International Pat. WO 2013131838, 2013.
- (22) Amstutz, V. Redox flow battery and indirect water electrolysis <https://infoscience.epfl.ch/record/213651> (accessed 2019 -10 -23). <https://doi.org/10.5075/epfl-thesis-6813>.
- (23) Peljo, P.; Vrubel, H.; Amstutz, V.; Pandard, J.; Morgado, J.; Santasalo-Aarnio, A.; Lloyd, D.; Gumy, F.; R. Dennison, C.; E. Toghiani, K.; H. Girault, H. All-Vanadium Dual Circuit Redox Flow Battery for Renewable Hydrogen Generation and Desulfurisation. *Green Chemistry* **2016**, *18* (6), 1785–1797. <https://doi.org/10.1039/C5GC02196K>.
- (24) Gentil, S.; Reynard, D.; Girault, H. H. Aqueous Organic and Redox-Mediated Redox Flow Batteries: A Review. *Current Opinion in Electrochemistry* **2020**, *21*, 7–13. <https://doi.org/10.1016/j.coelec.2019.12.006>.
- (25) Piwek, J.; Dennison, C. R.; Frackowiak, E.; Girault, H.; Battistel, A. Vanadium-Oxygen Cell for Positive Electrolyte Discharge in Dual-Circuit Vanadium Redox Flow Battery. *Journal of Power Sources* **2019**, *439*, 227075. <https://doi.org/10.1016/j.jpowsour.2019.227075>.
- (26) Hinnemann, B.; Moses, P. G.; Bonde, J.; Jørgensen, K. P.; Nielsen, J. H.; Horch, S.; Chorkendorff, I.; Nørskov, J. K. Biomimetic Hydrogen Evolution: MoS₂ Nanoparticles as Catalyst for Hydrogen Evolution. *J. Am. Chem. Soc.* **2005**, *127* (15), 5308–5309. <https://doi.org/10.1021/ja0504690>.
- (27) Lau, V. W.; Masters, A. F.; Bond, A. M.; Maschmeyer, T. Promoting the Formation of Active Sites with Ionic Liquids: A Case Study of MoS₂ as Hydrogen-Evolution-Reaction Electrocatalyst. *ChemCatChem* **2011**, *3* (11), 1739–1742. <https://doi.org/10.1002/cctc.201100212>.
- (28) Ge, P.; Scanlon, M. D.; Peljo, P.; Bian, X.; Vubrel, H.; O'Neill, A.; Coleman, J. N.; Cantoni, M.; Hu, X.; Kontturi, K.; Liu, B.; Girault, H. H. Hydrogen Evolution across Nano-Schottky Junctions at Carbon Supported MoS₂ Catalysts in Biphasic Liquid Systems. *Chem. Commun.* **2012**, *48* (52), 6484–6486. <https://doi.org/10.1039/C2CC31398G>.
- (29) Peng, K.; Wang, H.; Gao, H.; Wan, P.; Ma, M.; Li, X. Emerging Hierarchical Ternary 2D Nanocomposites Constructed from Montmorillonite, Graphene and MoS₂ for Enhanced Electrochemical Hydrogen Evolution. *Chemical Engineering Journal* **2020**, *393*, 124704. <https://doi.org/10.1016/j.cej.2020.124704>.
- (30) Vrubel, H.; Hu, X. Molybdenum Boride and Carbide Catalyze Hydrogen Evolution in Both Acidic and Basic Solutions. *Angewandte Chemie International Edition* **2012**, *51* (51), 12703–12706. <https://doi.org/10.1002/anie.201207111>.
- (31) Noh, H.; Kung, C.-W.; Otake, K.; Peters, A. W.; Li, Z.; Liao, Y.; Gong, X.; Farha, O. K.; Hupp, J. T. Redox-Mediator-Assisted Electrocatalytic Hydrogen Evolution from Water by a Molybdenum Sulfide-Functionalized Metal–Organic Framework. *ACS Catal.* **2018**, *8* (10), 9848–9858. <https://doi.org/10.1021/acscatal.8b02921>.

- (32) McCrory, C. C. L.; Jung, S.; Peters, J. C.; Jaramillo, T. F. Benchmarking Heterogeneous Electrocatalysts for the Oxygen Evolution Reaction. *Journal of the American Chemical Society* **2013**, *135* (45), 16977–16987. <https://doi.org/10.1021/ja407115p>.
- (33) Skyllas-Kazacos, M.; Cao, L.; Kazacos, M.; Kausar, N.; Mousa, A. Vanadium Electrolyte Studies for the Vanadium Redox Battery—A Review. *ChemSusChem* **2016**, *9* (13), 1521–1543. <https://doi.org/10.1002/cssc.201600102>.
- (34) Davis, M. E.; Davis, R. J. *Fundamentals of Chemical Reaction Engineering*, International ed.; McGraw-Hill chemical engineering series; McGraw-Hill: Boston, 2003.
- (35) Becker, C. From Langmuir to Ertl: The “Nobel” History of the Surface Science Approach to Heterogeneous Catalysis. In *Encyclopedia of Interfacial Chemistry*; Wandelt, K., Ed.; Elsevier: Oxford, 2018; pp 99–106. <https://doi.org/10.1016/B978-0-12-409547-2.13527-9>.
- (36) Girault, H. H. *Electrochimie physique et analytique*; Presses Polytechniques et Universitaires Romandes, 2007.
- (37) Bard, A. J.; Faulkner, L. R. *Electrochemical Methods: Fundamentals and Applications*, 2nd ed.; Wiley, 2001.
- (38) Niki, K.; Mizota, H. Effect of Specific Adsorbed Anions on the Electrode Kinetics of the V(III)/V(II) and Eu(III)/Eu(II) Couples. *Journal of Electroanalytical Chemistry and Interfacial Electrochemistry* **1976**, *72* (3), 307–317. [https://doi.org/10.1016/S0022-0728\(76\)80316-6](https://doi.org/10.1016/S0022-0728(76)80316-6).
- (39) G. Morales-Guio, C.; Stern, L.-A.; Hu, X. Nanostructured Hydrotreating Catalysts for Electrochemical Hydrogen Evolution. *Chemical Society Reviews* **2014**, *43* (18), 6555–6569. <https://doi.org/10.1039/C3CS60468C>.
- (40) Chen, Z.; Qing, H.; Zhou, K.; Sun, D.; Wu, R. Metal-Organic Framework-Derived Nanocomposites for Electrocatalytic Hydrogen Evolution Reaction. *Progress in Materials Science* **2020**, *108*, 100618. <https://doi.org/10.1016/j.pmatsci.2019.100618>.
- (41) Yang, W.; Chen, S. Recent Progress in Electrode Fabrication for Electrocatalytic Hydrogen Evolution Reaction: A Mini Review. *Chemical Engineering Journal* **2020**, *393*, 124726. <https://doi.org/10.1016/j.cej.2020.124726>.
- (42) McCrory, C. C. L.; Jung, S.; Peters, J. C.; Jaramillo, T. F. Benchmarking Heterogeneous Electrocatalysts for the Oxygen Evolution Reaction. *J. Am. Chem. Soc.* **2013**, *135* (45), 16977–16987. <https://doi.org/10.1021/ja407115p>.
- (43) Ambrosi, A.; Sofer, Z.; Pumera, M. Lithium Intercalation Compound Dramatically Influences the Electrochemical Properties of Exfoliated MoS₂. *Small* **2015**, *11* (5), 605–612. <https://doi.org/10.1002/sml.201400401>.
- (44) Yu, S. H.; Chua, D. H. C. Toward High-Performance and Low-Cost Hydrogen Evolution Reaction Electrocatalysts: Nanostructuring Cobalt Phosphide (CoP) Particles on Carbon Fiber Paper. *ACS Applied Materials & Interfaces* **2018**, *10* (17), 14777–14785. <https://doi.org/10.1021/acsami.8b02755>.
- (45) Lin, H.; Shi, Z.; He, S.; Yu, X.; Wang, S.; Gao, Q.; Tang, Y. Heteronanowires of MoC–Mo₂C as Efficient Electrocatalysts for Hydrogen Evolution Reaction. *Chem. Sci.* **2016**, *7* (5), 3399–3405. <https://doi.org/10.1039/C6SC00077K>.
- (46) He, C.; Tao, J. Synthesis of Nanostructured Clean Surface Molybdenum Carbides on Graphene Sheets as Efficient and Stable Hydrogen Evolution Reaction Catalysts. *Chem. Commun.* **2015**, *51* (39), 8323–8325. <https://doi.org/10.1039/C5CC01240F>.
- (47) Ma, L.; Ting, L. R. L.; Molinari, V.; Giordano, C.; Yeo, B. S. Efficient Hydrogen Evolution Reaction Catalyzed by Molybdenum Carbide and Molybdenum Nitride Nanocatalysts Synthesized via the Urea Glass Route. *Journal of Materials Chemistry A* **2015**, *3* (16), 8361–8368. <https://doi.org/10.1039/C5TA00139K>.

- (48) Wan, C.; Regmi, Y. N.; Leonard, B. M. Multiple Phases of Molybdenum Carbide as Electrocatalysts for the Hydrogen Evolution Reaction. *Angewandte Chemie International Edition* **2014**, 53 (25), 6407–6410. <https://doi.org/10.1002/anie.201402998>.
- (49) Song, B.; Li, K.; Yin, Y.; Wu, T.; Dang, L.; Cabán-Acevedo, M.; Han, J.; Gao, T.; Wang, X.; Zhang, Z.; Schmidt, J. R.; Xu, P.; Jin, S. Tuning Mixed Nickel Iron Phosphosulfide Nanosheet Electrocatalysts for Enhanced Hydrogen and Oxygen Evolution. *ACS Catalysis* **2017**, 7 (12), 8549–8557. <https://doi.org/10.1021/acscatal.7b02575>.
- (50) Delgado, D.; Minakshi, M.; Kim, D.-J. Electrochemical Impedance Spectroscopy Studies on Hydrogen Evolution from Porous Raney Cobalt in Alkaline Solution. *Int. J. Electrochem. Sci.* **2015**, 10, 16.

Appendix IV

Appendix IV-1: Details of the kinetic experiments in transient conditions

Table A4.1 Formulation of the electrolyte solutions for the study of the dependence of the overall rate of reaction with the concentration of V^{2+} .

$[V^{2+}] / M$	SOC / %	1.5 M V^{2+} (in 2M H_2SO_4) / mL	1.5 M V^{3+} (in 2M H_2SO_4) / mL	2 M H_2SO_4 / mL	V_{tot} / mL	$m(cat)/mg$
0.5	50	20.0	20.0	20	60	50 ± 1
0.25	50	10.0	10.0	40	60	50 ± 1
0.125	50	5.0	5.0	50	60	50 ± 1
0.0625	50	2.5	2.5	55	60	50 ± 1
0.025	50	1.0	1.0	58	60	50 ± 1

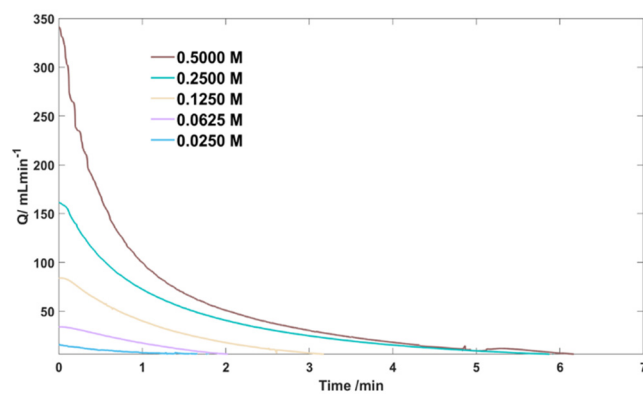
Table A4.2 Formulation of the electrolyte solutions for the study of the dependence of the overall rate of reaction with state-of-charge.

$[V^{2+}] / M$	SOC / %	1.5 M V^{2+} (in 2M H_2SO_4) / mL	1.5 M V^{3+} (in 2M H_2SO_4) / mL	2 M H_2SO_4 / mL	V_{tot} / mL	$m(cat)/mg$
0.15	90	1	0.10	8.90	10	50 ± 1
0.15	80	1	0.25	8.75	10	50 ± 1
0.15	70	1	0.42	8.58	10	50 ± 1
0.15	60	1	0.67	8.33	10	50 ± 1
0.15	50	1	1.00	8.00	10	50 ± 1
0.15	40	1	1.50	7.50	10	50 ± 1
0.15	30	1	2.30	6.70	10	50 ± 1
0.15	20	1	4.00	5.00	10	50 ± 1
0.15	10	1	9.00	0.00	10	50 ± 1

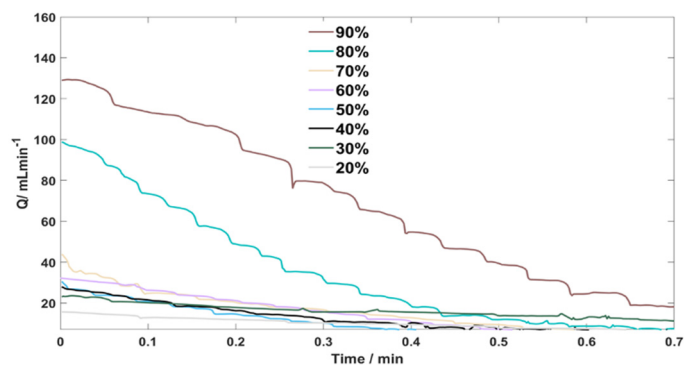
Table A4.3 Formulation of the electrolyte solutions for the study of the dependence of the overall rate of reaction with the amount of catalyst.

$[V^{2+}] / M$	SOC / %	1.5 M V^{2+} (in 2M H_2SO_4) / mL	1.5 M V^{3+} (in 2M H_2SO_4) / mL	2 M H_2SO_4 / mL	V_{tot} / mL	$m(cat)/mg$
0.375	50	5	5	10	20	25.0 ± 1
0.375	50	5	5	10	20	12.5 ± 1
0.375	50	5	5	10	20	6.0 ± 1
0.375	50	5	5	10	20	3.0 ± 1
0.375	50	5	5	10	20	1.5 ± 1

$$\Delta[V^{2+}]$$



$$\Delta\text{SOC}$$



$$\Delta m(\text{cat})$$

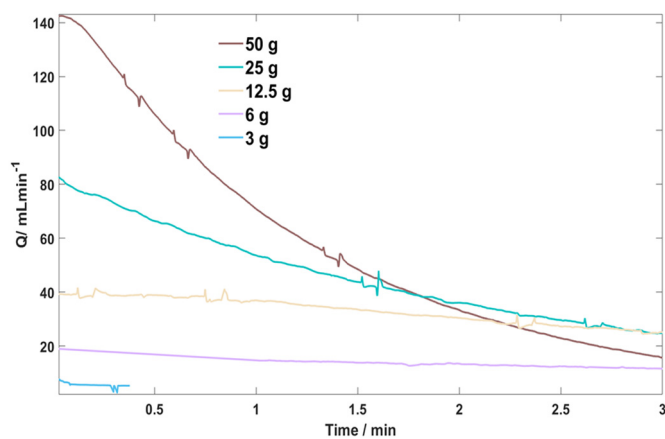


Figure A4.1 The recorded hydrogen flowrate profile throughout the chemical discharge for various V^{2+} concentration, state-of-charge (SOC) and catalyst load.

Appendix IV-2: Calibration curves

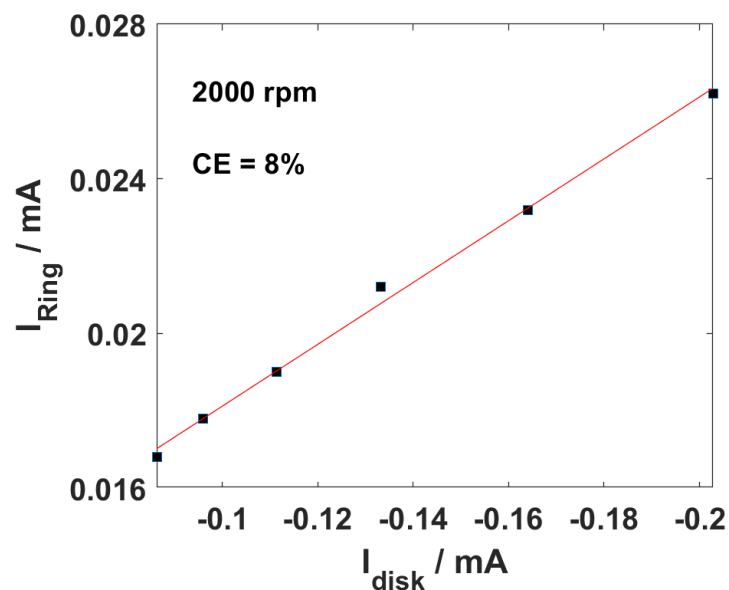


Figure A4.2 Plot of the ring current as a function of the disk current with the slope indicating the collection efficiency of the Mo₂C film-Pt RRD device.

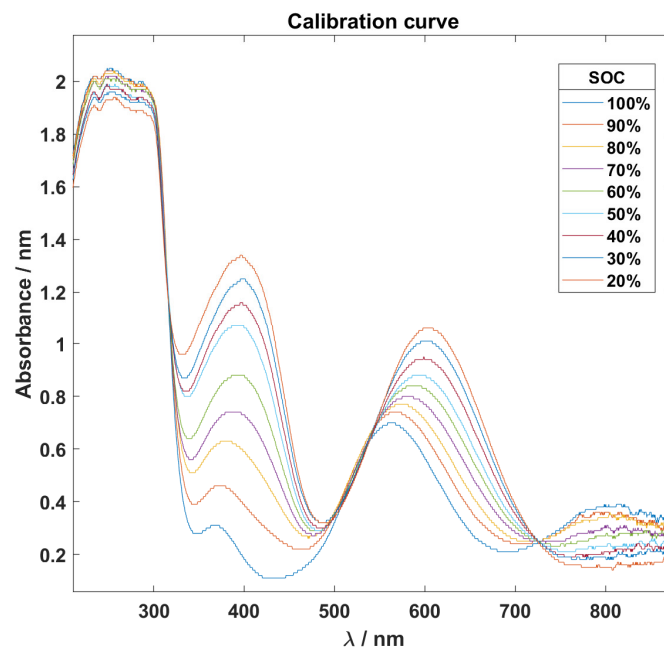


Figure A4.3 UV-vis spectra of 1.44 M V²⁺/V³⁺ solution in 2 M H₂SO₄ at SOC ranging from 20 to 100%. The background was normalized using the isosbestic point at 725 nm (Absorbance = 0.25).

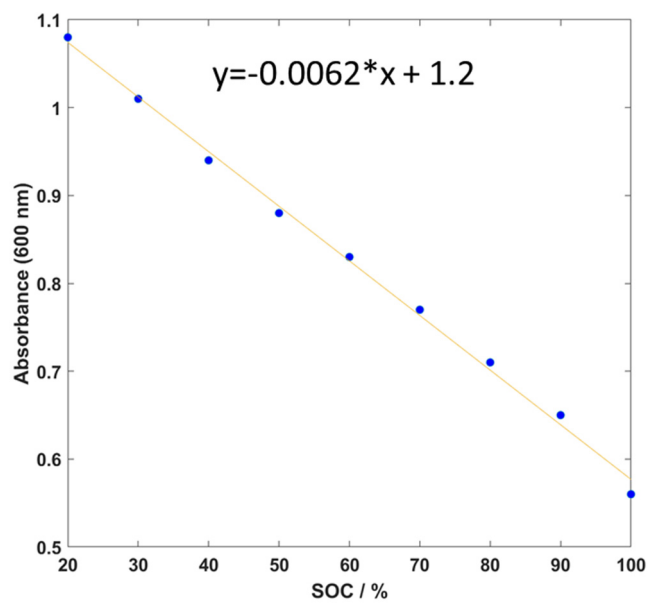
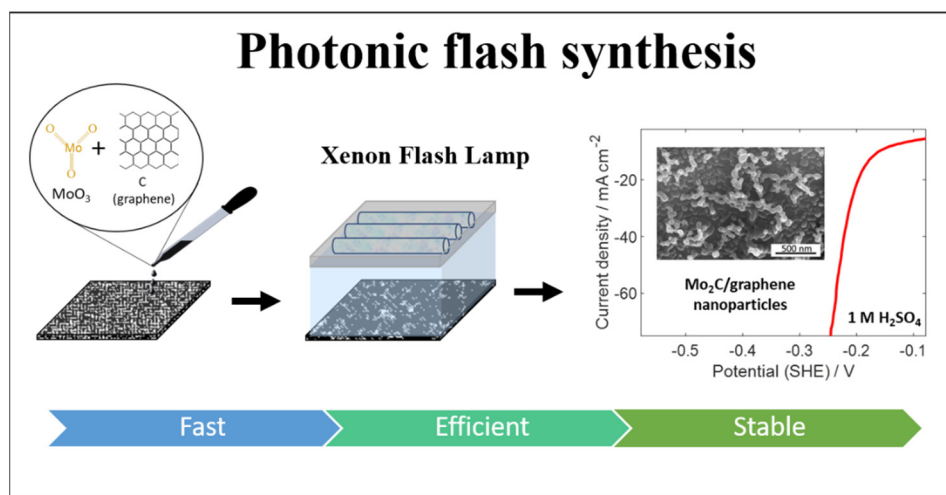


Figure A4.4 Resulting calibration curve relating the state-of-charge of 1.44 M V^{2+}/V^{3+} solution in 2 M H_2SO_4 with the absorbance at 600 nm.

CHAPTER V

Photonic flash synthesis of Mo_2C electrocatalyst for the hydrogen evolution reaction

The results presented in this chapter are adapted with permission from D. Reynard, B. Nagar, H. Girault, Photonic Flash Synthesis of Mo_2C /Graphene Electrocatalyst for the Hydrogen Evolution Reaction, ACS Catalysis 2021, 11 (9), 5865-5872 DOI: 10.1021/acscatal.1c00770 © Copyright © 2021 American Chemical Society.



Abstract

The present chapter aims to propose a fast and simple process for the fabrication of a Mo_2C -based electrocatalyst on carbon cloth substrate by photonic flash synthesis (PFS) from a MoO_3 /graphene precursor under ambient atmosphere. SEM, XRD, and XPS results reveals the successful thermal decomposition of molybdenum oxides into porous nanostructure of β - Mo_2C after exposing the precursor material with a 575 V lamp flash for 4 successive pulses. As a result, the as-prepared $\text{Mo}_2\text{C}@575\text{V-4p}$ demonstrate a Tafel slope of $63 \text{ mV} \cdot \text{dec}^{-1}$ and a low overpotential of $\sim 160 \text{ mV}$ and $\sim 230 \text{ mV}$ to drive $10 \text{ mA} \cdot \text{cm}^{-2}$ and $50 \text{ mA} \cdot \text{cm}^{-2}$ in acidic media, respectively. Furthermore, high catalytic stability is observed, validating further the strategy for the design of the catalytic bed reactor of the redox dual-flow battery.

5.1 Introduction

Transition metal carbides (TMCs) are known to have high thermal properties. The unique metal-to-carbide bond (d-state density around the Fermi level) provides noble-metal-like catalytic properties drawing great interest for those low-cost materials, especially for catalyst applications.^{1,2} Among them, molybdenum carbide (Mo₂C) exhibits excellent catalytic properties for various reactions including ammonia synthesis, hydrocarbon conversion and hydrogen evolution reaction (HER).¹⁻⁵

As most of the carbide compounds, Mo₂C is not naturally present on Earth and must be synthesized. The choice of the preparation route can largely affect the electrocatalytic properties such as particle size, morphology, crystal structure and specific surface area.^{6,7} Traditionally, bulk Mo₂C was prepared by carburization of the metal with a carbon source at high temperatures (>1000°C). This method is limited for catalyst preparation due to low purity and metal sintering minimizing the active surface area.^{3,8} Since 1980s, Boudart *et al.* developed the so-called temperature-programmed reduction (TPR) method in order to produce unsupported Mo₂C electrocatalyst with a high-surface area (50-90 m²·g⁻¹).⁹ The method consists to react molybdenum oxide precursors (MoO₃ or/and MoO₂) with a gas carbon source (*e.g.* CH₄, C₂H₆, C₃H₈, C₄H₁₀...) diluted in hydrogen atmosphere through a temperature-programmed process. Typically, the reaction occurs under 20% CH₄/H₂ (150 cm³/min) atmosphere with a temperature raising from 300°C and 700°C at a rate of 1°C/min, and keeps for 2h.^{10,11} However, TPR suffers from carbon-based deposition concerns inhibiting active sites, and the need for highly flammable gas atmosphere leads to safety concerns for industrial production.^{1,8} More recently, several carbo-thermal reduction processes using solid carbon-containing compound as carbon sources were reported, including active carbon,^{12,13} nano-structure¹⁴⁻²⁰ or organics.^{21,22} Others processes were developed using liquid carbon source such as urea^{23,24} or carbon tetrabromide.²⁵ Besides conventional carbo-thermal reduction, new methods were reported using sono-chemical synthesis,²⁶ chemical-vapor deposition (CVD),²⁷⁻³⁰ microwave^{31,32} or plasma deposition.³³

To our knowledge, no synthetic protocol has been reported using photonic flash synthesis (PFS). PFS is based on the principle that (deep) colored materials/nanomaterials absorb light with specific wavelengths in the visible light spectrum causing increases in their temperature. In the process, an optimal (voltage, duration and frequency) pulse of white light is generated *via* a Xenon lamp causing a local rise of temperature to the exposed material (up to several

hundred of degrees Celsius) without affecting its surrounding. Since the pulse duration is generally in the few micro-milliseconds range, the cooling process is very fast, giving an advantage to be used over temperature sensitive substrates like polymer films such as PET. For this reason, photonic sintering is most commonly applied in printed electronics for curing of (nanomaterial-based) inks for flexible electronics.³⁴ Photonic flashes have also been used for the synthesis of various nanoparticles over flexible electrodes,^{35–38} and even for reduction of oxygen groups from graphene to form conductive reduced graphene oxide in ambient atmosphere^{39,40} or for removal of binders from the carbon based inks.⁴¹ It is important to mention that PFS reactions include both oxidation as in the production of Prussian Blue⁴² and reduction reactions as in the production of metallic nanoparticles.³⁵

This chapter reports the photochemical synthesis of Mo_2C nanoparticles electrocatalysts on a carbon material (carbon cloth with GDL) through thermal decomposition of MoO_3 /graphene precursor within few seconds under ambient atmosphere using photonic flashing technique. Carbon sources such as graphite, Vulcan carbon, activated carbon, carbon nanofiber, graphene etc. have been continuously used as the carbon source in the conventional carbothermal processes and as supports.^{43–46} Graphene is yet another sp^2 hybridized carbon allotrope with exceptional conductivities and chemical and mechanical stabilities.^{47,48} Mildly edge oxidized graphene oxide sheets that are few micrometers in width were selected with the objective to have higher surface loading and facile carbide formation due to the presence of edge functionalities. The present chapter proposes a fast and safe two-step protocol to prepare efficiently Mo_2C -based electrocatalyst towards HER (Figure 5.1).

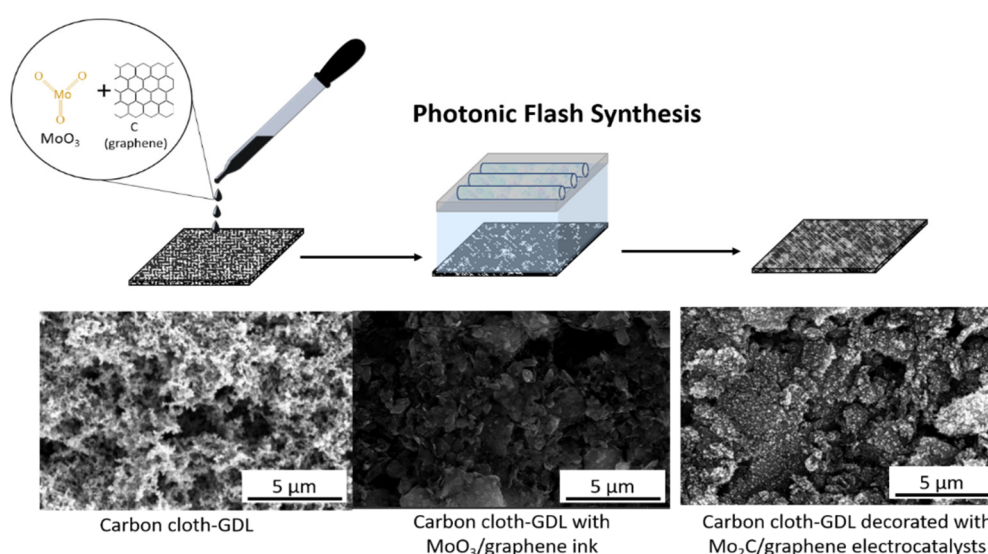


Figure 5.1 Schematic of the proposed synthetic pathway for the preparation of Mo_2C -based electrocatalyst using photonic flash synthesis.

The as-prepared electrocatalyst was characterized by scanning electron microscopy (SEM), X-ray diffraction (XRD), X-ray photoelectron spectroscopy (XPS) and electrochemical measurements.

5.2 Experimental method

5.2.1 Chemicals

All reagents were commercially available and were used as supplied without further purification, Ammonium Molybdate tetrahydrate (NH₄)₆Mo₇O₂₄·4H₂O (AHM), N-Methyl Pyrrolidine, Mildly edge-oxidized graphene nanosheets (EOGNs, 15–20 sheets, 4–10% edge-oxidized, Sigma Aldrich) and Carbon Cloth with GDL (GoodFellow) and deionized water were used throughout the experiments. Sulfuric acid (H₂SO₄, 95–97%) was purchased from Merck and used without further purification. Molybdenum carbide (Mo₂C, 99%, β -form, hcp structure) was purchased from Sigma Aldrich.

5.2.2 Instrumentation

All electrochemical measurements were performed with an Autolab potentiostat PGSTAT204 (Metrohm). SEM images were performed with a Teneo SEM (FEI, USA) equipped with a Schottky field emission gun. Secondary electron detection was carried out with an Everhart–Thornley detector and an in-lens detector. X-ray photoelectron spectroscopy (XPS) was conducted with a VersaProbe II from Physical Electronics. The X-ray diffraction patterns (XRD) were measured using Bruker D8 Discover diffractometer, which employs Cu-K α source ($\lambda = 1.54060$ Å) and a VÅNTEC-1 detector. The measured 2θ degree range was from 25 - 80. Phase analysis was based on the matching pattern with PDF4+ (2019) database records. The distance between sample and the detector was kept at 351.5 mm.

5.2.3 Precursor ink formulation

The precursor ink was prepared by adding 40 mg of graphene oxide (EOGN) and 160 mg of ammonium molybdate tetrahydrate (molybdenum oxide precursor) were added to N-Methyl Pyrrolidone (NMP) to reach a concentration of 30 mg/mL. The solution was then sonicated for 15 min at 40% amplitude using Sonics Vibra Cell 505 sonicator with the “cup-horn” arrangement.

5.2.4 Photonic flash synthesis route

For the PFS process, 50 μL of the precursor ink was drop-casted over a 4 mm diameter circular carbon substrate (with a gas diffusion layer) and thermally dried at 200°C for 10 min. The cloth was placed over a microscopy glass slide and exposed under the flash lamp for the PFS at a working distance of 2 mm from the radiation source. It is important to note that the glass slide was just used as a support and did not actively participate in the synthesis process. PulseForge 1300 photonic curing system (Novacentrix, USA) containing a xenon flashlamp was used for the PFS process, 3 different lamp charging voltages of 300 V, 450 V and 575 V (limiting value of the flashlamp device) with 18 μs pulses spread over a period of 20,000 μs were tested that emitted a theoretical energy density of 3.6, 8.5 and 12.8 $\text{J}\cdot\text{cm}^{-2}$ respectively.

5.2.5 Electrochemical characterization

All the electrochemical measurements were performed using a three-electrode electrochemical cell at room temperature equipped with a working electrode, an Ag|AgCl (sat. KCl) reference electrode and a carbon counter electrode. All the experiments were carried out in an aqueous acidic media (1 M aqueous H₂SO₄, pH=0) and the analyte was purged with Argon for 10 minutes to remove dissolved oxygen. The carbon cloth containing the Mo₂C-graphene was screwed to a carbon coated titanium current collector electrode (geometrical surface area = 0.2 cm^2). Please note, a magnetic stirrer was placed near the working electrode to dissipate the generated H₂ bubbles during all the measurements. An activation process was performed to each catalytic sample by cathodic galvanostatic electrolysis during 20 minutes at $-20 \text{ mA}\cdot\text{cm}^{-2}$. This step was done to remove the presence of molybdenum oxides (MoO₃ and MoO₂) and enhance the wettability of the electrode surface. The electrocatalytic activity towards HER (Tafel slopes) was examined by polarization curve (LSV measurements) at a scan rate of 0.01 $\text{V}\cdot\text{s}^{-1}$ and electrochemical impedance spectroscopy (EIS) in the frequency range from 100 kHz to 1Hz with a single modulated AC potential of 10 mV at a constant overpotential of 250 mV towards HER. Electrochemical capacitance of each electrode was determined by carrying out cyclic voltammetry (CV) in a 0.1 V potential window centered on the open-circuit potential (OCP) (non-faradaic region) for various scan rates ranging from 0.05 $\text{V}\cdot\text{s}^{-1}$ to 0.60 $\text{V}\cdot\text{s}^{-1}$. The working electrode was held at each potential vertex for 15s before beginning each linear sweep polarization (LSV). The electrocatalytic stability of the Mo₂C-based electrode under catalytic conditions was examined by controlled-current electrolysis. The catalyst was held at a constant

current density of 20 mA·cm⁻² per geometric area for 10 h under continuous stirring. The standard deviation of the overpotential before and after the stability test were then compared. All experimental data were fitted with the software Matlab™ (version R2018a).

5.3 Results and discussion

The photonic flashing synthesis of Mo₂C-based catalyst was carried out in a two-steps synthetic route: (a) drop-casting of 50 μL MoO₃/Graphene precursor ink having a concentration of 30 mg/mL total (24 mg/mL of MoO₃ precursor) on a carbon substrate (b) photonic flashing synthesis (PFS). Figure 5.2 compares the typical morphology and structure of the as-prepared Mo₂C-based catalyst throughout the synthesis process of a sample exposed to four pulses at a voltage of 575V (Mo₂C@575V-4p).

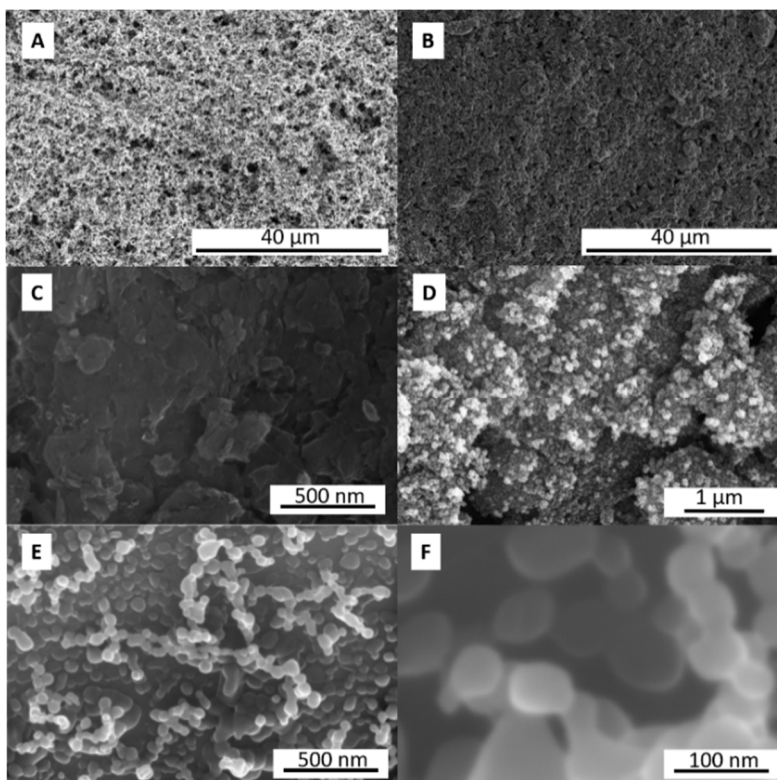


Figure 5.2 SEM images of carbon cloth-GDL substrate (A), carbon cloth-GDL substrate covered with MoO₃/graphene ink (B-C), synthesized Mo₂C/graphene electrocatalyst (D-F).

Figure 5.2-A shows the highly-porous carbon network of the carbon cloth-GDL (GDL side) used as a substrate for the synthesis reaction. After drop-casting the ink MoO₃/graphene ink, the substrate was shown to be covered with a homogenous layer of precursor material (Figure 5.2-B and Figure 5.2-C). After PFS, spherical nanoparticles of about 10-50 nm were observed on the surface (Figure 5.2-D, Figure 5.2-E and Figure 5.2-F). The formation of the particles was

homogenously dispersed over the surface exposed to the lamp light. The crystalline phase composition of the synthesized material (Mo₂C@575V-4p) was determined by X-ray diffraction (XRD). When the MoO₃ precursors was light-flashed, the resulting product shows the characteristic diffraction peaks at 34.6°, 38.0°, 39.8°, 53.9°, 62°, 69.9° and 74.9° corresponding to the (100), (002), (101), (102), (110), (103), and (112) planes of hexagonal close-packed ABAB β-Mo₂C structure respectively.^{46,49,50} This confirms the successful synthesis of crystalline β-Mo₂C nanoparticles over graphene sheets from the decomposition of molybdenum oxide (MoO₃) at high temperature using PFS. A prominent shoulder peak at 26.2° after PFS in Figure 5.3 is associated with the characteristic (002) plane of layered graphite, which in the present case corresponds to few layered mildly-edges oxidized graphene nanosheet (EOGN) representing an interlayer distance of ~0.35 nm. Mo₂C crystallite size was also calculated using the Debye Scherrer equation using the peak broadening at 39.8° which was 20 nm, corroborating with the SEM observations. A comparative broader peak at 26° comes from the carbon of the cloth substrate (Appendix V-1).

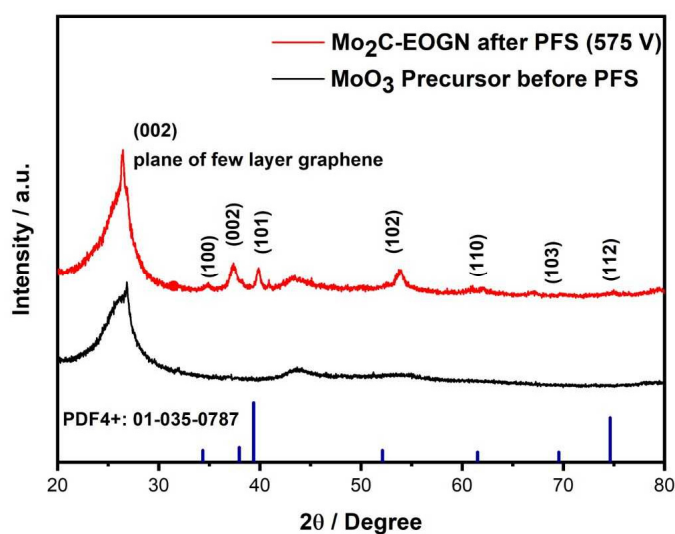


Figure 5.3 X-ray diffraction pattern of molybdenum precursor/EOGN before and after PFS.

To probe the evolution of the surface electronic state and the composition throughout the catalyst preparation, X-ray photoelectron spectroscopy (XPS) was performed over both MoO₃/Graphene precursor ink and Mo₂C@575V-4p. The C1s spectrum (Figure 5.5-a) of MoO₃/Graphene sample presents a main peak at a binding energy of 284.0 eV associated to the presence of graphene oxides (C=C, *sp*²). Smaller other peaks are observed at binding energy of 284.5, 285.6, 287.8 and 291 eV corresponding to C-C(*sp*³), C-O, C=O and C-F, respectively. The signal of fluorine is believed to reflect the presence of a fluorinated polymer in the

composition of the gas diffusion layer of the carbon substrate. After flashing the MoO₃/graphene ink (Figure 5.5-d), a clear peak attributed to Mo-C bonding is observed at binding energy of 283.3 eV for Mo₂C@575V-4p, which confirms the successful thermal decomposition of MoO₃ into Mo₂C. The Mo 3d spectra (Figure 5.5-b, Figure 5.5-e and Figure 5.5-h) were well-fitted into deconvolution analysis, and four oxidation states were determined for Mo species (+II, +IV, +V, +VI).⁵¹ The spectrum of MoO₃/Graphene ink was dominated by a doublet with two sharp peaks located at 232.4 and 235.7 eV which came from Mo⁶⁺ species (MoO₃). No peaks that corresponded to Mo²⁺ (Mo₂C) were observed. After PFS process, Mo₂C@575V-4p Mo 3d spectrum (Figure 5.5-e) displays a new dominant doublet at 228.2 and 231.4 eV corresponding to Mo 3d_{5/2} and Mo 3d_{3/2} of Mo₂C, along with MoO₃ doublet weakening, confirming the formation of Mo₂C from MoO₃ thermal decomposition. Furthermore, a simple quantitative analysis of the relative atomic concentration of Mo (Mo 3d Mo₂C) and C (C1s Carbides) confirmed the stoichiometric ratio of Mo₂C (2:1). Detailed information about percentage concentration for each species are available in Appendix V-1.

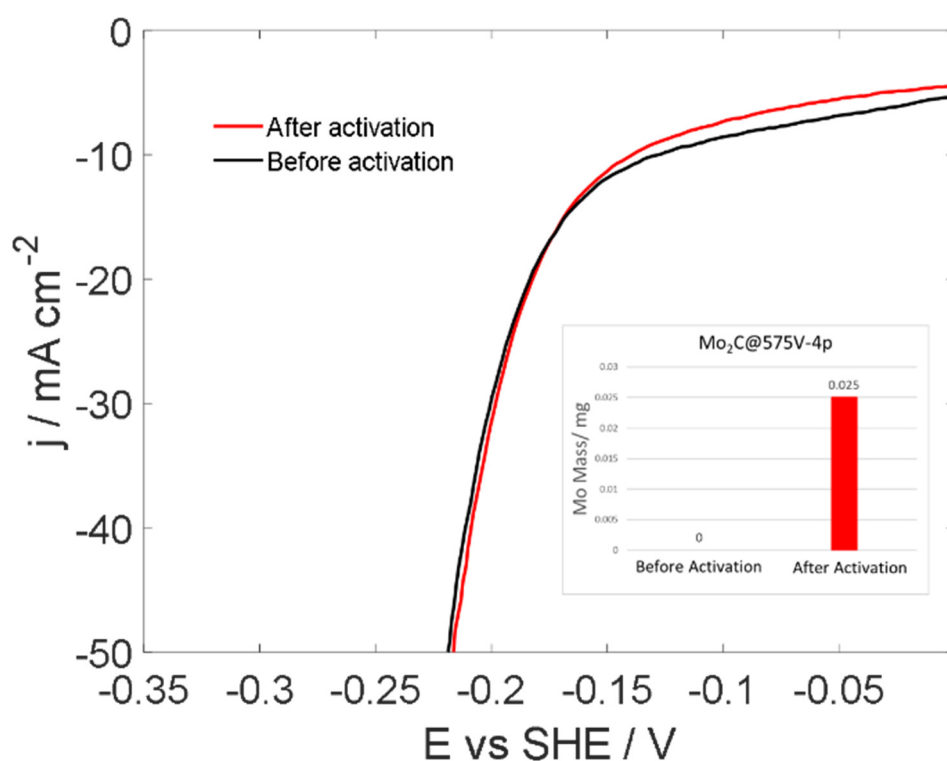


Figure 5.4 Cathodic polarization curves of Mo₂C@575V-4p before and after activation at controlled-current electrolysis at $-20 \text{ mA} \cdot \text{cm}^{-2}$ in 1 M H₂SO₄ for 20 minutes. Inset: Amount of dissolved molybdenum measured by ICP-MS in the analyte before and after activation of Mo₂C@575V-4p.

In order to remove the traces of oxides, an activation protocol was achieved on freshly-prepared Mo₂C-based by carrying out a galvanostatic electrolysis for 20 min at 20 mA·cm⁻², as depicted in Figure 5.4. Although negligible changes were observed on the intrinsic activities, we believe the removal of oxides is important to enhance the conductivity and the wettability of the catalytic material. The effect of the activation was further probed by XPS analysis of the catalytic surface before and after the activation. The analysis revealed a significant contamination of the surface with MoO₃ before activation (Figure 5.5-e and Figure 5.5-f), which corresponds to unreacted precursors. Besides, another doublet appears at binding energy of 229.2 and 232.4 eV that came from MoO₂ that might be a side-product of the thermal reduction of MoO₃ (Appendix V-2).²⁸ Similarly, O1s spectrum displays a dominant peak at 530.3 eV that was assigned to Mo-O (Figure 5.5-f) on freshly-prepared Mo₂C@575V-4p (before activation), while the shoulder at 531.7 eV related to the others oxygen bindings (OH groups,...). After carrying out the electrochemical activation process, the Mo-O signal (O1s) spectrum and the signal for Mo⁴⁺, Mo⁵⁺, and Mo⁶⁺ (Mo 3d) greatly diminished. In addition, the amount of dissolved molybdenum after activation was measured by ICP-MS to about 0.025 mg. Only few traces of molybdenum oxides were remaining on the catalytic surface, ascertaining the necessity for activation process to remove residual surface molybdenum oxides (Figure 5.5). The remaining oxides might be due to the unavoidable air oxidation on the surface as we operate in ambient atmosphere. The activity and the stability of the as-prepared Mo₂C-based materials catalyst towards HER were investigated by electrochemical characterization. The voltage of the lamp flash and the number of pulsed were varied to determine optimal process conditions. The prepared samples and their corresponding PFS parameters are summarized in Table 5.1.

Table 5.1 Photonic flashing synthesis conditions for the various prepared Mo₂C samples.

Sample	Lamp distance /mm	PFS Voltage /V	Pulses number
Mo ₂ C@575V-1p	2	575	1
Mo ₂ C@575V-2p	2	575	2
Mo ₂ C@575V-3p	2	575	3
Mo ₂ C@575V-4p	2	575	4
Mo ₂ C@300V-3p	2	300	3
Mo ₂ C@450V-3p	2	450	3

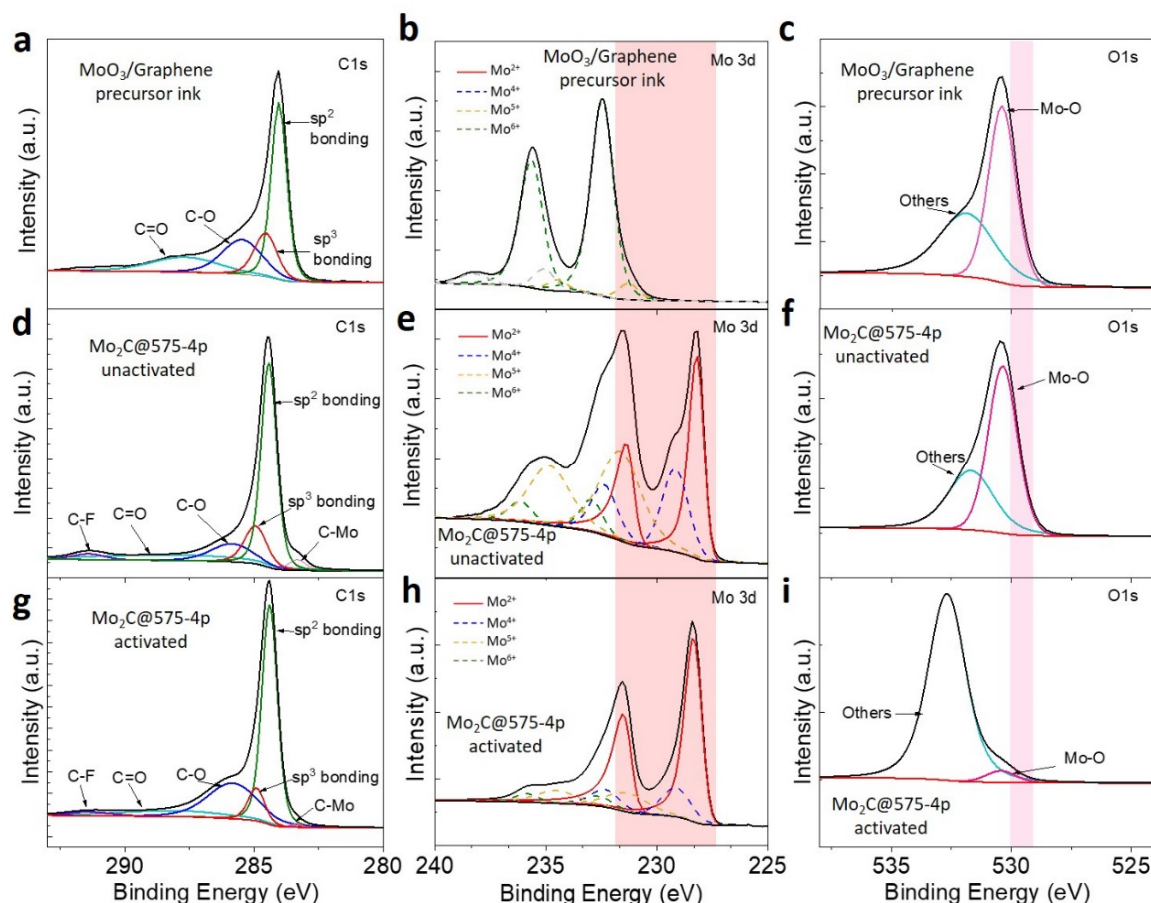


Figure 5.5 XPS spectra: (a) C1s spectrum of MoO₃/Graphene precursor ink (b) Mo 3d spectrum of MoO₃/Graphene precursor ink (c) C1s spectrum of MoO₃/Graphene precursor ink (d) C1s spectrum of Mo₂C@575V-4p before activation (e) Mo 3d spectrum of Mo₂C@575V-4p before activation (f) C1s spectrum of Mo₂C@575V-4p before activation (g) C1s spectrum of Mo₂C @575V-4p after activation (h) Mo 3d spectrum of Mo₂C @575V-4p after activation (i) C1s spectrum of Mo₂C @575V-4p after activation.

The catalytic activity of each sample was determined by LSV-based Tafel slopes analysis and electrochemical impedance spectroscopy in 1 M H₂SO₄. The ohmic drop was corrected to compensate the external resistance, which was measured by impedance spectroscopy. For comparison, the activity of the carbon substrate electrode, the MoO₃/Graphene precursor ink and platinum electrode were studied. It is worth to note that all the current densities in Figure 5.6 were calculated from the geometrical surface area to allow accurate comparison between every samples. In fact, it is difficult to isolate with precision the Mo₂C active surface area in presence of carbon material with a very high surface area (gas diffusion layer and graphene). Figure 5.6-A and Figure 5.6-B show the resulting polarizations curves (Linear Sweep Voltammetry (LSV), scan rate of 0.01 V·s⁻¹). In agreement with previous reports,^{52,53} Pt and carbon electrode respectively exhibits polarization curve with onset overpotential close to ~ 0 mV and ~ - 400 mV and a Tafel slope around 37 mV·dec⁻¹ and 185 mV·dec⁻¹ (Figure 5.6 A

and Figure 5.6-D). After drop-casting the MoO₃/graphene ink, the electrode presents an activity comparable to the carbon substrate. Among all Mo₂C-based electrode prepared by PFS, the as-prepared Mo₂C@575V-4p achieves a very high activity towards HER with a small onset overpotential of about 140 mV. Furthermore, the overpotential required to drive a current density of 10 mA·cm⁻² (η_{10}) and 50 mA·cm⁻² (η_{50}) were observed at ~160 mV and ~230 mV, respectively. The resulting Tafel slope was measured to be 63 mV·dec⁻¹. As shown on Table 5.2, the activity of the prepared catalyst competes with the best activities of reported β -Mo₂C catalyst prepared from other approaches. To corroborate those results, electrochemical impedance spectroscopy (EIS) was performed. Figure 5.6-C displays the Nyquist impedance curves of the MoO₃/Graphene and Mo₂C@575V-4p (after activation) with an overpotential of 250 mV scanning from 100 kHz to 1 Hz. The experimental data were fitted using a two-time constant model including the external resistance (R_s) in series with a parallel constant phase element-resistance (CPE-R) representing the charge transfer resistance towards HER. The diameter of the semi-circle was shown to drastically decrease after the photonic flashing of the precursor with a resulting charge resistance transfer of about 50 Ω ·cm⁻². The HER performances of the prepared Mo₂C samples correlate with the increase of the photonic flash voltage (Figure 5.6-A) and the number of successive pulses (Figure 5.6-B). As the voltage increased from ~300 to ~575 V, the η_{50} was decreased from ~410 to ~245 mV (3 successive pulses). Furthermore, η_{50} decreased up from ~270 mV to ~230 mV when increasing the pulses from 1 to 4 for a lamp voltage of 575 V. Further increasing the pulses number showed no significant improvement. The improvement in performance is believed to be associated to an increase of local temperature enhancing the yield of MoO₃ decomposition, and thus the amount of Mo₂C active sites per geometric area.

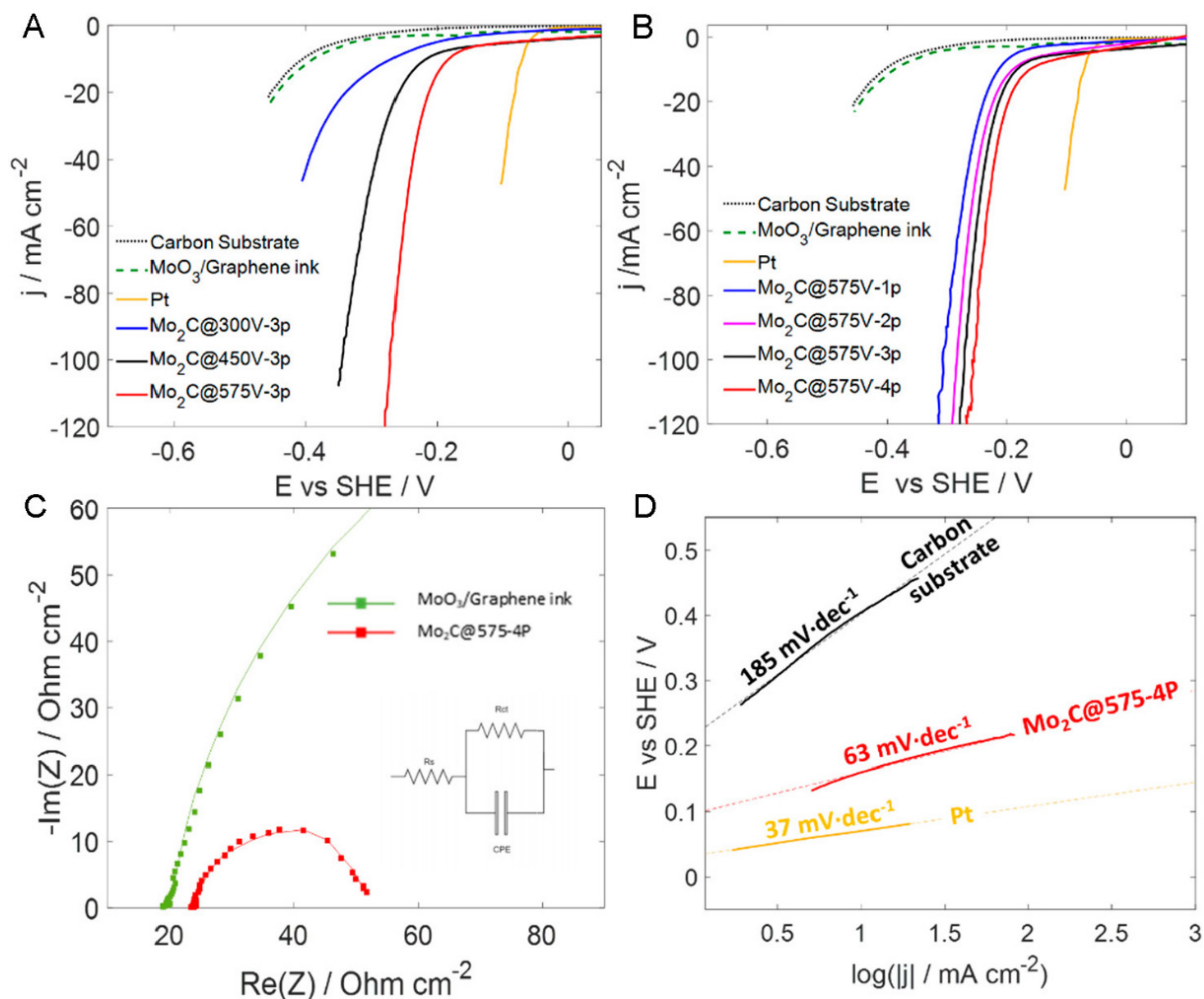


Figure 5.6 (A) Cathodic polarization curves at scan rate of $10 \text{ mV} \cdot \text{s}^{-1}$ in $1 \text{ M H}_2\text{SO}_4$ of MoO₃/Graphene precursor ink, Mo₂C@300V-3p, Mo₂C@450V-3p, Mo₂C@575V-3p, carbon substrate (with GDL) and Pt electrode. (B) Cathodic polarization curves at scan rate of $10 \text{ mV} \cdot \text{s}^{-1}$ in $1 \text{ M H}_2\text{SO}_4$ of MoO₃/Graphene precursor ink, Mo₂C@575V-1p, Mo₂C@575V-2p, Mo₂C@575V-3p, Mo₂C@575V-4p, carbon substrate (with GDL) and Pt electrode. (C) Electrochemical impedance spectra of MoO₃/Graphene precursor ink and Mo₂C@575V-4p. Inset is the simplified Randles equivalent electrical circuit used to model the electrode set-up, where R_s is the internal resistance (from the working electrode to the reference electrode), R_{ct} is the charge transfer resistance, and CPE denotes the constant phase element (related to the double-layer capacitance). (D) The resulting Tafel plot of carbon substrate, Mo₂C@575V-4p, and Pt electrode.

In addition, we normalized the currents from the polarization curves by the electrochemically active surface area (ECSA) measured from the double-layer capacitance of the electrode surface (Figure 5.7). The ECSA was roughly estimated by dividing the obtained double-layer capacitance by the reported general specific capacitance of $C_s = 0.035 \text{ mF} \cdot \text{cm}^{-2}$.⁵⁴ As shown on Figure 5.9, we observed a gradual increase of the ECSA while varying the pulses from 1 to 4, which might be related to the increase of Mo₂C nanoparticles density per geometric surface.

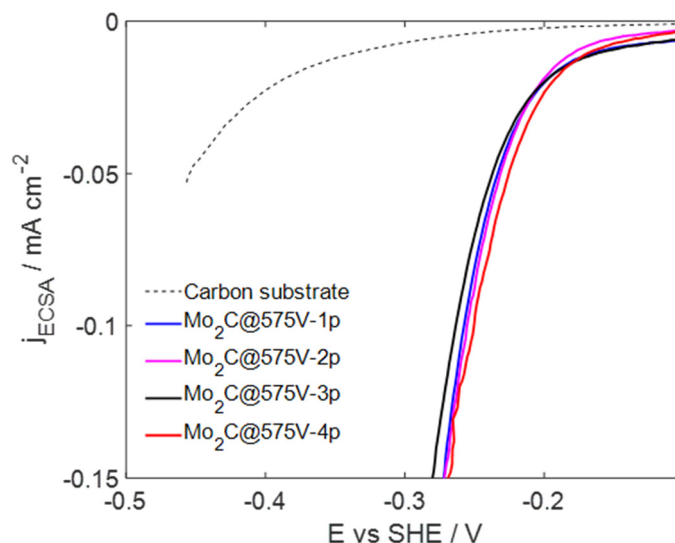


Figure 5.7 Polarization curves normalized by ECSA for carbon substrate, $\text{Mo}_2\text{C}@575\text{V-1p}$, $\text{Mo}_2\text{C}@575\text{V-2p}$, $\text{Mo}_2\text{C}@575\text{V-3p}$, $\text{Mo}_2\text{C}@575\text{V-4p}$.

Furthermore, the short-term stability of the catalytic material which had the best catalytic performance towards HER ($\text{Mo}_2\text{C}@575\text{V-4p}$) was investigated by controlled-current electrolysis. The sample was held at $-20 \text{ mA}\cdot\text{cm}^{-2}$ in 1 M H_2SO_4 under agitation in order to reproduce the practical working conditions of the catalyst. After 10 hours of constant polarisation, moderate change was observed in the polarisation curves and the overpotential to drive $-20 \text{ mA}\cdot\text{cm}^{-2}$ (Figure 5.8), confirming the significant stability of the $\text{Mo}_2\text{C}@575\text{V-4p}$ electrocatalyst prepared by photonic flashing synthesis.

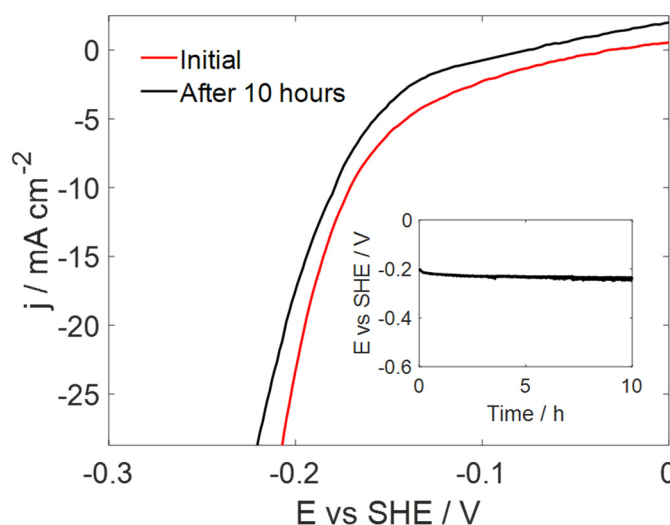


Figure 5.8 Cathodic polarization curves of $\text{Mo}_2\text{C}@575\text{V-4P}$ before and after 10 hours of controlled-current electrolysis at $-20 \text{ mA}\cdot\text{cm}^{-2}$ in 1 M H_2SO_4 . Inset is the time-dependent potential of $\text{Mo}_2\text{C}@575\text{V-4P}$ under a static cathodic current of $20 \text{ mA}\cdot\text{cm}^{-2}$.

Table 5.2 Comparison of performances of various representative Mo₂C-based catalysts for HER.

Catalyst	Method	Media	$\eta_{10\text{ mA}\cdot\text{cm}^{-2}}$	C_{dl} /mF·cm ⁻²	Tafel slope	Stability	Ref.
Bulk Mo₂C	Commercially available	1 M H ₂ SO ₄	210		56	48h	4
Mo₂C-NP	Annealing (4h at 800°C under flowing Ar)	0.5 M H ₂ SO ₄	167	11.56	73	10h	55
Mo₂C-NT	Annealing (16h at 750°C under flowing N ₂)	0.5 M H ₂ SO ₄	172	-	62	8h	19
Mo₂C/ Graphene	Annealing (2h at 900°C under flowing Ar)	0.5 M H ₂ SO ₄	150	-	57	20h	56
Mo₂C-Nanowires	Annealing (5h at 725°C under flowing Ar)	0.5 M H ₂ SO ₄	- ($\eta_{60}=200\text{mV}$)	~9.5	53	25h	15
Mo₂C/ Graphene	CVD on liquid Sn-Cu-Mo alloy (880-1050°C under flowing CH ₄ /H ₂ mixture, 7 Torr)	0.5 M H ₂ SO ₄	275	0.22	66	-	29
Mo₂C/ Graphene	CVD in Cu vapors (950°C under flowing CH ₄ /H ₂ mixture, 4 Torr)	0.5 M H ₂ SO ₄	270		56	-	30
Mo₂C-NP/ Graphene	Microwave irradiation (10s)	0.5 M H ₂ SO ₄	200	13.7	88	10h	32
Mo₂C-NP/ CNT	Microwave irradiation (10s)	0.5 M H ₂ SO ₄	182	6.3	84	10h	32
Mo₂C-NP/ CF	Microwave irradiation (10s)	0.5 M H ₂ SO ₄	166	-	80	100h	32
Mo₂C-NP Graphene	Photonic flash synthesis (few seconds)	1 M H ₂ SO ₄	160	20	63	13h	This work

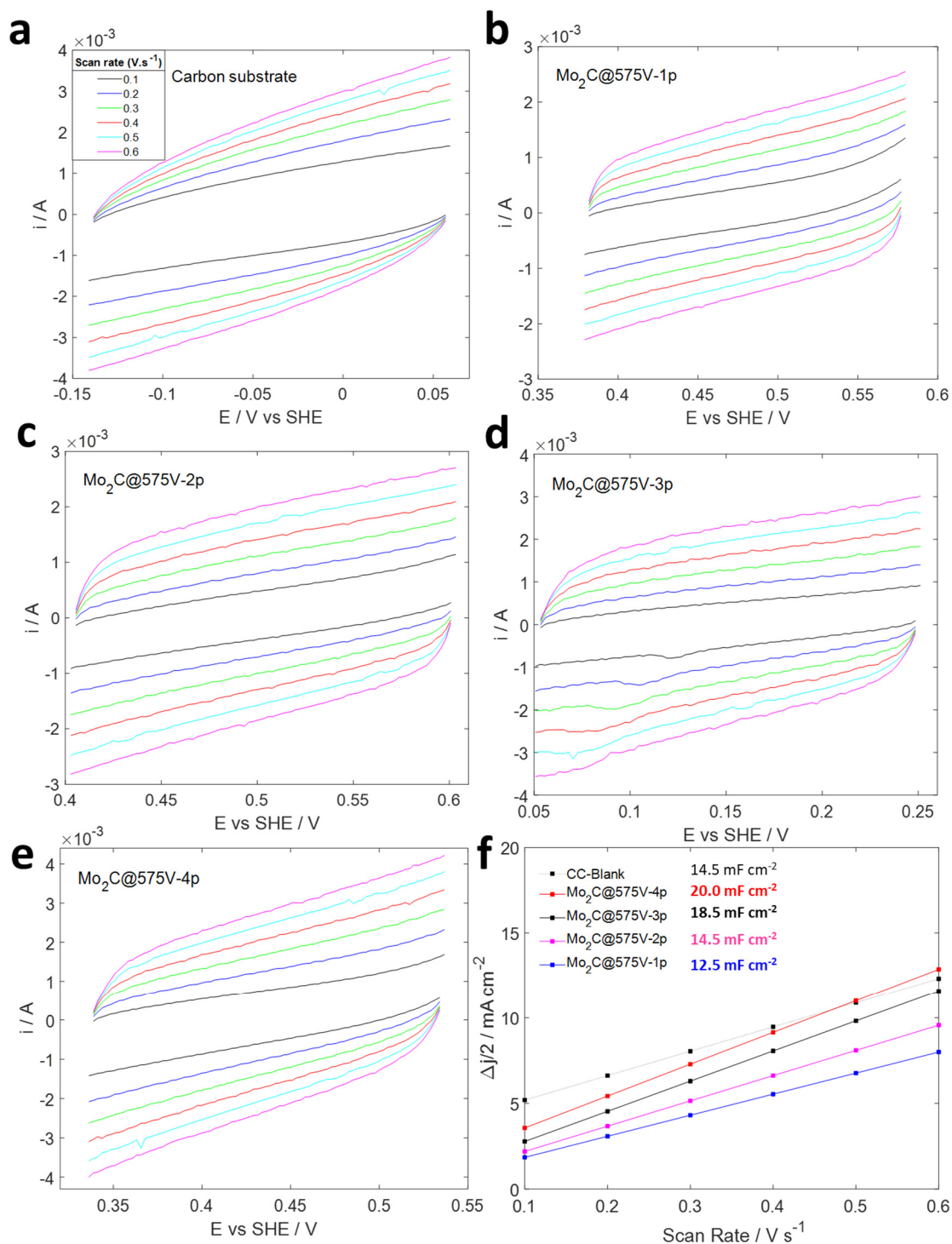


Figure 5.9 (a-e) Cyclic voltammograms at scan-rate comprised between 0.1 to 0.6 V·s⁻¹ in the potential range: [OCP - 0.05 V, OCP + 0.05 V] for the different electrodes: (a) Carbon substrate (b) Mo₂C@575-1p (c) Mo₂C@575-2p (d) Mo₂C@575-3p (e) Mo₂C@575-4p. (f) Plots of the non-faradaic current measured at the OCP in function of the scan-rate with the resulting measured specific capacitance for the carbon substrate, Mo₂C@575-1p, Mo₂C@575-2p, Mo₂C@575-3p and Mo₂C@575-4p.

5.4 Conclusion

In this chapter, a simple and fast two-step process has been developed using PFS to synthesize Mo₂C-based electrocatalysts with carbon cloth (including GDL) as carbon source and MoO₃/Graphene ink as Mo precursor. The formation of a homogenous layer of β -Mo₂C nanoparticles over the carbon substrate after four successive pulses at 575V was confirmed by SEM, XPS and XRD analysis. An activation process was noticed to remove the residual molybdenum oxides over the catalytic surface. The activity of the catalyst was shown to increase with the flash lamp voltage and the number of successive pulses during the PFS. We interpret those improvements by an enhancement of the yield of MoO₃ thermal decomposition, resulting in a higher amount of Mo₂C over the surface. Mo₂C@575V-4p was demonstrated to exhibit surprisingly high activity towards HER in acidic conditions. In fact, the nanostructures of Mo₂C achieved low overpotential of 160 mV to drive a current density of 10 mA·cm⁻² (η_{10}) and an excellent electrochemical stability over catalytic conditions.

Regarding the vanadium-manganese redox dual-flow battery, the proposed synthetic route offers the opportunity to design rapidly and efficiently catalytic reactors to perform the redox-mediated hydrogen evolution reaction. This chapter demonstrates the promising future of PFS for carbides electrocatalysts synthesis and open the way for many other material syntheses such electrocatalytic electrodes to carry redox-mediated oxygen evolution reaction.

Furthermore, it is important to mention that the present process is well adapted to the industrial large-scale production of electrocatalytic carbon electrodes and membrane electrode assemblies (MEA). Indeed, the dropcasting of the precursor can be easily replaced by inkjet printing or other liquid deposition processes, and the photonic light synthesis can easily be adapted to a continuous reel-to-reel production process as commonly performed in printed electronic applications. All in all, the present chapter provides opportunities for the development of industrial applications in the growing field of electrocatalytic electrodes.

References

- (1) Ma, Y.; Guan, G.; Hao, X.; Cao, J.; Abudula, A. Molybdenum Carbide as Alternative Catalyst for Hydrogen Production – A Review. *Renewable and Sustainable Energy Reviews* **2017**, *75*, 1101–1129. <https://doi.org/10.1016/j.rser.2016.11.092>.
- (2) Luo, Y.; Wang, Z.; Fu, Y.; Jin, C.; Wei, Q.; Yang, R. In Situ Preparation of Hollow Mo₂C–C Hybrid Microspheres as Bifunctional Electrocatalysts for Oxygen Reduction and Evolution Reactions. *Journal of Materials Chemistry A* **2016**, *4* (32), 12583–12590. <https://doi.org/10.1039/C6TA04654A>.
- (3) Wolden, C. A.; Pickerell, A.; Gawai, T.; Parks, S.; Hensley, J.; Way, J. D. Synthesis of β -Mo₂C Thin Films. *ACS Appl. Mater. Interfaces* **2011**, *3* (2), 517–521. <https://doi.org/10.1021/am101095h>.
- (4) Vrubel, H.; Hu, X. Molybdenum Boride and Carbide Catalyze Hydrogen Evolution in Both Acidic and Basic Solutions. *Angewandte Chemie International Edition* **2012**, *51* (51), 12703–12706. <https://doi.org/10.1002/anie.201207111>.
- (5) Reynard, D.; Bolik-Coulon, G.; Maye, S.; Girault, H. H. Hydrogen Production on Demand by Redox-Mediated Electrocatalysis: A Kinetic Study. *Chemical Engineering Journal* **2021**, *407*, 126721. <https://doi.org/10.1016/j.cej.2020.126721>.
- (6) Yang, W.; Chen, S. Recent Progress in Electrode Fabrication for Electrocatalytic Hydrogen Evolution Reaction: A Mini Review. *Chemical Engineering Journal* **2020**, *393*, 124726. <https://doi.org/10.1016/j.cej.2020.124726>.
- (7) G. Morales-Guio, C.; Stern, L.-A.; Hu, X. Nanostructured Hydrotreating Catalysts for Electrochemical Hydrogen Evolution. *Chemical Society Reviews* **2014**, *43* (18), 6555–6569. <https://doi.org/10.1039/C3CS60468C>.
- (8) Gavrilova, N.; Dyakonov, V.; Myachina, M.; Nazarov, V.; Skudin, V. Synthesis of Mo₂C by Thermal Decomposition of Molybdenum Blue Nanoparticles. *Nanomaterials (Basel)* **2020**, *10* (10). <https://doi.org/10.3390/nano10102053>.
- (9) Volpe, L.; Boudart, M. Compounds of Molybdenum and Tungsten with High Specific Surface Area: II. Carbides. *Journal of Solid State Chemistry* **1985**, *59* (3), 348–356. [https://doi.org/10.1016/0022-4596\(85\)90302-0](https://doi.org/10.1016/0022-4596(85)90302-0).
- (10) Zhang, A.; Zhu, A.; Chen, B.; Zhang, S.; Au, C.; Shi, C. In-Situ Synthesis of Nickel Modified Molybdenum Carbide Catalyst for Dry Reforming of Methane. *Catalysis Communications* **2011**, *12* (9), 803–807. <https://doi.org/10.1016/j.catcom.2011.01.019>.
- (11) Zhang, S.; Shi, C.; Chen, B.; Zhang, Y.; Zhu, Y.; Qiu, J.; Au, C. Catalytic Role of β -Mo₂C in DRM Catalysts That Contain Ni and Mo. *Catalysis Today* **2015**, *258*, 676–683. <https://doi.org/10.1016/j.cattod.2015.01.014>.
- (12) Fan, M.; Chen, H.; Wu, Y.; Feng, L.-L.; Liu, Y.; Li, G.-D.; Zou, X. Growth of Molybdenum Carbide Micro-Islands on Carbon Cloth toward Binder-Free Cathodes for Efficient Hydrogen Evolution Reaction. *Journal of Materials Chemistry A* **2015**, *3* (31), 16320–16326. <https://doi.org/10.1039/C5TA03500G>.
- (13) Yan, Q.; Yang, X.; Wei, T.; Zhou, C.; Wu, W.; Zeng, L.; Zhu, R.; Cheng, K.; Ye, K.; Zhu, K.; Yan, J.; Cao, D.; Wang, G. Porous β -Mo₂C Nanoparticle Clusters Supported on Walnut Shell Powders Derived Carbon Matrix for Hydrogen Evolution Reaction. *Journal of Colloid and Interface Science* **2020**, *563*, 104–111. <https://doi.org/10.1016/j.jcis.2019.12.059>.
- (14) Han, J.; Duan, J.; Chen, P.; Lou, H.; Zheng, X.; Hong, H. Nanostructured Molybdenum Carbides Supported on Carbon Nanotubes as Efficient Catalysts for One-Step Hydrodeoxygenation and Isomerization of Vegetable Oils. *Green Chem.* **2011**, *13* (9), 2561–2568. <https://doi.org/10.1039/C1GC15421D>.

- (15) Liao, L.; Wang, S.; Xiao, J.; Bian, X.; Zhang, Y.; D. Scanlon, M.; Hu, X.; Tang, Y.; Liu, B.; H. Girault, H. A Nanoporous Molybdenum Carbide Nanowire as an Electrocatalyst for Hydrogen Evolution Reaction. *Energy & Environmental Science* **2014**, 7 (1), 387–392. <https://doi.org/10.1039/C3EE42441C>.
- (16) Chen, W.-F.; Wang, C.-H.; Sasaki, K.; Marinkovic, N.; Xu, W.; Muckerman, J. T.; Zhu, Y.; Adzic, R. R. Highly Active and Durable Nanostructured Molybdenum Carbide Electrocatalysts for Hydrogen Production. *Energy Environ. Sci.* **2013**, 6 (3), 943–951. <https://doi.org/10.1039/C2EE23891H>.
- (17) Zhang, K.; Zhao, Y.; Fu, D.; Chen, Y. Molybdenum Carbide Nanocrystal Embedded N-Doped Carbon Nanotubes as Electrocatalysts for Hydrogen Generation. *J. Mater. Chem. A* **2015**, 3 (11), 5783–5788. <https://doi.org/10.1039/C4TA06706A>.
- (18) Highly Active and Stable Hydrogen Evolution Electrocatalysts Based on Molybdenum Compounds on Carbon Nanotube–Graphene Hybrid Support | ACS Nano <https://pubs.acs.org/doi/10.1021/nn5012144> (accessed 2020 -11 -16).
- (19) Ma, F.-X.; Wu, H. B.; Xia, B. Y.; Xu, C.-Y.; Lou, X. W. (David). Hierarchical β -Mo₂C Nanotubes Organized by Ultrathin Nanosheets as a Highly Efficient Electrocatalyst for Hydrogen Production. *Angewandte Chemie International Edition* **2015**, 54 (51), 15395–15399. <https://doi.org/10.1002/anie.201508715>.
- (20) In Situ Preparation of Mo₂C Nanoparticles Embedded in Ketjenblack Carbon as Highly Efficient Electrocatalysts for Hydrogen Evolution | ACS Sustainable Chemistry & Engineering <https://pubs.acs.org/doi/10.1021/acssuschemeng.7b03317> (accessed 2021 -01 -28).
- (21) Kaewpanha, M.; Guan, G.; Ma, Y.; Hao, X.; Zhang, Z.; Reubroychareon, P.; Kusakabe, K.; Abudula, A. Hydrogen Production by Steam Reforming of Biomass Tar over Biomass Char Supported Molybdenum Carbide Catalyst. *International Journal of Hydrogen Energy* **2015**, 40 (25), 7974–7982. <https://doi.org/10.1016/j.ijhydene.2015.04.068>.
- (22) Ma, Y.; Guan, G.; Phanthong, P.; Li, X.; Cao, J.; Hao, X.; Wang, Z.; Abudula, A. Steam Reforming of Methanol for Hydrogen Production over Nanostructured Wire-like Molybdenum Carbide Catalyst. *International Journal of Hydrogen Energy* **2014**, 39 (33), 18803–18811. <https://doi.org/10.1016/j.ijhydene.2014.09.062>.
- (23) Giordano, C.; Erpen, C.; Yao, W.; Antonietti, M. Synthesis of Mo and W Carbide and Nitride Nanoparticles via a Simple “Urea Glass” Route. *Nano Lett.* **2008**, 8 (12), 4659–4663. <https://doi.org/10.1021/nl8018593>.
- (24) Ma, L.; Lin Ting, L. R.; Molinari, V.; Giordano, C.; Siang Yeo, B. Efficient Hydrogen Evolution Reaction Catalyzed by Molybdenum Carbide and Molybdenum Nitride Nanocatalysts Synthesized via the Urea Glass Route. *Journal of Materials Chemistry A* **2015**, 3 (16), 8361–8368. <https://doi.org/10.1039/C5TA00139K>.
- (25) Gu, Y.; Li, Z.; Chen, L.; Ying, Y.; Qian, Y. Synthesis of Nanocrystalline Mo₂C via Sodium Co-Reduction of MoCl₅ and CBr₄ in Benzene. *Materials Research Bulletin* **2003**, 38 (7), 1119–1122. [https://doi.org/10.1016/S0025-5408\(03\)00132-6](https://doi.org/10.1016/S0025-5408(03)00132-6).
- (26) Hyeon, T.; Fang, M.; Suslick, K. S. Nanostructured Molybdenum Carbide: Sonochemical Synthesis and Catalytic Properties. *J. Am. Chem. Soc.* **1996**, 118 (23), 5492–5493. <https://doi.org/10.1021/ja9538187>.
- (27) Nakajima, T.; Shirasaki, T. Chemical Vapor Deposition of Tungsten Carbide, Molybdenum Carbide Nitride, and Molybdenum Nitride Films. *J. Electrochem. Soc.* **1997**, 144 (6), 2096. <https://doi.org/10.1149/1.1837747>.
- (28) He, M.; Shi, H.; Wang, P.; Sun, X.; Gao, B. Porous Molybdenum Carbide Nanostructures Synthesized on Carbon Cloth by CVD for Efficient Hydrogen Production. *Chemistry –*

- A European Journal* **2019**, 25 (70), 16106–16113. <https://doi.org/10.1002/chem.201904100>.
- (29) Chaitoglou, S.; Giannakopoulou, T.; Speliotis, T.; Vavouliotis, A.; Trapalis, C.; Dimoulas, A. Mo₂C/Graphene Heterostructures: Low Temperature Chemical Vapor Deposition on Liquid Bimetallic Sn–Cu and Hydrogen Evolution Reaction Electrocatalytic Properties. *Nanotechnology* **2019**, 30 (12), 125401. <https://doi.org/10.1088/1361-6528/aaf9e8>.
- (30) Chaitoglou, S.; Giannakopoulou, T.; Papanastasiou, G.; Tsoutsou, D.; Vavouliotis, A.; Trapalis, C.; Dimoulas, A. Cu Vapor-Assisted Formation of Nanostructured Mo₂C Electrocatalysts via Direct Chemical Conversion of Mo Surface for Efficient Hydrogen Evolution Reaction Applications. *Applied Surface Science* **2020**, 510, 145516. <https://doi.org/10.1016/j.apsusc.2020.145516>.
- (31) Pang, M.; Li, C.; Ding, L.; Zhang, J.; Su, D.; Li, W.; Liang, C. Microwave-Assisted Preparation of Mo₂C/CNTs Nanocomposites as Efficient Electrocatalyst Supports for Oxygen Reduction Reaction. *Ind. Eng. Chem. Res.* **2010**, 49 (9), 4169–4174. <https://doi.org/10.1021/ie901741c>.
- (32) Huang, H.; Yu, C.; Huang, H.; Guo, W.; Zhang, M.; Han, X.; Wei, Q.; Cui, S.; Tan, X.; Qiu, J. Microwave-Assisted Ultrafast Synthesis of Molybdenum Carbide Nanoparticles Grown on Carbon Matrix for Efficient Hydrogen Evolution Reaction. *Small Methods* **2019**, 3 (11), 1900259. <https://doi.org/10.1002/smt.201900259>.
- (33) Bystrov, Yu. A.; Vetrov, N. Z.; Lisenkov, A. A. Plasmachemical Synthesis of Carbide Compounds in Metal-Containing Plasma Jet from Vacuum Arc Discharge. *Tech. Phys. Lett.* **2008**, 34 (9), 734–736. <https://doi.org/10.1134/S1063785008090046>.
- (34) Albrecht, A.; Rivadeneyra, A.; Abdellah, A.; Lugli, P.; Salmerón, J. F. Inkjet Printing and Photonic Sintering of Silver and Copper Oxide Nanoparticles for Ultra-Low-Cost Conductive Patterns. *J. Mater. Chem. C* **2016**, 4 (16), 3546–3554. <https://doi.org/10.1039/C6TC00628K>.
- (35) Costa Bassetto, V.; Oliveira Silva, W.; Pereira, C. M.; Girault, H. H. Flash Light Synthesis of Noble Metal Nanoparticles for Electrochemical Applications: Silver, Gold, and Their Alloys. *J Solid State Electrochem* **2020**, 24 (8), 1781–1788. <https://doi.org/10.1007/s10008-020-04521-5>.
- (36) Lesch, A. Print-Light-Synthesis of Platinum Nanostructured Indium-Tin-Oxide Electrodes for Energy Research. *Advanced Materials Technologies* **2018**, 3 (2), 1700201. <https://doi.org/10.1002/admt.201700201>.
- (37) Rosen, Y. S.; Yakushenko, A.; Offenhäusser, A.; Magdassi, S. Self-Reducing Copper Precursor Inks and Photonic Additive Yield Conductive Patterns under Intense Pulsed Light. *ACS Omega* **2017**, 2 (2), 573–581. <https://doi.org/10.1021/acsomega.6b00478>.
- (38) Cronin, H. M.; Stoeva, Z.; Brown, M.; Shkunov, M.; Silva, S. R. P. Photonic Curing of Low-Cost Aqueous Silver Flake Inks for Printed Conductors with Increased Yield. *ACS Appl. Mater. Interfaces* **2018**, 10 (25), 21398–21410. <https://doi.org/10.1021/acsami.8b04157>.
- (39) Cote, L. J.; Cruz-Silva, R.; Huang, J. Flash Reduction and Patterning of Graphite Oxide and Its Polymer Composite. *J. Am. Chem. Soc.* **2009**, 131 (31), 11027–11032. <https://doi.org/10.1021/ja902348k>.
- (40) Chae, W.; Kim, M.; Kim, D.; Park, J.-H.; Choi, W.; Lee, J. Photo-Reduction of Graphene Oxide by Using Photographic Flash-Light. *Science of Advanced Materials* **2018**, 10 (1), 130–133. <https://doi.org/10.1166/sam.2018.2930>.
- (41) Potts, S.-J.; Lau, Y. C.; Dunlop, T.; Claypole, T.; Phillips, C. Effect of Photonic Flash Annealing with Subsequent Compression Rolling on the Topography, Microstructure

- and Electrical Performance of Carbon-Based Inks. *J Mater Sci* **2019**, *54* (11), 8163–8176. <https://doi.org/10.1007/s10853-019-03462-3>.
- (42) Silva, W. O.; Costa Bassetto, V.; Baster, D.; Mensi, M.; Oveisi, E.; Girault, H. H. Oxidative Print Light Synthesis Thin Film Deposition of Prussian Blue. *ACS Appl. Electron. Mater.* **2020**, *2* (4), 927–935. <https://doi.org/10.1021/acsaelm.9b00854>.
- (43) Jongerius, A. L.; Gosselink, R. W.; Dijkstra, J.; Bitter, J. H.; Bruijninx, P. C. A.; Weckhuysen, B. M. Carbon Nanofiber Supported Transition-Metal Carbide Catalysts for the Hydrodeoxygenation of Guaiacol. *ChemCatChem* **2013**, *5* (10), 2964–2972. <https://doi.org/10.1002/cctc.201300280>.
- (44) Zhang, G.; Zhou, Y.; Yang, F. Hydrogen Production from Microbial Fuel Cells-Ammonia Electrolysis Cell Coupled System Fed with Landfill Leachate Using Mo₂C/N-Doped Graphene Nanocomposite as HER Catalyst. *Electrochimica Acta* **2019**, *299*, 672–681. <https://doi.org/10.1016/j.electacta.2019.01.055>.
- (45) Wei, H.; Xi, Q.; Chen, X.; Guo, D.; Ding, F.; Yang, Z.; Wang, S.; Li, J.; Huang, S. Molybdenum Carbide Nanoparticles Coated into the Graphene Wrapping N-Doped Porous Carbon Microspheres for Highly Efficient Electrocatalytic Hydrogen Evolution Both in Acidic and Alkaline Media. *Advanced Science* **2018**, *5* (3), 1700733. <https://doi.org/10.1002/advs.201700733>.
- (46) Nadar, A.; Banerjee, A. M.; Pai, M. R.; Antony, R. P.; Patra, A. K.; Sastry, P. U.; Donthula, H.; Tewari, R.; Tripathi, A. K. Effect of Mo Content on Hydrogen Evolution Reaction Activity of Mo₂C/C Electrocatalysts. *International Journal of Hydrogen Energy* **2020**, *45* (23), 12691–12701. <https://doi.org/10.1016/j.ijhydene.2020.02.156>.
- (47) Geim, A. K. Graphene: Status and Prospects. *Science* **2009**, *324* (5934), 1530–1534. <https://doi.org/10.1126/science.1158877>.
- (48) Geim, A. K.; Novoselov, K. S. The Rise of Graphene. *Nature Materials* **2007**, *6* (3), 183–191. <https://doi.org/10.1038/nmat1849>.
- (49) Wan, C.; Regmi, Y. N.; Leonard, B. M. Multiple Phases of Molybdenum Carbide as Electrocatalysts for the Hydrogen Evolution Reaction. *Angewandte Chemie* **2014**, *126* (25), 6525–6528. <https://doi.org/10.1002/ange.201402998>.
- (50) Yan, G.; Feng, X.; Khan, S. U.; Xiao, L.; Xi, W.; Tan, H.; Ma, Y.; Zhang, L.; Li, Y. Polyoxometalate and Resin-Derived P-Doped Mo₂C@N-Doped Carbon as a Highly Efficient Hydrogen-Evolution Reaction Catalyst at All PH Values. *Chemistry – An Asian Journal* **2018**, *13* (2), 158–163. <https://doi.org/10.1002/asia.201701400>.
- (51) Murugappan, K.; Anderson, E. M.; Teschner, D.; Jones, T. E.; Skorupska, K.; Román-Leshkov, Y. Operando NAP-XPS Unveils Differences in MoO₃ and Mo₂C during Hydrodeoxygenation. *Nature Catalysis* **2018**, *1* (12), 960–967. <https://doi.org/10.1038/s41929-018-0171-9>.
- (52) Ambrosi, A.; Sofer, Z.; Pumera, M. Lithium Intercalation Compound Dramatically Influences the Electrochemical Properties of Exfoliated MoS₂. *Small* **2015**, *11* (5), 605–612. <https://doi.org/10.1002/smll.201400401>.
- (53) Toward High-Performance and Low-Cost Hydrogen Evolution Reaction Electrocatalysts: Nanostructuring Cobalt Phosphide (CoP) Particles on Carbon Fiber Paper | ACS Applied Materials & Interfaces <https://pubs.acs.org/doi/10.1021/acsaami.8b02755> (accessed 2021 -01 -28).
- (54) McCrory, C. C. L.; Jung, S.; Peters, J. C.; Jaramillo, T. F. Benchmarking Heterogeneous Electrocatalysts for the Oxygen Evolution Reaction. *Journal of the American Chemical Society* **2013**, *135* (45), 16977–16987. <https://doi.org/10.1021/ja407115p>.
- (55) Chen, J.; Yang, H.; Xu, X.; Su, Z.; Guo, Y.; Wang, Q. Mo₂C Based Electrocatalyst with Filter Paper Derived N-Doped Mesoporous Carbon as Matrix for H₂ Production. *Applied Surface Science* **2018**, *455*, 187–194. <https://doi.org/10.1016/j.apsusc.2018.05.112>.

- (56) He, C.; Tao, J. Synthesis of Nanostructured Clean Surface Molybdenum Carbides on Graphene Sheets as Efficient and Stable Hydrogen Evolution Reaction Catalysts. *Chem. Commun.* **2015**, 51 (39), 8323–8325. <https://doi.org/10.1039/C5CC01240F>.

Appendix V

Appendix V-1: Details of XRD measurements

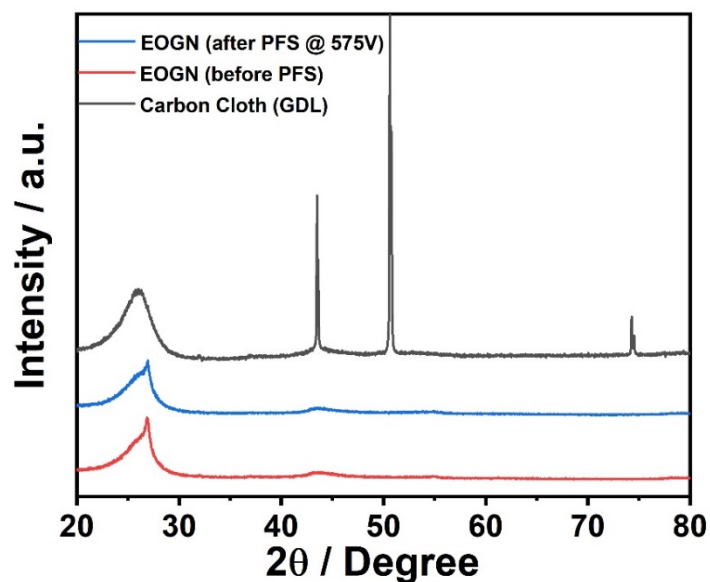


Figure A5.1 X-ray diffraction patterns of blank carbon cloth substrate (C-Cloth), C-cloth coated with edge oxidized graphene nanosheets (EOGN) unflashed and flashed.

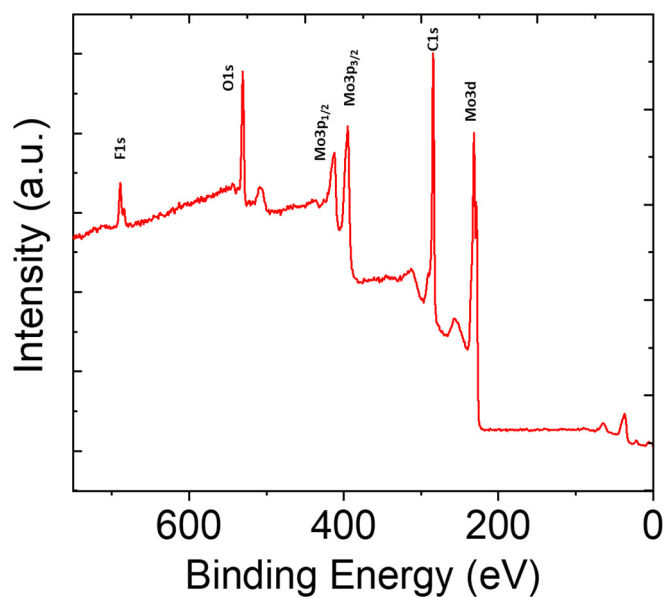


Figure A5.2 The wide spectrum of $\text{Mo}_2\text{C}@575\text{V}-4\text{p}$.

Table A5.1 XPS relative atomic concentrations of Mo and C from molybdenum carbides for MoO₃/Graphene precursor ink, Mo₂C@575V-4p before activation and Mo₂C@575V-4p after activation.

Sample Identifier	C1s Carbides CPSeV	Mo3d CPSeV	Mo ₂ C C1s Carbides %	Mo3d Mo ₂ C %
MoO ₃ /Graphene ink	0.00	$2.33 \cdot 10^{-21}$	0.00	$1.00 \cdot 10^2$
Mo ₂ C@575-4p before activation	$2.47 \cdot 10^3$	$3.97 \cdot 10^3$	38.3	61.7
Mo ₂ C@575-4p after activation	$7.01 \cdot 10^2$	$1.45 \cdot 10^3$	32.5	67.5

Table A5.2 XPS percentage concentration of various species for MoO₃/Graphene precursor ink, Mo₂C@575V-4p before activation and Mo₂C@575V-4p after activation.

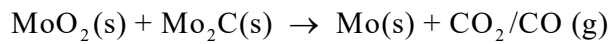
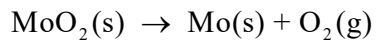
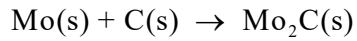
Sample Identifier	C1s sp3 %	C1s C-O %	C1s %	C=O %	C1s %	CFx %	C1s Carbides %	C1s sp2 %
MoO ₃ /Graphene ink	11.06	15.39	11.29	1.68	0.00	30.78		
Mo ₂ C@575-4p before activation	10.87	9.73	11.49	2.29	2.15	41.23		
Mo ₂ C@575-4p after activation	7.61	24.84	9.17	2.43	0.48	47.56		

Sample Identifier	Mo3d unknown (grey) %	Mo3d Mo(II) %	Mo3d Mo(IV) %	Mo3d Mo(V) %	Mo3d Mo(VI) %
MoO ₃ /Graphene ink	0.55	0.00	0.00	0.28	6.04
Mo ₂ C@575-4p before activation	0.03	3.46	2.13	2.41	0.76
Mo ₂ C@575-4p after activation	0.00	1.00	0.23	0.14	0.09

Sample Identifier	O1s metal oxide %	O1s other %
MoO ₃ /Graphene ink	12.53	10.22
Mo ₂ C@575-4p before activation	7.33	4.52
Mo ₂ C@575-4p after activation	0.27	6.10

Appendix V-II: Hypothetical synthetic pathway of thermal decomposition of MoO₃

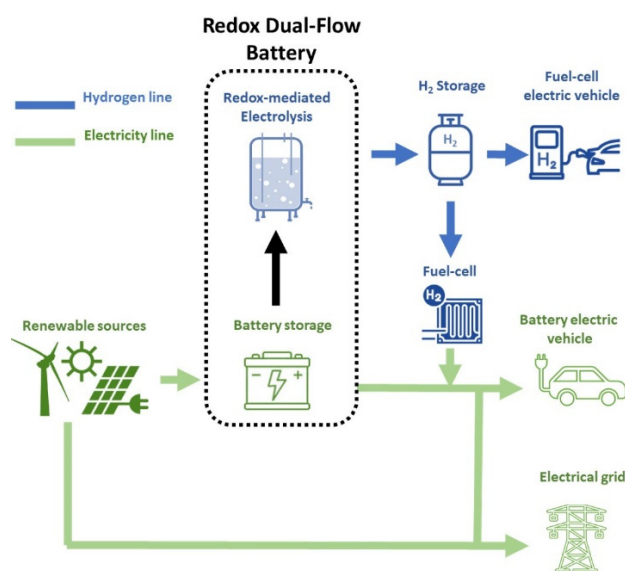
This synthetic pathway was proposed by He *et al.*²⁸



CHAPTER VI

Vanadium-manganese redox dual-flow battery for electricity storage and hydrogen production

The results presented in this chapter are adapted with permission from D. Reynard and H. Girault, Combined hydrogen production and electricity storage using a vanadium-manganese redox dual-flow battery, Cell Reports Physical Science 2021, 2, 100556, DOI: 10.1016/j.xcrp.2021.100556. 2021 © The Authors. This is an open access article under the CC BY license.



Abstract

In this chapter, the practical feasibility of a vanadium-manganese redox dual-flow battery is demonstrated. The system respectively uses aqueous solutions of $\text{Mn}^{3+}/\text{Mn}^{2+}$ and $\text{V}^{3+}/\text{V}^{2+}$ as positive and negative electrolytes. The redox-mediated oxygen evolution reaction (OER) and the hydrogen evolution reaction (HER) are performed in RuO_2 -based and Mo_2C -based catalytic reactor. As a result, the system demonstrates an average energy battery efficiency of 68% at a current density of $50 \text{ mA} \cdot \text{cm}^{-2}$ (cell voltage = 1.92 V) and a relative battery energy density 45% higher than the conventional all-vanadium RFB. Both electrolytes are successfully discharged through redox-mediated HER and OER with a faradaic efficiency close to 100%. All in all, the energy consumption for hydrogen production is ca. 50 kWh/kg H_2 .

6.1 Introduction

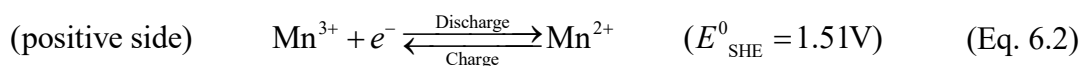
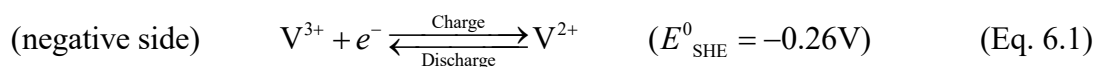
In the previous chapters, important achievements for the development of a vanadium-manganese dual-flow battery were reported. First, the stabilization of Mn^{3+} with the addition of VO_2^+ presented in chapter III is a significant outcome bringing the vanadium-manganese battery as a very promising candidate to apply the concept of redox dual-flow battery.

Then, the kinetic study of the redox-mediated process detailed in chapter IV was essential to provide significant insights into the mechanisms of the catalytic production of hydrogen. The resulting rate law is an efficient tool in order to control the kinetic parameters for an optimal hydrogen rate of production, especially for grid applications that require flexibility and reactivity.

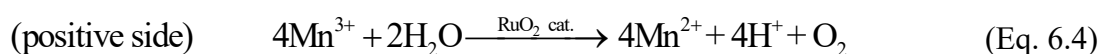
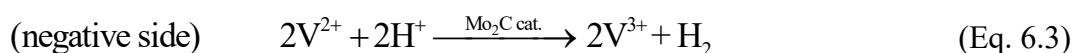
Furthermore, the photonic flash synthetic pathway developed in chapter V offers the opportunity to prepare Mo_2C electrocatalytic materials in a fast and efficient way. This enables tailor-made design for the catalytic reactor of the redox dual-flow system presented in this thesis.

In this chapter, the feasibility of a vanadium-manganese redox dual-flow battery was assessed. An experimental system was built using an aqueous solution of 1 M $\text{V}^{2+}/\text{V}^{3+}$ in 3 M H_2SO_4 as the negative electrolyte and an aqueous solution of 1 M $\text{Mn}^{3+}/\text{Mn}^{2+}$ - VO_2^+ (1:1) in 3 M H_2SO_4 as the positive electrolyte.

Upon battery operations, the electrolytes can be charged and discharged electrochemically according to the following redox reactions:



In the external catalytic reactors, the positive electrolyte and the negative electrolyte can alternatively be discharged through redox-mediated HER and OER, over respectively Mo_2C -based and RuO_2 -based redox electrocatalysts:



During the redox-mediated HER, the electrons are supplied by the oxidation of V^{2+} and drawn by the reduction of protons.¹² Similarly, during the redox-mediated OER, the electrons are supplied by the oxidation of water and drawn by the reduction of Mn^{3+} .

Figure 1A illustrates the overall process with the vanadium/manganese RFB in the middle and the two gas evolving reactors on the outside, and Figure 1B schematically describes the thermodynamic parameters. The performances of the vanadium-manganese redox flow battery were evaluated and compared to a conventional vanadium-vanadium system. Catalytic reactors were designed to carry out the chemical discharge of the electrolytes towards redox-mediated water splitting.

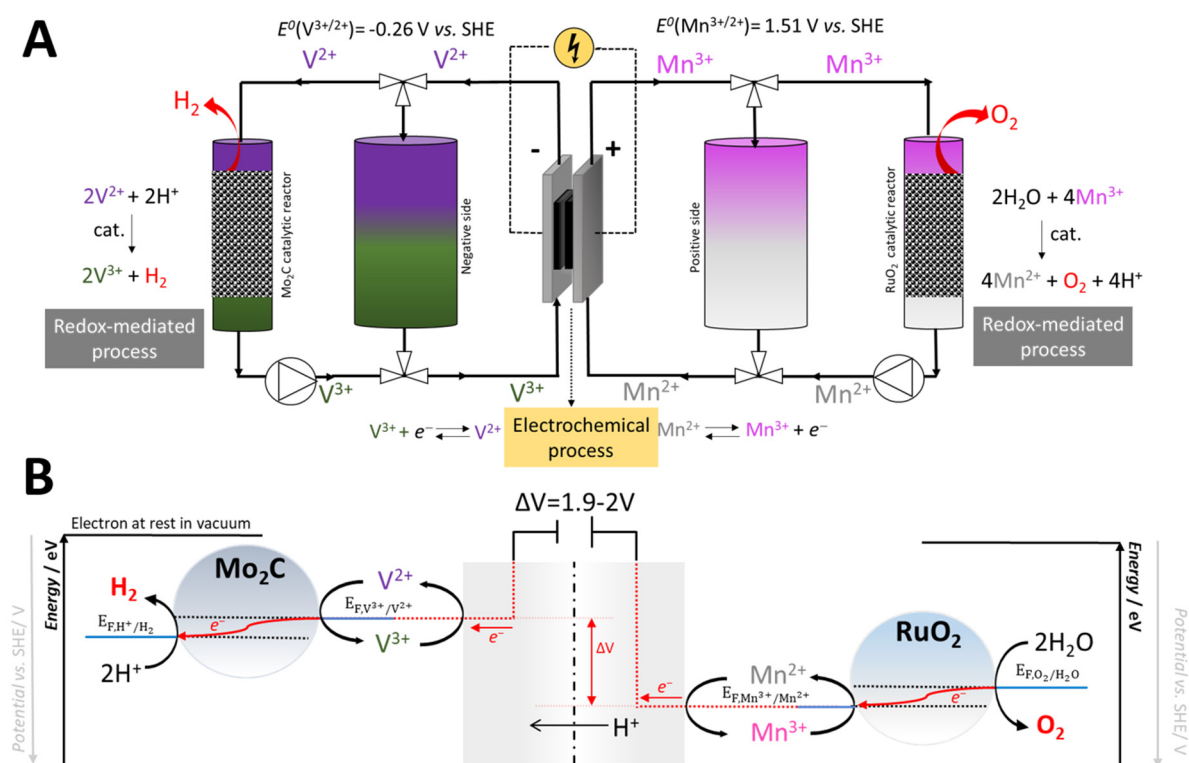


Figure 6.1 (A) Schematic of the reported vanadium-manganese dual-flow battery (B) Energy diagram of the redox-catalytic HER and OER using V^{3+}/V^{2+} and Mn^{3+}/Mn^{2+} as redox mediators, respectively. Molybdenum carbide and ruthenium oxide are respectively employed as HER and OER catalysts.

6.2 Experimental section

6.2.1 Electrolytes preparation

A commercial vanadium electrolyte composed of an aqueous solution of 1.6 M V(III)/ 1.6M V(IV) (ca. 50:50), 2 M sulfuric acid (H_2SO_4), and 50 mM H_3PO_4 was purchased from Reactana and used without further purification. Manganese sulfate monohydrate ($\text{MnSO}_4 \cdot \text{H}_2\text{O}$, >99 %) and sulfuric acid (H_2SO_4 , 95-97%) were purchased from Sigma Aldrich and used without further purification. The commercial electrolyte was electrolysed in a single-flow cell with carbon felt electrodes to prepare solution of 1.5 M V^{2+} and 1.5 M VO_2^+ in 2 M H_2SO_4 . These solutions were used for the preparation of the positive (1 M VO_2^+ - Mn^{2+} (1:1) in 3 M H_2SO_4) and the negative electrolyte (1 M V^{3+} in 3 M H_2SO_4). The electrolyte density was measured around $1.3 \text{ kg} \cdot \text{L}^{-1}$.

6.2.2 Catalysts preparation

6.2.2.1 Molybdenum carbide

Ammonium Molybdate tetrahydrate ($(\text{NH}_4)_6\text{Mo}_7\text{O}_{24} \cdot 4\text{H}_2\text{O}$), N-Methyl Pyrrolidine (NMP), mildly edge-oxidized graphene nanosheets (EOGNs, 15–20 sheets, 4–10% edge-oxidized, Sigma Aldrich), carbon cloth with GDL (GoodFellow), sulfuric acid (H_2SO_4 , 95–97%, Merck) and deionized water were used as supplied without further purification. The Mo_2C electrocatalyst was prepared according to the method described in chapter V.²⁴ Briefly, we prepared a precursor ink of $30 \text{ mg} \cdot \text{mL}^{-1}$ of ammonium molybdate tetrahydrate and graphene oxide in 1:4 ratio by dissolving in NMP. After sonication of the solution for 15 minutes, the precursor ink was drop-casted over a carbon substrate ($0.1 \text{ mL} \cdot \text{cm}^{-2}$) and thermally dried at 200°C for 10 min. The sample was exposed to 4 pulses at 575 V using a PulseForge 1300 photonic curing system (Novacentrix, USA) containing a xenon flashlamp. Each pulse consisted of 18 long μs pulses spread over a period of 20,000 μs that emitted a theoretical energy density of $12.8 \text{ J} \cdot \text{cm}^{-2}$.

6.2.2.2 Ruthenium oxide

Ruthenium chloride hydrate ($\text{RuCl}_3 \cdot x\text{H}_2\text{O}$), zinc chloride (ZnCl_2 , 98.5%) and hydrochloric acid (HCl , 36% wt.) were used without further purification. An ultrafine defective RuO_2 electrocatalyst was prepared on carbon substrate according to the protocol reported by Chen *et*

*al.*²⁵ Briefly, a precursor ink was prepared by dissolving 1.2 g of ruthenium chloride hydrate, 0.4 g of zinc chloride and 0.5 mL hydrochloric acid (HCl) in 10 mL of deionized water under stirring. The carbon substrate (carbon cloth with GDL or carbon felt) was dipped into the ink for 5 s and dried under 60°C. Then, the samples were annealed at 350°C for 3 hours at a ramping rate of 10°C·min⁻¹ in air. The samples were finally washed in 1 M H₂SO₄ for 18 hours, dried and partially dehydrated in atmosphere at 150°C.

6.2.3 Instrumentation

ICP-MS analyses were performed on a PerkinElmer Nexion 300D using an external calibration method. UV/vis measurements were performed with a flame spectrometer from Ocean Optics. Electrochemical characterizations and battery testing were performed with a Biologic potentiostat SP-300 and the electrolysis for the preparation of the electrolytes was performed with a Biologic HCP-1005 (100 A booster). Scanning electron microscopy images were obtained with a Teneo SEM (FEI, USA) equipped with a Schottky field emission gun. Secondary electron detection was carried out with an Everhart–Thornley detector and an in-lens detector. Gas chromatography was performed using a Trace 1300 gas chromatograph from Thermo Fischer Scientific, equipped with a thermal conductivity detector (TCD) and a 5 Å molecular sieves (80/100 mesh) column. Argon was used as carrier gas.

6.2.4 Physical and electrochemical characterization

6.2.4.1 Mediators

The cyclic voltammograms were conducted in a three-electrode system at 50 mV·s⁻¹ using a Biologic potentiostat SP-300. A carbon working electrode, an Ag/AgCl (filled with *sat.* KCl) electrode and a carbon felt electrode were used as the working, reference and counter electrodes, respectively. The CVs were performed in a solution of 0.1 M V²⁺/V³⁺ (1:1) with 3 M H₂SO₄ for the negative electrolyte and 0.1 M Mn²⁺/Mn³⁺ (1:1) + 0.1 M VO₂⁺ with 3 M H₂SO₄ for the posolyte. The potential window of the negative and the positive electrolytes were comprised between -0.6 V to 0.2 V and between 1.3 V to 1.8 V vs. SHE, respectively.

6.2.4.2 Electrocatalysts

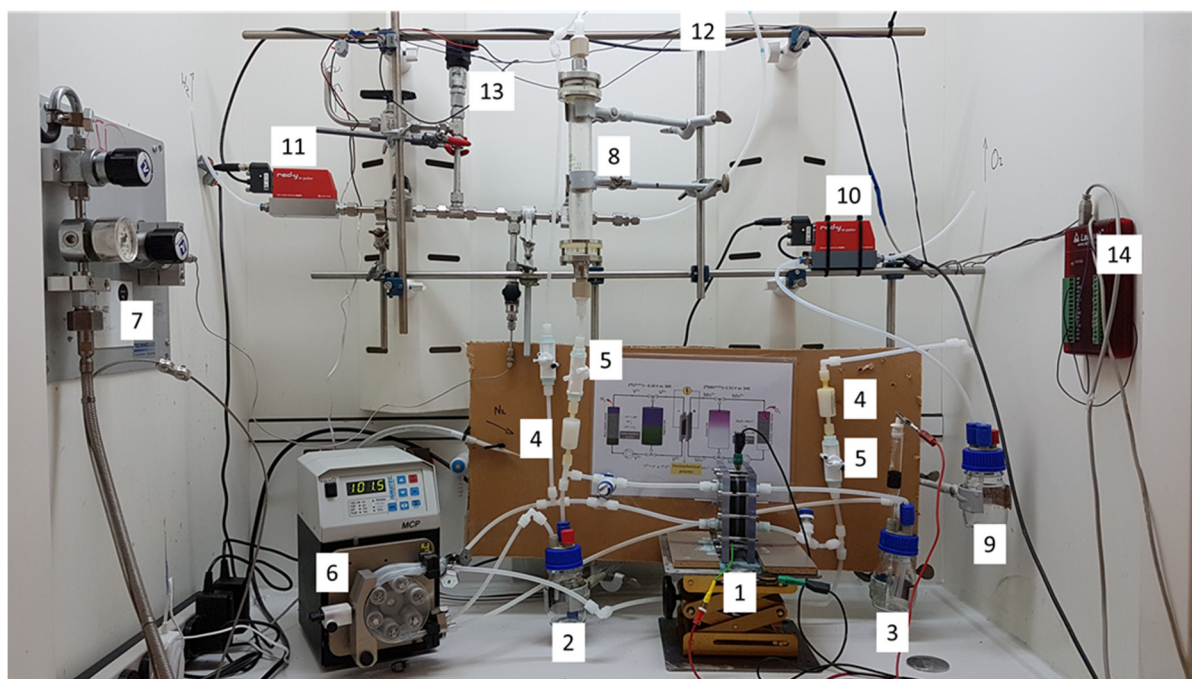
All the electrochemical measurements were carried out in aqueous acidic media with 3 M H₂SO₄ in a three-electrode electrochemical system equipped with the working electrode, a carbon felt counter electrode and a Ag|AgCl (*sat.* KCl) reference electrode. The electrocatalyst

supported on carbon cloth was screwed on a carbon coated titanium current collector electrode (geometrical surface area = 0.2 cm^2). A magnetic stirrer was placed near the working electrode to dissipate the generated bubbles during the measurements. The electrocatalyst activities were electrochemically evaluated by linear sweep voltammetry (LSV) in 3 M H_2SO_4 at a scan rate of $10 \text{ mV}\cdot\text{s}^{-1}$. For comparison, the activity of the carbon substrate electrode was studied. The electrochemically active surface area (ECSA) was estimated from the double-layer capacitance measurements of the catalytic surface, which was measured from the scan-rate dependence of static cyclic voltammetry (CV). The CV's were performed in a 0.1 V potential window centered on the open-circuit potential (OCP) (non-faradaic region) at scan rate ranging from 0.1 to $0.5 \text{ V}\cdot\text{s}^{-1}$. The electrocatalytic stability was evaluated by controlled-current electrolysis under catalytic conditions ($-20 \text{ mA}\cdot\text{cm}^{-2}$ per geometric area during 13 h for Mo_2C and $15 \text{ mA}\cdot\text{cm}^{-2}$ per geometric area during 8 h for RuO_2) under continuous stirring. Additional structural information for the as-prepared Mo_2C and RuO_2 catalyst has been published elsewhere.^{24,25}

6.2.5 Dual-circuit RFB set-up

All the battery tests were performed in a flow cell made of two half-cell compartments consisted of a graphite current collector and a carbon felt electrode (10 cm^2). The carbon felt electrodes were pretreated at 400°C in atmosphere for 48 h. The positive and the negative compartment were separated using an anion exchange membrane (FAP-450) purchased from Fumatech. The flow cell was sealed using silicon gaskets and polycarbonate plates (with an included flow path) were used to hold all the cell components together and prevent from electrolyte leakages. The positive and negative electrolytes were circulated from the electrolyte container (100 mL glass Schott Bottle) to the electrochemical cell using a peristaltic pump (Ismatec) with piping made of flexible LDPE tube. The catalytic hydrogen production reactor consisted of a tubular glass reactor (Büchiglassuster) that was separated from the single-cell unit using PVDF valves. The reactor was connected to a Red-y hydrogen flow meter ($5\text{-}600 \text{ ml}\cdot\text{min}^{-1}$, Vögtlin), a pressure sensor (0-25 bar, Gems) and a hydrogen purging system with PVDF (Semadeni) and stainless-steel tubing and valves (Swagelock). The system included pressure relief valves of 10 bar to maintain the pressure in the safety range. On the other side, the catalytic oxygen production was performed in a 100 mL Schott Bottle connected with PVDF tubing to an oxygen flow meter ($10\text{-}600 \text{ ml}\cdot\text{min}^{-1}$, Vögtlin). A detailed scheme of the experimental set-up is shown in Figure 6.2.

Dual-flow circuit redox flow battery



- | | | | |
|-----------------------|--------------------------------|-------------------------------------|---------------------|
| 1. Flow cell | 5. Valves | 9. Oxygen production reactor | 13. Pressure sensor |
| 2. Negative container | 6. Peristaltic pump | 10. O ₂ Flow meter | 14. Data logger |
| 3. Positive container | 7. Hydrogen purging system | 11. H ₂ Flow meter | |
| 4. Filters | 8. Hydrogen production reactor | 12. Pressure relief valve (10 bars) | |

Flow cell

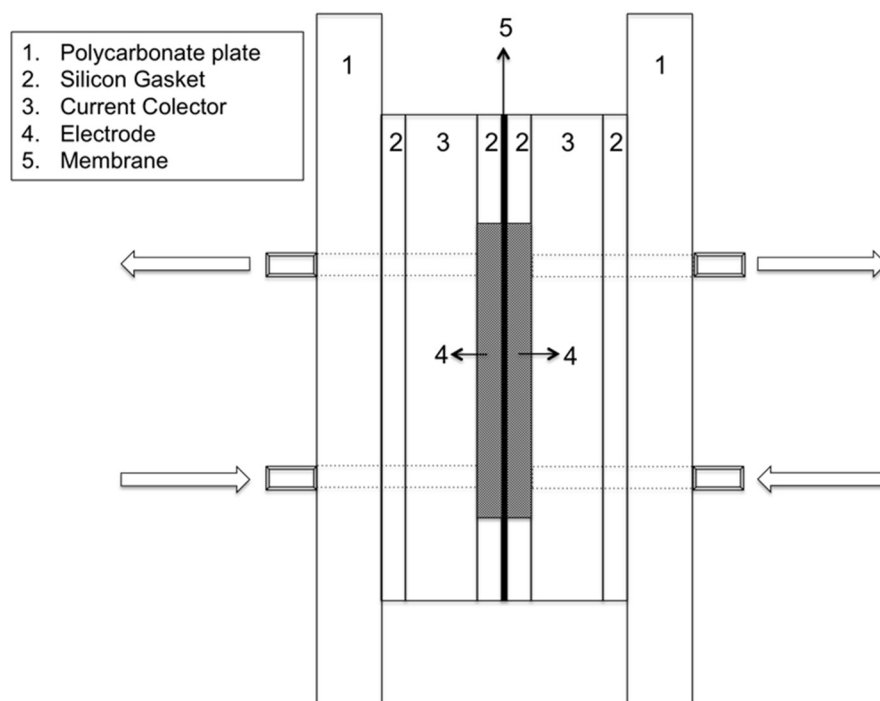


Figure 6.2 Experimental set-up of the dual-circuit redox flow battery and schematic of the flow-cell architecture including polycarbonate plates (thickness = 1 cm, weight \approx 140 g), silicon gasket, current collectors (thickness = 1 cm, weight \approx 80 g), porous carbon felts electrode (thickness = 0.4 cm, area=10 cm²) and anion exchange membrane (FAP-450, thickness = 50 μ m).

6.2.6 Single-cell and catalytic water splitting experiments

All the battery experiments were performed in the flow-cell described in the previous section. The vanadium-manganese redox flow battery was cycled at $50 \text{ mA} \cdot \text{cm}^{-2}$ at about 20°C for 50 cycles between 25 and 75% SOC with the reference electrode placed on the positive side. To ensure that the capacity of the battery was always limited by the positive half-cell, the volume of negolyte electrolyte was larger than the posolyte. Each experiment started with 1 M V^{3+} in $3 \text{ M H}_2\text{SO}_4$ (40 mL) on the negative side and 1 M Mn^{2+} , 1 M VO_2^+ in $3 \text{ M H}_2\text{SO}_4$ on the positive side (20 mL). The SOC of the battery was controlled by the positive half-cell potential. Note that the volumetric energy density was calculated considering the same volume of positive and negative electrolyte. For comparison, similar experiments were performed with an all-vanadium redox flow battery using a solution of $1 \text{ M V}^{3+}/\text{V}^{2+}$ on the negative side (40 mL) and $1 \text{ M VO}_2^+/\text{VO}^{2+}$ on the positive side (15 mL). For the characterization of the redox flow cell, coulombic, voltage and energy efficiencies were calculated according to the following equation:

$$\eta_{\text{Coulombic}} = \frac{\int i_{\text{discharge}} dt_{\text{discharge}}}{\int i_{\text{charge}} dt_{\text{charge}}} = \frac{Q_{\text{discharge}}}{Q_{\text{charge}}} \quad (\text{Eq. 6.5})$$

$$\eta_{\text{Voltage}} = \frac{\frac{1}{t_{\text{Discharge}}} \int_0^{t_d} V_{\text{Discharge}} dt}{\frac{1}{t_{\text{Charge}}} \int_0^{t_c} V_{\text{Charge}} dt} = \frac{\bar{V}_{\text{Discharge}}}{\bar{V}_{\text{Charge}}} \quad (\text{Eq. 6.6})$$

$$\eta_{\text{Energy}} = \eta_{\text{Coulombic}} \cdot \eta_{\text{Voltage}} = \frac{\int V_{\text{discharge}} dQ_{\text{discharge}}}{\int V_{\text{charge}} dQ_{\text{charge}}} = \frac{E_{\text{discharge}}}{E_{\text{charge}}} \quad (\text{Eq. 6.7})$$

Redox-mediated hydrogen evolution was performed in a reactor containing a sheet of 40 cm^2 of $\text{Mo}_2\text{C}/\text{graphene}$ supported on carbon cloth (precursor load: 96 mg). The hydrogen reactor was previously purged with hydrogen. The redox-mediated HER reaction was monitored at atmospheric pressure using 100 mL of $1 \text{ M V}^{3+}/\text{V}^{2+}$ at a SOC of 90% with gas flow measurement. Besides, the reaction was also performed under pressure in an autoclave using 30 mL of $1 \text{ M V}^{3+}/\text{V}^{2+}$ at a SOC of 90% with a headspace of 50 mL. The redox-mediated OER was performed in a reactor containing 10 cm^2 of RuO_2 catalyst supported on carbon felt (ca. $12.5 \text{ mg} \cdot \text{cm}^{-2}$). The discharge was studied using a 0.1 M and a $1 \text{ M Mn}^{3+}/\text{Mn}^{2+}$ at a SOC of

75% in 3 M H₂SO₄. The quantity of produced O₂ gas was determined by water displacement with a burette filled with water and connected to the reactor.

6.3 Results and discussion

6.3.1 Mediators and electrocatalysts

The essential prerequisite for the redox dual-flow battery is to select suitable redox-mediators. The choice of redox couples must fulfill various criteria to guarantee the performance of the redox flow battery such as reversibility, solubility and stability. Besides, a wise choice must be done regarding the standard potential of the selected mediators. In fact, it is critical that the mediators can address optimally the two different modes of discharge. The redox-mediators must have a standard potential within the water stability range under the battery operation conditions (carbon electrodes) in order to avoid oxygen and hydrogen evolution reaction within the electrochemical cell. However, the potential must be sufficient to promote HER and OER during the chemical discharge in the external catalytic bed over the selected redox electrocatalyst. Thus, the critical point of the system is to select redox mediators with a standard potential above the kinetic overpotential towards HER and OER of the selected redox electrocatalyst and below the kinetic overpotential towards HER and OER of the carbon electrodes (blue zone in Figure 6.3). It is important to point out that if the gas evolving reactions occur on the redox electrocatalyst, the electron transfer reactions of the redox mediators may also occur on the carbon substrate, as its Fermi level is in equilibrium with those of the redox electrocatalysts. As depicted on Figure 6.3-A and Figure 6.3-B, the V³⁺/V²⁺ redox couple has a standard potential of -0.26 V vs. SHE and the Mn³⁺/Mn²⁺ redox couple has a standard potential of 1.51 V vs. SHE in acidic solutions (3 M H₂SO₄). To carry out redox electrocatalytic hydrogen evolution (Eq. 6.3) and oxygen production (Eq. 6.4), molybdenum carbide (Mo₂C) and ruthenium oxide (RuO₂) were synthesized and used as heterogenous electrocatalysts in the system. Both electrocatalysts were prepared on a carbon substrate to minimize catalyst particle dispersion and to improve the conductivity of the material.

For the hydrogen evolution reaction, we prepared Mo₂C/graphene on a carbon substrate (a carbon cloth as used for gas diffusion layer (GDL) in a fuel cell) by photonic flash synthesis.²⁴ For the oxygen evolution reaction, an ultrafine defective RuO₂ was prepared on a carbon substrate (carbon cloth as above or carbon felt) by annealing as described by Chen *et al.*²⁵ The

method consists in doping the RuO_2 with divalent Zn in order to create oxygen vacancies and reduce the crystallinity of RuO_2 , improving the intrinsic activity of the catalyst. In the meantime, the Zn species are removed by acid treatment (EDX spectra available in Appendix VI-1), which downsizes further the RuO_2 nanocrystals, enhancing the electrochemical active surface area (ECSA) of the prepared redox catalyst. The detailed morphological of the as-prepared Mo_2C and RuO_2 electrocatalysts are available in Figure 6.4 and Figure 6.5.

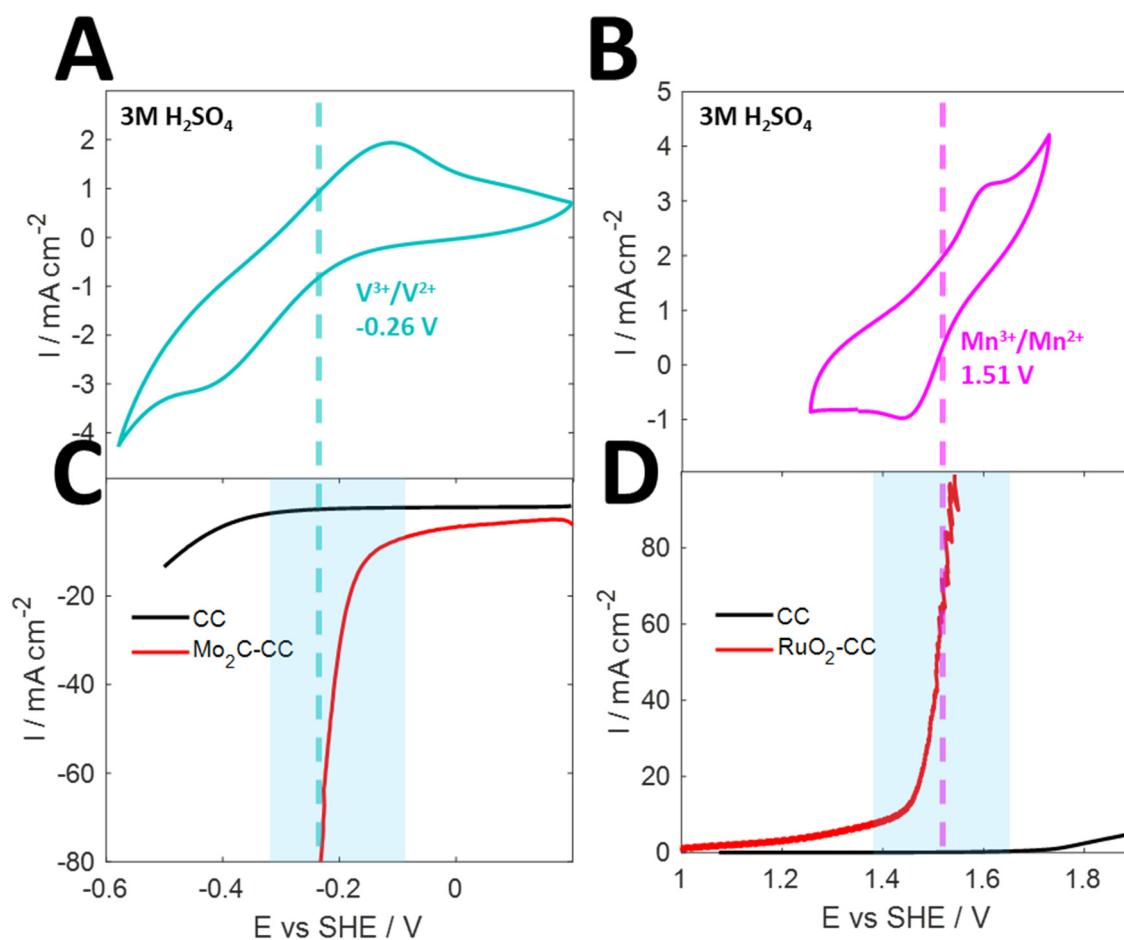


Figure 6.3 Electrochemical characterizations between the catalysts and the mediators of the redox dual-flow battery (A) Cyclic voltammogram of $100\text{ mM } \text{V}^{3+}/\text{V}^{2+}$ in $3\text{ M } \text{H}_2\text{SO}_4$ solution at a scan rate of $50\text{ mV}\cdot\text{s}^{-1}$. (B) Cyclic voltammogram of $100\text{ mM } \text{Mn}^{3+}/\text{Mn}^{2+} + 100\text{ mM } \text{VO}_2^+$ in a $3\text{ M } \text{H}_2\text{SO}_4$ solution at a scan rate of $50\text{ mV}\cdot\text{s}^{-1}$. (C) Cathodic polarization curve at a scan rate of $10\text{ mV}\cdot\text{s}^{-1}$ in $3\text{ M } \text{H}_2\text{SO}_4$ of the carbon cloth without (CC) and with the molybdenum carbide catalyst (Mo_2C -CC). (D) Anodic polarization curve at a scan rate of $10\text{ mV}\cdot\text{s}^{-1}$ in $3\text{ M } \text{H}_2\text{SO}_4$ of the prepared of the carbon cloth without (CC) and with the ruthenium oxide catalyst (RuO_2 -CC).

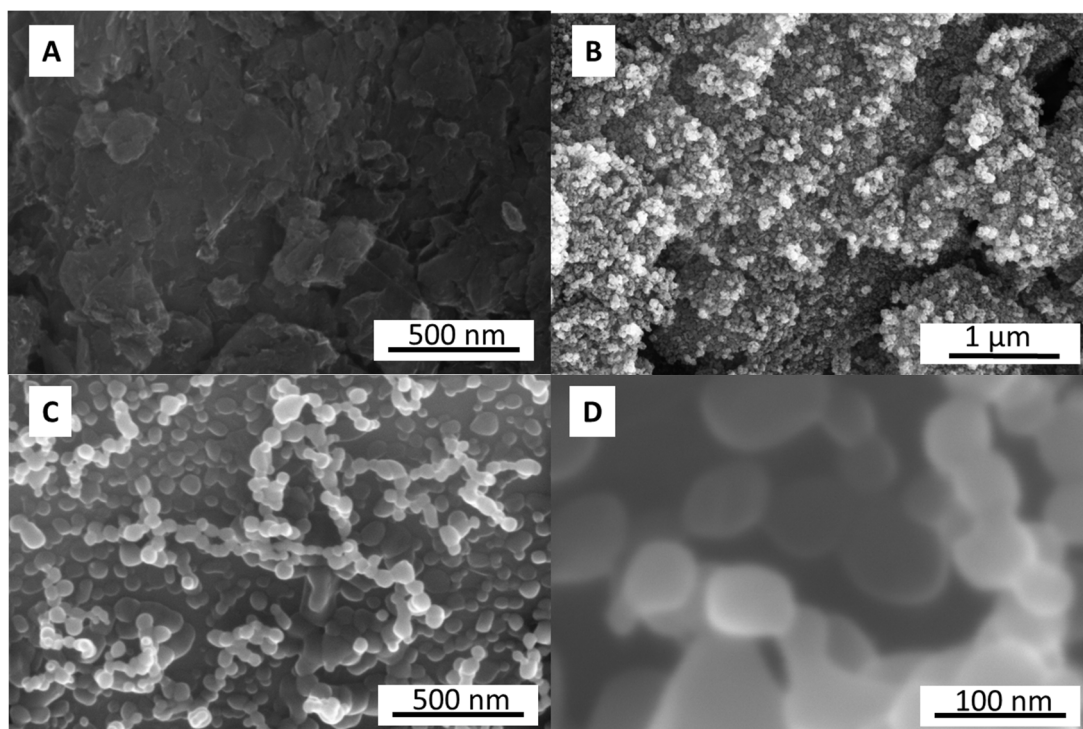


Figure 6.4 SEM images of (A) carbon cloth-GDL substrate covered with MoO₃/Graphene ink and (B-D) synthesized Mo₂C-Graphene catalyst by photonic flash synthesis.

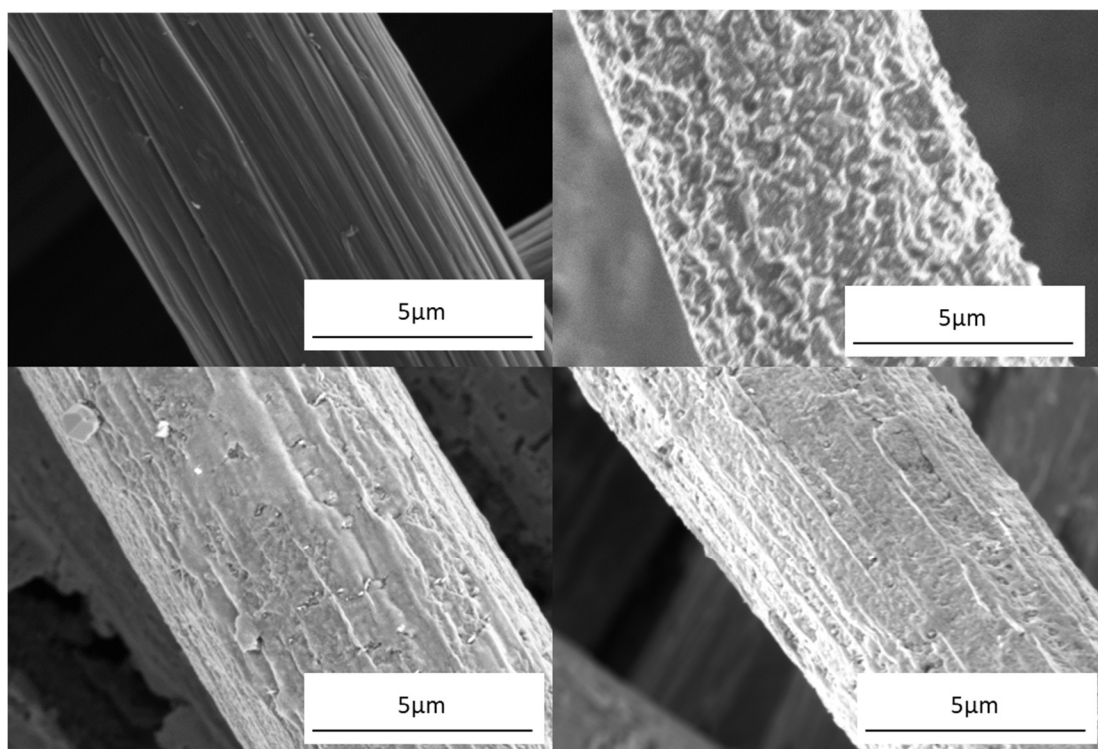


Figure 6.5 SEM images of (A) carbon cloth substrate (B) RuO₂ prepared by annealing without Zn doping (C-D) RuO₂ prepared by annealing with Zn doping.

The as-prepared electrocatalysts were first tested electrochemically in 3 M H₂SO₄ electrolyte free of redox-mediators and were compared to a bare carbon electrode. To compare the kinetic of both HER and OER reactions on the carbon electrode and the selected electrocatalysts, linear sweep voltammetry was performed on each material. For HER, the carbon electrode exhibits an onset overpotential close to 370 mV, while the as-prepared Mo₂C catalyst exhibits a much lower value around 140 mV (−0.14 V *vs.* SHE). Consequently, the electron mediator (V²⁺) can spontaneously transfer the electrons to the protons in order to generate hydrogen (Eq. 6.3) in the external catalytic reactor, without being subject to catalytic redox-mediated HER in the redox flow cell. Similarly, while the posolyte is in presence of the as-prepared RuO₂ electrocatalyst, the kinetic overpotential towards OER drops exhibiting a kinetic onset overpotential of around 220 mV (1.45 *vs.* SHE), and the electron acceptor (Mn³⁺) spontaneously accepts the electrons from the water to achieve the oxygen evolution reaction (Eq. 6.4). Again, the redox-mediator potential remains low enough to prevent from redox-mediated OER on the bare carbon electrode within the flow cell. The detailed electrochemical characterization of the as-prepared electrocatalysts is shown in Figure 6.6, including polarization curves (Figure 6.6-A and Figure 6.6-B), specific capacitance measurement (Figure 6.6-C and Figure 6.6-D) and stability test (Figure 6.6-E and Figure 6.6-F).

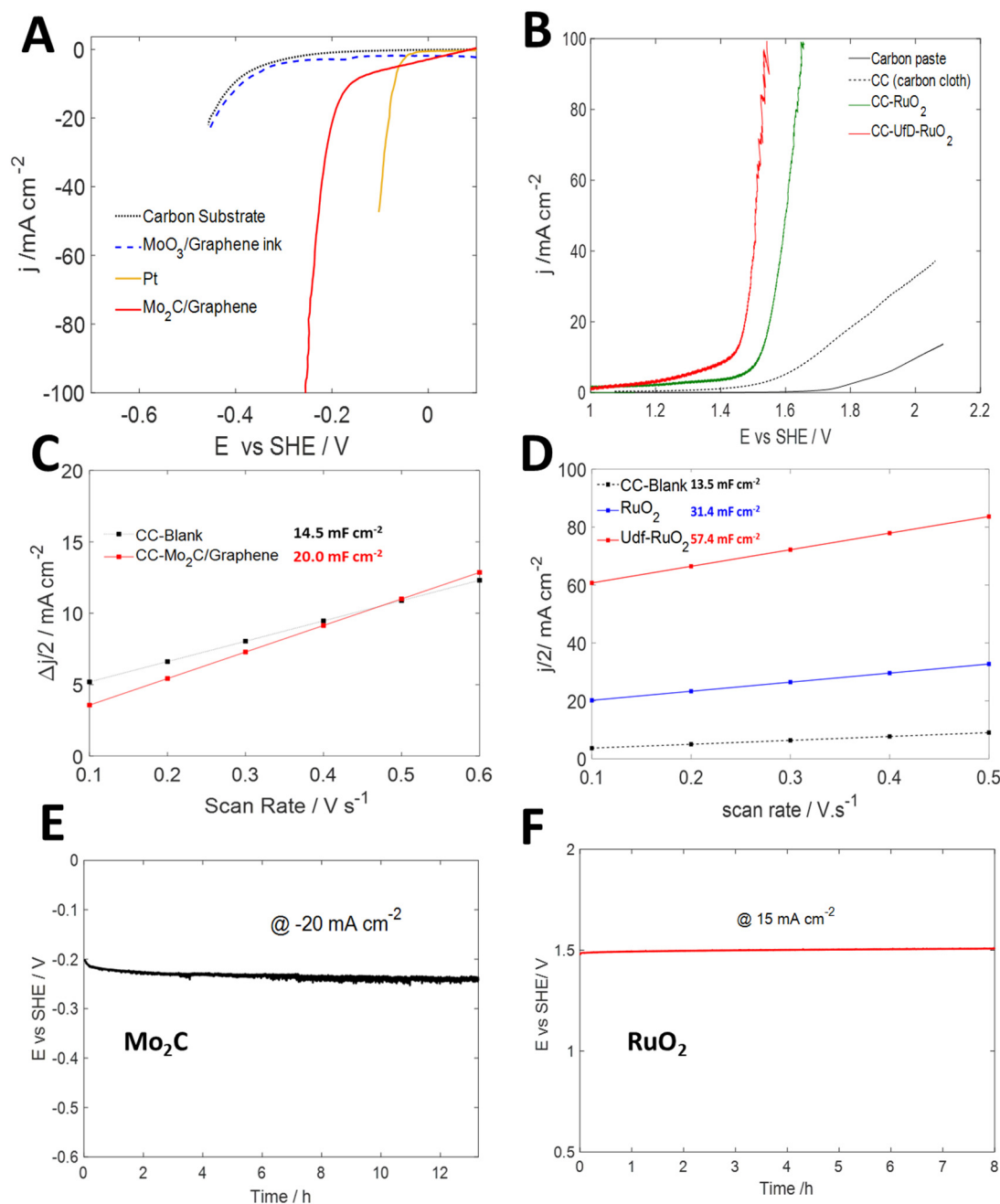
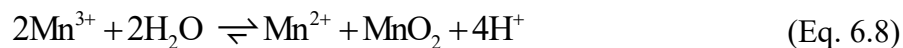


Figure 6.6 Electrochemical characterization of the prepared Mo₂C and RuO₂ electrocatalysts: (A) Polarization curves of MoO₃/Graphene ink supported on carbon cloth (with GDL), Mo₂C/Graphene supported on carbon cloth (with GDL), carbon substrate (with GDL) and platinum electrodes. (B) Polarization curves of RuO₂ supported on carbon cloth (CC-RuO₂), Zn-doped RuO₂ supported on carbon cloth (UfD-RuO₂), carbon paste and carbon cloth electrodes. (C) Plots of the non-faradaic current measured at the OCP in function of the scan-rate with the resulting measured specific capacitance for the Mo₂C/Graphene supported on carbon cloth (with GDL) and the carbon substrate (with GDL). (D) Plots of the non-faradaic current measured at the OCP in function of the scan-rate with the resulting measured specific capacitance for the carbon cloth, the RuO₂ supported on carbon cloth, and the ultrafine defective RuO₂ (Zn-doped) supported on carbon cloth. (E) Time-dependent potential of the prepared Mo₂C/Graphene catalyst under static cathodic current density of 20 mA·cm⁻². (F) Time-dependent potential of the prepared RuO₂ (Zn-doped) catalyst under static anodic current density of 15 mA·cm⁻².

6.3.2 Vanadium-Manganese redox flow battery for energy storage

The use of $\text{Mn}^{3+}/\text{Mn}^{2+}$ ($E^0 = 1.51$ V vs. SHE) has been considered to replace the conventional $\text{VO}_2^+/\text{VO}^{2+}$ positive redox couple of the all-vanadium redox flow battery in order to increase the open-circuit voltage of the cell. Although advantageous in terms of energy density in sulfuric acid media, Mn^{3+} is unstable and is subject to disproportionation reaction:



The formation of MnO_2 particles altered severely the lifetime and the performance of the battery because of electrode and redox electrocatalyst passivation, mass transport resistance, and irreversible capacity decays.²⁶ To mitigate this issue, several studies reported the use of TiO^{2+} as stabilizing agent or/and the increase of acidic concentration up to 6 M.^{27–31} More recently, the addition of VO_2^+ was observed as an efficient substitute to titanium additives to diminish the formation of MnO_2 and to improve the cyclability of manganese electrolyte for the use in redox flow battery.^{32–34}

The performances of a vanadium ($\text{V}^{3+}/\text{V}^{2+}$) - manganese ($\text{Mn}^{3+}/\text{Mn}^{2+}$) redox flow battery (V/Mn(-V)) in 3 M H_2SO_4 was evaluated with a concentration of vanadium and manganese fixed at 1 M. To mitigate Mn^{3+} disproportionation and preventing from battery decay, vanadium (VO_2^+) was also added on the positive side at a concentration of 1 M (Mn-V, 1:1), based on the results reported in our previous work.³⁴ For comparison, the performance of a vanadium ($\text{V}^{3+}/\text{V}^{2+}$) - vanadium ($\text{VO}_2^+/\text{VO}^{2+}$) redox flow battery (V-V) in 3 M H_2SO_4 was investigated using 1 M of vanadium ions on both sides. First, discharge polarizations curves were performed at 75% battery state-of-charge at a fixed flow rate of ca. $50 \text{ ml} \cdot \text{min}^{-1}$. The open-circuit potentials of the V/Mn(-V) and V/V cells were measured at around 1.8 and 1.4 V, respectively. The resulting polarization curves and power curves of the cells at current densities ranging from 0 to $200 \text{ mA} \cdot \text{cm}^{-2}$ are compared on Figure 6.8-A. Given the higher standard potential of the $\text{Mn}^{3+}/\text{Mn}^{2+}$ (1.51 V vs. SHE) redox couple as compared to $\text{VO}_2^+/\text{VO}^{2+}$ (1.00 V vs. SHE), the V/Mn(-V) cell exhibits higher cell voltage and power density, with a maximum of ca. $230 \text{ mW} \cdot \text{cm}^{-2}$ (at $200 \text{ mA} \cdot \text{cm}^{-2}$). No limiting current density due to mass-transport limitation was observed below $200 \text{ mA} \cdot \text{cm}^{-2}$. The iR corrected power and polarization curves are shown in Appendix VI-2.

The V/Mn(-V) was cycled between 25 and 75% SOC at a current density of $50 \text{ mA} \cdot \text{cm}^{-2}$. The resulting charge-discharge potential curves of the V/Mn(-V) flow cell are shown on Figure 6.7. As comparison, similar experiments were performed with the V/V flow cell (Appendix VI-3)

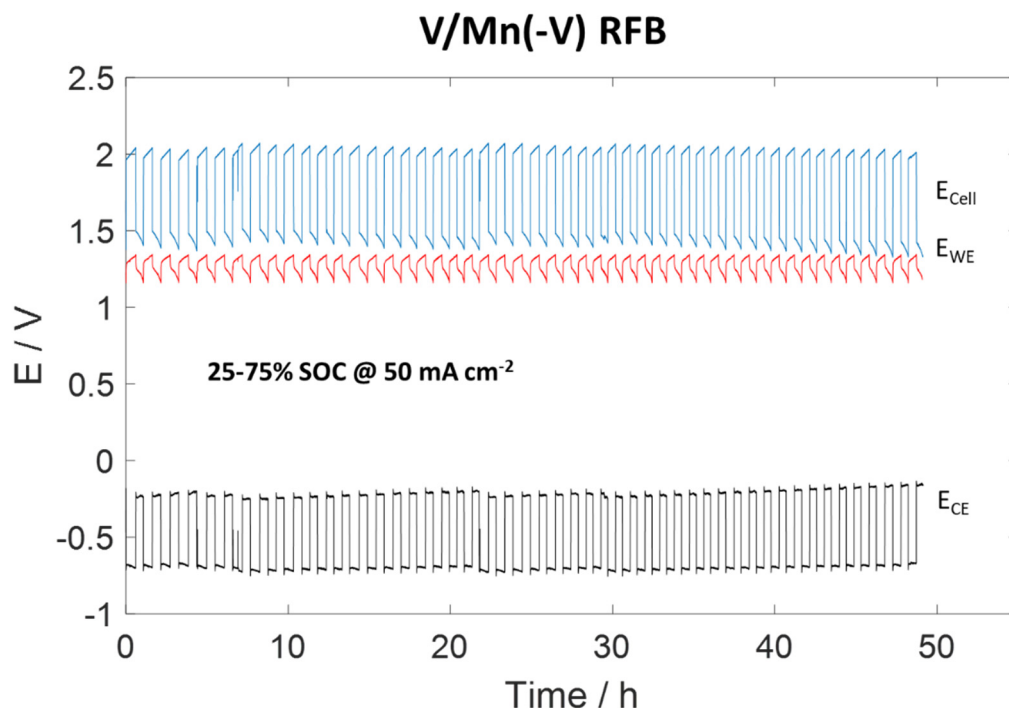


Figure 6.7 Voltage profile of the 1 M V/Mn(-V) flow cell operating between 25 and 75% SOC at a current density of $50 \text{ mA} \cdot \text{cm}^{-2}$.

Figure 6.8-B shows the stable performances of V/Mn(-V) over 50 cycles. The average coulombic (CE), voltage (VE) and energy efficiency (EE) were respectively calculated to 94.3, 71.4 and 67.4 %. A slight decay of the voltage efficiency was observed and was correlated to the slow air oxidation of V^{2+} increasing the negolyte potential. As a comparison (Appendix VI-3), the V/V cell demonstrates close performances with an average coulombic, voltage and energy efficiencies respectively at 99.1, 71.0 and 70.3%, which is consistent with reported values regarding V-V flow cells using anion exchange membranes.³⁵ The major difference between the two cells consists of a lower coulombic efficiency for the V/Mn(-V) cell, which is primarily attributed to the potential formation of MnO_2 (Eq. 6.8) affecting the amount of active Mn^{3+} . Additionally, a slight crossflow of manganese ions through the membrane was determined by ICP-MS in the V/Mn(-V) cell after 50 cycles (Figure S18). Nevertheless, as depicted on Figure 6.8-C, no significant capacity and energy density decay was observed for the V/Mn(-V) cell during the 50 cycles, which contrasts with the large capacity fade reported for conventional V/Mn cell^{26,33} and confirms the stabilizing role of VO_2^+ ions on the posolyte.

The average energy density was measured to $10.4 \text{ Wh} \cdot \text{L}^{-1}$, which corresponds to an increase of about 45% compared with that of the V/V cell (Figure 6.9), owing to the higher standard potential of $\text{Mn}^{3+}/\text{Mn}^{2+}$ redox couple (1.51 V vs. SHE). It is worth to note that here vanadium ions behave only as stabilizing agent within the posolyte and do not contribute to the charge capacity of the RFB. However, the total concentration of actives ions could be increased by using vanadium ions as redox active species on the posolyte, as demonstrated by Park *et al.*³³ Figure 6.8-D shows the performances of the V/Mn(-V) cell at various current densities (30, 50, 70 and $90 \text{ mA} \cdot \text{cm}^{-2}$). As expected, the voltage efficiency raises along with the current density decrease with a maximum value of 77.5% at $30 \text{ mA} \cdot \text{cm}^{-2}$. Similar trend was observed for the V-V system (Appendix VI-3). All the detailed charge-discharge potential curves are included in Appendix VI-4. Table 6.1 summarizes the main performance parameters for the V/Mn(-V) and the V/V cell.

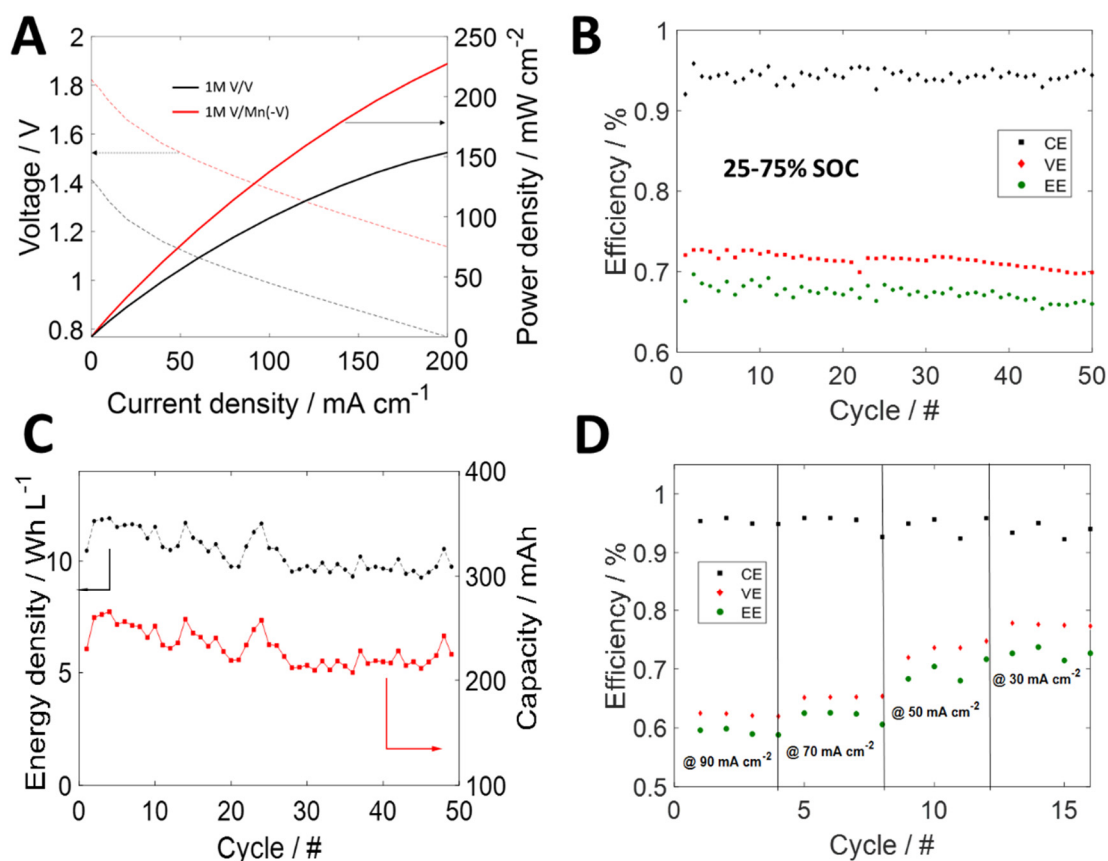


Figure 6.8 (A) Polarization curves and power curves of the V/V and V/Mn(-V) flow cells at current density ranging from 0 to $200 \text{ mA} \cdot \text{cm}^{-2}$ (B) Coulombic, voltage and energy efficiencies (CE, VE, EE) for the V/Mn(-V) flow cell cycled between 25 and 75% SOC at $50 \text{ mA} \cdot \text{cm}^{-2}$. (C) Discharge energy density and discharge capacity of the V/Mn(-V) flow cell at $50 \text{ mA} \cdot \text{cm}^{-2}$. (D) Coulombic, voltage and energy efficiencies (CE, VE, EE) for the V/Mn(-V) flow cell cycled between 25 and 75% SOC at various current densities ranging from 30 to $90 \text{ mA} \cdot \text{cm}^{-2}$.

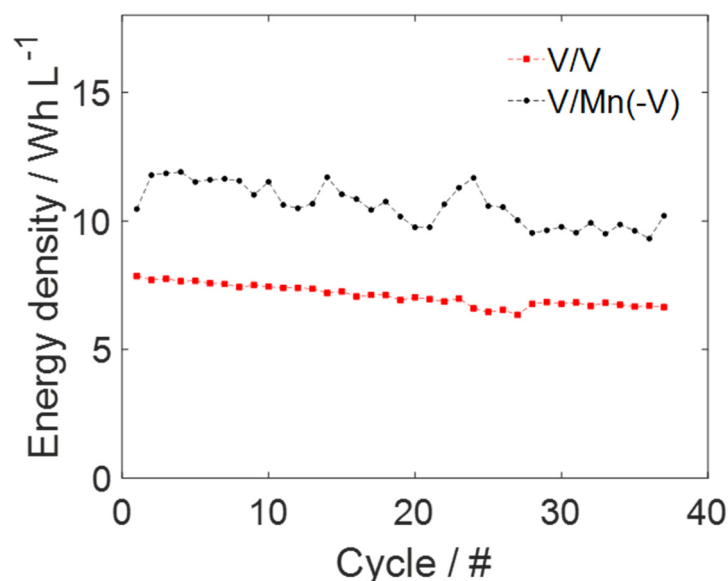


Figure 6.9 (A) Comparison of the discharge energy density of the 1 M V/V and the 1 M V/Mn(-V) flow cells operating between 25 and 75% SOC at $50 \text{ mA} \cdot \text{cm}^{-2}$.

Table 6.1 (A) Summary of the main performances for the V/V and the V/Mn(-V) redox flow batteries.

RFB	Conc / M.	SOC %	Energy density / $\text{Wh} \cdot \text{L}^{-1}$	Current density / $\text{mA} \cdot \text{cm}^{-2}$	Coulombic Efficiency (CE)	Voltage Efficiency (VE)	Energy Efficiency (EE)
V/Mn(-V)	1	25-75	10.4	50	94.3	71.4	67.3
V/V	1	25-75	7.2	50	99.1	71.0	70.3

Furthermore, additional cycles were performed with the V/Mn(-V) flow cell from 0 to 100% SOC in order to evaluate the stability of the electrolyte above 75% SOC (Charge-discharge potential curves are available in Appendix VI-4). As expected, the performances decrease since the rate of disproportionation of Mn^{3+} increases under these conditions. The resulting average coulombic efficiency declines to an average value of 71%, yielding to an average energy efficiency of 46% (Figure 6.10-A). As a result, the average charge capacity of the cell was measured to be 387 mAh, which is 38% below the theoretical value. Interestingly, the discharge and charge capacity of the battery is stable through the cycles (Figure 6.10-B). This may be due to the fact that the produced MnO_2 was reversibly reduced into Mn^{2+} during the discharge process preventing the system from irreversible capacity decay. Similar effects were already observed by Park *et al.* who highlighted the positive effect of vanadium ions on the growth of MnO_2 particles.³³

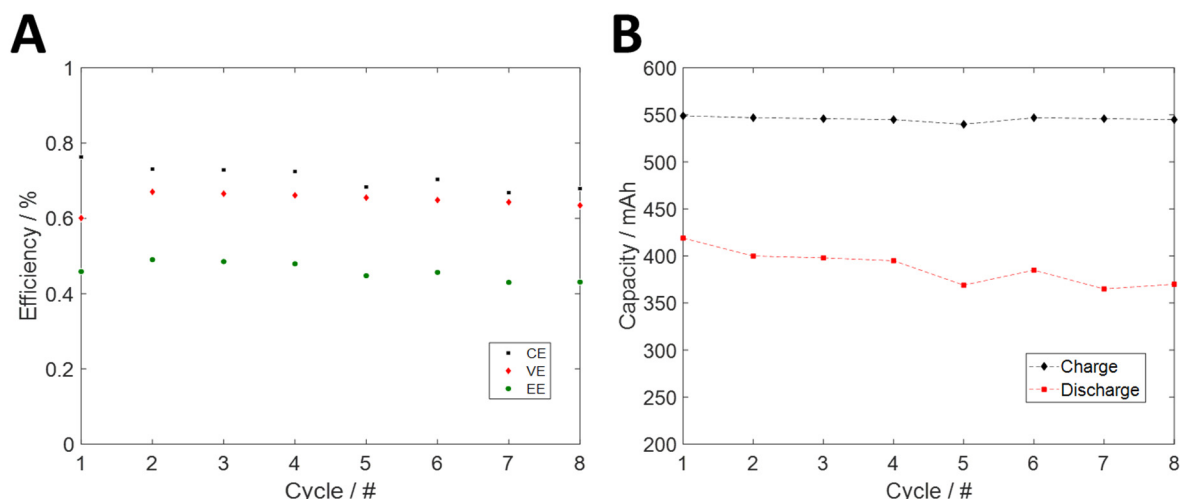


Figure 6.10 Coulombic, voltage and energy efficiencies (CE, VE, EE) for the 1 M V/V flow cell cycled between 0 and 100% SOC at $50 \text{ mA} \cdot \text{cm}^{-2}$. Charging and discharging capacity for the 1 M V/Mn(-V) flow cell operating between 0 and 100% SOC at a current density of $50 \text{ mA} \cdot \text{cm}^{-2}$.

6.3.3 Redox-mediated water splitting

On the basis of the above, a V-Mn redox flow cell was assembled with two external catalytic bed reactors in order to carry out the chemical discharge of the posolyte and the negolyte towards redox-mediated water splitting (Figure 6.2). In the present system, the negolyte can be circulated through a $\text{Mo}_2\text{C}/\text{Graphene}$ (supported on carbon cloth) catalytic bed reactor, where V^{2+} donates electrons to reduce the protons into hydrogen ((Eq. 6.3), Figure 6.11-E). In previous studies, the global parameters of the reaction have been already investigated. Initially, Amstutz *et al.* achieved the redox-mediated HER at a production yield of $96 \pm 4\%$ using a commercial catalyst.¹¹ In chapter III, we conducted a detailed kinetic study of the reaction.¹² At low pH, the oxidation of V^{2+} was ascertained as the rate-determining step of the mediated electron process and the investigations revealed that the kinetic of the reaction depends on the concentration of V^{2+} , the state-of-charge of the electrolyte and the catalytic material and the amount of available catalytic sites according to the following rate law:

$$v_{\text{rxn}} = k_{\text{rxn}} \left(\frac{\text{SOC}}{1 - \text{SOC}} \right)^{0.57} [\text{V}^{2+}][*] \quad (\text{Eq. 6.9})$$

Where v_{rxn} is the overall reaction rate, k_{rxn} is the kinetic rate constant, SOC is the state-of-charge of the vanadium electrolyte, $[\text{V}^{2+}]$ is the concentration in V^{2+} ions in solution and $[*]$ is the concentration of all catalytic active sites.

On the basis of these previous studies using a commercial catalyst, we investigated the redox-mediated HER (Eq. 6.3) in a catalytic reactor designed with the as-prepared Mo₂C/Graphene (supported on a carbon cloth). An aqueous solution of 100 ml of 1 M V³⁺/V²⁺ (90% SOC) in 3 M H₂SO₄ was discharged through the catalytic reactor integrating 40 cm² of the as-prepared catalyst (batch configuration) at ambient conditions and under stirring. As shown on Figure 6.11-A, the rate of reaction was monitored by determining the amount of H₂ produced in the reactor using a calibrated flowmeter. For comparison, the model-predicted evolution of H₂ produced was plotted from the rate law expressed in (Eq. 6.9). Even though the generation of H₂ was recorded during 40 minutes before reaching the detection limit of the flowmeter (5 mL·min⁻¹, Appendix VI-5), the good agreement between the calculated H₂ prediction and the experimental data is clear and demonstrates the applicability of the rate law on the system presented in this work. To overcome the challenges to determine the concentration of catalytic active sites, we measured an apparent kinetic rate constant ($k_{app} = k_{rxn}[*]$) by fitting the data to the first experimental data. The resulting value was measured to 6.85·10⁻⁶ L·s⁻¹. By normalizing to the geometrical surface area of the catalytic cloth used, we can determine a specific apparent kinetic rate constant of 1.71·10⁻⁷ L·s⁻¹·cm⁻² (per square centimeter of catalytic cloth). Note that this value depends on the surface concentration of Mo₂C catalyst on the carbon cloth, which is considered uniform for every catalyst samples prepared in this work.

After performing the reaction at ambient conditions, we explore the generation of hydrogen under pressure, by discharging 30 mL of 1M V³⁺/V²⁺ (90% SOC) in 3M H₂SO₄ over 40 cm² of catalytic cloth in an autoclave (headspace=50 mL). As depicted on Figure 6.11-C and Figure 6.11-D, the pressure inside the autoclave reaches a maximum value at 7 bars, generating a total of 280 mL of hydrogen after 200 minutes. In this particular case, the deviation between the experimental data and the model prediction reveals a significant effect of the pressure increase on the kinetic of the reaction. In spite of the deviation, the total amount of hydrogen produced was in accordance with the calculated value considering a full conversion of V²⁺ (100% Faradaic efficiency). Finally, the generated H₂ gas at the outlet of the reactor was further analyzed by gas chromatography (GC). As revealed on Figure 6.11-B, oxygen content was determined below 0.01%, which confirms the high purity of the gas generated in the present system. For comparison, typical content in oxygen without treatment in alkaline electrolysis is ca. 0.2-0.6%.³⁶

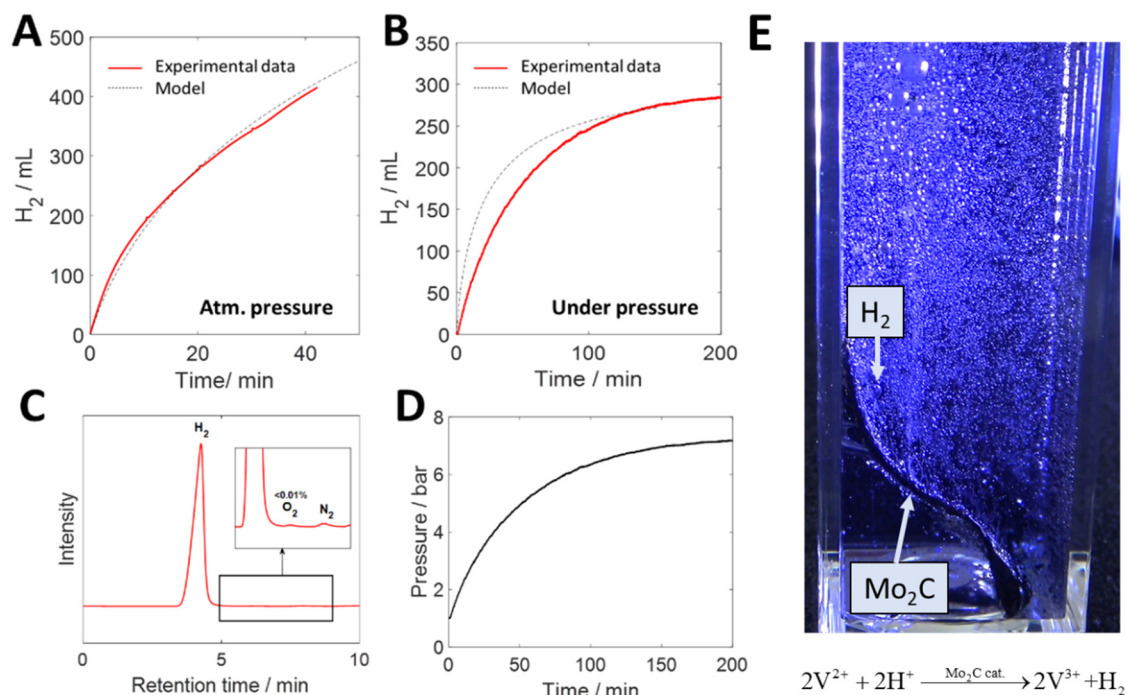


Figure 6.11 (A) Evolution of the amount of hydrogen produced as a function of time during the catalytic discharge of 100 mL of 1 M V^{3+}/V^{2+} (90% SOC) in 3 M H_2SO_4 at ambient pressure (Red line) Experimental data (Black line) Model predictions from the kinetic rate law (B) Evolution of the amount of hydrogen produced as a function of time during the discharge of 30 mL of 1 M V^{3+}/V^{2+} (90% SOC) in 3 M H_2SO_4 under pressure (Red line) Experimental data (Black line) Model predictions from the kinetic rate law (C) Gas chromatograph of the gas sample collected at the outlet of the catalytic reactor (D) Evolution of the pressure in the autoclave as a function of time during the discharge of 30 mL of 1 M V^{3+}/V^{2+} (90% SOC) in 3 M H_2SO_4 under pressure. (E) Image of the vanadium-mediated hydrogen production over Mo_2C redox electrocatalyst.

Similarly, the posolyte can be circulated through a RuO_2 supported on a carbon felt catalytic bed reactor, where Mn^{3+} accepts electrons to oxidize the water into oxygen ((Eq. 6.4), Figure 6.12-D). The redox-mediated OER was also investigated by monitoring the amount of oxygen produced and the state-of-charge of the electrolyte (UV-vis details in Appendix VI-6). First, an aqueous solution of 40 ml of 0.1 M $Mn^{3+}/Mn^{2+} + VO_2^+$ (75% SOC) in 3 M H_2SO_4 was discharged through the catalytic reactor integrating 10 cm^2 (catalyst load=12.5 $mg \cdot cm^2$) of the as-prepared catalyst (batch configuration) at ambient pressure and under stirring. As expected, the reaction rate slows down with the decrease of the state-of-charge of the solution as the driving force of redox-mediated process is set by the difference of the Fermi levels between the two redox couples (Figure 6.1-B). The outlet gas was analyzed by GC to confirm the generation of oxygen (Figure 6.12-C). After 150 minutes of reaction, the state-of-charge reached a value of about 20% and 13 mL of oxygen was collected. As observed on Figure 6.12-A, the recorded O_2 generated is in accordance with the theoretical values (blue cross) calculated from the SOC

measurements assuming 100% of conversion efficiency. This reveals that no significant side reaction occurs in the catalytic reactor. Additionally, an aqueous solution of 40 mL of 1 M $\text{Mn}^{3+}/\text{Mn}^{2+} + \text{VO}_2^+$ (75% SOC) in 3 M H_2SO_4 was discharged under the same conditions than described above. Figure 6.12-B shows the recorded oxygen produced during the reaction. Surprisingly, O_2 seems to be generated at a rate close to the discharge of 0.1 M $\text{Mn}^{3+}/\text{Mn}^{2+} + \text{VO}_2^+$, with around 15 mL of O_2 produced after 150 minutes. The results of this study suggest that the rate of the redox-mediated OER (Eq. 6.4) is governed by the oxidation of water and that the intrinsic concentration of Mn^{3+} in the bulk does not influence the kinetics.

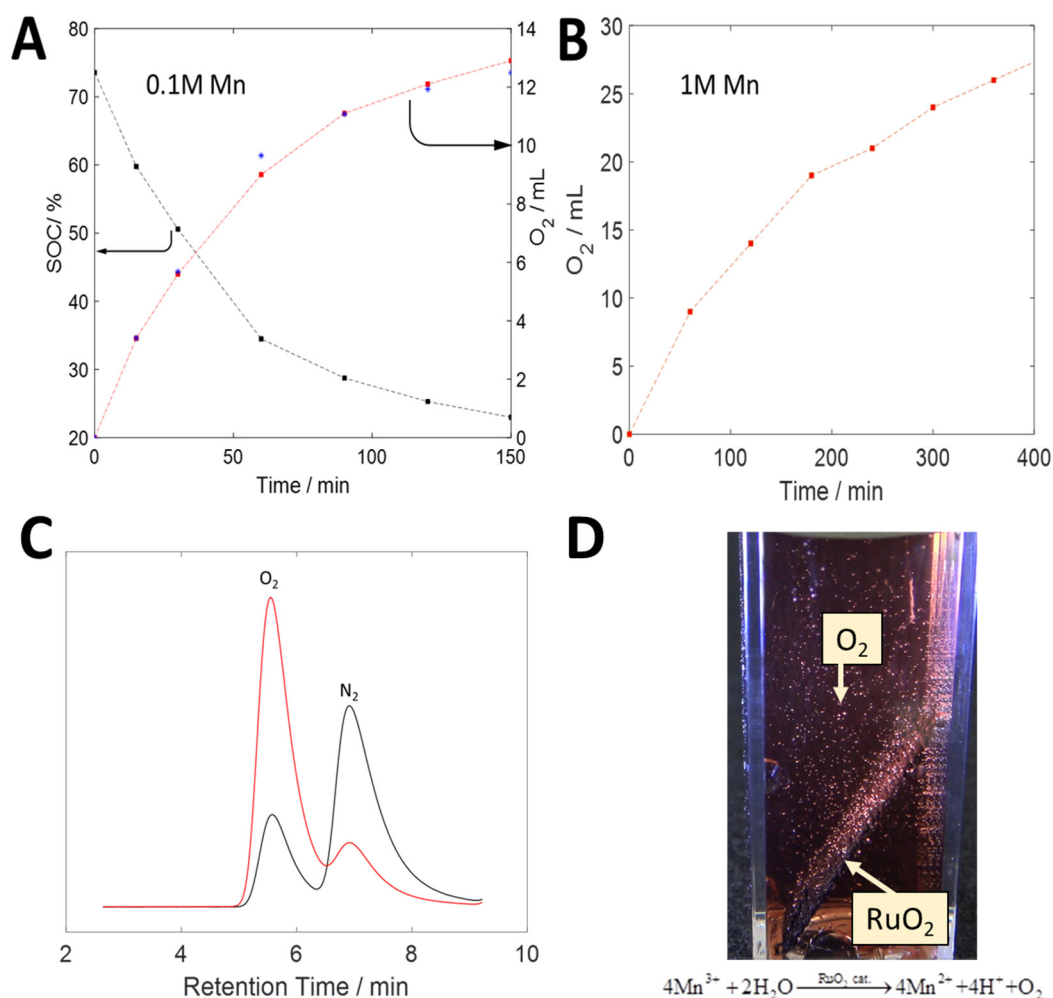


Figure 6.12 (A) Evolution of the electrolyte SOC and the amount of oxygen produced as a function of time during the catalytic discharge of 40 mL of 0.1 M $\text{Mn}^{3+}/\text{Mn}^{2+}$ (75% SOC) + 0.1 M VO_2^+ in 3 M H_2SO_4 at ambient pressure blue marks: theoretical calculated O_2 quantity from the experimentally measured SOC assuming 100% Faradaic efficiency (B) Evolution of the amount of oxygen produced as a function of time during the catalytic discharge of 40 mL of 0.1 M $\text{Mn}^{3+}/\text{Mn}^{2+}$ (75% SOC) + 0.1 M VO_2^+ in 3 M H_2SO_4 at ambient pressure. (C) Gas chromatograph of the gas sample collected at the outlet of the catalytic reactor before the reaction (black line) and after the reaction (red line). (D) Image of the manganese-mediated oxygen production over RuO_2 redox electrocatalyst.

Once the electrolytes are charged, the decoupled HER and OER are spontaneous processes and require only mechanical energy inputs to transfer the electrolytes into the catalytic reactors. Hence, the energy efficiency of the redox-mediated water splitting will essentially rely on the energy injected during the charge of the posolyte and negolyte within the redox flow battery. From this statement and assuming a conversion yield close to 100%, we can roughly estimate the energy efficiency for the water splitting as follows:

$$\eta = \frac{E^0_{\text{O}_2/\text{H}_2\text{O}} - E^0_{\text{H}^+/\text{H}_2}}{E_{\text{cell}}} \times 100 \quad (\text{Eq. 6.10})$$

On the basis of the battery cycling experiments, the system was charged from 25 to 75% SOC by applying an average cell voltage of 1.86, 1.92, 1.96 and 2 V at current density of 30, 50, 70, 90 mA·cm⁻², respectively. From (Eq. 6.10), the resulting energy efficiency of the redox-mediated water splitting presented here is calculated to 66.1, 64.1, 62.8 and 61.42 % at current density of 30, 50, 70, 90 mA·cm⁻² at ambient temperature, respectively. The resulting energy required to produced 1 kg of H₂ is calculated to be 49.4-53.2 kWh·kg⁻¹. Note that those efficiencies do not take into consideration the energy consumption from the pumps and all the other auxiliary components. By analogy, a conventional alkaline electrolysis operating at a current density of 200-400 mA·cm⁻² and a cell voltage of 1.8-2.4 V (cell temperature = 60-80°C) achieve voltage efficiencies of 51-68% with that are in the vicinity of the efficiencies of the reported system.³⁷

6.4 Conclusion

To summarize, we have successfully developed the concept of dual-circuit redox flow battery using an acidic vanadium-manganese redox flow system. In this approach, electrical energy is employed to charge the positive (oxidation of Mn^{2+} into Mn^{3+}) and the negative electrolytes (reduction of V^{3+} into V^{2+}) in an electrochemical flow cell holding bare carbon electrodes. Once the battery is charged, the electrolytes can either be electrochemically discharged by reverse reactions to liberate the stored electrical energy or be chemically discharged in a secondary energy platform (external reactors) through redox-mediated HER and OER. During the latter discharge mode, the polysolite (Mn^{3+}) acts as an electron acceptor to oxidize water into O_2 on RuO_2 -based catalyst and the negative electrolyte (V^{2+}) acts as an electron donor to reduce the proton into H_2 on Mo_2C -based catalyst. The redox-mediated HER and OER occurs spontaneously while transferred in the respective catalytic reactors.

With the addition of VO_2^+ ions as stabilizing agent of the manganese electrolyte, a 1 M V/Mn(-V) redox flow battery presented great stability over 50 cycles with an average energy efficiency of 68% at a current density of $50 \text{ mA} \cdot \text{cm}^{-2}$ between 25 and 75% SOC. Besides the comparable reversibility of the V/Mn(-V) with the conventional V-V RFB, the reported system takes advantage of the higher potential of $\text{Mn}^{3+}/\text{Mn}^{2+}$ resulting in an energy density increase of 45%. Additionally, the redox-mediated electrolysis enables to store energy beyond the energy capacity of the reported redox flow battery ($10 \text{ Wh} \cdot \text{L}^{-1}$) according to the higher volumetric energy density of gaseous hydrogen carrier ($870\text{-}1300 \text{ Wh} \cdot \text{L}^{-1}$ at storing pressure ranging from 350-750 bar, lower heating value (LHV)).³⁸ Moreover, in case of electrolyte overcharging, the formed MnO_2 could be reversibly reduced into Mn^{2+} during the discharge step preventing the system from irreversible decay. Furthermore, the redox-mediated HER and OER in 3 M H_2SO_4 were conducted with production yield close to 100%.

The performance analysis demonstrated that a V-Mn redox dual-flow battery provides a hybrid and competitive alternative for energy storage solution for both distributed energy storage and on-demand hydrogen generation, especially when the electricity is produced from intermittent sources such as solar and wind.

References

- (1) Gallo, A. B.; Simões-Moreira, J. R.; Costa, H. K. M.; Santos, M. M.; Moutinho dos Santos, E. Energy Storage in the Energy Transition Context: A Technology Review. *Renewable and Sustainable Energy Reviews* **2016**, *65*, 800–822. <https://doi.org/10.1016/j.rser.2016.07.028>.
- (2) Kittner, N.; Lill, F.; Kammen, D. M. Energy Storage Deployment and Innovation for the Clean Energy Transition. *Nature Energy* **2017**, *2* (9), 1–6. <https://doi.org/10.1038/nenergy.2017.125>.
- (3) Dunn, B.; Kamath, H.; Tarascon, J.-M. Electrical Energy Storage for the Grid: A Battery of Choices. *Science* **2011**, *334* (6058), 928–935. <https://doi.org/10.1126/science.1212741>.
- (4) Divya, K. C.; Østergaard, J. Battery Energy Storage Technology for Power Systems—An Overview. *Electric Power Systems Research* **2009**, *79* (4), 511–520. <https://doi.org/10.1016/j.epsr.2008.09.017>.
- (5) Yang, Y.; Bremner, S.; Menictas, C.; Kay, M. Battery Energy Storage System Size Determination in Renewable Energy Systems: A Review. *Renewable and Sustainable Energy Reviews* **2018**, *91*, 109–125. <https://doi.org/10.1016/j.rser.2018.03.047>.
- (6) Weber, A. Z.; Mench, M. M.; Meyers, J. P.; Ross, P. N.; Gostick, J. T.; Liu, Q. Redox Flow Batteries: A Review. *J Appl Electrochem* **2011**, *41* (10), 1137. <https://doi.org/10.1007/s10800-011-0348-2>.
- (7) Alotto, P.; Guarnieri, M.; Moro, F. Redox Flow Batteries for the Storage of Renewable Energy: A Review. *Renewable and Sustainable Energy Reviews* **2014**, *29*, 325–335. <https://doi.org/10.1016/j.rser.2013.08.001>.
- (8) Reynard, D.; Dennison, C. R.; Battistel, A.; Girault, H. H. Efficiency Improvement of an All-Vanadium Redox Flow Battery by Harvesting Low-Grade Heat. *Journal of Power Sources* **2018**, *390*, 30–37. <https://doi.org/10.1016/j.jpowsour.2018.03.074>.
- (9) Soloveichik, G. L. Flow Batteries: Current Status and Trends. *Chem. Rev.* **2015**, *115* (20), 11533–11558. <https://doi.org/10.1021/cr500720t>.
- (10) Ponce de León, C.; Frías-Ferrer, A.; González-García, J.; Szánto, D. A.; Walsh, F. C. Redox Flow Cells for Energy Conversion. *Journal of Power Sources* **2006**, *160* (1), 716–732. <https://doi.org/10.1016/j.jpowsour.2006.02.095>.
- (11) Amstutz, V.; Toghiani, K. E.; Powlesland, F.; Vrabel, H.; Comninellis, C.; Hu, X.; Girault, H. H. Renewable Hydrogen Generation from a Dual-Circuit Redox Flow Battery. *Energy Environ. Sci.* **2014**, *7* (7), 2350–2358. <https://doi.org/10.1039/C4EE00098F>.
- (12) Reynard, D.; Bolik-Coulon, G.; Maye, S.; Girault, H. H. Hydrogen Production on Demand by Redox-Mediated Electrocatalysis: A Kinetic Study. *Chemical Engineering Journal* **2020**, 126721. <https://doi.org/10.1016/j.cej.2020.126721>.
- (13) Symes, M. D.; Cronin, L. Decoupling Hydrogen and Oxygen Evolution during Electrolytic Water Splitting Using an Electron-Coupled-Proton Buffer. *Nature Chemistry* **2013**, *5* (5), 403–409. <https://doi.org/10.1038/nchem.1621>.
- (14) Dotan, H.; Landman, A.; Sheehan, S. W.; Malviya, K. D.; Shter, G. E.; Grave, D. A.; Arzi, Z.; Yehudai, N.; Halabi, M.; Gal, N.; Hadari, N.; Cohen, C.; Rothschild, A.; Grader, G. S. Decoupled Hydrogen and Oxygen Evolution by a Two-Step Electrochemical–Chemical Cycle for Efficient Overall Water Splitting. *Nature Energy* **2019**, *4* (9), 786–795. <https://doi.org/10.1038/s41560-019-0462-7>.
- (15) Huang, J.; Wang, Y. Efficient Renewable-to-Hydrogen Conversion via Decoupled Electrochemical Water Splitting. *Cell Reports Physical Science* **2020**, *1* (8), 100138. <https://doi.org/10.1016/j.xcrp.2020.100138>.

- (16) McHugh, P. J.; Stergiou, A. D.; Symes, M. D. Decoupled Electrochemical Water Splitting: From Fundamentals to Applications. *Advanced Energy Materials* n/a (n/a), 2002453. <https://doi.org/10.1002/aenm.202002453>.
- (17) Wallace, A. G.; Symes, M. D. Decoupling Strategies in Electrochemical Water Splitting and Beyond. *Joule* **2018**, 2 (8), 1390–1395. <https://doi.org/10.1016/j.joule.2018.06.011>.
- (18) Zhang, F.; Wang, Q. Redox-Mediated Water Splitting for Decoupled H₂ Production. *ACS Materials Lett.* **2021**, 3 (5), 641–651. <https://doi.org/10.1021/acsmaterialslett.1c00074>.
- (19) Zhang, F.; Zhang, H.; Salla, M.; Qin, N.; Gao, M.; Ji, Y.; Huang, S.; Wu, S.; Zhang, R.; Lu, Z.; Wang, Q. Decoupled Redox Catalytic Hydrogen Production with a Robust Electrolyte-Borne Electron and Proton Carrier. *J. Am. Chem. Soc.* **2021**, 143 (1), 223–231. <https://doi.org/10.1021/jacs.0c09510>.
- (20) Peljo, P.; Vrabel, H.; Amstutz, V.; Pandard, J.; Morgado, J.; Santasalo-Aarnio, A.; Lloyd, D.; Gumy, F.; Dennison, C. R.; Toghiani, K. E.; Girault, H. H. All-Vanadium Dual Circuit Redox Flow Battery for Renewable Hydrogen Generation and Desulfurisation. *Green Chem.* **2016**, 18 (6), 1785–1797. <https://doi.org/10.1039/C5GC02196K>.
- (21) Piwek, J.; Dennison, C. R.; Frackowiak, E.; Girault, H.; Battistel, A. Vanadium-Oxygen Cell for Positive Electrolyte Discharge in Dual-Circuit Vanadium Redox Flow Battery. *Journal of Power Sources* **2019**, 439, 227075. <https://doi.org/10.1016/j.jpowsour.2019.227075>.
- (22) Reynard, D.; Maye, S.; Peljo, P.; Chanda, V.; Girault, H. H.; Gentil, S. Vanadium–Manganese Redox Flow Battery: Study of Mn(III) Disproportionation in the Presence of Other Metallic Ions. *Chemistry – A European Journal* **2020**, 26 (32), 7250–7257. <https://doi.org/10.1002/chem.202000340>.
- (23) Peljo, P.; Scanlon, M. D.; Olaya, A. J.; Rivier, L.; Smirnov, E.; Girault, H. H. Redox Electrocatalysis of Floating Nanoparticles: Determining Electrocatalytic Properties without the Influence of Solid Supports. *J. Phys. Chem. Lett.* **2017**, 8 (15), 3564–3575. <https://doi.org/10.1021/acs.jpclett.7b00685>.
- (24) Reynard, D.; Nagar, B.; Girault, H. Photonic Flash Synthesis of Mo₂C/Graphene Electrocatalyst for the Hydrogen Evolution Reaction. *ACS Catal.* **2021**, 5865–5872. <https://doi.org/10.1021/acscatal.1c00770>.
- (25) Ge, R.; Li, L.; Su, J.; Lin, Y.; Tian, Z.; Chen, L. Ultrafine Defective RuO₂ Electrocatalyst Integrated on Carbon Cloth for Robust Water Oxidation in Acidic Media. *Advanced Energy Materials* **2019**, 9 (35), 1901313. <https://doi.org/10.1002/aenm.201901313>.
- (26) Lee, H. J.; Park, S.; Kim, H. Analysis of the Effect of MnO₂ Precipitation on the Performance of a Vanadium/Manganese Redox Flow Battery. *J. Electrochem. Soc.* **2018**, 165 (5), A952. <https://doi.org/10.1149/2.0881805jes>.
- (27) Dong, Y.-R.; Kawagoe, Y.; Itou, K.; Kaku, H.; Hanafusa, K.; Moriuchi, K.; Shigematsu, T. Improved Performance of Ti/Mn Redox Flow Battery by Thermally Treated Carbon Paper Electrodes. *ECS Trans.* **2017**, 75 (18), 27. <https://doi.org/10.1149/07518.0027ecst>.
- (28) Kaku, H.; Dong, Y.-R.; Hanafusa, K.; Moriuchi, K.; Shigematsu, T. Effect of Ti(IV) Ion on Mn(III) Stability in Ti/Mn Electrolyte for Redox Flow Battery. *ECS Trans.* **2016**, 72 (10), 1. <https://doi.org/10.1149/07210.0001ecst>.
- (29) Dong, Y.-R.; Kaku, H.; Hanafusa, K.; Moriuchi, K.; Shigematsu, T. A Novel Titanium/Manganese Redox Flow Battery. *ECS Trans.* **2015**, 69 (18), 59. <https://doi.org/10.1149/06918.0059ecst>.
- (30) Tokuda, K.; Iihara, J.; Saito, Y.; Masuno, A.; Inoue, H. Structural Analysis of Sulfuric Acid Solutions Containing Ti and Mn Using X-Ray Diffraction, x-Ray Absorption Fine Structure, and Molecular Dynamics Simulation. *J. Chem. Phys.* **2018**, 149 (1), 014503. <https://doi.org/10.1063/1.5024950>.

- (31) Rubio-Garcia, J.; Kucernak, A.; Zhao, D.; Li, D.; Fahy, K.; Yufit, V.; Brandon, N.; Gomez-Gonzalez, M. Hydrogen/Manganese Hybrid Redox Flow Battery. *J. Phys. Energy* **2018**, *1* (1), 015006. <https://doi.org/10.1088/2515-7655/aace17>.
- (32) Kear, G.; Shah, A. A.; Walsh, F. C. Development of the All-Vanadium Redox Flow Battery for Energy Storage: A Review of Technological, Financial and Policy Aspects. *International Journal of Energy Research* **2012**, *36* (11), 1105–1120. <https://doi.org/10.1002/er.1863>.
- (33) Park, S.; Lee, H.; Lee, H. J.; Kim, H. New Hybrid Redox Flow Battery with High Energy Density Using V–Mn/V–Mn Multiple Redox Couples. *Journal of Power Sources* **2020**, *451*, 227746. <https://doi.org/10.1016/j.jpowsour.2020.227746>.
- (34) Reynard, D.; Maye, S.; Peljo, P.; Chanda, V.; Girault, H. H.; Gentil, S. Vanadium–Manganese Redox Flow Battery: Study of MnIII Disproportionation in the Presence of Other Metallic Ions. *Chemistry – A European Journal* **2020**, *26* (32), 7250–7257. <https://doi.org/10.1002/chem.202000340>.
- (35) Chen, D.; Hickner, M. A.; Agar, E.; Kumbur, E. C. Selective Anion Exchange Membranes for High Coulombic Efficiency Vanadium Redox Flow Batteries. *Electrochemistry Communications* **2013**, *26*, 37–40. <https://doi.org/10.1016/j.elecom.2012.10.007>.
- (36) Ligen, Y.; Vrubel, H.; Girault, H. Energy Efficient Hydrogen Drying and Purification for Fuel Cell Vehicles. *International Journal of Hydrogen Energy* **2020**. <https://doi.org/10.1016/j.ijhydene.2020.02.035>.
- (37) Carmo, M.; Fritz, D. L.; Mergel, J.; Stolten, D. A Comprehensive Review on PEM Water Electrolysis. *International Journal of Hydrogen Energy* **2013**, *38* (12), 4901–4934. <https://doi.org/10.1016/j.ijhydene.2013.01.151>.
- (38) Ligen, Y. Electrochemical systems for hydrogen fuel cell and battery electric vehicle infrastructure <https://infoscience.epfl.ch/record/282095> (accessed 2021 -06 -25). <https://doi.org/10.5075/epfl-thesis-7916>.

Appendix VI

Appendix VI-1: Energy-dispersive X-ray (EDX) spectroscopy

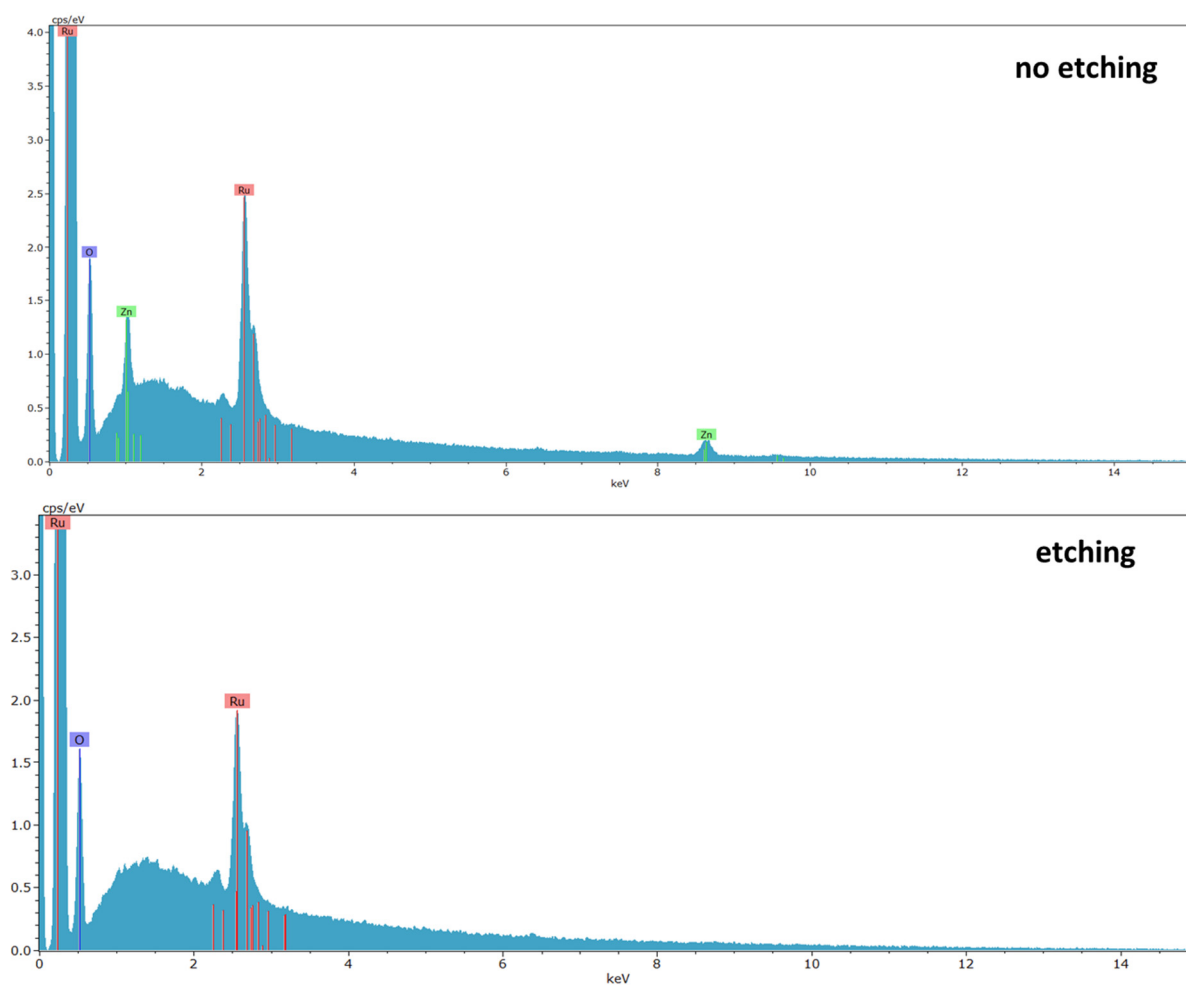


Figure A6.1 EDX spectrum of the prepared ultrafine defective RuO_2 before etching and after etching in acid to remove the zinc salts.

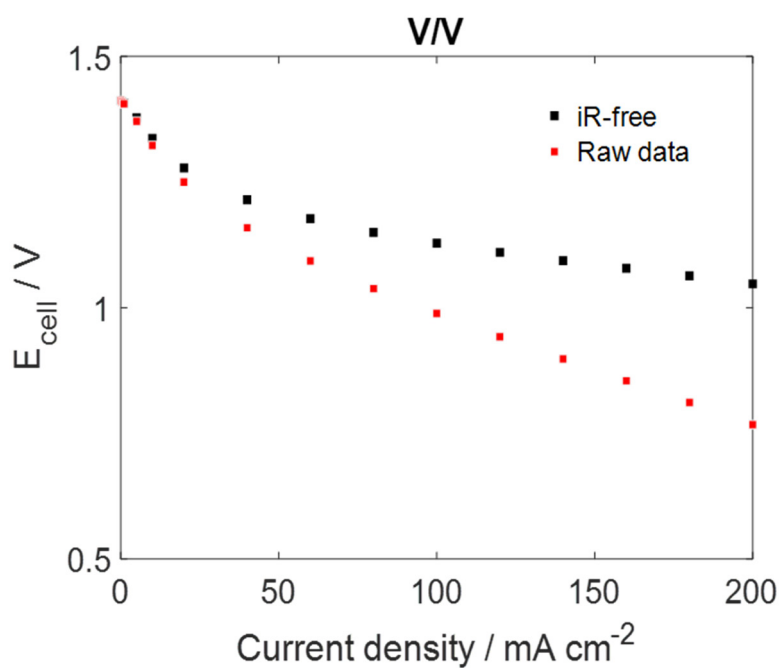
Appendix VI-2: Polarisation and power curves

Figure A6.2 Discharging polarization curve for the 1 M V/V flow cell under 75% SOC with and without iR correction.

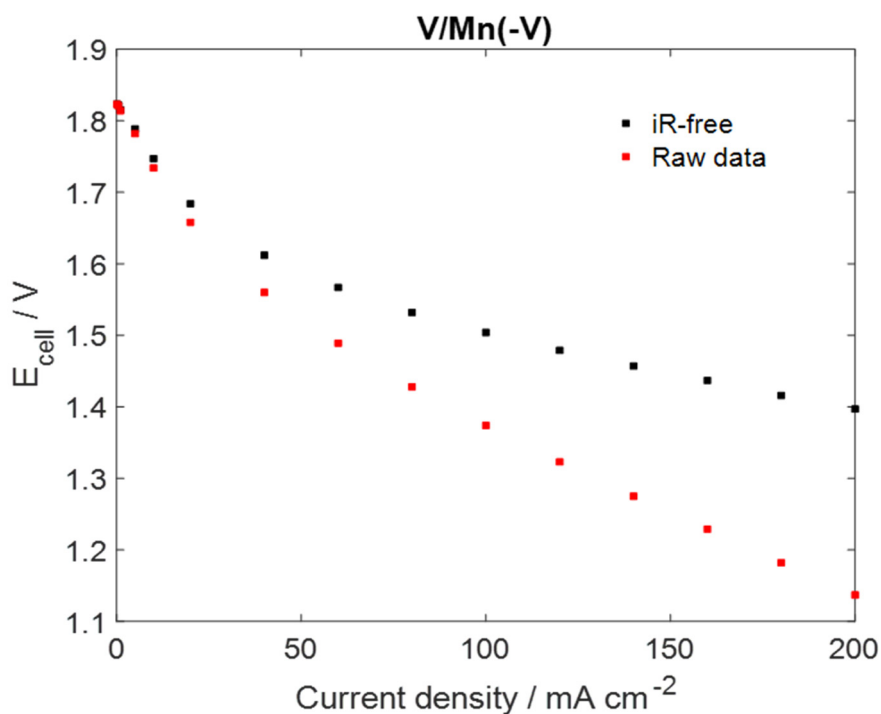


Figure A6.3 Discharging polarization curve for the 1 M V/Mn(-V) flow cell under 75% SOC with and without iR correction.

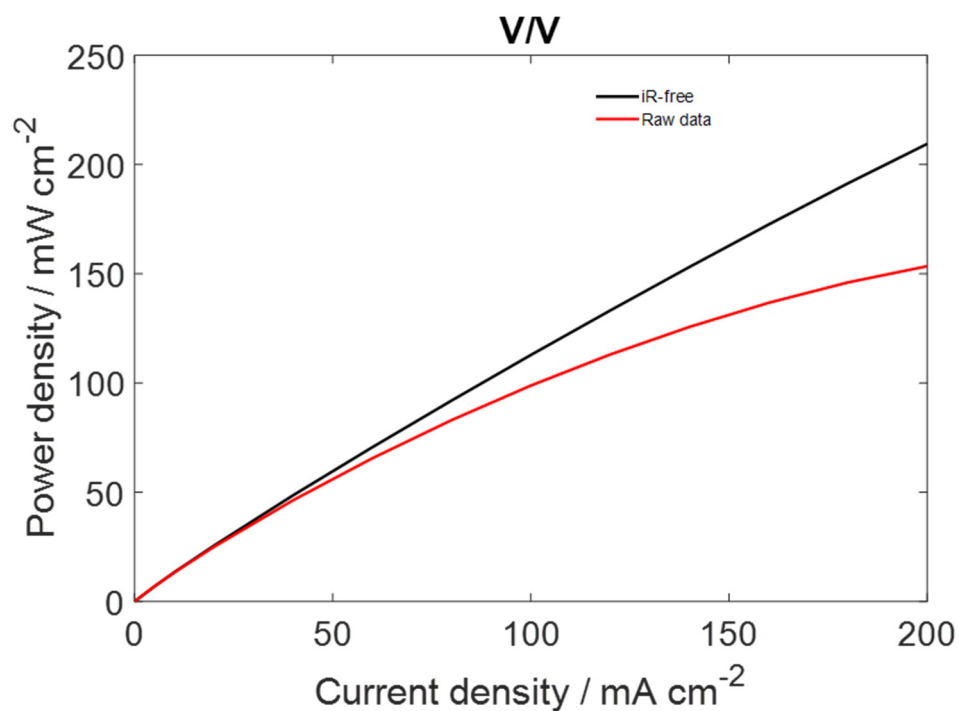


Figure A6.4 Power curves for the 1 M V/V flow cell under 75% SOC with and without iR correction.

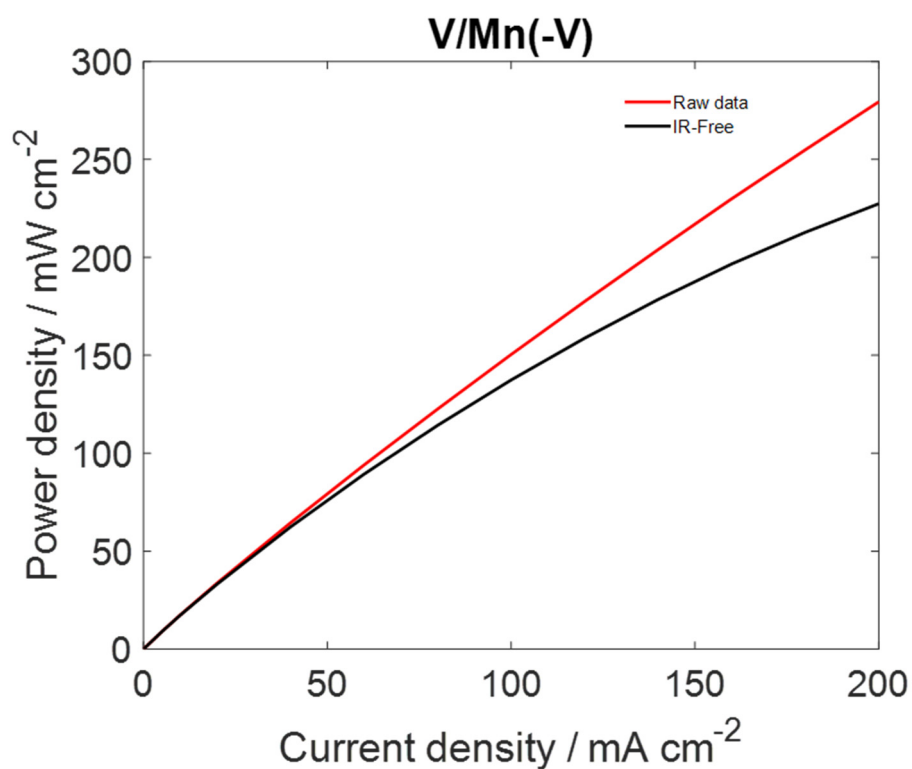


Figure A6.5 Power curves for the 1 M V/Mn(-V) flow cell under 75% SOC with and without iR correction.

Appendix VI-3: Performance of V-V flow cell

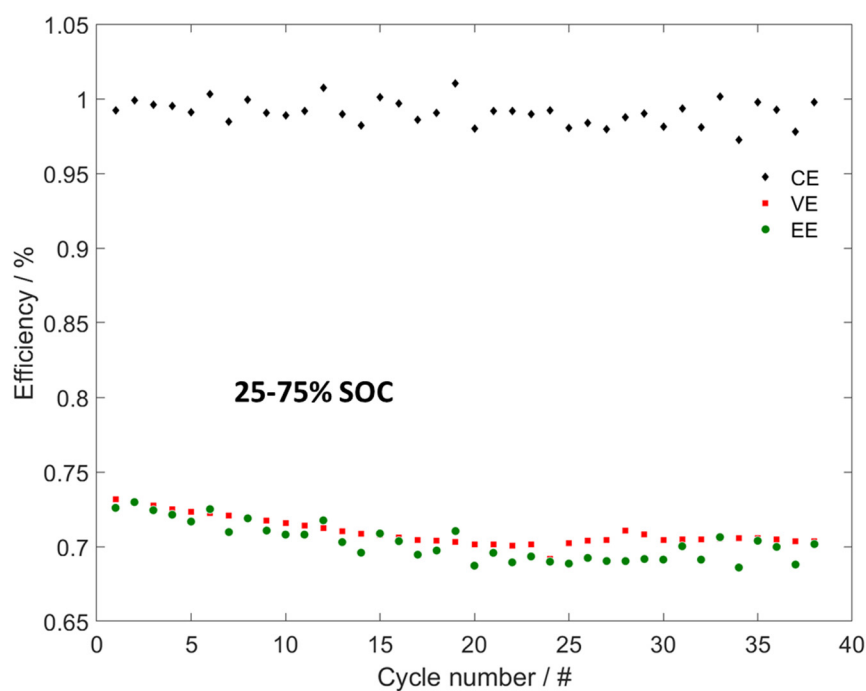


Figure A6.6 Coulombic, voltage and energy efficiencies (CE, VE, EE) for the 1 M V/V flow cell cycled between 25 and 75% SOC at 50 mA cm^{-2} .

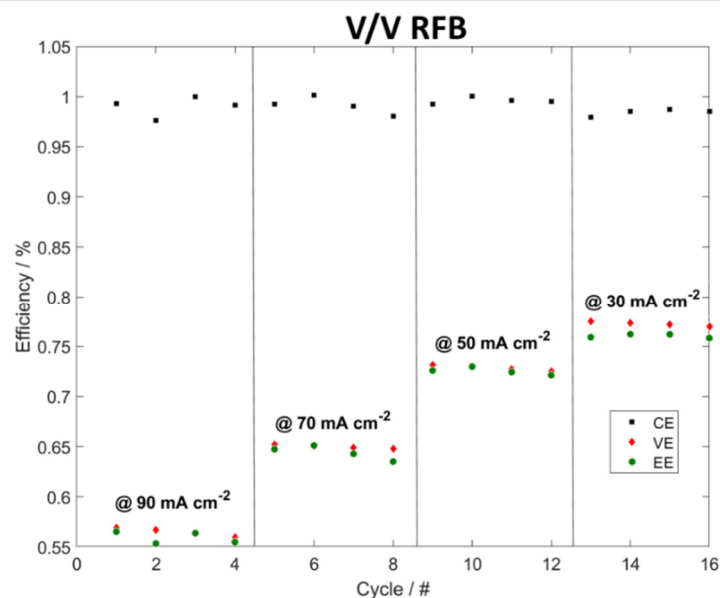


Figure A6.7 Coulombic, voltage and energy efficiencies (CE, VE, EE) for the 1 M V/V flow cell cycled between 25 and 75% SOC at various current densities ranging from 30 to 90 mA cm^{-2} .

Appendix VI-4: Charge-discharge potential curves

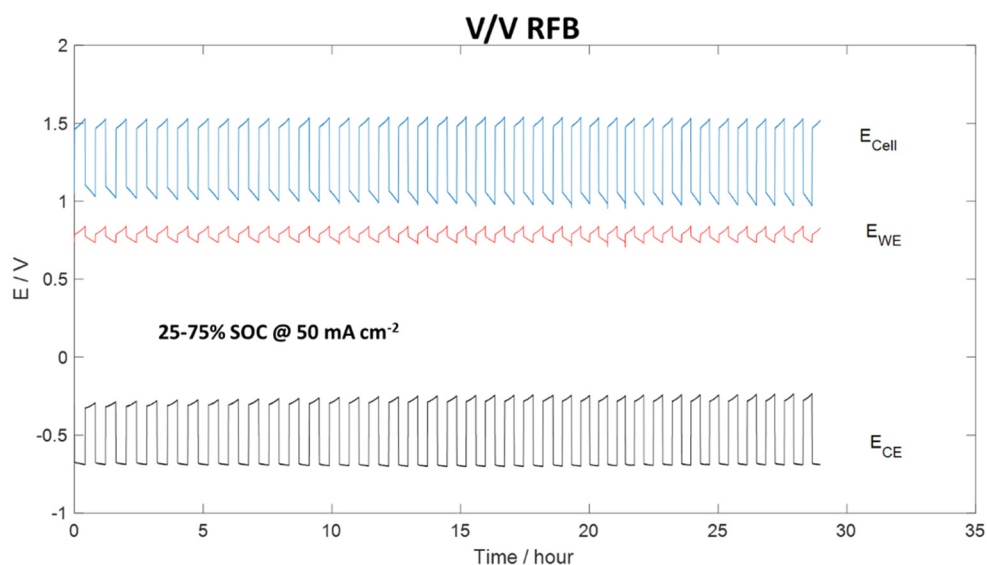


Figure A6.8 Voltage profile of the 1 M V/V flow cell operating between 25 and 75% SOC at a current density of 50 mA cm^{-2} .

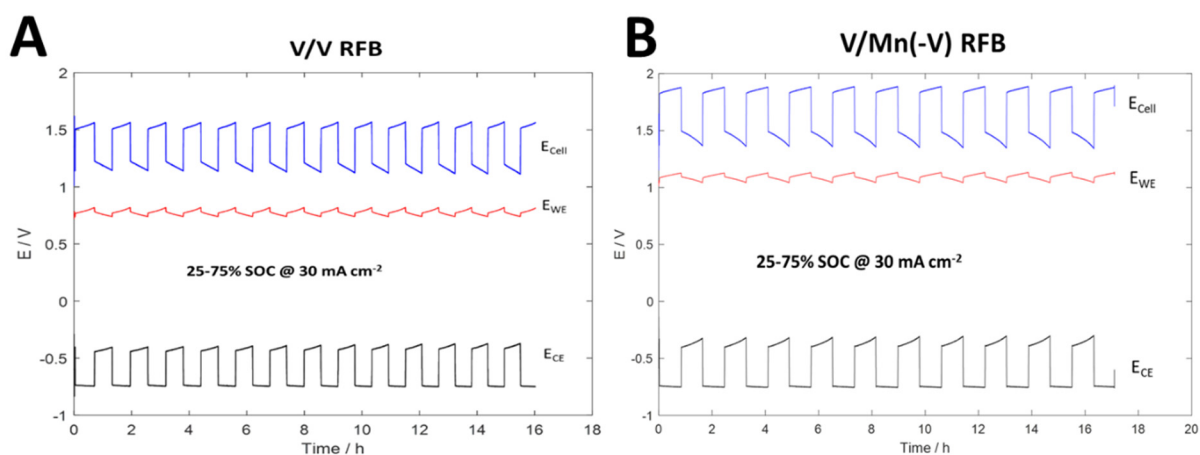


Figure A6.9 Voltage profile of the (A) 1 M V/V and (B) 1 M V/Mn(-V) flow cell operating between 25 and 75% SOC at a current density of 30 mA cm^{-2} .

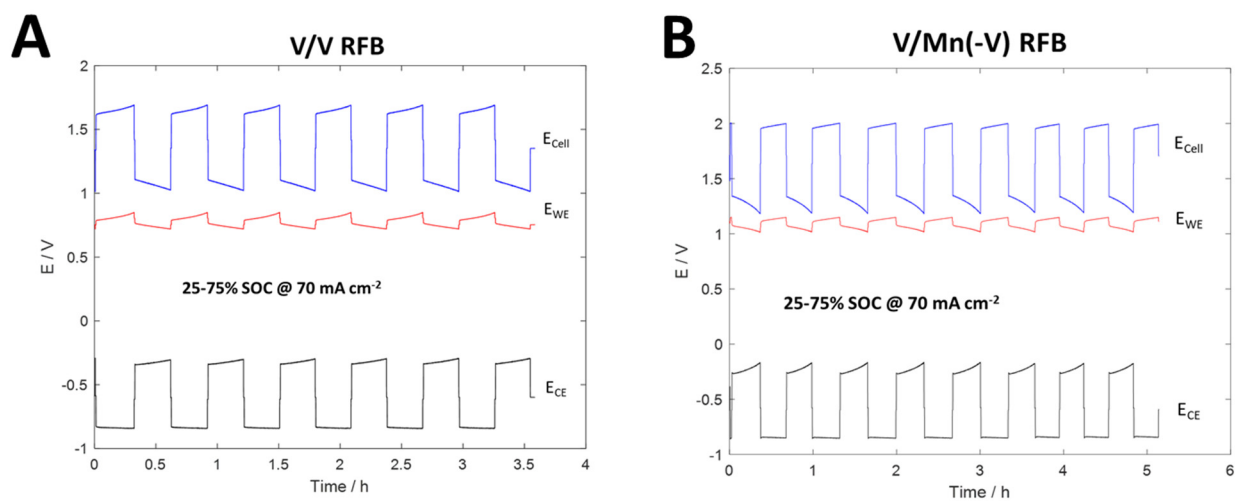


Figure A6.10 Voltage profile of the (A) 1 M V/V and (B) 1 M V/Mn(-V) flow cell operating between 25 and 75% SOC at a current density of 70 mA cm^{-2} .

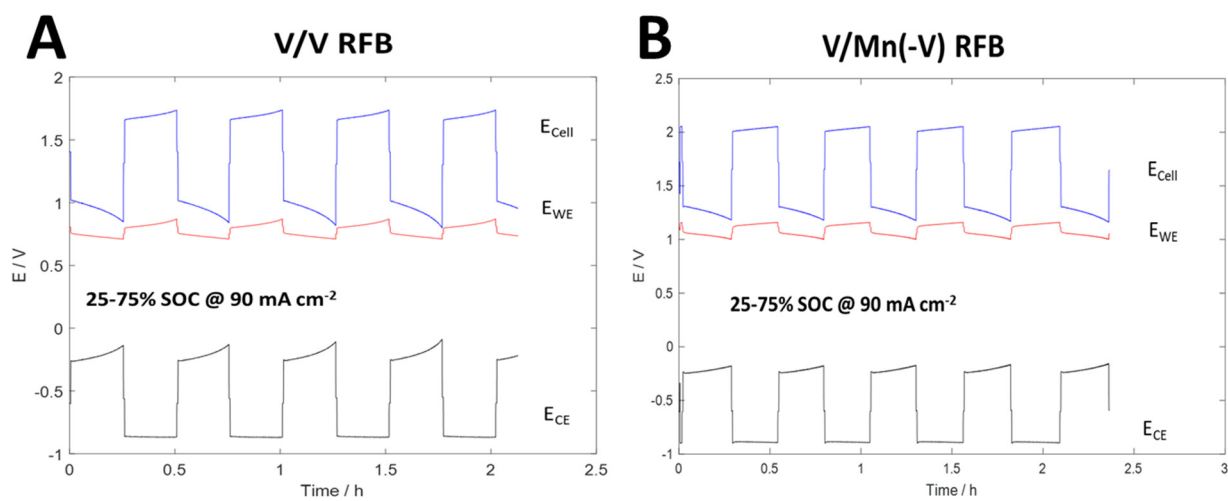


Figure A6.11 Voltage profile of the (A) 1 M V/V and (B) 1 M V/Mn(-V) flow cell operating between 25 and 75% SOC at a current density of 90 mA cm^{-2} .

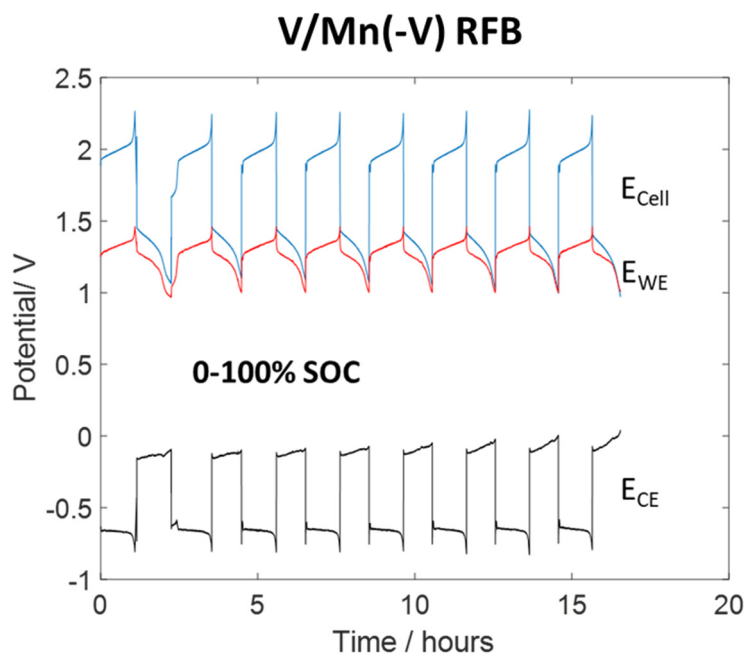


Figure A6.12 Voltage profile of the 1 M V/Mn(-V) flow cell operating between 0 and 100% SOC at a current density of $50 \text{ mA} \cdot \text{cm}^{-2}$.

Appendix VI-5: Redox-mediated hydrogen evolution reaction

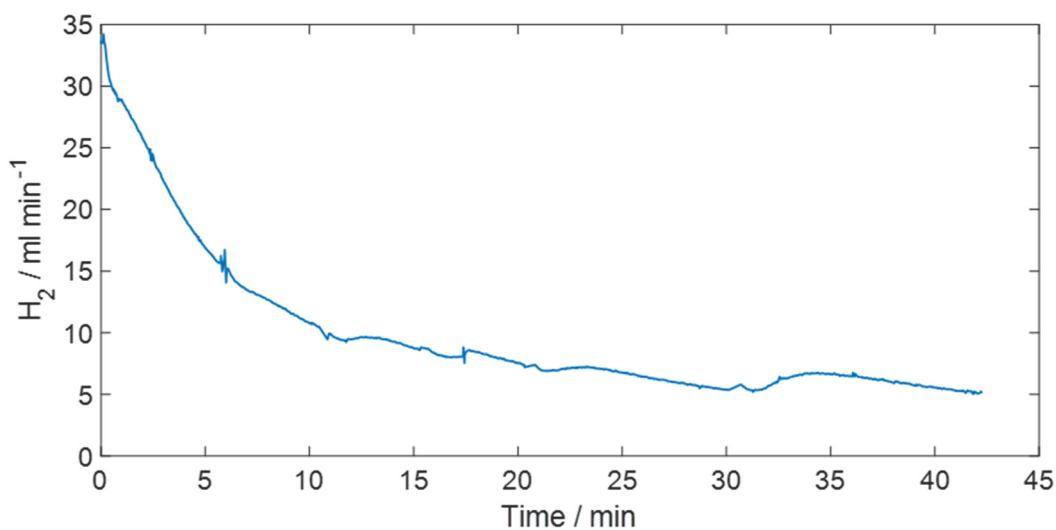


Figure A6.13 Recorded flowrate of hydrogen produced during the chemical discharge of 100 mL of 1 M $\text{V}^{3+}/\text{V}^{2+}$ (90% SOC) in 3 M H_2SO_4 at ambient pressure.

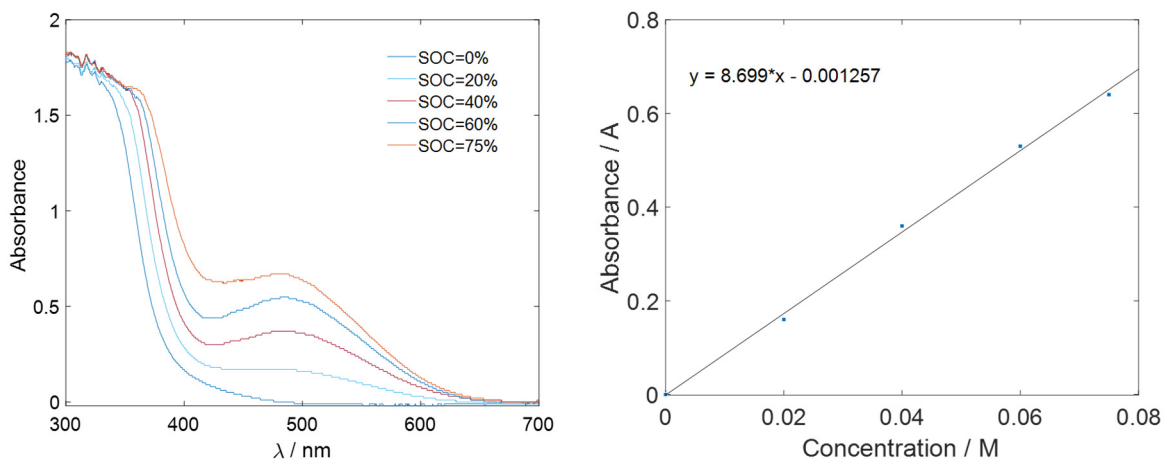


Figure A6.14 UV-vis spectra of 1 M $\text{Mn}^{3+}/\text{Mn}^{2+}$ + 1 M VO_2^+ solution in 3 M H_2SO_4 at SOC ranging from 0 to 75% and the resulting calibration curve relating the state-of-charge of the solution and the absorbance at 500 nm.

Appendix VI-6: Redox-mediated oxygen evolution reaction

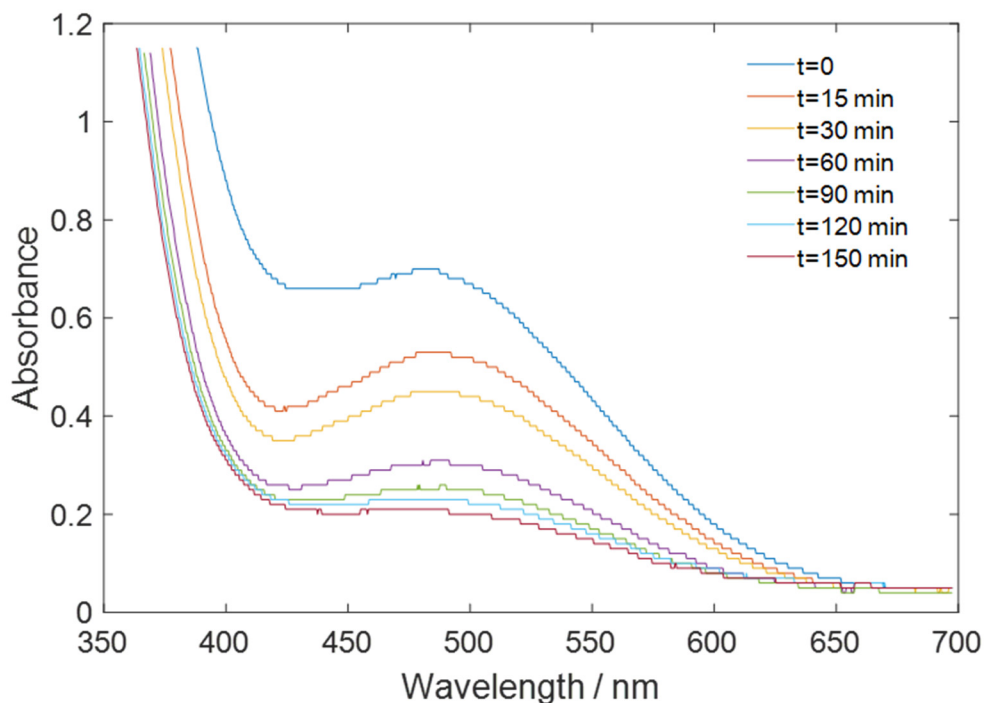


Figure A6.15 UV-vis spectra of the sample take throughout the chemical discharge of 40 mL of 0.1 M $\text{Mn}^{3+}/\text{Mn}^{2+}$ (75% SOC) + 0.1 M VO_2^+ in 3 M H_2SO_4 at ambient pressure.

CHAPTER VII

Conclusion and perspectives

Energy storage is key for the energy transition process towards a carbon-free future. With the ability to convert electricity to chemical energy and *vice versa*, battery storage and hydrogen storage stand out as two important technologies for grid-scale energy storage applications such as the implementation of renewables power sources and electric vehicle infrastructure.

Among battery technologies, redox flow batteries (RFB) have drawn considerable attention in the past years. They have the advantage to operate in safer conditions and to decouple power and capacity, offering high flexibility for large-scale energy storage. However, RFB's suffer from low energy densities and a lack of reliability on the actual life-time and cost, limiting their market penetration. In the framework of the demonstrator Electromobilis located in Martigny, premature degradations were observed on a commercial all-vanadium RFBs, mainly due to uncontrolled electrolyte imbalance and battery overcharging. As discussed in chapter II, advanced carbon corrosion on the positive half-cell led to stack leakage, copper-contamination of the electrolyte and system failure. The presence of copper in electrolyte caused a negative feedback loop by increasing the hydrogen gassing on the negative side, and thus the electrolyte imbalance. To address those issues, a purification strategy was developed on-site and was successfully employed to regenerate 6 m³ of vanadium electrolyte. The reported issues revealed the important improvements that are required in terms of operation management in order to preserve the battery from premature failure.

The concept of redox dual-flow battery was proposed as a novel approach to store energy at grid-scale. The system consists of a redox flow battery that can couple electrochemical and chemical energy storage by including a secondary energy platform, in which electrical energy can be converted into hydrogen *via* decoupled water splitting. The dual-flow system offers numerous advantages including an enhanced flexibility with two discharged mode (hydrogen or electricity generation), a storage capacity beyond the conventional RFB, a water electrolysis method able to decouple HER and OER in time, and a facilitated electrolyte balance management between the positive and the negative side.

In that respect, the main goal of the thesis was to develop a novel and eco-friendly redox dual-flow battery using a vanadium-manganese flow battery. The first challenge was to improve the stability of the manganese electrolyte in order to prevent the disproportionation of Mn^{3+} onto Mn^{2+} and MnO_2 and guarantee good performance of the system. In chapter III, the influence of TiO^{2+} or/and VO_2^+ on Mn^{3+} stability in acidic conditions was thoroughly studied. As a result, VO_2^+ was found to be an efficient substitute to TiO^{2+} for stabilizing Mn^{3+} with a net decrease of the rate of disproportionation, which was of high interest for the development of the vanadium-manganese redox dual-flow battery.

In chapter IV, the reaction kinetics of the vanadium-mediated hydrogen evolution reaction on Mo_2C electrocatalyst was studied. On the basis of a suggested reaction mechanism, a kinetic rate law was established as a function of the state-of-charge of the vanadium electrolyte, the concentration of V^{2+} and the amount of catalytic site. The proposed kinetic model was validated experimentally. Complementary, process simulations of an isothermal semi-batch reactor were performed in order to predict the optimal conditions for efficient discharge for various demands in hydrogen.

In chapter V, a simple and fast two-step process by photonic flash synthesis to prepare Mo_2C -based electrocatalysts was developed. The prepared catalyst demonstrated high activity towards HER in acidic conditions and an excellent electrochemical stability over catalytic conditions. The method was further used to design the Mo_2C catalytic reactor of the redox dual-flow battery.

The final chapter of the thesis (chapter IV) was devoted to the design, the assembly and the proof-of-concept of the vanadium-manganese redox dual-flow prototype at laboratory scale. The system employed an aqueous vanadium solution (1 M $\text{V}^{3+}/\text{V}^{2+}$ in 3 M H_2SO_4) as negative electrolyte and an aqueous manganese solution stabilized with VO_2^+ (1 M $\text{Mn}^{3+}/\text{Mn}^{2+}$ - VO_2^+ (1:1) in 3 M H_2SO_4) as positive electrolyte. The performance of the V/Mn(-V) flow cell to store electricity and to generate renewable hydrogen was evaluated. As a result, the battery mode presented great stability over 50 cycles with an average energy efficiency of 68% at a current density of $50 \text{ mA} \cdot \text{cm}^{-2}$ between 25 and 75% SOC, with an energy density 45% higher to the conventional VRFB. Furthermore, the redox-mediated HER and OER in 3 M H_2SO_4 were spontaneously conducted with production yield close to 100%. The resulting energy required to produced 1 kg of H_2 was calculated to be ca. $50 \text{ kWh} \cdot \text{kg}^{-1}$, which is in the range

of conventional electrolysis.

From a scientific point of view, several aspects would be relevant to investigate further. First, although the manganese-mediated OER was demonstrated on RuO_2 , it remains the major drawback of the presented system in terms of kinetics and cost. Therefore, further development of cheaper and more active redox electrocatalysts for OER is desired. Besides, the synthetic pathway developed in chapter V could be applied for the preparation of electrocatalytic electrodes to carry redox-mediated oxygen evolution reactions. Moreover, kinetic parameters of the redox mediated OER remains unknown, supporting further studies towards the development of a kinetic model. Note that the determination of the thermodynamic parameters such as temperature or pressure effect on the redox-mediated HER and OER was not covered in this thesis and is an essential investigation in order to design and optimize the reactions. In addition, further investigations are required to optimize the formulation of the electrolyte (acid concentration, solubility limit, manganese-vanadium ratio...). Finally, the use of vanadium ions as redox active species in the posolyte consists of a further improvement in order to enhance the energy capacity of the battery.

In the regard of a scale-up, the system must face several technical challenges that are not encountered at laboratory scale. First, the positive electrolyte was observed to be sensitive to rise of temperature by increasing the disproportionation rate. Thus, it would be necessary to perform system heat testing in order to manage optimally the operating temperature at larger scale. Then, the energy capacity, the efficiency and the lifetime of the system must be evaluated on longer period of time considering the issues that can rise from a scale-up (*e.g.* electrolyte crossover, electrolyte precipitation, electrolyte imbalance, catalytic stability and activity, catalyst migration in the electrochemical cell...)

All in all, this thesis demonstrated that the vanadium-manganese dual-flow system provides a promising alternative for energy storage solution for both distributed energy storage and on-demand hydrogen generation, especially when power is generated by renewable resources. In addition to the energy performance of the system, the decoupled feature of the redox-mediated water splitting offers several advantages for the on-demand production of renewable hydrogen in terms of purity, efficiency and kinetics. As a future perspective, the presented redox dual-flow battery can be exploited for the development of future service station for both fast charging of electric vehicles and hydrogen refilling of fuel cell vehicles (Figure 7.1).

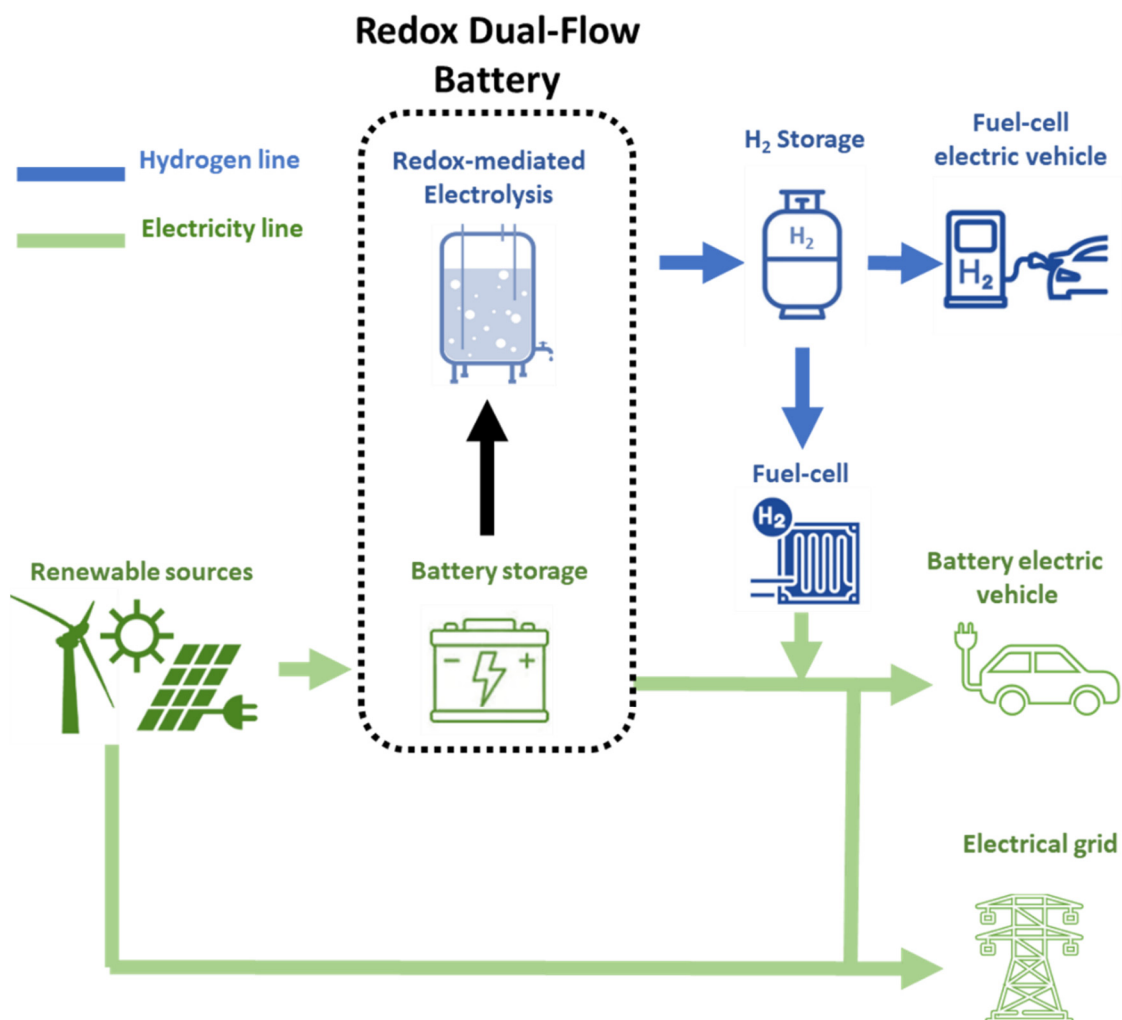


Figure 7.1 Schematic of a service station for hydrogen fuel cell and battery electric vehicle infrastructure using a redox dual-flow battery system.

Danick REYNARD

Rue de Vétroz 12
1964 Conthey

☎ 079/ 297 13 45

✉ danick.reynard@gmail.com

28-year-old

15.06.1993

Switzerland

Single

**Formation and Diploma**

- ❖ **Master in chemical engineering and biotechnology-** École Polytechnique Fédérale de Lausanne-*Master project, EPFL: Low-grade heat recovery with all-vanadium redox flow battery* 2015-2017
- ❖ **Bachelor in chemistry and chemical engineering** - École Polytechnique Fédérale de Lausanne - *Exchange during 3^d year, Lunds Tekniska Högskola, Sweden* 2012-2015
- ❖ **Federal high-school diploma of science** - Lycée-Collège de la Planta, Sion VS 2007-2012

Professional Experience

- ❖ **Doctoral assistant**– Laboratory of physical and analytical electrochemistry, LEPA, EPFL 2017-2021
 Research duties: *Electrochemical solutions for energy storage (battery and hydrogen economy)*
 Teaching duties: *Electrochemistry, chemistry and chemical engineering laboratory work*
 Other duties: *Supervision and technical expertise for research and consulting projects in chemical engineering and energy field*
 Award: *Best poster and presentation, International Flow Battery Forum, 2021*
- ❖ **R&D Engineer internship** – Stérilux SA, Yverdon-Les-Bains 2016-2017
 Development of low-temperature sterilization device, technical expertise for analytical techniques, project management in development
- ❖ **Tutoring in math and chemistry** 2009-2016
- ❖ **Handwork** 2009-2015
 Baumgartner et Léger, Savièse VS, *sanitary-tinware-heating tasks*
 Videsa Sion, Sion VS, *sanitation compagne*
 Public work. Municipality of Savièse VS. various maintenance tasks

Competences

- ❖ Excellent skills of analysis, planification, communication and team working
- ❖ Advanced knowledge in chemical engineering, process development and process safety
- ❖ Excellent expertise in edition software (MS Office, Latex), data analysis software (Matlab, Excel Office, Origin) and process simulator (Aspen Plus, DWSIM)
- ❖ Ability to lead a project, independent worker, quick learner, curious and sociable

Languages

- | | |
|-----------|---------------------|
| ❖ English | Advanced (CEFR :C1) |
| ❖ German | Basic (CEFR : B1) |
| ❖ French | Mother tongue |

Other activities

- ❖ Vice-president de GABA : transmetteur de découvertes – organisation of conferences
- ❖ Vice-president of Classe 1993 Savièse – organisation of events
- ❖ Running, mountain, squash, travelling, cooking, brewing and winemaking

Main scientific publications

- ❖ D. Reynard and H. Girault, Combined hydrogen production and electricity storage using a vanadium-manganese redox dual-flow battery, Cell Reports Physical Science, 2021
- ❖ D. Reynard, B. Nagar, H. Girault, Photonic flash synthesis of Mo₂C/Graphene Electrocatalyst for the hydrogen evolution reaction, ASC Catalysis, 2021
- ❖ D. Reynard, G. Bolik-Coulon, S. Maye, H. Girault, Hydrogen production on demand by redox-mediated electrocatalysis: A kinetic study, Chemical Engineering Journal, 2020
- ❖ D. Reynard, S. Gentil, Hubert H. Girault, Aqueous organic and redox-mediated redox flow batteries: a review, Current Opinion in Electrochemistry, 2020
- ❖ D. Reynard, S. Maye, P. Peljo, H. Girault, S. Gentil, Vanadium–Manganese redox flow battery: Study of Mn(III) disproportionation in the presence of other metallic ions, Chemistry–A European Journal, 2019
- ❖ D. Reynard, H. Vrubel, C.R. Dennison, A. Battistel, H. H. Girault, On-site purification procedure of a copper-contaminated vanadium electrolyte in a VRFB system, ChemSusChem, 2019
- ❖ D. Reynard, C. R. Dennison, A. Battistel, H. H. Girault, Efficiency improvement of an all-vanadium redox flow battery by harvesting low-grade heat, Journal of Power Sources, 2018